

Development of a Cold Stage to Measure Ice Nucleating Activity Produced by Biomass Burning: Ash, Aerosol, and Aging

Submitted in partial fulfillment of the requirements for

the degree of

Doctor of Philosophy

in

Chemistry

Michael J. Polen Jr.

B.S., Chemistry, Widener University

Carnegie Mellon University

Pittsburgh, Pennsylvania, USA

July, 2018

©Michael Joseph Polen Jr., 2018

All Rights Reserved

Dedicated to my parents, my sisters and my grandparents for their support over the years

Acknowledgements

I would firstly like to thank my adviser, Ryan Sullivan for affording me the opportunity to work with him on these projects and others during my time at CMU. He was supportive of my efforts both in and out of the lab and helped me become the researcher and scientist I am today.

I would also like to thank my committee: Neil Donahue, Linda Peteanu, and Peter Adams. You have all provided support throughout my tenure here and guided me to become as successful as I am now.

Funding was provided by the NSF Graduate Student Fellowship. I am also thankful for the Steinbrenner Fellowship and the Joseph A. Solomon Jr. Memorial Fellowship.

For being my biggest role model and the reason I pursued academia as long as I have, I want to thank Mr. Glenn Adams from Pottsgrove High School. He was the reason I chose to continue my career in chemistry and to explore the scientific world after high school.

The Widener University Chemistry Department was filled to the brim with amazing professors and mentors that all worked their hardest to help me succeed. For that I am eternally grateful.

Thanks to Lydia Jahl for making most of the biomass burning work possible. She was the responsible one who got those experiments to work every time. And it was a joy road tripping with her to North Carolina and collecting samples in the wetlands despite the mass of insects and critters.

Thanks to Tom Brubaker for pushing so hard on developing the image analysis and making it as robust as it is now. And of course for all the distractions and fun times we shared.

Kyle Gorkowski, Adam Ahern, and Hassan Beydoun were great mentors and friends who taught me the ropes of being a researcher and a CAPSian. Thanks for the long discussions of research and life.

Qing Yi, Leif Jahn, and Bailey Bowers are great colleagues, scholars, and friends and I'm thankful for getting to know you all over the last few years.

Thanks to Emily Lawlis, Holly Stokes, Mahir Kothari, Rushi Dave, Anirudh Narain, and Josh Somers for being the undergraduate researchers who made a lot of this work possible and more enjoyable.

I also have to thank Gabrielle Clark for being an amazing addition to my life since starting this research. She has helped me get through all the good and bad times and always with a smile. I'm very much looking forward to continuing to grow and explore with you. I love you.

And last but not least, support from my parents, grandparents, sisters, and other friends and family have been a constant motivator even at a distance. Thank you all for everything.

Abstract

Ice nucleation is a fundamental process in the atmosphere that is difficult to study in a controlled manner. In this dissertation I developed a cold stage instrument to study the properties of ice nucleating particles found in the atmosphere. The CMU-Cold Stage has been used to probe many different particle types to determine the impact they have on cloud glaciation. To properly assess the capabilities of the CMU-CS, I performed numerous tests of the background pure water signal and impacts of water source and surface interactions. To compare the abilities this system against other ice nucleation instruments I examined the ice nucleating ability of a biological particle surrogate, Snomax. However, atmospheric ice nucleating particles are much more complex than simple ice nucleating standards, so I studied different ice nucleating particles produced by biomass combustion. In particular, I examine the mechanisms and ice activity of the ash generated by biomass burning and the emissions given off by the combustion process. This work for the first time explores the ice nucleating activity of different products of biomass burning and their impacts on cloud glaciation.

I designed a substrate-based droplet freezing instrument to explore immersion mode freezing of microliter volume droplets. For any substrate-based freezing experiments, I identified important considerations that should be tested by all researchers. I examined the effect of different surfaces on pure water nucleation as well as water generation and source. I established a list of recommendations for all researchers to follow to improve the uniformity of ice nucleation methods.

I compared the CMU-CS against other methods by using the biological particle surrogate Snomax. Snomax has previously been shown to be a good proxy for biological ice nucleating particles. However, I found that the product does not behave consistently when stored for long periods of time. Its IN ability decreases to the level of weaker monomers and dimers of the ice-active protein as opposed to the high temperatures of the aggregates. This effect was also observed for repeated freezing and thawing of the droplets containing Snomax. I saw similar activity to other methods with the caveats of that activity not being consistent over time. For the first time I showed that Snomax should be cautiously used as a surrogate for biological particles and never over long periods of time.

I then used the CMU-CS to study the products of biomass burning ash. Ash from combustion was recently found to contain ice nucleating particles. However, this was never examined for grasses, which are the most susceptible to wildfires. I found that grass ash, unlike wood ash, contains high amounts of mineral phases compared to amorphous material. This is correlated to the amount of ice nucleating potential of the ash. Grasses burn with much higher temperature, which is also correlated to the amount of mineral phases present in the ash produced. For the first time I linked biomass burning efficiency to the ice nucleating particles present in the ash generated.

I also performed experiments examining the ice nucleating particles emitted from biomass burning. These particles are known to be inconsistently produced by combustion of biomass and the mechanisms that cause them to be active are still unknown. I also examined how this ice nucleating ability was altered by atmospheric chemical aging by various oxidation mechanisms. I found that many tall grasses produce ice nucleating particles which are enhanced by oxidation. However, one instance where elevated organic

aerosol was present I saw a decrease in ice nucleating ability upon aging. I saw that emission from wood burning contain almost no ice nucleating particles unlike grasses, a similar result to the ash findings. I also began testing a microfluidic device to lower the variable background of the CMU-CS traditional method, which helps to detect low activity particles from biomass burning aerosol.

These experiments improve our current understanding of the ice nucleating properties of particles in the atmosphere and how we measure them. While the method itself is not new, the methods I used to approach these measurements were novel and important to developing our understanding of ice nucleation. This work will lead to better understanding of atmospheric ice nucleation and its effects on clouds, weather, and climate.

Table of Contents

Acknowledgements	iv
Abstract	vii
Table of Contents	x
List of Tables	xvi
List of Figure.....	xvii
1 Introduction.....	1
1.1 The importance of ice nucleation in the atmosphere.....	1
1.2 Mechanisms of ice nucleation	3
1.3 Known types and sources of ice nucleating particles in the atmosphere	7
1.4 Methods of measuring immersion-mode ice nucleating particles.....	12
1.5 Thesis overview.....	18
2 Instrumentation design, experimental methods, and data analysis approaches	22
2.1 Basic design considerations	22
2.2 First iteration of the CMU cold stage.....	22
2.3 Second iteration of the CMU cold stage	24
2.4 Improvements to droplet imaging analysis	26
2.5 Analysis software in Igor Pro.....	28

2.6	Analyzing droplet freezing measurements	28
3	Cleaning up our water: reducing interferences from non-homogeneous freezing of “pure” water in droplet freezing assays of ice nucleating particles	31
3.1	Abstract	31
3.2	Introduction	32
3.3	Droplet freezing methodology	38
3.4	Ice nucleating particle analysis	41
3.5	Results	43
3.5.1	Droplet immersion matrix: oil versus air	43
3.5.2	Water sources and purification	46
3.5.3	Substrate tests.....	50
3.5.4	Droplet creation methods.....	61
3.6	Discussion	62
3.7	Recommendations for droplet freezing method and analysis protocols	64
4	The unstable ice nucleation properties of Snomax® bacterial particles.....	72
4.1	Abstract	72
4.2	Introduction	73
4.3	Methods and Materials	76
4.4	Results and Discussion.....	80
4.4.1	Decrease in Ice Nucleation Ability Over Months Timescale	80

4.4.2	Effect of Immersion Oil on Snomax Freezing Temperature during Refreezes	86
4.4.3	Effects of Different Immersion Oils on Droplet Refreezes	90
4.4.4	Effects of Time versus Refreezes on Loss of Most Efficient Ice Nucleants	94
4.4.5	Comparison to Other Oil Immersion Droplet Freezing Experiments on Bacterial Particles	97
4.5	Conclusions	98
5	Entrained ash and soil particles: an unrecognized source of ice nucleating particles from biomass burning	100
5.1	Abstract	100
5.2	Introduction	101
5.3	Samples and Methodology	104
5.4	Results and Discussion.....	107
5.4.1	Dependence of ash freezing ability on fuel type and combustion efficiency	107
5.4.2	Influence of combusted soil particles on the resulting ash	113
5.5	Conclusions and Atmospheric Implications.....	115
6	The impact of aging on ice nucleating particles produced from biomass burning .	117
6.1	Abstract	117
6.2	Introduction	118

6.3	Biomass burning experimental setup	123
6.4	2015 initial BBA experiments.....	124
6.4.1	Aging of sawgrass burning aerosol slightly enhances INP.....	127
6.5	Probing INP production from a variety of fuels.....	129
6.5.1	Comparison of ice-activity of BBA produced from wood vs. tall grasses	130
6.5.2	Contribution of root combustion and soil to ice-activity of biomass-burning aerosol	134
6.5.3	Enhancement of ice-activity following aging of BBA from cutgrass combustion.....	135
6.6	Isolating important fuels for INP measurements.....	138
6.6.1	Investigating the impact of soil and roots on INPs emitted by combustion of cutgrass and <i>Arundo</i>	139
6.6.2	Investigation of the impact of aging on wiregrass BBA.....	142
6.6.3	Testing a new microfluidic device for assessment of INPs in BBA with reduced background freezing interference.....	144
6.7	Initial BBA experiments using high-volume droplet arrays	145
6.7.1	Effect of dark ozonolysis on the ice-activity of sawgrass BBA	146
6.7.2	Effect of dark ozonolysis on the ice-activity of cutgrass BBA.....	148
6.8	Conclusions	150
7	Conclusions.....	152
7.1	Future Directions.....	156

8	Appendix A.....	159
8.1	Temperature Calibrations.....	159
8.2	Post analysis	163
8.3	Active site density calculations.....	170
8.4	Statistical Analysis	171
	References.....	180

List of Tables

Table 4.1. Reported fluid properties of the three immersion oils used in our droplet freezing experiments.....	94
Table 5.1 Ash sample characteristics for our samples and related literature reports. BET surface area values, total particle surface area per droplet, and mineral phase % composition from XRD analysis.....	111

List of Figure

Figure 1.1. Schematic of different ice nucleation mechanisms. Brown cubes represent ice nucleating particles, blue circles represent liquid, supercooled water, and white hexagons represent ice crystals. Figure is adapted from Hoose and Möhler [2012].	4
Figure 1.2. Diagram of the CMU-CS. Reprinted from Polen et al. [2016].	14
Figure 1.3. Schematics showing the droplet array from our microfluidic chip used for ice nucleation measurements. Left: the complete device consists of 720 droplet holding wells. Right: dimensions of an individual well in the left image.	15
Figure 1.4. Schematic of the Cryogenic Refrigerator Applied to Freezing Test (CRAFT). Reprinted from Tobo [2016].	16
Figure 1.5. Schematic of the LACIS instrument. The abbreviations stand for TH: thermostat, DPM: dew point hygrometer, CPC: condensational particle counter, OPC: optical particle counter. Reprinted from Hartmann et al. [2011].	17
Figure 1.6. Diagram of the AIDA cloud expansion chamber. Reprinted from Möhler et al. [2001].	18
Figure 2.1. CMU cold stage (CMU-CS) first iteration design. Image taken from Polen et al. [2016].	23
Figure 2.2. CMU-CS second iteration	25
Figure 3.1. Comparison of averaging data from droplet freezing experiments on 120 total droplets measured using three replicate arrays of 40 droplets each (red with error bars) versus combining those 120 droplets into one single hypothetical array of droplets (blue).	

The standard deviation from the average of the three replicate arrays is shown by the vertical error bars.41

Figure 3.2. Progression of frost halos in one pure water droplet freezing experiment without an oil matrix. Dark droplets are frozen. The black line highlights the frost growth (which is visible in the image but difficult to see) spreading from the bottom left toward the top of the image. Aside from the indicated frost growth, we can also see that other droplets induce freezing in neighboring droplets, such as the droplet on the far right in image 1 (red arrow) and the top right droplet in image 2 (yellow arrow). Subsequently induced droplets are indicated by similarly colored arrows.45

Figure 3.3. Comparison of pure water freezing using filtered MilliQ produced water and filtered purchased HPLC water. Shown are the measured droplet freezing temperature spectra (left) and the derived INP concentration (right). HPLC water was filtered using a new Anotop 0.02 μm filter for each bottle of water (blue), or the same filter for multiple stock bottles of water (black). The results from typical MilliQ water arrays are shown in purple. The parentheses next to each legend entry contains the number of arrays of droplets (A) and the total number of droplets across all arrays (N).....48

Figure 3.4. A series of tests on MilliQ generated water droplets to determine contamination sources. Droplets displayed inexplicably high freezing temperatures compared to filtered HPLC water at the time (solid brown with error bars). Temperatures for N_{50} ranged from -20 °C to -29 °C from day to day. Error bars indicate standard deviation of data for the filtered HPLC water.49

Figure 3.5. Droplet freezing temperature spectra (left) and apparent ice nuclei concentration, c_{IN} , (right) for pure water droplet freezing measurements on a hydrophobic

cover slip. In all experiments HPLC water that was filtered using an Anotop 0.02 μm syringe filter was used. Each data series has been binned into 0.5 $^{\circ}\text{C}$ temperature increments. The red data series is from large (1.0 μL) droplets, green is from large (1.0 μL) droplets measured alongside biomass burning aerosol sample droplets (Figure 3.12), blue is from small (0.1 μL) droplets using a new Anotop filter for each stock bottle of filtered water, and black is small droplets using a singular Anotop filter for many different stock bottles of water. The parentheses next to each legend entry contains the number of arrays of droplets (A) and the total number of droplets across all arrays (N) tested for each experiment type. Error bars are standard deviations for the replicate droplet arrays.52

Figure 3.6. Comparison of freezing on silicon wafer chips (green) against hydrophobic cover slips (blue), following Figure 3.5. The freezing temperature spectrum is on the left, and the retrieved c_{IN} is on the right. Both datasets use 0.1 μL droplets. The data from all replicate arrays using silicon (green) are combined into one series and thus no error bars can be determined. The parentheses next to each legend entry contains the number of arrays of droplets (A) and the total number of droplets across all arrays (N).54

Figure 3.7. Pure water droplet experiments on a Vaseline coated substrate, following Figure 3.5. The HPLC water using a silanized coverslip data in blue are displayed for comparison and is the data from the hydrophobic cover slip using small droplets (Figure 3.5, blue). The data from replicate arrays for Vaseline is combined as described in Section 2 and thus no error bars are determined for these. Three sets of experiments on Vaseline are shown: black is small droplets (0.1 μL) of HPLC filtered water in oil, red is large droplets (1.0 μL) without oil, and green is large droplets of MilliQ water without

oil. The parentheses next to each legend entry contains the number of arrays of droplets (A) and the total number of droplets across all arrays (N).56

Figure 3.8. Measurements of pure water droplet freezing on gold substrates are shown following Figure 3.5. The data from small HPLC water droplets on a silanized cover slip are displayed in blue for comparison (Figure 3.5, blue). The gold data displayed are using HPLC water droplets on a gold wafer substrate (brown), small MilliQ droplets on a gold-coated glass coverslip (GCS) (lilac), and large HPLC water droplets on a GCS (green). Also displayed are data from small droplets on another gold wafer upon first use (red), and subsequent small droplet arrays on the same wafer following cleaning and drying, with associated error bars (orange). The parentheses next to each legend entry contains the number of arrays of droplets (A) and the total number of droplets across all arrays (N). Error bars show standard deviation from replicate droplets arrays. The data from the gold wafer (brown and red) and small droplets on a GCS (lilac) were combined into one series and so no error bars are derived.....58

Figure 3.9. Measurements of HPLC pure water droplet freezing on PDMS are shown in red and green, following Figure 3.5. The data from small droplets on a silanized coverslip are displayed for comparison in blue (Figure 3.5, blue). The PDMS data was obtained using treated (red) and untreated (green) PDMS polymer with small droplets. The parentheses next to each legend entry contains the number of arrays of droplets (A) and the total number of droplets across all arrays (N). Error bars on green data show standard deviation from replicate arrays, while the red data are combined into one series as explained in section 2.....60

Figure 3.10. Comparison of pure water droplet freezing in our new microfluidic chip (red) versus using a silanized cover slip (CS) (blue), following Figure 3.5. Droplets in the microfluidic chip are 6 nL in volume and droplets on the CS are 0.1 μ L. Error bars show variability of droplet freezing between different replicate arrays. The parentheses next to each legend entry contains the number of arrays of droplets (A) and the total number of droplets across all arrays (N).61

Figure 3.11. Summary of pure water droplet freezing spectra for different substrates tested. Boxes show the 25% and 75% frozen quartiles and the median, N_{50} , is indicated by the line inside each box. Red markers are the temperatures of the first onset freezing droplets with error bars showing variability between different replicate droplet arrays. No error bars for the onset freezing for Vaseline and gold wafer are shown because only one array was run of each. Whiskers show the 10% and 90% droplet frozen fractions. Next to each substrate name in parentheses is the number of droplets tested. Filtered HPLC water droplets produced by an electronic pipette were used in all of these measurements, except for the microfluidic chip which generated the droplets on-chip. Droplets were 0.1 μ L in volume, except for the 1.0 μ L on the coverslip, and the 6 nL droplets created in the microfluidic chip.64

Figure 3.12. Image of droplets containing biomass burning aerosol (left half) and pure water droplets (right half) immersed in squalene oil on a silanized glass cover slip. Droplets containing aerosol sample have mostly frozen (turned dark) and pure water droplets have remained largely unfrozen (grey) at -23 $^{\circ}$ C.....70

Figure 4.1. Diagram of the CMU-CS immersion freezing cold stage measurement system. The liquid chilled plate is maintained at -25 $^{\circ}$ C using the recirculating chiller. The Peltier

element is ramped between 10 °C and -40 °C, or until all droplets are frozen, typically at 1 °C/min. Dry air above and below the acrylic window keeps the surface of the oil and window dry. Droplets are visualized using the optical microscope and camera, and their temperature determined by the thermistor placed under the aluminum sample dish.79

Figure 4.2. Freezing temperature curve of 0.01 wt% Snomax droplets immersed in squalene oil, from the first freezing cycle. Open diamonds represent the old Snomax batch that was stored in a freezer for 11 months before use. The new batch of Snomax (solid squares) was purchased and used immediately. Number of months indicates the time between the date the Snomax batch was received and the respective freezing experiment. After a few months of experiments, the freezing curves shifted to lower temperatures for both the new and old Snomax batches.....81

Figure 4.3. Ice nucleation active site density of Snomax normalized to particle mass concentration in the droplets (n_m), as a function of temperature for the old (left) and new (right) batches of Snomax. A wide variety of Snomax in droplet mass concentrations were used, and several concentrations were repeated (indicated by the number in parentheses). Squalene immersion oil was used for all these experiments. Freezing experiments on the new Snomax batch were performed within three months of receiving the material. Experiments of the old Snomax batch were performed between 11 and 14 months after receiving the material. The gray region indicates the bounds of the Wex et al. [2015] results for Snomax. Note the x-axis is reversed to be consistent with the results of Wex et al. [2015].83

Figure 4.4. Comparison of the freezing temperature of an array of droplets with 0.01 wt% Snomax particles in squalene from the old or new Snomax batch. The bottom axis

represents the amount of time the sample was in our possession before the given experiment, and stored in a freezer when not in use. The box and whisker plot displays the median and quartile freezing temperature as the lines in the box, and the 10th and 90th percentiles as the whisker lines.....86

Figure 4.5. Freezing curves for multiple refreezes of the same Snomax containing droplets in squalene oil, at decreasing Snomax in water concentrations going from the top left to bottom right panels. The new Snomax sample was used for all these experiments. Repeated freezing decreased the ice nucleation activity of Snomax, and this effect was observed in the three highest concentrations shown. The lowest concentration (bottom right) does not show this behavior. The droplet array was immediately thawed at 10 °C after each freezing cycle, and then the subsequent cooling cycle was initiated.88

Figure 4.6. Freezing curves from five freeze/thaw cycles of the same 0.0001 wt% Snomax in an array of twenty-four 1 μ L droplets on the cold stage and exposed to air. No immersion oil was used in this experiment, to eliminate possible oil partitioning effects.....90

Figure 4.7. Top plots show freezing temperature spectra of 0.0063 wt% Snomax for five consecutive freezes in squalene (top left) and six consecutive freezes in mineral oil (top right). Bottom plot shows the droplet freezing temperatures as a box and whisker plot for the same 0.0063 wt% Snomax droplets after subsequent refreezes in squalene (red circles), mineral oil (green triangles), and silicone oil (blue diamonds). The values on the bottom axis correspond to the amount of time in minutes between the first freeze and the respective freeze for that experiment. All three droplet arrays were created using the same Snomax suspension.91

Figure 4.8. Freezing curves of 0.03 wt% Snomax droplets immersed in squalene oil and frozen immediately after droplet array creation (solid lines), or after waiting 90 minutes to begin the freezing (dashed lines). The time indicated for each line corresponds to when that freezing was started relative to the time the droplet array was deposited into the squalene oil.96

Figure 5.1. Averaged droplet freezing temperature spectra from triplicate arrays of all ash samples using the droplet-in-oil method (filled circles). Two grasses are shown: cutgrass (cyan) and NC grass (orange). In addition, a microfluidic device was used to measure birch ash (red, open) and cutgrass + soil (blue and green, open). The microfluidic birch ash was the only sample run once, not in triplicate. Microfluidic droplets (open circles) were generated in two different sizes for the cutgrass + soil sample, 6 nL (blue, open) and 13 nL (green, open). Average pure water controls are shown for both systems in black (solid, droplets-in-oil; dashed, microfluidic). Particle weight percent concentrations are around 0.01 wt% in all cases; particle surface area concentrations are shown in Table 5.1.....108

Figure 5.2. Plot of average ice active site density, n_s , of various ash samples. Cross symbols are bottom ash samples measured using the droplet in oil method. Circles are ash samples measured in the microfluidic device using 6 nL droplets, and squares for 13 nL droplets. Triangles are measurements of soil using the droplet-in-oil method. The solid black line shows a fit for a domestic bottom ash sample from Umo et al. [2015]. Solid pink line is the fit of K-feldspar minerals from Atkinson et al. [2013].109

Figure 5.3. XRD results for ash produced from open pan combustion of birch wood, soil, cutgrass, and cutgrass + soil. Amorphous material is indicated by a rise in intensity at

lower 2θ values. Amorphous content is visible in both birch ash and cutgrass ash, but not in the other samples. Peaks in each spectrum are assigned by matching to a database of known spectra. C: calcite, K: KCl, O: K_2SO_4 , M: Mixed sulfates, A: alkali feldspars, S: SiO_2 , P: plagioclase feldspars, D: dolomite, blue region: amorphous material.

Assignments can be found in Table 5.1.....113

Figure 6.1. Freezing spectra of first sawgrass burn collected on a nuclepore filter, compared to pure water and a blank filter. Droplets used for this experiment were 0.1 μL , particle concentration in the chamber was unknown because no SMPS was used. Error bars on the pure water indicate the standard deviation of pure MilliQ water droplets taken throughout 2015.....125

Figure 6.2. Temperature freezing spectrum (left) and ice-active site density (n_s) spectrum (right) for fresh and aged sawgrass samples obtained in 2015. Droplets used for this experiment were 0.1 μL . Particle concentration in the chamber was 20-30 $\mu g/m^3$ for each of these 5 sawgrass burns. Error bars represent the standard error of the frozen fraction and n_s for respective sample types. The pure water tests indicate the number of pure water control droplets (n) included in this analysis.128

Figure 6.3. Droplet freezing temperature spectra for BBA produced by combustion of fatwood (left) and birch wood (right). Both show ice-activity similar to the pure water background signal. Droplets used for these experiments were 0.1 μL . Particle concentration in the chamber was 65 $\mu g/m^3$ for the birch burn and 500 $\mu g/m^3$ for the fatwood burn. Error bars represent standard deviation of the frozen fraction of replicate arrays for respective sample types.131

Figure 6.4. Left: SEM image of fresh chamber particles collected during the fatwood burn. Large soot aggregates display highly fractal structure, suggesting high elemental carbon composition. Right: Results from the Soot-Particle Aerosol Mass Spectrometer (SP-AMS) showing the much higher black carbon (BC) content compared to other aerosol chemical components.133

Figure 6.5. Temperature freezing spectra for *Arundo perennis* (left) and *Arundo* with roots and soil attached (right) including aged samples (red). Two arrays for each sample are shown for reproducibility. Droplets used for these experiments were 0.1 μL . Particle concentration in the chamber was 54 $\mu\text{g}/\text{m}^3$ for the *Arundo* burn and 29 $\mu\text{g}/\text{m}^3$ for the *Arundo*+roots burn. Error bars represent standard deviation of the frozen fraction for respective sample types. The pure water controls indicate the number of droplets of pure water included in this analysis.135

Figure 6.6. Freezing spectra for fresh and aged cutgrass BBA for two different chamber experiments. Droplets used for these experiments were 0.1 μL . Particle concentration in the chamber was 60 $\mu\text{g}/\text{m}^3$ (left) and 20 $\mu\text{g}/\text{m}^3$ (right). Error bars represent standard deviation of the frozen fraction for respective sample types. The left graph shows the same cutgrass burn as the data presented in Figure 6.7.136

Figure 6.7. SP-AMS measurements of aerosol composition from one cutgrass burn. All measured species concentrations are depicted on the left axis except organics shown on the right axis. Aging occurs by OH radicals when the UV lights are turned on, shown by the blue shaded region. The data is taken from the same burn as the left graph in Figure 6.6.137

Figure 6.8. Left: Temperature freezing spectra comparing *Arundo*+roots, cutgrass, and cutgrass+soil. Droplets used for these experiments were 1.0 μL . Particle concentration in the chamber was 1700 $\mu\text{g}/\text{m}^3$ for the cutgrass burn, 1000 $\mu\text{g}/\text{m}^3$ for the cutgrass+soil burn and 500 $\mu\text{g}/\text{m}^3$ for the *Arundo*+roots burn. Pure water data is a statistical average of the pure water droplets frozen side-by-side with each of these BBA samples. Error bars show standard deviation of multiple runs of the same sample. Right: n_s plot showing data from both *Arundo*+roots burns (2016 (Figure 6.5) in dark green, 2017 in blue), cutgrass (light green), cutgrass+soil (orange).141

Figure 6.9. Freezing temperature spectra of wiregrass BBA before and after H_2O_2 aging compared against pure water controls (left) and corresponding ice active site density (n_s) plots for the fresh and aged samples (right). Droplets used for these experiments were 1.0 μL . Particle concentration in the chamber was 146 $\mu\text{g}/\text{m}^3$. Error bars represent standard deviation between different droplet arrays of the sample. 1.0 μL droplets were used for all these measurements.143

Figure 6.10. Comparison of droplet freezing spectra for fresh and aged BBA from a sawgrass burn between the traditional cold plate method (1.0 μL droplets, crosses) and the microfluidic device (80 nL droplets, lines). Particle concentration in the chamber was 434 $\mu\text{g}/\text{m}^3$. All datasets are averaged over 3 or 4 arrays of droplets. Error bars are standard deviation of pure water samples.145

Figure 6.11. Freezing spectra of fresh sawgrass BBA and O_3 -aged BBA obtained using 6 nL droplets in the microfluidic device. All BBA samples are based on one array from a single device. The error bars for the pure water data are the standard deviation of several replicate runs.147

Figure 6.12. SP-AMS measurements of aerosol composition from sawgrass ozonolysis. Aging occurs by dark ozonolysis; ozone was injected at the red arrow. During this experiment the SP laser that measures BC was not functioning.....	148
Figure 6.13 Freezing spectra of cutgrass BBA fresh and O ₃ -aged using 6 nL droplets in the microfluidic device. All BBA samples are based on one array from a single device. The error bars on the pure water data are standard deviation of several runs.....	150

1 Introduction

1.1 The importance of ice nucleation in the atmosphere

Clouds in the atmosphere are formed when water condenses onto small particles called cloud condensation nuclei. These particles are hygroscopic and upon reaching critical supersaturation will grow exponentially into cloud droplets. Some of these particles are also able to cause glaciation or ice nucleation under supercooled conditions. Ice nucleation occurs when a particle provides a favorable site for supercooled water to gather forming an ice embryo that ultimately will grow to become an ice crystal. The formation of ice in a cloud has numerous effects on radiative forcing, cloud lifetime and structure, and precipitation [Lohmann and Feichter, 2005; Lohmann and Diehl, 2006; DeMott *et al.*, 2010; Gettelman *et al.*, 2010; Hoose and Möhler, 2012; Murray *et al.*, 2012; Lawson and Gettelman, 2014]. It is a complicated process that is not well constrained and is only minimally addressed in the most recent Intergovernmental Panel on Climate Change assessment report [Stocker *et al.*, 2013]. Ice nucleation in the atmosphere can happen via different mechanisms that will be discussed below. Briefly, water freezes homogeneously at temperatures below $-38\text{ }^{\circ}\text{C}$ in the atmosphere or via heterogeneous mechanisms as warm as $0\text{ }^{\circ}\text{C}$ catalyzed by atmospheric particles known as ice nucleating particles (INPs). INPs are present in the atmosphere at concentrations around 1 in 10^6 particles. Despite this rarity, they are incredibly important for cloud microphysics, weather, and climate.

The phase of water, ice or liquid, has a large impact on clouds and the impact those clouds have on climate. All clouds absorb outgoing longwave radiation due to the strong absorption of water in the IR range [Haywood and Boucher, 2000; Feingold *et al.*, 2016].

Liquid clouds, or warm clouds, are lower tropospheric stratus or cumulus clouds composed of liquid water. Liquid clouds are thick and fluffy and they reflect back substantial incoming solar radiation [Chen *et al.*, 2000; Twohy *et al.*, 2005]. Overall liquid clouds tend to have a net cooling effect on the planet because they reflect incoming solar shortwave radiation, which overwhelms its absorption of outgoing longwave terrestrial radiation. Ice clouds, or cold clouds, tend to exist in the highest levels of the troposphere and are largely wispy cirrus clouds composed entirely of ice crystals [Heymsfield *et al.*, 1998; Murray *et al.*, 2010, 2012]. Due to their sub-visible nature ice clouds do not reflect much light, but they very efficiently absorb outgoing IR radiation due to the larger size of ice crystals compared to liquid droplets [Zhang *et al.*, 1999; Dupont and Haeffelin, 2008; Burkhardt and Kärcher, 2011]. Thus, ice clouds have a net warming effect on the planet's climate. Mixed-phase clouds are clouds that possess both liquid and ice phases and have the most dynamic properties. This type of clouds will largely be similar to warm clouds due to their thickness and opacity. Thus, in general they will cool the planet's climate. However, mixed-phase clouds have other impacts on the environment as well. They are largely responsible for precipitation over land masses and are the types of clouds that bring thunderstorms [Mülmenstädt *et al.*, 2015]. Precipitation happens when ice crystals grow too large to be supported by the buoyant air and gravity takes over. Crystals grow rapidly at the expense of liquid droplets because of the thermodynamic instability of having three phases of water present in the same environment; this growth is known as the Wegener-Bergeron-Findeisen (WBF) process [Korolev, 2007; Storelvmo *et al.*, 2008]. Precipitating clouds have an overall cooling effect because of their optical thickness, but they also have shorter lifetimes because of rain out [Stevens and Feingold, 2009]. In addition to cloud

lifetime, studies have found that ice crystal concentration alters cloud reflectivity [Storelvmo *et al.*, 2011; Vergara-Temprado *et al.*, 2018]. The amount of ice present is dependent on INP concentration, updraft velocities, and the atmospheric temperature profile. Modeling these complex clouds is a major area of research currently. One of the biggest issues is understanding which phases exist where in the cloud; some of the difficulties are outlined by Korolev *et al.* [2017]. Both satellite and ground-based measurements struggle to accurately define the full structure within clouds, particularly what phases are present at various altitudes. This is important because given the same amount of total water content, the climate effects of a mostly ice cloud versus a mostly liquid cloud are very different. The mostly ice cloud will have much fewer but larger crystals decreasing reflectivity, while the mostly liquid cloud will have far more droplets with smaller sizes decreasing chances of rain out. We know that models currently have a major problem predicting the amount of supercooled water within clouds, which makes understanding the dynamics of ice nucleation within a mixed-phase cloud environment incredibly important.

1.2 Mechanisms of ice nucleation

There are five major known ice nucleation mechanisms. Homogeneous freezing occurs without the need for a surface or particle, through the nucleation of small ice crystal embryos in supercooled water. When an embryo unstably grows past a critical size threshold before dissolution, the entire water volume will quickly freeze. Heterogeneous freezing is catalyzed by a surface, such as particle surfaces in atmospheric cloud droplets. Heterogeneous ice nucleation is typically separated into four distinct modes: deposition, contact, condensation, and immersion. These modes and others are shown in Figure 1.1.

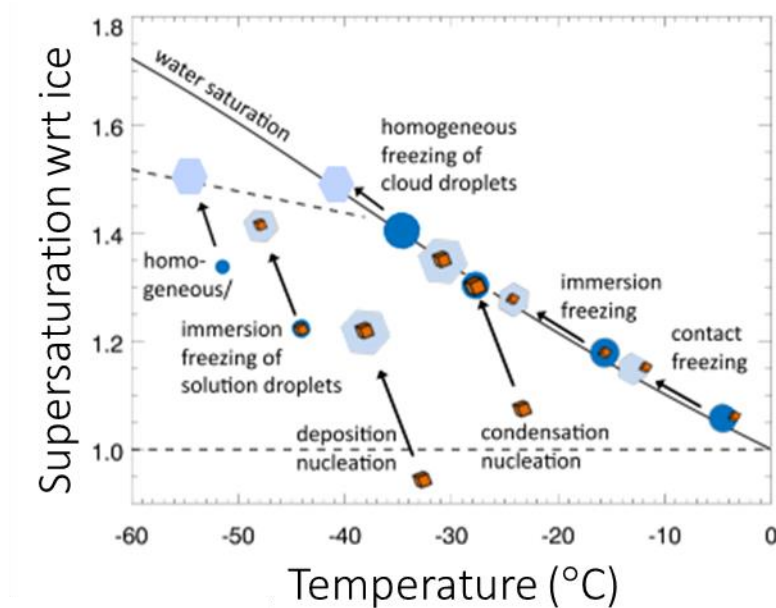


Figure 1.1. Schematic of different ice nucleation mechanisms. Brown cubes represent ice nucleating particles, blue circles represent liquid, supercooled water, and white hexagons represent ice crystals. Figure is adapted from Hoose and Möhler [2012].

Homogeneous ice nucleation occurs at temperatures below -38°C without the presence of an ice-active surface/particle. It requires the formation of a critical ice nucleus or ice embryo. Classical Nucleation Theory (CNT) is used to describe homogeneous ice nucleation [Vali, 1971, 1999, 2008, 2014; Hoose and Möhler, 2012; Murray *et al.*, 2012; Vali *et al.*, 2015; Koop and Murray, 2016]. Nucleation rate coefficients are used to define the homogeneous nucleation rate. Koop *et al.* [2000] first parametrized the solute effects that alter homogeneous ice nucleation of pure water using the activity of water. In the atmosphere, homogeneous freezing only occurs when INPs are limited and at very low temperatures below -38°C , such as in cirrus clouds.

Deposition freezing occurs when a particle is in an environment that is subsaturated with respect to supercooled water and supersaturated with respect to ice [Dymarska *et al.*,

2006; *Shilling et al.*, 2006; *Baustian et al.*, 2010; *Wang et al.*, 2012; *Schill et al.*, 2013]. This mechanism is believed to only be relevant at cirrus temperatures due to the presence of large amounts of liquid water in lower tropospheric clouds. Additionally, recent studies have suggested this mechanism is not deposition of ice directly onto the surface as was originally theorized, but freezing of supercooled water condensed inside microscopic pores, referred to as pore condensation freezing (PCF) [*Marcolli*, 2014; *Wagner et al.*, 2016; *Alstadt et al.*, 2017].

Contact nucleation is a rare mechanism that occurs when an INP contacts the external surface of a supercooled droplet and immediately causes ice nucleation [*Fukuta*, 1975; *Bunker et al.*, 2012; *Gurganus et al.*, 2014; *Davis et al.*, 2015; *Collier and Brooks*, 2016]. This mechanism is difficult to study, but most studies that have examined it find that it is highly efficient due to the imparting of additional energy by the initial contact between particle and droplet. However, a few studies found no preference for contact nucleation on various substrates [*Gurganus et al.*, 2011; *Campbell et al.*, 2015; *Häusler et al.*, 2018]. Some recent studies observed a similar process that occurs when an immersed particle contacts the surface of the droplet from the inside initiating freezing; this process has been deemed “inside out” contact freezing [*Durant and Shaw*, 2005; *Shaw et al.*, 2005; *Fornea et al.*, 2009].

Condensation is a mechanism that is traditionally paired with immersion freezing due to their mechanistic similarities. At this point, there is little evidence for the existence of condensation freezing separate from immersion freezing [*Vali et al.*, 2015]. It is defined as occurring at the boundary of water saturation and is characterized by ice formation concurrent with liquid water condensation onto a particle. This mechanism is difficult to

study on its own because particle hygroscopicity tends to lead to droplet activation before freezing initiates, thus making distinctions between immersion and condensation nearly impossible.

Immersion freezing is one of the simplest mechanisms to examine and the most important when discussing mixed phase clouds; thus, it is the focus of this dissertation. Immersion freezing occurs when a particle immersed in a droplet, following cloud droplet activation, initiates freezing above the homogeneous nucleation temperature. Thus the particle experiences supersaturation with respect to both ice and water [*Pinti et al.*, 2012; *Wright et al.*, 2013; *Diehl et al.*, 2014; *Grawe et al.*, 2016; *Tobo*, 2016]. INPs in mixed-phase clouds are most likely to undergo immersion mode nucleation as most particles will have activated into cloud droplets during cloud evolution prior to reaching freezing conditions. Though there are still uncertainties about how this type of freezing occurs, it is believed to be largely related to the surface structure of the immersed particle [*Fornea et al.*, 2009; *Augustin-Bauditz et al.*, 2014; *Hiranuma et al.*, 2014b, 2015a; *Fitzner et al.*, 2015; *Beydoun et al.*, 2016; *Bi et al.*, 2016]. In general strong immersion mode INPs possess cracks/crevices or crystal facets similar in lattice geometry to cubic or hexagonal ice [*Murray et al.*, 2012; *Cox et al.*, 2013; *Fraux and Doye*, 2014; *Kiselev et al.*, 2017] or particular functionalities or regions that have a strong affinity for ice activation [*Gorbunov et al.*, 2001; *Lupi and Molinero*, 2014; *Wex et al.*, 2015; *Pandey et al.*, 2016; *Polen et al.*, 2016].

1.3 Known types and sources of ice nucleating particles in the atmosphere

Atmospheric ice nucleating particles are present in a wide range of concentrations, compositions, and critical freezing temperatures. Some known types and sources of atmospheric INPs include biological particles, such as bacteria and fungi, and their associated macromolecules, mineral dust, volcanic ash, combustion ash, soot, and soil.

Biological particles are among the most active INPs [Després *et al.*, 2012]. Ice-active bacteria in particular are able to nucleate ice as warm as -2 °C. Some bacteria, such as *Pseudomonas syringae*, possess genes that code for the production of membrane proteins that have strong nucleation ability [Lindow, 1989; Schmid *et al.*, 1997; Morris *et al.*, 2008; Pietsch *et al.*, 2015; Polen *et al.*, 2016]. This is believed to be an evolutionary trait that allows the bacteria to nucleate ice to rupture and infiltrate a plant's cell wall. These and other bacteria are commonly found on leaves and in soil, but have also been identified in cloud water and precipitation [Schnell and Vali, 1972, 1976; Morris *et al.*, 2004; Christner *et al.*, 2008; Conen *et al.*, 2011; Joly *et al.*, 2013; Šantl-Temkiv *et al.*, 2015]. Chapter 4 on the ice nucleation properties of Snomax (a product made from *Pseudomonas syringae*) focuses on stability of these bacterial ice nucleating protein aggregates. In addition to ice nucleating bacteria, other biological organisms and macromolecules have been suggested as potential INPs. Some fungus species or fungal spores have been proposed as INPs due to their higher atmospheric abundance relative to *Pseudomonas* bacteria, though they are typically much less active, freezing at temperatures closer to -20 °C [Iannone *et al.*, 2011]. Some unique fungal species, such as those from *Fusarium avenicium*, display very high freezing onset starting at -3 °C [Morris *et al.*, 2013; Fröhlich-Nowoisky *et al.*, 2015].

Several studies have also examined pollen and macromolecules ejected from pollen that have ice nucleating abilities [Pummer *et al.*, 2012, 2015; Augustin *et al.*, 2013; Hader *et al.*, 2014; O'Sullivan *et al.*, 2015, 2016]. These macromolecules in particular are of interest because they are predominantly composed of carbohydrates, and thus they are more likely to survive atmospheric transport and nucleate unlike the more fragile bacteria and fungi. However, these pollen-derived ice nucleants are expected to be even less abundant than either bacteria or fungi in the atmosphere.

By far the highest concentration INPs in the atmosphere are composed of mineral dust particles. Mineral dust can be composed of various mineral phases that each possess differing abilities to nucleate ice. A vast amount of literature has discussed the importance of various minerals to ice nucleation in the atmosphere [Sullivan *et al.*, 2010; Hoose and Möhler, 2012; Murray *et al.*, 2012; Atkinson *et al.*, 2013; Wex *et al.*, 2014; Hiranuma *et al.*, 2015a; Zolles *et al.*, 2015]; here I will only discuss one class of minerals relevant to my thesis work. Feldspars are believed to be the most active ice nucleating mineral phase currently. They come in two forms: alkali (Na/K) and plagioclase (Na/Ca). Alkali feldspars are the more ice-active of the two variants due to defects in the crystal lattice on which ice efficiently nucleates [Kiselev *et al.*, 2017]. Kiselev *et al.* [2017] performed environmental SEM experiments that observed the growth of ice crystals to be preferential on the (100) face of large K-feldspar particles. These recent findings shed a brilliant new light onto the microscopic and nanoscopic mechanisms of atmospheric ice nucleation, and how highly selective the physicochemical properties of ice active sites can be.

Volcanic ash has been suggested as a source of ice nucleating particles as well. Mineral phases including feldspars in volcanic ash are largely responsible for this ice

activity, but most of the few studies of volcanic ash show huge diversity in the IN activity [Durant *et al.*, 2008; Fornea *et al.*, 2009; Hoyle *et al.*, 2011; Schill *et al.*, 2013; Gibbs *et al.*, 2015; Kulkarni *et al.*, 2015; Mangan *et al.*, 2017]. This is most likely a result of differences in the eruption type and conditions, which effects the specific mineral phases present in the emitted ash, as well as chemical aging of the ash in the plume. Some ash from a single volcano can show freezing activity as high as -10 °C or as low as -35 °C [Mangan *et al.*, 2017]. Many of these differences have not been explored and future experiments, including in our lab, hope to explain them in the near future.

Soil particles have also been studied recently to explore their potential ice nucleating ability [O'Sullivan *et al.*, 2014; Tobo *et al.*, 2014; Hill *et al.*, 2016; Steinke *et al.*, 2016]. Soil is composed of mineral, organic, and biological components, all of which can participate in ice nucleation. Biological material in soil has been known to be ice active since early experiments on leaf litter and plant debris [Schnell and Vali, 1976]. Mineral and biological activity have been established as mentioned above, but organic material in soil has only recently been established as IN active. Hill *et al.* [2016] showed that on top of ice-active bacteria and mineral dust, various agricultural soils contained ice-active organic material. The temperatures at which each of the components is active can vary greatly, but in general, biologicals are active at temperatures above -10 °C, minerals are active between -15 °C and -25 °C, while organics can be active from -10 to -30 °C [Hill *et al.*, 2016]. These different sources of soil INP can be distinguished using various methods. Biological components can be tested using PCR or removed with heat or enzymes that denature the proteins. Organic components can be reacted with H₂O₂. After each of these

treatments mineral ice activity will remain because they are resistant to both treatments. Through this series of tests, soil ice activity can be classified by INP type.

Another source of INPs that will be explored further in this dissertation are particles emitted from combustion. Combustion creates soot particles that are predominantly elemental carbon, and ash particles that are predominantly mineral phases and some carbonaceous material (elemental and organic carbon). Many prior studies have found that soot from simple hydrocarbon combustion does not act as an INP except through very low temperature deposition freezing [DeMott, 1990a; Dymarska *et al.*, 2006; Koehler *et al.*, 2009; Friedman *et al.*, 2011]. Thus soot is not considered to be important in general for atmospheric ice nucleation. However, soot from hydrocarbon combustion is not an atmospherically relevant form of soot. Therefore, studying biomass burning, or combustion of woods and grasses, affords more realistic emissions for understanding wildfires. Biomass burning is complex by nature as it produces carbon dioxide, carbon monoxide, nitrogen oxides, volatile organic compounds, and particulate matter, including soot. Several recent studies have found that biomass burning (BB) events can produce atmospheric INPs [DeMott *et al.*, 2009; Petters *et al.*, 2009b; Twohy *et al.*, 2010; Prenni *et al.*, 2012]. This means that either soot produced by more complex combustion is ice-active or there are other components in environmentally-relevant combustion that is ice-active. Levin *et al.* [2014, 2016] found that ~50% of BB-produced INPs contain soot, which means that soot is not always present to act as an INP and thus may not be a major contributor to IN activity. In Chapter 6 I explore our own measurements of biomass burning emissions and share some insights into the effects that aging has on the ice nucleating properties of these emissions, which has never been examined previously.

Combustion ash has been suggested as a source of INPs recently as it does contain a high percentage of mineral phases, particularly at high combustion temperatures [*Umo et al.*, 2015; *Grawe et al.*, 2016]. Umo et al. [2015] found that bottom ash from domestic and wood burning are more ice-active than from coal, however coal fly ash was the most active. Their results also show that coal fly ash is composed of a higher fraction of aluminosilicates and amorphous material, while the coal bottom ash contained a high amount of calcite, which is known to be very poor ice nucleant. This could mean that smaller particles are produced from higher temperature combustion and thus have more active mineral composition. This could have significant implications for the production of INPs from biomass burning; it may be a result of the highly active mineral components of BB fly ash particles. One other possible cause of elevated INP concentration within biomass-burning plumes is the entrainment of soil particles from the surface of plants burned or the surrounding environment. Soil particles, as discussed above, have the potential to be quite ice-active, and updrafts from wildfires and intense combustion could result in the suspension of soil particles in the atmosphere. However, the important question that we probe in this Chapter 5 is, do the soil particles emitted by biomass-burning combustion retain their ice nucleation activity through the combustion process?

The diversity of INPs in the atmosphere and the activity they possess is a major complication for understanding their impact on climate. The following are some major questions regarding the nature of INPs that still need to be explored:

1. What effect does atmospheric oxidation have on INPs? Many biological and carbonaceous particles can be greatly altered by oxidation, which may impact

their IN ability. Aging of INPs has not been performed a great deal in the community.

2. What in biomass burning plumes is active? Is it related to soot as is the general thought? Or is it production of mineral phases in the ash that get lofted into the plume? Does soil play a part in these emissions?
3. What are the major factors that govern the ice nucleation ability of volcanic ash? Does aging in the volcanic plume or downstream of the plume alter the activity greatly?
4. Of the major classes of INPs, which contribute the most to cloud glaciation? To what extent is this spatially- or temporally-dependent?

1.4 Methods of measuring immersion-mode ice nucleating particles

There are five major categories of instrument currently used to measure ice nucleating particles: droplets-in-oil, microfluidic, droplets-in-air, cloud expansion chambers, and continuous flow diffusion chambers. These methods are used with several goals in mind. First is to obtain freezing temperature spectra of the particles involved in the freezing process. Additionally, they are used to determine the concentration of those particles that are active at specific temperatures, or relative humidities in the case of expansion and diffusion chambers. This section explores the benefits and issues with each type of methodology and explains why we chose to use the methods that produced the results discussed in this dissertation.

Droplet-in-oil measurements are some of the most simple and convenient methods to do a large amount of bulk measurements [Bigg, 1953; Hoffer, 1961; Murray *et al.*, 2011; Pummer *et al.*, 2012; Hader *et al.*, 2014; Peckhaus *et al.*, 2016; Polen *et al.*, 2016]. In droplet-in-oil methods droplets containing a suspected INP are deposited into an oil matrix (Figure 1.2). The oil matrix sits within a temperature controlled chamber. Often droplets lie on top of a substrate that is hydrophobic in nature to limit the interactions with the surface. We use these methods predominantly because they enable measurements over the largest temperature range that are most relevant for mixed-phase clouds. Additionally, the oil environment, though not atmospherically relevant, allows consistent and relatively artifact-free freezing and thawing to occur [Hader *et al.*, 2014; Polen *et al.*, 2018]. For these measurements, droplets of a bulk suspension of particles are pipetted onto a hydrophobic surface to reduce the amount of surface interactions. The oil environment reduces contamination from the air and inhibits Wegener-Bergeron-Findeisen (WBF) effects and frost halo formation [Jung *et al.*, 2012]. WBF is a process by which ice crystals grow at the expense of nearby supercooled, and thus metastable, liquid droplets. Frost halos are caused when condensed water within the sample dish starts to freeze and causes droplet freezing at warmer temperatures than should occur when contacted by the growing frost. Droplet-in-oil measurements have been used since the first examinations of ice nucleating activity and are still used today by several research groups [Bigg, 1953]. The biggest concern for droplet-in-oil methods is surface interactions between the droplet and substrate that can induce freezing [Hader *et al.*, 2014; Whale *et al.*, 2015; Tobo, 2016; Polen *et al.*, 2018]. This issue makes homogeneous freezing temperatures difficult to achieve experimentally and artificially elevates the background ice nucleation signal, making it

hard to probe low temperature ice nucleation below $-30\text{ }^{\circ}\text{C}$. This important experimental interferences are discussed in detail in Chapter 3 on strategies to reduce background freezing in pure water droplet freezing measurements.

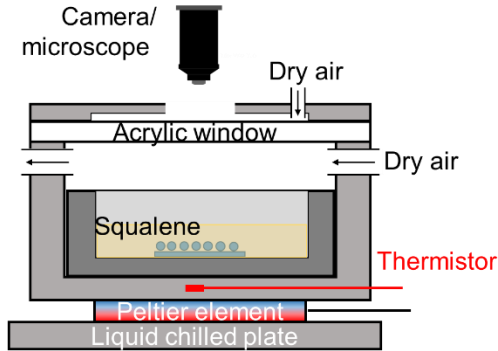


Figure 1.2. Diagram of the CMU-CS. Reprinted from Polen et al. [2016].

One of the most recent method advances is the implementation of microfluidics for ice nucleation experiments [Stan et al., 2009b; Sgro and Chiu, 2010; Riechers et al., 2013; Reicher et al., 2018; Tarn et al., 2018]. Microfluidic measurements are closely related to droplet-in-oil methods, but have distinct differences and tremendous benefits. Some groups use microfluidics just to generate microdroplets that are then frozen in a sample dish, while others have used continuous flow through a microfluidic device to freeze thousands of droplets in a minute. Our group has developed a “store-and-create” microfluidic method, shown in Figure 1.3, that allows us to generate hundreds of droplets within a microfluidic chip and freeze them similar to traditional droplet-in-oil methods [Brubaker et al., 2018; Polen et al., 2018]. Storing droplets within the chip greatly reduces the background freezing of water because droplets in the chip are completely encased in a layer of oil and have no contact with the surface of the device.

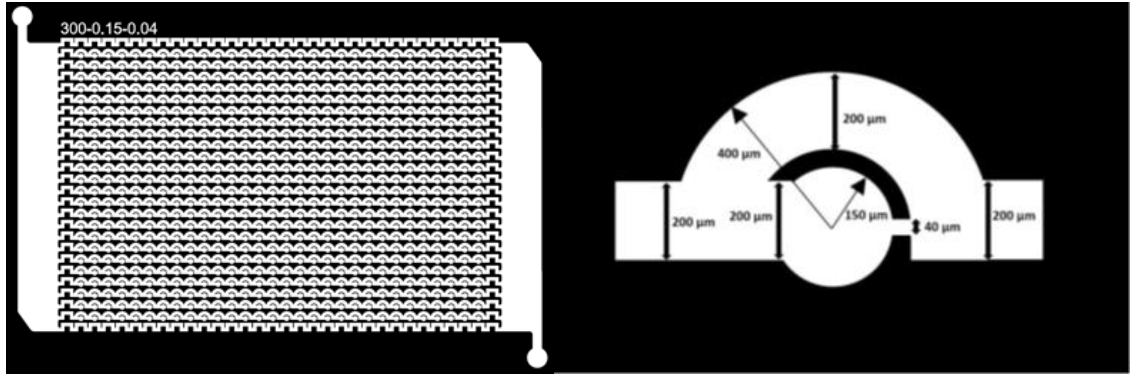


Figure 1.3. Schematics showing the droplet array from our microfluidic chip used for ice nucleation measurements. Left: the complete device consists of 720 droplet holding wells. Right: dimensions of an individual well in the left image.

The droplets-in-air approach is similar to droplets-in-oil but without the oil environment [Li *et al.*, 2012; Budke and Koop, 2015; Whale *et al.*, 2015]. The droplets are placed on a solid substrate and exposed to air in an enclosed environment. Thus, this method can suffer from WBF and frost halos if the system is not designed with that in mind. Most of the groups that use droplet-in-air methods have designs that work well for their intended purpose and show minimal or few contamination and background freezing issues. Tobo [2016] created a system that simply uses Vaseline as the surface coating that the droplets are placed on, and is able to achieve freezing near homogeneous temperatures of $-38\text{ }^{\circ}\text{C}$ for large $5\text{ }\mu\text{L}$ droplets (Figure 1.4). Other groups have utilized substrate-less methods for performing freezing of droplets suspended in air by adapting an electrodynamic balance (EDB), wind tunnel, or acoustic levitator to achieve ice nucleation [Szakáll *et al.*, 2009; Hoffmann *et al.*, 2013; Diehl *et al.*, 2014]. These methods entirely remove the issue of surface contact that substrate-based techniques suffer from. Unlike the droplets-in-oil, droplet-in-air methods can be designed to specifically target immersion or deposition freezing. Without oil, the temperature as well as the relative humidity conditions

can be controlled to simulate specific conditions in the atmosphere. These methods however are not portable and are not suitable for directly sampling ambient aerosol particles, or from chamber reactors.

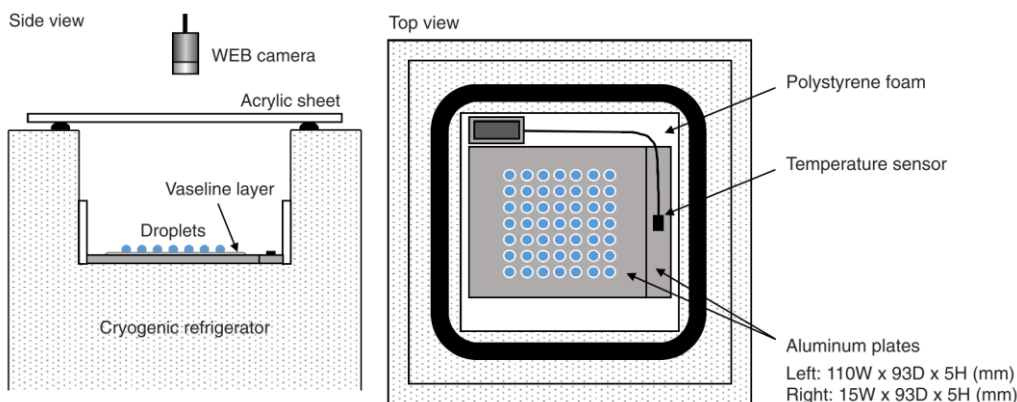


Figure 1.4. Schematic of the Cryogenic Refrigerator Applied to Freezing Test (CRAFT). Reprinted from Tobo [2016].

One of the most common methods for real-time analysis of ice nucleating particles is the continuous flow diffusion chamber (CFDC) [Möhler *et al.*, 2007; Garcia *et al.*, 2012; Hiranuma *et al.*, 2015a; Mason *et al.*, 2015; DeMott *et al.*, 2017]. CFDCs utilize temperature differentials between two parallel ice-coated plates, or concentric cylinders, to produce an environment that is supercooled and supersaturated with respect to ice [Rogers, 1988; Rogers *et al.*, 1998]. A CFDC can probe both immersion (saturated with respect to water) and deposition (subsaturated with respect to water) freezing regimes and can investigate individual particles in laboratory or ambient studies. Various diffusion chamber instruments have been developed to improve upon the original design, including the Leipzig Aerosol Cloud Interaction Simulator (LACIS) (Figure 1.5) [Stratmann *et al.*, 2004; Hartmann *et al.*, 2011, 2013], Zurich Ice Nucleation Chamber (ZINC) [Welti *et al.*, 2009; Lüönd *et al.*, 2010], Frankfurt (Fast) Ice Nucleation CHamber (FINCH) [Bundke *et al.*,

2008], and others. Diffusion chambers allow more realistic measurements of ice nucleants in the atmosphere compared to substrate methods. However, the tremendous amount of maintenance, often high background signal, small sampling volume (and thus poor detection limits), and the generally limited temperature regime that can be probed make it a more challenging approach than the offline droplet-on-substrate techniques described above.

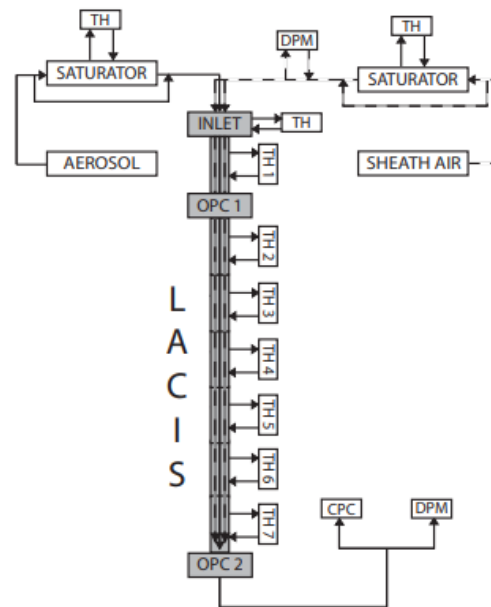


Figure 1.5. Schematic of the LACIS instrument. The abbreviations stand for TH: thermostat, DPM: dew point hygrometer, CPC: condensational particle counter, OPC: optical particle counter. Reprinted from Hartmann et al. [2011]

The other main class of ice nucleation instruments is the expansion chamber [Möhler et al., 2001, 2003; Tajiri et al., 2013]. Cloud expansion chambers are massive instruments that have fine-tuned temperature, relative humidity, and pressure control. These devices are designed to simulate the adiabatic expansion and cooling of a rising air parcel that leads to cloud formation and thus have the most realistic conditions of all IN measurements. The

formation of liquid cloud droplets and ice crystals during an expansion is detected using optical sensors that interrogate the large chamber volume. The Aerosol Interaction and Dynamics in the Atmosphere (AIDA) instrument, shown in Figure 1.6, is one of the handful of expansion chambers that is used for ice nucleation measurements [Möhler *et al.*, 2001, 2003; Tajiri *et al.*, 2013]. It is often combined with an array of other instruments to gather various ice nucleating properties simultaneously, and the aerosol particles and cloud particles contained within the large chamber volume can be sampled by other instruments such as a CFDC or mass spectrometer.

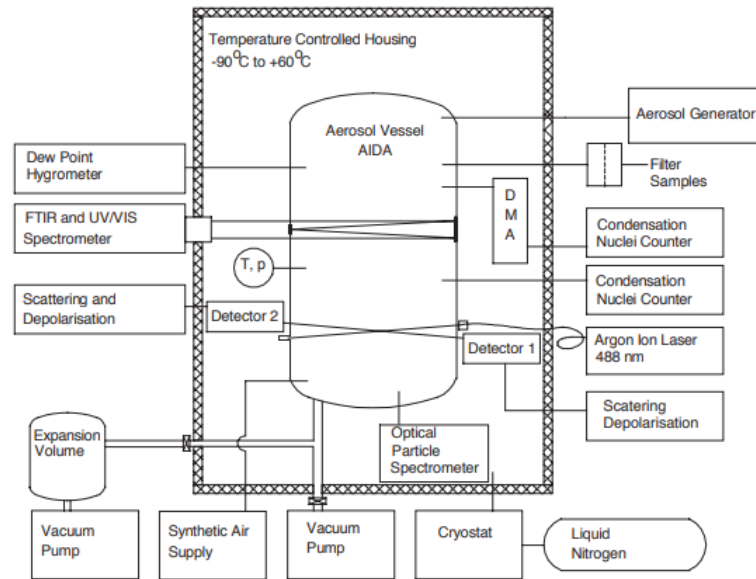


Figure 1.6. Diagram of the AIDA cloud expansion chamber. Reprinted from Möhler *et al.* [2001]

1.5 Thesis overview

In Chapter 2 I present the evolution of the in-house designed ice nucleation system, CMU-Cold Stage (CMU-CS). This chapter discusses the thought and design process I went through at each phase of the project. This chapter includes our initial design considerations, as well as two of the major iterations that the system underwent. I also discuss the

improvements that were made by myself and Tom Brubaker to the analysis methods for droplet imaging as well as post analysis. These design choices and analysis methods were vital to the rest of the accomplishments made in this dissertation.

In Chapter 3 I use the CMU-CS to perform extensive experiments on the ice nucleation of pure water because having an established background freezing spectrum is necessary to assign ice nucleating activity to weak INPs. In this section I discuss the major limitation of substrate-based freezing techniques and how ice nucleation researchers can go about designing methods and instruments to work around these limitations. This chapter includes examination of various substrates to reduce droplet-surface contact nucleation, issues with water contamination, and contamination from droplet generation methods. I also lay out steps for researchers to take in methodology and representation of their data to improve our understanding of the limitations of substrate-based ice nucleation measurements. I also introduce our first tests of the microfluidic chip that Tom Brubaker designed and utilizes for IN measurements. Chapter 3 was published in *Atmospheric Measurement Techniques Discussions* and will be published in *Atmospheric Measurement Techniques* soon [Polen et al., 2018].

In Chapter 4 I present work on Snomax, a manufactured biological product based on *Pseudomonas syringae*, which has been suggested as a standard for biological ice nucleating particles. The use of standards in ice nucleation measurements is key to understanding the fundamental freezing mechanisms in more complex atmospheric INPs. Therefore, having standards that can represent atmospheric INP in a controlled and consistent manner is highly valuable. We found that Snomax ice activity is not consistent, and is reduced by extended storage time and repeated removal from storage in a freezer.

We also found that Snomax ice nucleation is reduced with each freeze/thaw cycle when measured in oil. We found that the ability of the strongest ice nucleating proteins in the bacteria were eliminated for each of these reductions. Chapter 4 was published in the *Journal of Geophysical Research – Atmospheres* [Polen *et al.*, 2016].

In Chapter 5 I present measurements of the ice nucleating activity of biomass combustion ash. Domestic wood burning ash and coal fly ash were found recently to create INPs, and the idea that ash from grass fires might contain also INP makes it a very important research topic because it could be a source of INP from wildfires. We found that ash from different types of fuels results in very different ice activity. Specifically, grasses that combust with high fire intensity produced higher ice-activity than wood burns with lower fire intensity did. This suggests that ash particles that can be lofted during biomass burning may impact atmospheric INP. Additionally, we tested the ice-activity of soil particles that were present on the fuel during a fire. The soil still possessed its ice-activity and mineral phases after the combustion event, which suggest that soil lofting could also be a potential source of INP in the atmosphere if it gets entrained in the plume. Chapter 5 is in preparation for submission.

In Chapter 6 I discuss the history of biomass burning experiments and the ice nucleating ability of the aerosol generated by the burns performed by our group. Biomass burning aerosol has been shown to contain INP but at variable amounts and abilities. Our experiments are an attempt to explore mechanisms by which BBA activity may change in the atmosphere due to oxidative aging. The goal of these experiments is to explore the impact of chemical aging on INP produced by biomass burning, and to identify the components that drive the production and release of INPs. In these experiments various

aging mechanisms were tested including dark ozonolysis to oxidize organic vapors and produce secondary organic aerosol (SOA) that condenses onto the particles, OH oxidation to oxidize organic vapors as well as soot and other particle surfaces produced by the burn, and thermal denuding to remove volatile organics followed by OH oxidation to oxidize the soot particle surfaces only. Our initial results suggest that aging has variable effects on BBA. Some emissions have enhanced INP following aging while others show no effect or a decrease in INP. This research is being continued currently by other members of the group.

In Chapter 7 I conclude with the major findings from this dissertation and present some future experiments that should be explored in this area. I discuss future experiments that are being planned for our group in the near future including more measurements of ash particles and biomass emissions. For example, attempting to identify mineral phases in the aerosol to understand if ash or other minerals could be responsible for the variable INP production.

2 Instrumentation design, experimental methods, and data analysis approaches

2.1 Basic design considerations

I designed the CMU cold stage (CMU-CS) for droplet freezing assays based on the method reported by Hader et al. [2014]. I wanted a method that was inexpensive and easy to use for simple ice nucleation experiments that provided reliable and valuable measurements of the freezing temperature spectrum of INPs, and expected to make further improvements after the first few papers. A later design (current version) used what I learned in the first iteration to improve the output and accuracy of the system, but still has some remaining issues. The CMU-CS was intended to be used primarily as a droplet-in-oil method, but could alternatively be used as a droplet-in-air method.

2.2 First iteration of the CMU cold stage

The initial design of the CMU-CS, shown in Figure 2.1, was a simple aluminum chamber with air ports to allow dry or humidified air to be injected as needed. An aluminum sample dish that contains the sample droplets was created as well to allow easy removal and replacement when starting and cleaning up after an experiment. The aluminum chamber sat atop an aluminum block that had copper tubing running through it, which allowed the flow of a coolant that cooled the chamber. The liquid chiller used to pump the coolant was already available and in use by other instruments in the lab. The chiller was able to reach the temperatures ($< -40\text{ }^{\circ}\text{C}$) necessary to perform these ice nucleation experiments. Between the heat sink and the aluminum chamber sat a thermoelectric cooler

(TEC, TETech Inc. Model: VT-127-1.4-1.5-72) that provided fine temperature control to the chamber and sample dish. Fine temperature control and a steady cooling rate are necessary for these measurements to be accurate. The chamber was topped with a clear acrylic pane as a viewing window and another aluminum top that allowed air to flow between it and the acrylic pane to defog the outside of the window. A stereomicroscope (AmScope, Model: SM-4TZ-144) with camera (Mightex Systems, Model: SME-B050-U) is used to image droplets immersed in oil in the sample dish. Magnification is variable but typically is used between 10X and 15X.

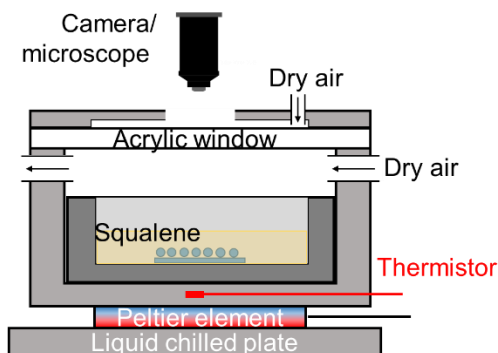


Figure 2.1. CMU cold stage (CMU-CS) first iteration design. Image taken from Polen et al. [2016].

This first iteration of the cold stage worked well enough but had some issues that needed to be addressed in future iterations. One of the biggest issues with the design is the dish was only a few micrometers smaller than the chamber and thus needed a mechanism to remove it. This was a simple enough fix but did not work properly every time. One incident in which the dish got wedged in the chamber resulted in us having to get the machine shop to use their expertise to remove it. Another issue in the original design was excessive use of aluminum. With a fully metal chamber and lid, the heat transfer through the walls of the chamber from the outside during the temperature ramps meant we needed

to fully insulate the chamber. This was not a major problem but could be prevented with a change in materials and chamber design. A more significant change that needed to be made was the small window size. The small window restricted us to only place droplets on the portion of the cover slip surface that was viewable and thus our droplet arrays were fairly small in number throughout the lifetime of this version. The use of air ports and constant air flow started to become a problem especially in the summer months when humidity is severe. The air ports allowed a lot of humid air in, despite drying the air with desiccant, and that resulted in fogging over of the window or oil surface preventing imaging of droplets. The last issue was that experiments took an extra-long amount of time to setup because the large liquid chiller we were using took over an hour to get to sufficiently cold temperatures to begin the experiment. In addition to all of these issues, the group was starting to develop microfluidic methods and thus a larger sample dish was needed to allow us to freeze droplets generated in those devices using the cold stage for temperature ramps.

2.3 Second iteration of the CMU cold stage

In the second – and most recent – iteration of the CMU-CS, many of the issues mentioned above have been resolved through redesign, but some still remain. The CMU-CS version 2 is shown in Figure 2.2. A three-stage cascade TEC heat sink (TECA, Model: AHP-1200CAS) is now used instead of the liquid chilled cold plate. The intention of this was to have the cascade TEC be the heat sink as well as the fine tune temperature control. However, the air chilled cascade TEC heat sink was not able to dissipate enough heat to provide a consistent linear temperature ramp of 1 °C/min. Therefore, we decided to incorporate the same single-stage TEC cooling element as was used in the first iteration of the CMU-CS. The single-stage Peltier TEC sits atop the cascade TEC heat sink within an

aluminum mounting block that holds the sample dish. Within the aluminum block lies the thermistor (TETech Inc., Model: MP-3176) used for measuring the temperature of the sample dish where the droplets reside. The sample dish is now contained within an acrylic chamber, which allows full view of the sample droplets as well as a better insulated chamber so external insulation isn't necessary. In addition to these changes, the dish is also significantly wider and shorter than the previous dish to house the larger microfluidic devices and to prevent excessive use of squalene oil to cover the droplets for standard droplet-on-substrate usage. To prevent the dish getting stuck in the chamber as happened with the previous version, the dish now simply sits inside of the aluminum mount, which has lower walls than the dish, and the chamber attaches to the mount that seals the dish inside.

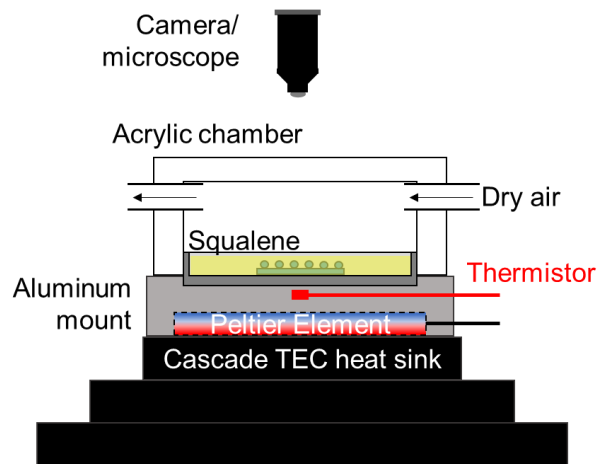


Figure 2.2. CMU-CS second iteration

While these changes have improved the system's ease of use and performance, there are still kinks to work out. One consideration that we had not considered but may be a concern is the use of the acrylic chamber in temperatures that change frequently between warm and cold. The chamber has shown evidence of fracture since its development. This

could also be related to the fittings used for the air ports. One of the biggest issues currently is the need for both the cascade TEC as well as the single-stage TEC to provide temperature control. The single-stage TEC outputs much more heat than the cascade TEC can withstand (due to it being an air-chilled model instead of a liquid chilled one), thus at room temperature the cascade TEC cannot displace the heat that the single-stage needs to reach its set temperature. This causes the system to overheat and can result in extremely high temperatures ($> 90\text{ }^{\circ}\text{C}$) if the single-stage TEC is left running overnight, for example. This is an issue because the single-stage TEC program does not have an automated shut-off. As long as the CMU-CS is used properly this is never a problem, but carelessness can cause issues and has for many users of the instrument. This model of chamber still has air ports for use if droplet-in-air methods are desired, however, this version still experiences frost growth and their related interferences at temperatures above homogeneous freezing. For future models, if droplet-in-air is an intended method, then a proper moisture purging technique needs to be implemented.

2.4 Improvements to droplet imaging analysis

To perform ice nucleation measurements, the temperature of the droplets containing particles needs to be precisely controlled and accurately known, and so does visualization of the droplet freezing events. Droplet freezing is visually observed by the sudden change in reflectance that occurs upon freezing; in our setup frozen droplets appear dark while unfrozen droplets are clear/bright. Thus, the CMU-CS requires an imaging method and a way to analyze the acquired images. Images from the stereomicroscope's camera were previously taken every 10 seconds, and are now taken every 5-6 seconds.

There have been several improvements to the analysis of the droplet images obtained. The first analysis was completely manual and took a long time to complete for a one-hour long cooling assay. Images were manually inspected for changes in droplet color to identify frozen droplets. These freezing events were recorded with image times, which were then manually compared to the 1 Hz temperature data measured by the thermocouple from the TEC software. The data could then be imported to Excel or Matlab to plot droplet freezing temperature spectra. This entire process took around 20-30 minutes per cooling assay depending on the amount of droplets in the array and how fast the user could analyze them.

The next iteration of analysis was a slightly more automated program. I developed code that automated the syncing between images and temperature data using data timestamps. This automation saved roughly 10 minutes, making manual image analysis take 10-20 minutes for a typical assay, especially for larger arrays (~40 droplets). Unfortunately, in this method a significant chunk of time is still taken for the manual image analysis.

Since then Tom Brubaker has developed a fantastic improvement to process the raw droplet image data almost entirely automatically in seconds. He has designed Matlab programs to take images and sync them with the temperature measurements. The program identifies droplets using an edge finding Matlab toolbox, and cycles through all images recorded to determine when freezing of that particular droplet occurs. The algorithm detects freezing based on the change in greyscale value of each identified droplet [*Budke and Koop*, 2015]. It then assigns the freezing temperature measured at the time of the image. This program is able to rapidly output droplet freezing temperature spectra and Excel spreadsheets with all the information needed to analyze and interpret the results of

the experiment. The program also instantly obtains the pixel radius size of each droplet as well, which was not possible without an external program previously. This program is able to do all of this analysis for any sized droplet array in under 20 seconds, a huge step forward for our ice nucleation experimental methods.

2.5 Analysis software in Igor Pro

The post analysis I perform to retrieve all figures created for publications and this dissertation are done in Igor Pro v. 6.37. This code has evolved more than the cold stage itself and all iterations of the code have been maintained. The code was recently reorganized by myself and Will Fahy, a current undergraduate student in the Sullivan group. The code is presented in Appendix A. There are three sections: Frozen Fraction analysis for retrieving all information necessary for depicting freezing distributions, Active Site Density calculations for retrieving n_s , n_m , INP concentration, and other metrics using each of the methods we currently run, and Statistics calculations for combining data or calculating statistical information that is used to produce box and whisker plots or error bars.

2.6 Analyzing droplet freezing measurements

Ice-activity is determined using the data gathered by the above setup. Analyzing this data can be done in a number of ways. Typical assessments of ice nucleating ability include: droplet freezing spectra, concentration of ice nucleating particles (c_{INP}), and active site density normalized to particle mass (n_m) and normalized to particle surface area (n_s). In this section I will discuss the process of deriving these values and the uses of each.

The droplet freezing spectrum is displayed as the cumulative fraction of droplets in an array of droplets as a function of the temperature of freezing. This representation is the simplest representation and is the basis for all other types of analysis. The frozen fraction (y-axis) is the number of droplets frozen at a given temperature divided by the total number of droplets in the population of the array and ranges from 0 to 1. This representation can be used for any type of sample including pure water.

The concentration of ice nucleating particles (c_{INP}) is the next step of analysis. In this representation c_{INP} is given as:

$$c_{INP} = -\frac{\ln(1 - FF)}{V_{drop}}$$

where FF is the y-value of the droplet freezing spectrum, and V_{drop} is the average volume of droplets in the population. Ideally, droplets in an array should be identical. The c_{INP} is often used as a step in calculating the n_m or n_s . However, it can also be used to quickly compare samples and experimental blanks and to perform background correction. This is because the c_{INP} is simply normalizing the freezing activity to the volume of water present in the droplets.

The typical representation used in literature is the n_m or the n_s , the active site density normalized to mass or surface area, respectively. These values are calculated as follows:

$$n_m = \frac{c_{INP}}{m_p}$$

$$n_s = \frac{c_{INP}}{SA_p}$$

where m_p is the mass of particles in each droplet and SA_p is the surface area of particles per droplet. In each case, the ice activity is being normalized to a bulk particle property. Mass-normalized active site density is only used when the surface area is not able to be obtained or is not physically meaningful. For example, when classifying the activity of ice active proteins or bacteria knowing the mass of the bacteria is more meaningful than knowing the surface area of the cells because a cell is complex and most of the surface area of the cell is not participating in the ice activity. Whereas, the surface area-normalized active site density is more physically meaningful for minerals. The n_s is akin to obtaining the activity based on the contact angle of the particle surface. It acts in a more physically understandable way than the n_m does. It is notable that the n_s and n_m metrics are not applicable to pure water measurement because of the inability to quantify the surface area or mass of contaminants and thus only c_{INP} or droplet freezing spectra can be presented [Chapter 3].

3 Cleaning up our water: reducing interferences from non-homogeneous freezing of “pure” water in droplet freezing assays of ice nucleating particles

This Chapter is a manuscript under peer review for publication by the European Geophysical Union in *Atmospheric Measurement Techniques*, submitted 4/26/2018, available online at <https://www.atmos-meas-tech-discuss.net/amt-2018-134/>.

Polen, M., T. Brubaker, J. Somers, and R. C. Sullivan (2018), Cleaning up our water: reducing interferences from non-homogeneous freezing of “pure” water in droplet freezing assays of ice nucleating particles, *Atmos. Meas. Tech. Discuss.*, 1–31, doi:10.5194/amt-2018-134.

3.1 Abstract

Droplet freezing techniques (DFTs) have been used for half a century to measure the concentration of ice nucleating particles (INPs) in the atmosphere and determine their freezing properties to understand the effects of INPs on mixed phase clouds. The ice nucleation community has recently adopted droplet freezing assays as a commonplace experimental approach. These droplet freezing experiments are often limited by

contamination that causes non-homogeneous freezing of the “pure” water used to generate the droplets in the heterogeneous freezing temperature regime that is being measured. Interference from the early freezing of water is often overlooked and not fully reported, or measurements are restricted to analyzing the more ice-active INPs that freeze well above the temperature of the background water. However, this avoidance is not viable for analyzing the freezing behavior of less active INP in the atmosphere that still have potentially important effects on cold-cloud microphysics. In this work we review a number of recent droplet freezing techniques showing great promise in reducing these interferences and report our own extensive series of measurements using similar methodologies. By characterizing the performance of different substrates on which the droplets are placed and of different pure water generation techniques, we recommend best practices to reduce these interferences. We tested different substrates, water sources, droplet matrixes, and droplet sizes to provide deeper insight into what methodologies are best suited for DFTs. Approaches for analyzing droplet freezing temperature spectra and accounting and correcting for the background “pure” water control spectrum are also presented. Finally, we propose experimental and data analysis procedures for future homogeneous and heterogeneous ice nucleation studies to promote a more uniform and reliable methodology that facilitates the ready intercomparison of ice nucleating particles measured by DFTs.

3.2 Introduction

Pure water experiences extensive supercooling. Water droplets of cloud relevant diameters ($\sim 10\text{-}20\text{ }\mu\text{m}$) freeze homogeneously at temperatures $< -38\text{ }^{\circ}\text{C}$, and this temperature increases with increasing droplet volume [*Koop and Murray, 2016; O and Wood, 2016*]. Freezing between -38 and $0\text{ }^{\circ}\text{C}$ requires a catalyst, which in the atmosphere

is provided by rare ice nucleating particles (INPs). Most precipitation over land is triggered through the ice phase [Mülménstätt *et al.*, 2015], and INPs may have large impacts on cold-cloud microphysics, optical properties, lifetime, and structure [Yin *et al.*, 2002; Lohmann and Feichter, 2005; DeMott *et al.*, 2010; Creamean *et al.*, 2013; Vergara-Temprado *et al.*, 2018].

Droplet freezing techniques (DFTs) have been utilized for decades to assess the homogeneous freezing of pure water, and the immersion freezing properties of INPs immersed in the droplets [Bigg, 1953; Vali, 1971, 2014; Murray *et al.*, 2012; Wright and Petters, 2013; Wex *et al.*, 2015]. In general, these experiments work by depositing droplets containing particles onto a surface which is then cooled down to a low temperature by a cold plate heat sink [Cziczo *et al.*, 2017]. Droplets are then assigned a freezing temperature based on the temperature they were observed to freeze at during the cooling process. This data is compiled to produce a plot of frozen fraction of droplets versus temperature, referred to as the droplet freezing temperature spectrum. DFTs are utilized for both homogeneous and heterogeneous ice nucleation experiments [Vali and Stansbury, 1966; Zobrist *et al.*, 2008; Murray *et al.*, 2010, 2012; Hiranuma *et al.*, 2015b; Wilson *et al.*, 2015]. Homogeneous freezing can sometimes present a challenge for DFTs as it is difficult to avoid interference from unintended heterogeneous freezing [Hader *et al.*, 2014; O'Sullivan *et al.*, 2015; Whale *et al.*, 2015]. There are a number of variables within DFT setups that can influence the apparent homogeneous freezing temperature of pure water droplets that determines the background temperature spectrum and sets the lower temperature limit for assessing heterogeneous ice nucleation. Water contamination of substrate interferences can also induce freezing well above the homogeneous temperature limit of ~ -38 °C, restricting

the heterogeneous temperature regime accessible by DFTs. Particles and cloud droplets experience a wide range of cloud temperatures and it is important to characterize as much of the heterogeneous ice nucleation temperature spectrum down to $-38\text{ }^{\circ}\text{C}$ as possible. This requires reducing the influence of water contaminants and substrate effects in DFTs. Recently droplet freezing measurements in the warmer heterogeneous temperature regime $> -25\text{ }^{\circ}\text{C}$ have been combined with measurements in the colder regime of $-20 < T < -35\text{ }^{\circ}\text{C}$ by a continuous flow diffusion chamber to characterize the complete heterogeneous ice nucleation temperature spectrum of ambient particles [DeMott *et al.*, 2017]. We seek to improve and refine DFTs such that they can independently characterize the complete freezing temperature spectrum.

Nanoscale ice active surface sites on particles, macromolecules, and other surfaces are thought to control heterogeneous ice nucleation by helping supercooled water molecules to arrange into an ice embryo, thus reducing the nucleation energy barrier [Marcolli *et al.*, 2007; Gurganus *et al.*, 2014; Koop and Murray, 2016]. In DFTs the surface on which the droplets reside is thought to be one of the biggest factors that induces non-homogeneous freezing behavior, similar to other nucleation and crystallization processes [Diao *et al.*, 2011; Hader *et al.*, 2014]. Properties such as the contact angle between the droplets and the surface can be used to attempt to assess the ideality of the surface [Koop *et al.*, 1998; Murray *et al.*, 2010; Budke and Koop, 2015]. However, despite a large contact angle, surfaces may have micro- or nano-scale defects that induce ice nucleation. Recent work indicates that cracks, scratches, and other surface defects on surfaces and particles impact heterogeneous freezing [Varanasi *et al.*, 2010; Fitzner *et al.*, 2015; Wang *et al.*, 2016b; Kiselev *et al.*, 2017; Lo *et al.*, 2017]. In general, these studies have found that

defects, especially those with crystalline faces similar to ice, lower the barrier for ice nucleation and enhance ice formation above homogeneous temperatures.

Aside from surface induced effects, the environment surrounding the droplets may also influence freezing. Some research groups, including ours, deposit their droplets into an oil or other inert liquid to prevent contamination from the lab environment and eliminate the impact of the Wegener-Bergeron-Findeisen (WBF) process [Broadley *et al.*, 2012; Wright *et al.*, 2013; Pummer *et al.*, 2015; Zolles *et al.*, 2015; Polen *et al.*, 2016; Beydoun *et al.*, 2017; Reicher *et al.*, 2018]. The WBF process occurs when one droplet freezes and takes up water vapor at the expense of unfrozen droplets, potentially inducing evaporation of nearby droplets. Contact by the growing frost halo around the frozen droplet can also induce freezing of neighboring droplets [Jung *et al.*, 2012; Budke and Koop, 2015]. Freezing assays that don't use oil typically use fast cooling rates of up to 10 °C/min so there is not enough time for these WBF effects to manifest, but this shifts the observed freezing temperature several °C colder [Mason *et al.*, 2015]. A cooling rate of 1 °C/min is more representative of typical atmospheric updraft velocities and the associated cooling rates. The oil environment prevents evaporation and these interferences, enabling slower cooling rates and droplet refreeze experiments. However, little assessment has been done to determine how or if these oils are influencing droplet freezing. We found that the surrounding squalene oil reduces the observed freezing temperature of ice active biological particles (protein aggregate macromolecules) in successive droplet freeze-thaw-refreeze experiments of Snomax bacterial ice nucleants [Polen *et al.*, 2016]. We interpreted this as caused by the hydrophobic partitioning of the largest and most ice-active macromolecules into the highly hydrophobic squalene oil that was accelerated by droplet freezing, which

was previously suggested by Budke and Koop [2015]. Some recent microfluidic ice nucleation techniques use fluorinated oils and/or large concentrations of surfactant to stabilize the emulsified droplets [Stan *et al.*, 2009b; Reicher *et al.*, 2018]. Their measured homogeneous freezing temperatures are typically within the expected range (-35 to -37 °C), but the surfactant may have unrecognized influences on heterogeneous freezing processes since freezing is enhanced via contact between the immersed particle and droplet interface [Fukuta, 1975; Tabazadeh *et al.*, 2002; Durant and Shaw, 2005; Gurganus *et al.*, 2014].

A number of non-oil immersion alternatives to DFTs have arisen in the last few years. Some groups choose to keep droplets open to air and rely on a clean, dry flow of air or N₂ to prevent contamination and frost growth [Whale *et al.*, 2015]. One recent study created a completely enclosed droplet chamber by sandwiching an o-ring, water, and silicon substrate between cover slips and sealing it with vacuum grease [Li *et al.*, 2012]. This resulted in a very clean environment conducive to homogeneous freezing of droplets with no need for a dry air flow over the droplets. In a comparison of droplets-in-oil and droplets-in-air, Inada *et al.* [2014] froze individual 3 mL droplets in n-heptane and in air and found similar freezing activity on non-coated glass slides. They correlated early freezing for these tests to the interfacial surface contact with the glass.

In addition to issues with surfaces and droplet matrixes, the “pure” water itself can introduce artifacts. Almost no work has comprehensively examined the impact of source or purity of water on homogeneous freezing. Inada *et al.* [2014] briefly compared tap water and MilliQ water, but these sources showed little difference when droplets were in n-heptane with a surfactant. Aside from this one report, to our knowledge, no one else has

compared freezing temperatures of water from different sources. Most groups either use in-house MilliQ water systems or purchase commercial purified water, such as HPLC-grade water that is typically reserved for highly sensitive chemical analysis. A few groups additionally filter their water to remove larger particles [Hader *et al.*, 2014; Hill *et al.*, 2014]. It is difficult to assess how well different substrates, water purification, and other method details influence the background water freezing spectrum as these important details are often not described in papers that use DFTs and the water background freezing spectrum is not always presented.

Here we report a series of experiments we have performed on the ice nucleation ability of “pure” water as is dictated by variables including the substrate, water source, and droplet matrix. The following sections describe our experimental methodology, data analysis methods, results and analysis for the aforementioned method variables, and our recommendations for best practices for future ice nucleation experiments that use DFTs. We compare our results with those of previous reports that used analogous method parameters. Finally, we advance a simple proposal for future ice nucleation experiments that will allow ready comparison between different specific measurement systems, leading to more uniform analysis that will accelerate our understanding of ice nucleation. We believe the ice nucleation community has acquired many useful strategies for dealing with issues such as contamination but that this knowledge remains largely internal within research groups and is rarely properly communicated to the larger and quickly growing community. This can discourage further advances and improvements to current designs of droplet freezing systems for INP measurements and create barriers to new groups beginning ice nucleation research. We desire to make it common practice to report these

important method details and observations of pure water controls that are currently often overlooked, and begin a discussion of best practices in the community for ice nucleation experiments and droplet freezing spectrum analysis.

3.3 Droplet freezing methodology

The droplet freezing system used in this study has been updated slightly since we first described it in Polen et al. [2016]. Briefly, we use an oil-immersion droplet freezing system composed of a cascade three-stage thermoelectric air-chiller (TECA, AHP-1200CAS) as the heat sink, mounted under a single-stage thermoelectric element (TE Technology Inc., VT-127-1.4-1.5-72) for fine temperature control. An aluminum sample dish sits atop an aluminum block that contains the single-stage thermoelectric element and a thermistor (TE Technology Inc., MP-3176) for temperature measurements. Our temperature measurement has an uncertainty of ± 0.5 °C based on the thermistor's accuracy and our temperature calibrations. Droplets immersed in oil are placed in the aluminum dish, which is covered by a clear acrylic case for imaging by optical microscopy. No air is flown into the chamber over the oil.

Droplets are created using a variable electronic micropipette (SEOH, 3824-1LC) to deposit droplets of 1 or 0.1 μL volume. Droplets are deposited on a substrate that sits under squalene oil (VWR, squalene, $\geq 98\%$), mineral oil (VWR, mineral oil light), or just air. Several types of substrates were tested in this study: hydrophobic silanized glass coverslips (Hampton Research, HR3-231), silicon wafer chips (Ted Pella, 16007), Vaseline[®], a gold wafer (Ted Pella, 16012-G), a “new” gold wafer (Angstrom Engineering, 2WAU500-Q1), gold coated coverslips (Ted Pella, 260156-G), and solid polydimethylsiloxane (PDMS) polymer (Dow Corning, Sylgard 184). Water for these experiments is either from our in-

house MilliQ water purifier (EMD Millipore) or bottled HPLC-grade water (Sigma Aldrich, HPLC Plus 34877).

Substrates were cleaned or prepared in the following ways for these experiments. Silanized cover slips were used fresh from the box without any additional cleaning. A new silanized cover slip was used for each subsequent experiment. Silicon wafer chips were cleaned with HPLC water and acetone and allowed to air dry before use. Gold wafer and gold cover slips were cleaned with acetone and allowed to air dry before use. PDMS solid substrates were soaked in squalene oil for several days before use.

A CMOS camera attached to the microscope (5x magnification) acquires an image every 5-6 seconds. We are able to view on average 40-50 1 μ L droplets or 70-90 0.1 μ L droplets. Frozen droplets appear black, except in the case of a gold background in which the droplets become white. These images are processed using a custom Matlab program that determines freezing events based on a grayscale value [Jung *et al.*, 2012; Budke and Koop, 2015; Reicher *et al.*, 2018] and also determines the diameter of each droplet. Sizing is calibrated using a 1 mm micrometer with 0.01 mm divisions. Initial tests run on gold substrates could not be analyzed by this program because of the inverted color scale produced by the dark gold background, so they were analyzed manually; “new” runs were analyzed using an updated version of the program.

Data compilation and analysis is performed in one of two ways. The first is a typical statistical analysis to determine the average and standard deviation of all runs of the droplet frozen fraction as a function of temperature. This analysis is done when numerous arrays of many droplets have been measured, where each array is treated as a replicate experiment. This allows us to determine standard deviations to evaluate experiment-to-experiment

variability for replicate droplet arrays. The second approach combines all the individual arrays into a single data set. As an example, in two arrays of the same sample type, one of the arrays had a single droplet freeze early at -25°C and the second array had two droplets freeze at -25°C . In this case, combining the data would result in 3 droplets freezing at -25°C . This second method increases the number of droplets in a set when the number of droplets is fairly low per run; it is also used when the number of runs is small (e.g. 2 tests of a single substrate) because statistical methods are less meaningful for low droplet counts. Figure 3.1 shows an example of these two methods of data compilation of the freezing spectra. There is some deviation between the combined unified dataset (blue) and the average of the individual replicates (red), but the combined data never falls outside the standard deviation of the averaged data and thus we believe the combination approach is an acceptable representation of our results, especially when there are low droplet counts available for a given set of experimental parameters.

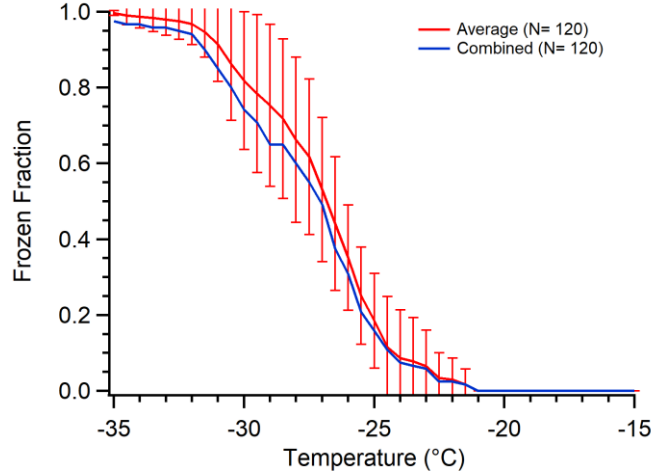


Figure 3.1. Comparison of averaging data from droplet freezing experiments on 120 total droplets measured using three replicate arrays of 40 droplets each (red with error bars) versus combining those 120 droplets into one single hypothetical array of droplets (blue). The standard deviation from the average of the three replicate arrays is shown by the vertical error bars.

3.4 Ice nucleating particle analysis

We present our data as the fraction of frozen droplets in combination with a metric derived from that freezing spectrum – the ice nuclei concentration (c_{IN}) – using Eq. (1) [Vali, 1971, 2008; Hader *et al.*, 2014; Hill *et al.*, 2016; DeMott *et al.*, 2017]. c_{IN} is a droplet volume-normalized representation of the unfrozen fraction of droplets,

$$c_{\text{IN}} = -\ln(N_{\text{unfrozen}})/V_d \quad (1)$$

where V_d is the average volume of the droplets as determined by the image analysis program and N_{unfrozen} is the fraction of droplets unfrozen at a given temperature. We assume the droplets are close to spherical during imaging in determining V_d . Hader *et al.* [2014] describe the derivation of Eq. (1) and present the apparent INP (or ice nuclei) concentration for pure water spectra in comparison to their particle samples. The concentration of ice nuclei per droplet volume provides a way to directly assess the impact on freezing caused

by a sample as compared to any contaminants or artifacts within the measurement. Normalizing the ice nuclei concentration by the surface area (or mass) of particles within the droplets defines the metric known as the ice nucleation active site density, n_s (or n_m). n_s and n_m are often used in the ice nucleation literature to compare different measurements of INPs. However, there are known discrepancies when assigning n_s or n_m values and then comparing identical particles under widely varying particle concentrations [Beydoun *et al.*, 2016]. In DFT one typically does not have any knowledge of the contaminants that induce freezing in pure water, thus we cannot determine the density of active sites (e.g. n_s or n_m) of the contaminants, unlike in studies of heterogeneous ice nucleation where the particle surface area or mass concentration is known or can be estimated. However, we still want to directly compare droplet freezing spectra from different experiments, and normalizing to the droplet volume provides a simple and useful way to do this. More importantly, the INP concentration is also the relevant parameter for assessing how INPs interact with and affect clouds [Hoose and Möhler, 2012]. Finally, the c_{IN} metric allows the ready comparison of droplet freezing spectra obtained using different droplet volumes, as different research groups use a range of droplet sizes in DFT. However, this is only possible if similar particle-in-water concentrations are used. n_s or n_m are often used to account for these particle concentration differences, but as discussed these metrics may not properly account for changes caused by differing surface area or mass concentrations. The c_{IN} metric, when appropriately used, is advantageous as it only assumes the INP concentration scales linearly with the droplet volume.

3.5 Results

Our results are divided into several sections that assess experimental variables tested in our DFT measurements such as substrate type and pure water generation methods. Each section begins with a brief review of previous results obtained by other ice nucleation groups using an analogous method and a discussion of why that specific method was chosen. The first section compares droplet freezing using oil immersion compared to in air. The next section goes into detail on the impact of using different sources and water purification. Then we discuss a variety of substrates examined and compare them to identify what substrates display the best performance for droplet freezing. The final section discusses tests on two droplet generation methods we used.

3.5.1 Droplet immersion matrix: oil versus air

A number of droplet freezing methods have created droplets without an oil matrix, exposing the droplets directly to air [*Li et al.*, 2012; *Mason et al.*, 2015; *Whale et al.*, 2015]. This method requires very clean, dry conditions to avoid artifacts such as the Wegner-Bergeron-Findeisen process and droplet contamination by aerosolized INP. In the case of the BINARY system, droplets are physically separated from one another by a PDMS mask [*Budke and Koop*, 2015]. For systems where droplet separation is not possible, dry air or nitrogen is typically flowed over the droplets to remove ambient water vapor [*Whale et al.*, 2015]. Flowing dry air, however, exacerbates the issue of droplet evaporation and thus large droplets must be used to limit the impact of evaporation over the whole course of the temperature ramp. One unique droplet-in-air measurement was achieved by sealing a chamber completely with a single water drop deposited on the substrate in the chamber and then evaporating and re-condensing the water vapor into many smaller droplets [*Li et al.*,

2012]. This method avoids the issue of ambient water vapor altogether by turning all the sample water into vapor and re-condensing before freezing.

We have attempted droplet-in-air measurements within our own system but consistently had issues with frost halo formation upon reaching $-20\text{ }^{\circ}\text{C}$ using a standard cooling rate of $1\text{ }^{\circ}\text{C}/\text{min}$ [Jung *et al.*, 2012; Budke and Koop, 2015]. A series of images in Figure 3.2 shows this frost growth, which resulted in freezing of nearly all pure water droplets by $-20\text{ }^{\circ}\text{C}$ on hydrophobic coverslips when oil wasn't used. Frost growth similar to this has been shown previously by Whale *et al.* [2015]. This suggests that our system is not air tight enough for this type of experiment. Li *et al.* [2012] froze their samples between two glass cover slides which were sealed together with vacuum grease for the entire experiment. Our chamber must be opened between runs which causes water vapor to condense onto the sample dish and elsewhere within the sample chamber. In this experiment, we had dry nitrogen flushing the chamber similar to previous methods but frost growth still occurred, though at much lower temperatures than tests without the nitrogen flow. Figure 3.2 shows the progression of frost starting at the bottom of the cover slip and continuing to grow toward the top of the glass. We consistently found that freezing and frost growth initiated around $-20\text{ }^{\circ}\text{C}$, and we were never able to approach homogeneous freezing, likely due to our slow but realistic $1\text{ }^{\circ}\text{C}/\text{min}$ cooling rate.

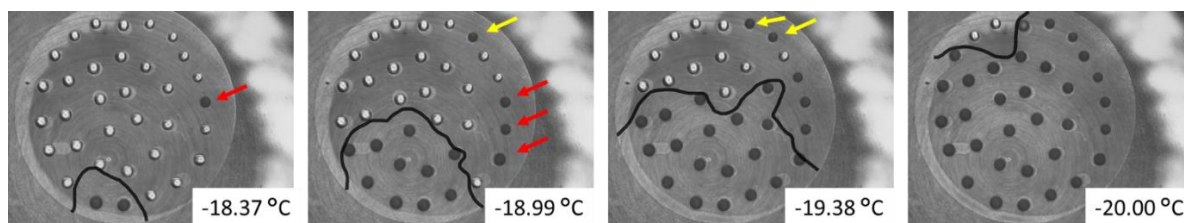


Figure 3.2. Progression of frost halos in one pure water droplet freezing experiment without an oil matrix. Dark droplets are frozen. The black line highlights the frost growth (which is visible in the image but difficult to see) spreading from the bottom left toward the top of the image. Aside from the indicated frost growth, we can also see that other droplets induce freezing in neighboring droplets, such as the droplet on the far right in image 1 (red arrow) and the top right droplet in image 2 (yellow arrow). Subsequently induced droplets are indicated by similarly colored arrows.

Many droplet freezing measurements use an oil matrix to prevent frost halos, droplet evaporation, and external contamination [Broadley *et al.*, 2012; Wright *et al.*, 2013; Pummer *et al.*, 2015; Zolles *et al.*, 2015], which is why we chose to use squalene oil for our measurements. Oil also facilitates droplet refreeze experiments to evaluate the repeatability of the ice nucleation process, and any time-dependent effects such as particle sedimentation or aggregation [Wright *et al.*, 2013; Emersic *et al.*, 2015]. In Polen *et al.* [2016], we proposed the use of mineral oil for biological samples, such as Snomax, to prevent changes in freezing behavior due to hydrophobic partitioning, which we suspected to be the case for refreezes performed in squalene oil ($C_{30}H_{50}$). However, in our attempts to use mineral oil in pure water measurements the mineral oil froze around $-30\text{ }^{\circ}\text{C}$. We consistently saw what we at first assumed to be fogging, but upon closer inspection we found that the mineral oil had frozen completely solid, precluding droplet freezing experiments. Though we never saw mention of the freezing point in the material safety data sheets provided for the mineral oils, this is a known issue in the use of mineral oil for

liquid chilling in desktop computers. However, we are also aware that the WISDOM microfluidic DFT device uses mineral oil for droplet creation and storage [Reicher *et al.*, 2018]. The device has successfully measured homogeneous ice nucleation down to -36 °C. Perhaps the surfactant (Span80, 2 wt%) used to stabilize the immersed droplets prevents freezing of the mineral oil. Alternatively, the optical fogging may not be visible when such a small volume of oil is above the droplets, as is the case for microfluidic devices. Despite the promising results from the WISDOM method, we are wary to suggest that any other groups attempt the use of mineral oil for droplet freezing measurements before further investigation into how the oil's freezing may impact water droplet freezing. For all oil-immersion experiments mentioned in the following sections, squalene oil was used as the oil matrix, following the method of Wright and Petters [2013]. Previously, we have shed light on squalene oil reducing the observed ice nucleation activity of Snomax bacterial particles and concluded this was due to hydrophobic partitioning of large protein aggregates [Polen *et al.*, 2016]. This was only observed in droplet refreeze experiments of Snomax, and we do not see this effect on any other particle sample type we have tested. Squalene oil remains our recommended immersion oil for most droplet freezing experiments.

3.5.2 Water sources and purification

Many in the ice nucleation community use MilliQ water or similar commercial systems to purify their laboratory's in-house water [Rigg *et al.*, 2013; Wright and Petters, 2013; Inada *et al.*, 2014; Pummer *et al.*, 2015; Umo *et al.*, 2015; Tobo, 2016]. Some groups have used bottled HPLC grade or other similar water for their DFT [Fornea *et al.*, 2009; Wright and Petters, 2013]. Still others use alternative methods, such as condensation, to

create droplets [Li *et al.*, 2012; Campbell *et al.*, 2015; Mason *et al.*, 2015]. We compared water produced by our in-house MilliQ system with bottled HPLC-grade water from Sigma Aldrich (Figure 3.3). Both water types were also filtered using 0.02 μm pore size Anotop filters before droplet generation. In general, the droplet freezing spectra obtained from the two types of water are very similar to one another. With ~ 1000 droplets for each water type, we find little difference in the apparent INP concentration as well. The biggest deviation came from runs of HPLC water that was filtered multiple times over many weeks using the same Anotop filter, which shows an increase in ice nuclei around $-25\text{ }^{\circ}\text{C}$, though this is not outside the standard deviation of our other samples. This result indicates that either purchased HPLC or produced MilliQ water could be useable for droplet freezing experiments. As MilliQ water systems use a series of filter cartridges and a membrane filter to remove dissolved contaminants, particles, and ions from the supplied water, the quality of the produced water achieved will depend on the quality of the original water supply source. The “house” water supply is beyond the control of most research groups. Along with other issues we have experienced using MilliQ water that we discuss below, high-quality bottled water may be a better and more reliable water source for ice nucleation studies.

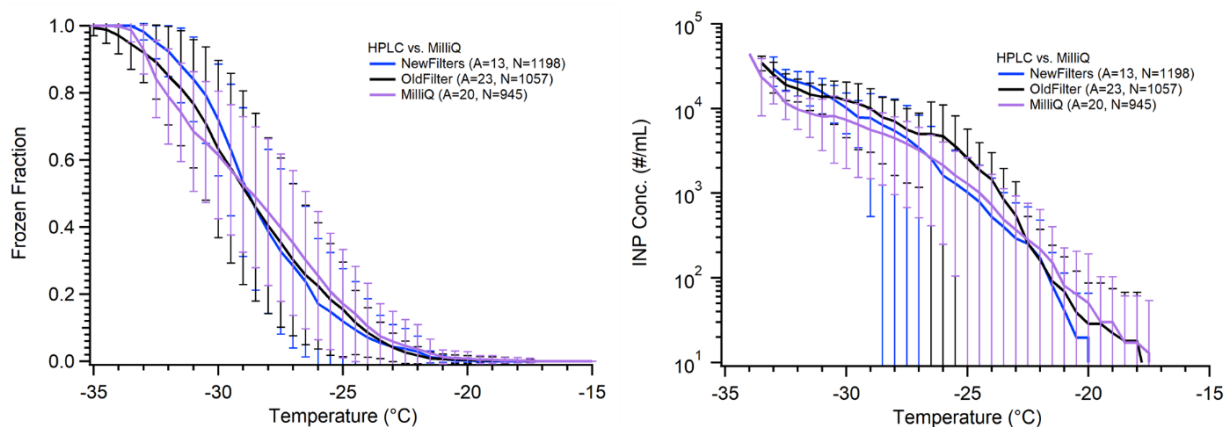


Figure 3.3. Comparison of pure water freezing using filtered MilliQ produced water and filtered purchased HPLC water. Shown are the measured droplet freezing temperature spectra (left) and the derived INP concentration (right). HPLC water was filtered using a new Anotop 0.02 μm filter for each bottle of water (blue), or the same filter for multiple stock bottles of water (black). The results from typical MilliQ water arrays are shown in purple. The parentheses next to each legend entry contains the number of arrays of droplets (A) and the total number of droplets across all arrays (N).

We experienced significant and unexpected issues in continuing to use MilliQ water for our droplet freezing tests and experiments that caused us to switch to bottled HPLC water for all our future experiments. The MilliQ-produced water can result in very inconsistent results for pure water droplet controls if the particle membrane filter is not changed on a regular basis. This is a serious concern as there is no easy way to determine the status of the filter; the MilliQ system only measures the resistivity of the water as a measurement of the ionic strength, as well as total carbon concentration. Figure 3.4 shows results from trying to diagnose the issue behind a much warmer than typical background freezing spectrum for MilliQ water droplets. The results were highly inconsistent, with droplets in some arrays freezing as warm as -13°C , some droplet arrays freezing completely before -25°C , and one array with a median freezing temperature, N_{50} , of -28

°C that rivaled our least contaminated pure water tests at the time. We also found a significant decrease in the early freezing droplets when we let the MilliQ system run for 5 minutes before collecting water used to generate the control droplets. These caveats in using MilliQ water will likely depend greatly on different lab environments, protocols, number of users, and differences in the original water supply sources. Thus, we chose to perform future experiments with bottled HPLC water in an attempt to improve experiment-to-experiment consistency by removing the variability posed by the MilliQ system's water quality. Additionally, we filter our water before use with a 20 nm pore size Anotop filter to further reduce variability and remove small particles that may be a source of INPs. The use of an Anotop filter was suggested to us by Thomas Hill, as is used in the CSU Ice Spectrometer system [Garcia *et al.*, 2012].

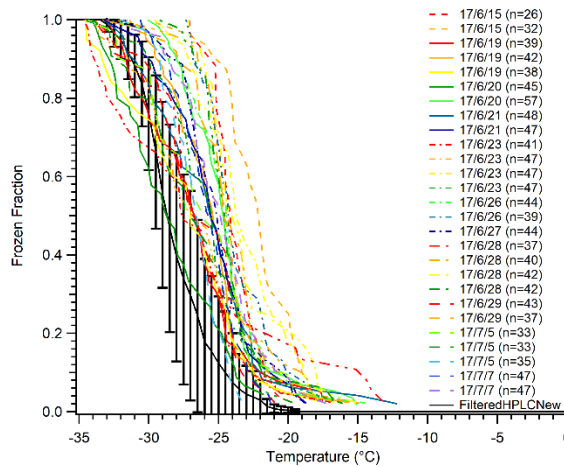


Figure 3.4. A series of tests on MilliQ generated water droplets to determine contamination sources. Droplets displayed inexplicably high freezing temperatures compared to filtered HPLC water at the time (solid brown with error bars). Temperatures for N_{50} ranged from -20 °C to -29 °C from day to day. Error bars indicate standard deviation of data for the filtered HPLC water.

3.5.3 Substrate tests

In this section we discuss an extensive series of experiments in which we tested the effect of various substrates on the observed freezing spectra for pure water droplets. Our goal is to identify substrates that display a reproducibly low amount of interference in the pure water controls by allowing the droplets to freeze close to the expected homogeneous freezing temperature. This is -33 to -35 °C for the droplet volumes used here based on Eq. 7 from Pruppacher (1995). Except when noted, all arrays were created using filtered HPLC water. Each of these substrates has been shown to work reasonably well for droplet freezing experiments in the past.

3.5.3.1 Hydrophobic cover slips

Hydrophobic cover slips are one of the most used substrates for DFTs [Bigg, 1953; Durant *et al.*, 2008; Iannone *et al.*, 2011; Murray *et al.*, 2011; Wright and Petters, 2013; Mason *et al.*, 2015]. These can be made in-laboratory by silanizing a standard glass slide [Fornea *et al.*, 2009; Wright and Petters, 2013], or can be purchased pre-silanized [Iannone *et al.*, 2011; Mason *et al.*, 2015; Whale *et al.*, 2015; Wheeler *et al.*, 2015; Beydoun *et al.*, 2016, 2017; Polen *et al.*, 2016]. In general, results of pure water freezing on hydrophobic cover slips are variable. Whale *et al.* [2015] reported the 50% droplet frozen fraction (N_{50}) close to -26 °C for 1 μ L droplets. Hader *et al.* [2014] reported N_{50} at -30 °C for 150 nL droplets, while Iannone *et al.* [2011] found N_{50} at -37 °C for 60 nL droplets. While an increase in homogeneous freezing temperature is expected for larger droplets, based on classical nucleation theory (CNT) we expect all of these droplet sizes to freeze homogeneously below -30 °C [Pruppacher, 1995; Vali, 1999; Koop and Murray, 2016].

This implies that the larger droplets froze heterogeneously due to some unintended ice nucleating material or surface.

Our results using pre-silanized hydrophobic coverslips are similar to those reported using analogous methods by Hader et al. [2014] and Whale et al. [2015] for our larger and smaller droplets, respectively. Figure 3.5 displays our freezing spectra for large and small HPLC droplets on hydrophobic cover slips. The N_{50} for smaller (0.1 μL) droplets (black and blue) is $-29\text{ }^{\circ}\text{C}$, and $-27\text{ }^{\circ}\text{C}$ for larger (1.0 μL) droplets. Freezing onset begins consistently around $-20\text{ }^{\circ}\text{C}$, and final droplets freeze between -33 to $-35\text{ }^{\circ}\text{C}$ as is expected for these droplet sizes. Importantly, we note that freezing pure water droplets simultaneously alongside sample droplets containing test particles (shown in green in Figure 3.5) does not impact the freezing temperature spectrum when compared to the same droplet size data (red). This, in conjunction with the similar literature results, suggests variability between different DFT systems for pure water controls using hydrophobic coverslips may be explained primarily by the droplet size. However, we find a counterintuitive trend when comparing the apparent INP concentration, c_{IN} , for these measurements. When comparing larger and smaller droplets, the concentration of ice nuclei is actually lower for larger droplets (red vs. blue points in Figure 3.5). This could mean that the INP concentration for these samples is not directly related to the droplet volume but instead is more directly tied to the contact surface area with the substrate. We propose that this may be caused by one of two effects: 1) smaller droplets have larger surface area-to-volume ratios and by normalizing to volume using c_{IN} we are under-correcting interferences caused by droplet-surface contact for small droplets; or 2) larger droplets have higher contact area with the surface and thus by correcting to volume we are

overcorrecting interference experienced by larger droplets. More work is necessary to connect the contact area to the elevated pure water freezing temperature. This size effect is also observed for the gold-coated substrates discussed in Gold-coated substrates.

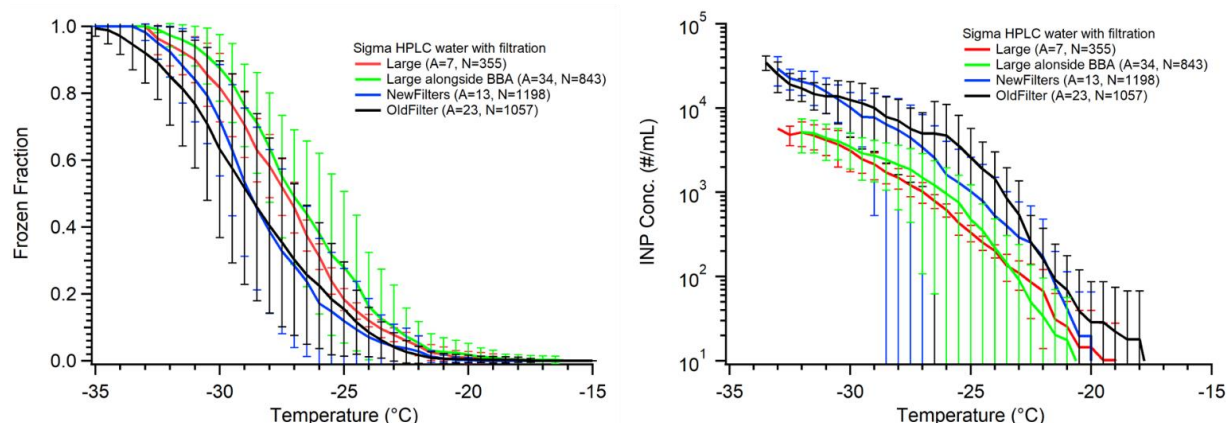


Figure 3.5. Droplet freezing temperature spectra (left) and apparent ice nuclei concentration, c_{IN} , (right) for pure water droplet freezing measurements on a hydrophobic cover slip. In all experiments HPLC water that was filtered using an Anotop 0.02 μm syringe filter was used. Each data series has been binned into 0.5 $^{\circ}\text{C}$ temperature increments. The red data series is from large (1.0 μL) droplets, green is from large (1.0 μL) droplets measured alongside biomass burning aerosol sample droplets (Figure 3.12), blue is from small (0.1 μL) droplets using a new Anotop filter for each stock bottle of filtered water, and black is small droplets using a singular Anotop filter for many different stock bottles of water. The parentheses next to each legend entry contains the number of arrays of droplets (A) and the total number of droplets across all arrays (N) tested for each experiment type. Error bars are standard deviations for the replicate droplet arrays.

We have also observed some batches of purchased coverslips to induce freezing as warm as -18°C , and with much greater variability in the freezing spectra. Thus, it is important to evaluate each batch of coverslips to test for these potential issues. Ideally pure water control droplets will be placed along with droplets containing the particle sample of interest on the *same* coverslip to directly evaluate the background freezing spectrum on

that specific cover slip. This is especially important when working with particle systems of weak ice-activity that freeze close to the background water temperature range.

3.5.3.2 Silicon wafers

A few groups have utilized silicon wafers for droplet freezing experiments [*Li et al.*, 2012; *Peckhaus et al.*, 2016]. Peckhaus et al. [2016] used droplets of 107 μm in diameter and found 90% of droplets froze below $-35\text{ }^{\circ}\text{C}$. All droplets reported by Li et al. [2012] froze below $-37.5\text{ }^{\circ}\text{C}$ for 10-70 μm in diameter. Additionally, Li et al. performed detailed assessment of hydrophobic and hydrophilic silicon wafers used in pure water ice nucleation experiments. They found that both types of wafer produced nearly homogeneous freezing for pure water droplets.

We investigated ice nucleation on silicon wafer chips typically used for SEM analysis. Several silicon chips were placed in the sample dish with squalene oil, and 0.1 μL ($\sim 600\text{ }\mu\text{m}$) HPLC droplets were deposited on them. Due to the small size (5x7 mm) of the chips, the number of droplets on each wafer chip was very low (~ 10), and thus we combined all the data from twelve chips as though it were a single surface containing 120 droplets (Figure 3.6). We find similar freezing activity to the hydrophobic cover slips with onset freezing beginning around $-21\text{ }^{\circ}\text{C}$, reaching 50% around $-26\text{ }^{\circ}\text{C}$, and finishing at $-35\text{ }^{\circ}\text{C}$. The apparent INP concentration for the silicon wafer also falls close to the cover slip data (Figure 3.6). We are using much larger droplets ($\sim 6\text{-}60\times$ diameter) than the groups who have used silicon substrates previously, so we do see higher freezing temperatures as expected. However, due to the similar behavior and apparent INP concentration we observe using the glass cover slips and the silicon wafer, we cannot conclude that silicon provides a more ideal surface for INP studies than silanized hydrophobic glass. The superior

performance reported by other groups using silicon wafers may be due to higher purity water than we have access to, or other method details that make a direct comparison challenging.

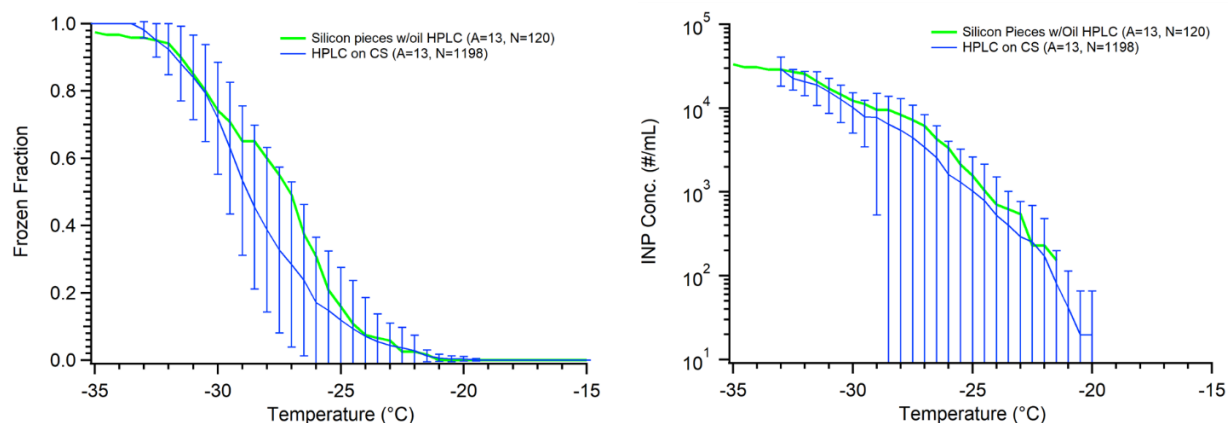


Figure 3.6. Comparison of freezing on silicon wafer chips (green) against hydrophobic cover slips (blue), following Figure 3.5. The freezing temperature spectrum is on the left, and the retrieved c_{IN} is on the right. Both datasets use 0.1 μL droplets. The data from all replicate arrays using silicon (green) are combined into one series and thus no error bars can be determined. The parentheses next to each legend entry contains the number of arrays of droplets (A) and the total number of droplets across all arrays (N).

3.5.3.3 Vaseline®

First utilized by Tobo [2016] for the Cryogenic Refrigerator Applied to Freezing Test (CRAFT) droplet freezing instrument, Vaseline® petroleum jelly can be spread onto a clean surface to create a makeshift hydrophobic substrate. The results from Tobo [2016] indicate great promise in this substrate for DFT as the large, 5 μL droplets froze with $N_{50} = -33\text{ }^{\circ}\text{C}$, approaching the temperature predicted by CNT for homogeneous freezing. We examined large (1.0 μL) droplets on Vaseline® spread onto our sample dish in air, similar to Tobo [2016], as well as smaller droplets (0.1 μL) on Vaseline® and within a squalene oil matrix. The results are shown in Figure 3.7. For tests without the oil matrix, we found

quite warm onset freezing temperatures while only a few droplets approached the homogeneous limit. We found similar trends whether we used MilliQ water or filtered HPLC water. However, once we utilized smaller droplets in an oil matrix, the early onset freezing vanished and we observed good background freezing curves with lower onset and N_{50} temperatures. We hypothesize that our inability to reproduce pure water freezing near the homogeneous limit using a Vaseline[®] coated substrate as in Tobo [2016] is due to the difference in cleanliness between laboratory environments as well as differences in applying the Vaseline[®] layer. The oil matrix does eliminate much of the early, high temperature freezing that is likely caused by contamination or an unevenly coated surface. This suggests the use of a laminar flow hood or glove box may be necessary to achieve such low background freezing temperatures without oil when the droplets are exposed to air. Tobo prepared their droplet arrays inside a glove box within a clean room environment, and such clean conditions are not readily available to many research groups. Uniform application of Vaseline[®] requires precision and a specialized spatula to get around the lipped design, and non-uniform application will increase the risk of surface-induced freezing by any exposed underlying substrate. Interestingly, we note that one benefit to Vaseline[®] is we did not observe evidence of WBF effects on neighboring droplets when in air, which makes it favorable for droplets-in-air experiments if interferences can be reduced. Creation of a surface specifically designed for Vaseline[®] application is an important consideration if this promising technique is to be utilized more widely.

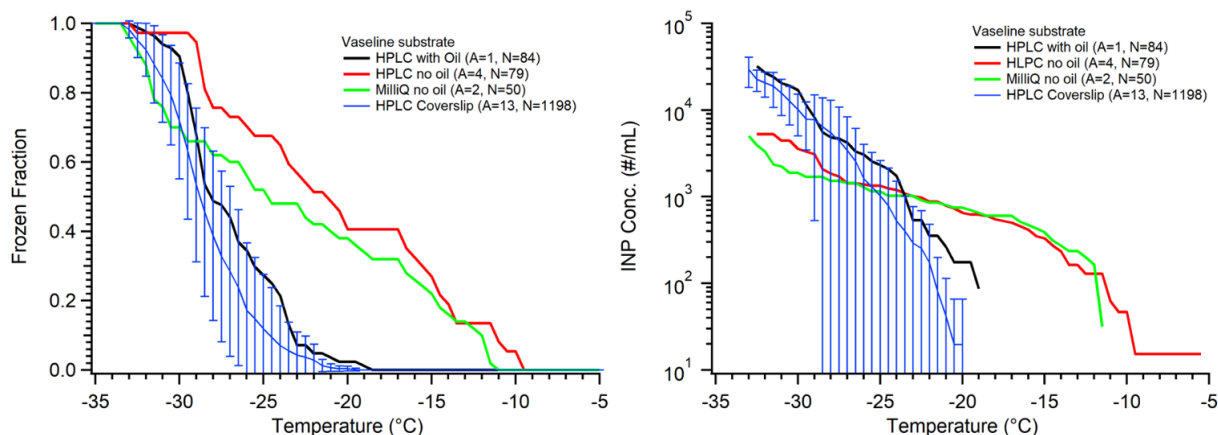


Figure 3.7. Pure water droplet experiments on a Vaseline coated substrate, following Figure 3.5. The HPLC water using a silanized coverslip data in blue are displayed for comparison and is the data from the hydrophobic cover slip using small droplets (Figure 3.5, blue). The data from replicate arrays for Vaseline is combined as described in Section 2 and thus no error bars are determined for these. Three sets of experiments on Vaseline are shown: black is small droplets (0.1 uL) of HPLC filtered water in oil, red is large droplets (1.0 uL) without oil, and green is large droplets of MilliQ water without oil. The parentheses next to each legend entry contains the number of arrays of droplets (A) and the total number of droplets across all arrays (N).

3.5.3.4 Gold-coated substrates

Limited tests have been reported using gold-coated substrates in DFTs. Häusler et al. [Häusler et al., 2018] etched the surface of a gold-coated substrate and found near-homogeneous freezing temperatures ($N_{50} \approx -37.3$ °C) for pure water droplets (45 μm) despite obvious nanoscale features in the freezing chip's cavities. In our tests we used two substrates: a gold-coated silicon wafer and a gold-coated glass cover slip (GCS). Our results are shown in Figure 3.8. The HPLC water on gold wafer produced a very low freezing temperature with N_{50} around -32 °C; similarly small droplets of MilliQ water on the GCS had N_{50} at -30.5 °C. Additionally, our first test on a second gold wafer (red) with many more droplets showed N_{50} at -33.9 °C. However, large HPLC water droplets on the

GCS ($N_{50} = -26.5$ °C) froze similar to large droplets on the hydrophobic silanized cover slip ($N_{50} = -27$ °C). When comparing the apparent INP concentrations, we again see the trend of larger droplets having lower c_{IN} than smaller droplets. In this case the difference is even starker with nearly half an order of magnitude difference in c_{IN} between large and small droplets on GCS at $T < -30$ °C. Additionally, we find that upon cleaning and reusing a gold wafer (orange) the freezing spectrum and apparent INP concentration increased compared to the first use (red) and became similar to the silanized cover slip. This could suggest that cleaning the surface with acetone and drying with dry, particle free air affects the surface in some way making it more ice active, or just does not adequately clean the substrate. More analysis should be performed to identify the impacts of cleaning on the gold surface. If this issue can be solved or avoided and the surface can be cleaned without introducing contamination or ice active surfaces, then gold has the potential to be a near ideal substrate. One issue with gold surfaces is they are soft and easy to scratch, even with careful handling using Teflon-coated tweezers. This could create more ice active surface sites over time, and also be an interference in the droplet optical microscopy imaging. Gold is also much darker than the other substrates we tested, requiring manual retrieval of the droplet freezing spectrum.

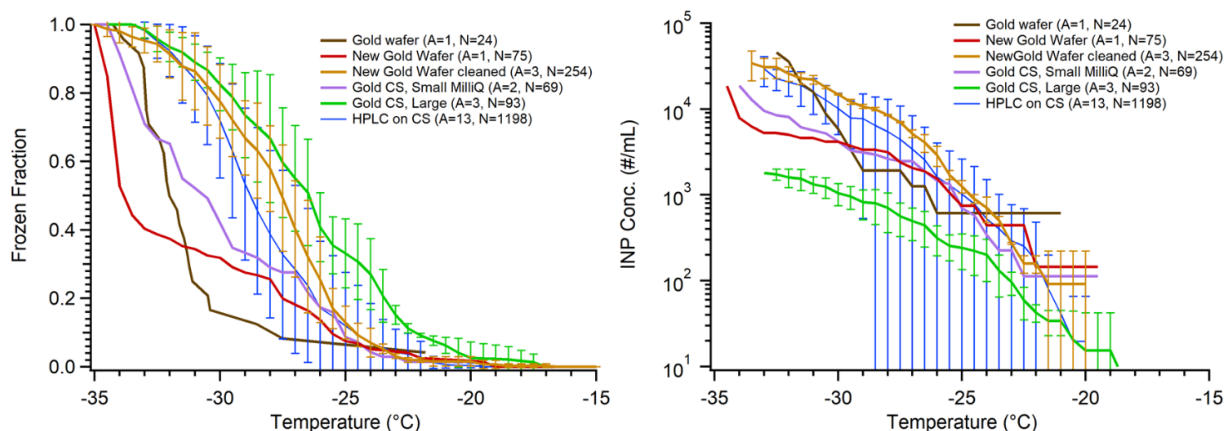


Figure 3.8. Measurements of pure water droplet freezing on gold substrates are shown following Figure 3.5.

The data from small HPLC water droplets on a silanized cover slip are displayed in blue for comparison (Figure 3.5, blue). The gold data displayed are using HPLC water droplets on a gold wafer substrate (brown), small MilliQ droplets on a gold-coated glass coverslip (GCS) (lilac), and large HPLC water droplets on a GCS (green). Also displayed are data from small droplets on another gold wafer upon first use (red), and subsequent small droplet arrays on the same wafer following cleaning and drying, with associated error bars (orange). The parentheses next to each legend entry contains the number of arrays of droplets (A) and the total number of droplets across all arrays (N). Error bars show standard deviation from replicate droplets arrays. The data from the gold wafer (brown and red) and small droplets on a GCS (lilac) were combined into one series and so no error bars are derived.

3.5.3.5 Polydimethylsiloxane (PDMS)

Polydimethylsiloxane (PDMS) is a widely used hydrophobic, cross-linked polymeric material. PDMS has been used in microfluidic droplet freezing approaches [Stan *et al.*, 2009b; Reicher *et al.*, 2018], but not as a substrate for conventional DFT. Reicher *et al.* [2018] provided a comparison of microfluidic systems with other DFTs that showed comparable homogeneous ice nucleation rates for all methods. The excellent performance of these published microfluidic techniques, and our own experience with microfluidic devices fabricated from PDMS for DFTs led us to test PDMS as a droplet freezing

substrate. We studied two types of PDMS: a squalene oil-soaked hydrophobic PDMS surface (untreated), and a surface that was exposed to a plasma, then baked at 180 °C, and soaked in squalene oil for several days (treated). The latter represents PDMS as would be typical for a microfluidic device fabricated using conventional soft lithography. One important note is the treated PDMS did return to its original hydrophobic form following plasma treatment and oil soaking and displayed similar freezing results as the untreated PDMS (Figure 3.9). The pure water freezing spectra are again similar to our silanized cover slip results, as we have seen for most of the other substrates tested. Each of the PDMS tests was within the standard deviation of the CS data, suggesting that the PDMS surface does not provide any inherent benefit over hydrophobic silanized glass. On the other hand, PDMS is quite cheap and easy to manipulate if you have the resources to do so, which makes it a quite useful substrate for IN studies. The hydrophobic nature of the polymer can make it prone to contamination however, and PDMS is often used as a sorbent in environmental contaminant sampling [*Choi et al.*, 2011; *Thomas et al.*, 2014]. One other potential downside to PDMS for DFTs is its poor heat transfer properties. The thickness of the PDMS layer must be consistent for each experiment or the temperature calibration will be inaccurate.

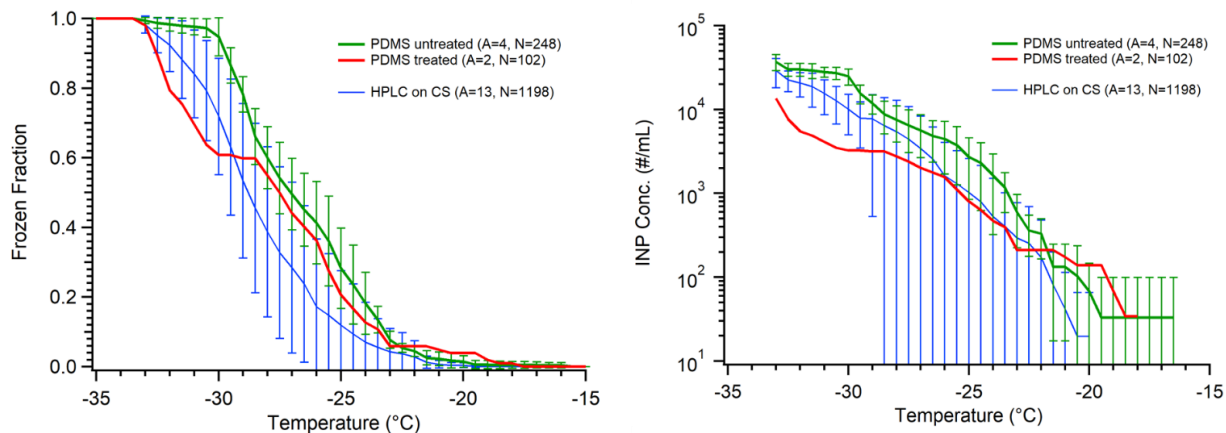


Figure 3.9. Measurements of HPLC pure water droplet freezing on PDMS are shown in red and green, following Figure 3.5. The data from small droplets on a silanized coverslip are displayed for comparison in blue (Figure 3.5, blue). The PDMS data was obtained using treated (red) and untreated (green) PDMS polymer with small droplets. The parentheses next to each legend entry contains the number of arrays of droplets (A) and the total number of droplets across all arrays (N). Error bars on green data show standard deviation from replicate arrays, while the red data are combined into one series as explained in section 2.

We have recently developed a new “store-and-create” microfluidic device that shows great promise in eliminating the interferences from surface interactions as seen in our and other groups’ DFTs [Boukellal *et al.*, 2009; Bithi and Vanapalli, 2010; Sun *et al.*, 2011]. This device will be fully described in a forthcoming manuscript. The PDMS device holds up to 600 droplets of ~6 nL volume encased in squalene oil. Each droplet is stored in an isolated microwell, completely engulfed by oil. Initial results for pure water droplet freezing are shown in Figure 3.10 and compared with hydrophobic silanized cover slips. We find a N_{50} around -34 °C with less than 10% of droplets freezing above -32 °C. Interestingly, we see that the apparent INP concentration continues the same trend as the 0.1 uL droplets on a hydrophobic cover slip. This is likely because the droplets lack contact

with any solid surface inside the microfluidic device and the contaminants causing this non-homogeneous freezing are related to water or oil contaminants.

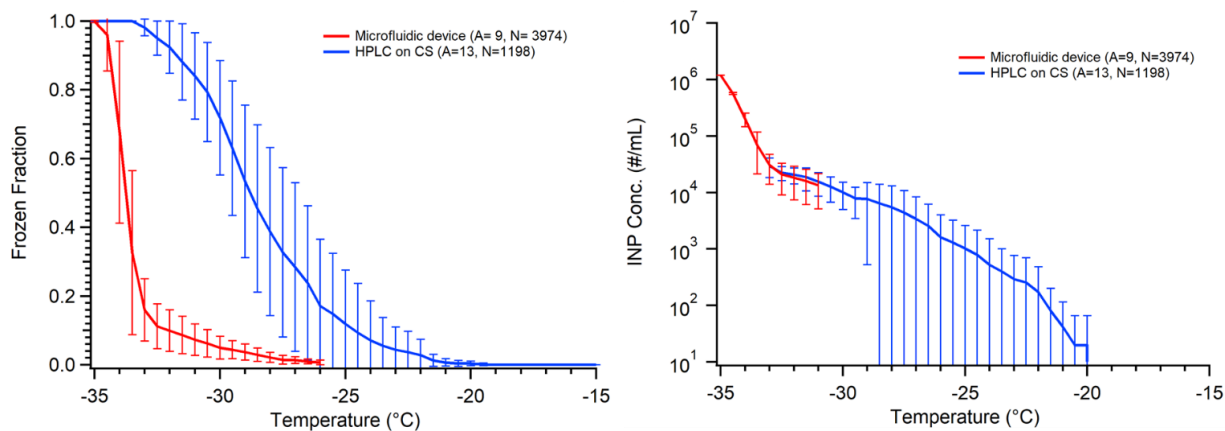


Figure 3.10. Comparison of pure water droplet freezing in our new microfluidic chip (red) versus using a silanized cover slip (CS) (blue), following Figure 3.5. Droplets in the microfluidic chip are 6 nL in volume and droplets on the CS are 0.1 μ L. Error bars show variability of droplet freezing between different replicate arrays. The parentheses next to each legend entry contains the number of arrays of droplets (A) and the total number of droplets across all arrays (N).

3.5.4 Droplet creation methods

Some experimentation was done to compare two types of droplet creation techniques, using a syringe or autopipette. We have experienced issues with both approaches that we briefly describe here so that other users can be vigilant in avoiding these problems. Syringes create droplets with volumes of 0.1 μ L that are very consistent in droplet size, much more consistent than pipettes working at similar volumes. However, using syringes has long term usage issues when the water is not completely particle free as they are difficult to clean. Each syringe (Hamilton Company, model 7001 KH) we used eventually became contaminated beyond use (evaluated by pure water control freezing spectra) and needed to be replaced. This becomes expensive when running freezing assays

repeatedly for weeks and months at a time. Syringes are also not automated and can be fragile, requiring careful use that can be time consuming when creating an array of 50+ droplets.

Switching from a syringe to an electronic pipette with disposable tips improved the long-term consistency of droplet creation. In our experience sterilized tips in boxes remain contamination free the longest. However, we are still uncertain about the amount of contamination introduced by the pipette tips. The best freezing experiments with pipetted droplets still freeze significantly above the homogeneous freezing limit, which could be caused in whole or in part by pipette tips, or by remaining water contaminants, or the silanized glass cover slip substrate.

3.6 Discussion

The results presented above provide a detailed account of many tests run on pure water ice nucleation measurements using our cold plate DFT. Figure 3.11 displays a summary of the major findings from different substrate tests. Vaseline provided the least consistency between droplet freezing temperatures with the highest onset freezing ($T = -18.5\text{ }^{\circ}\text{C}$), even when droplets were surrounded by oil. However, Vaseline[®] had the one benefit of preventing frost-induced freezing compared to hydrophobic cover slips, when droplets were not in oil. Despite this Vaseline[®] poses a significant number of issues, such as uneven surface coating and unclean lab environment, which makes it impractical for many researchers. The gold wafer showed the most promise for our standard droplet freezing method with N_{50} at $-33.9\text{ }^{\circ}\text{C}$, but it also had some quite warm onset freezing ($T = -19\text{ }^{\circ}\text{C}$) and when cleaned with acetone produced a similar freezing curve to other substrates (Figure 3.11). Gold wafers have the caveats that they are quite expensive and

the surface is easily scratched, as well as the potential for contamination when cleaning, which we saw using the gold wafer (“Cleaned” vs. “New”, Figure 3.11). PDMS, hydrophobic cover slips (both shown in Figure 3.11), and silicon wafer chips (not shown) displayed very similar freezing behavior with N_{50} between -27 and -29 °C, only slightly warmer than the gold wafer. Our new microfluidic device shows enormous improvements over these other methods with less than 10% of droplets freezing warmer than -32 °C, consistently. The reason this device has such low freezing is likely because droplets are completely engulfed by a layer of oil and have little to no contact with the PDMS surface, unlike typical droplet-in-oil DFTs. We also observed mineral oil freezing at temperatures warmer than homogeneous freezing, thus it should not be used for this type of analysis. We found that MilliQ water, when the system is operating properly, displays similar ice nucleating properties to filtered HPLC water. Few studies in the past have analyzed and compared different water sources, so it is difficult to assess its impact on the ice nucleation results. We experienced significant interferences using MilliQ water when the final particle filter suddenly went bad with no other indication. This issue cost us several weeks of intensive testing to identify and resolve, which is why we recommend the use of bottled HPLC-grade water, with additional particle filtering, to remove the variability in the quality of the water used.

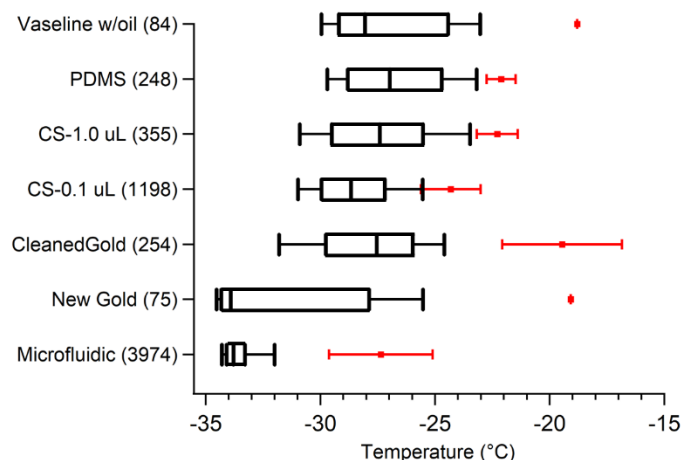


Figure 3.11. Summary of pure water droplet freezing spectra for different substrates tested. Boxes show the 25% and 75% frozen quartiles and the median, N_{50} , is indicated by the line inside each box. Red markers are the temperatures of the first onset freezing droplets with error bars showing variability between different replicate droplet arrays. No error bars for the onset freezing for Vaseline and gold wafer are shown because only one array was run of each. Whiskers show the 10% and 90% droplet frozen fractions. Next to each substrate name in parentheses is the number of droplets tested. Filtered HPLC water droplets produced by an electronic pipette were used in all of these measurements, except for the microfluidic chip which generated the droplets on-chip. Droplets were 0.1 μL in volume, except for the 1.0 μL on the coverslip, and the 6 nL droplets created in the microfluidic chip.

3.7 Recommendations for droplet freezing method and analysis protocols

The intent of this study is to bring to light some of the unpublished and under-reported results, experiences, and insights that are required to effectively examine heterogeneous ice nucleation using droplet freezing methods, especially when the ice nucleating particles have low freezing activity. Providing a basic overview of the best results obtained for pure water controls in our tests and the literature can lead to a series of best practices or recommendations and more method standardization. While DFTs have

improved to produce accurate and reliable immersion freezing measurements, we have certainly not achieved the ideal experimental methods and strategies. To continue to advance DFTs it is important that researchers present their raw data with all its imperfections, including pure water controls, comprehensive descriptions of method details and data analysis procedures, and raw droplet freezing temperature spectra. This is the information required for the ice nucleation community to learn from each other and continue to improve our experimental methods. This will also enable new research groups to start making accurate and reproducible freezing measurements more quickly and reliably. The following are recommendations that we propose all research groups incorporate into their droplet freezing experiments and publications of these results:

1. We suggest that researchers present an assessment of raw frozen fraction curves/spectra for all types of analysis performed (homogeneous and heterogeneous freezing). This practice is often followed in the literature, but there are plenty of instances where these data are not provided and instead the retrieved ice active site density (n_s , n_m) is the exclusive result published. Frozen fraction spectrum is a base level analysis that all groups must do to retrieve any further parameters such as n_s and n_m . Thus, presenting the raw frozen fraction curves for all data is a simple addition to any manuscript, even if it is presented within the supplemental section. The raw spectra can be used by the authors and others to diagnose contaminants or inconsistencies between similar droplet freezing experiments and methods.

We encourage retrieving the apparent INP concentration, c_{IN} , as an especially useful metric for quantifying the background freezing spectrum, and for comparison of different DFTs. This metric has often been used as an intermediate step to determine ice

active site density, but we believe it, in and of itself, is a useful metric that should be reported, especially when examining pure water controls. Since there is no way to know the specific properties of any contaminants within pure water droplets directly, having an idea of the level of contamination per volume of water provides useful insights into what may be preventing reaching the homogeneous freezing temperature limit. Contrary to the frozen fraction curves, INP concentration is normalized to the droplet volume, which makes it an effective way to compare pure water controls in different DFTs that invariably measure different droplet sizes.

We will note there are some unexpected trends for our results regarding the retrieved c_{IN} spectra when dealing with different droplet sizes. In particular, we see a lower concentration of ice nuclei when we use larger droplets, despite normalizing to the volume even when the same experimental conditions are used. This suggests that normalizing to volume may over-compensate for the differences between droplet sizes. We believe this may be because the apparent INP concentration is less influenced by the concentration of particles in the water and more influenced by the contact surface area between the droplet and the surface. Thus, normalizing to volume may not be the best metric for determining activity of contaminants in homogeneous nucleation. Fixing the droplet volume can remove this issue and is another one of our recommendations below.

2. Procedures to correct the raw freezing spectra for interference from background freezing observed in “pure” water droplets should be reported. Retrieval of c_{IN} following previous approaches [Vali, 1971, 2008; Hader *et al.*, 2014; Hill *et al.*, 2016; DeMott *et al.*, 2017] and as we have done here is our recommended approach. This background freezing spectrum should be reported, and then subtracted from the sample’s spectrum. Restricting

the freezing curve analysis to the 5-95% frozen droplet fraction as is now being done by some groups to exclude anomalously early and late freezing droplets is not recommended. The ice-activity of individual particles is very much a diverse spectrum, resulting in some droplets in a freezing array containing more rare ice-active INPs that induce freezing at warmer temperatures [Conen *et al.*, 2011; Pummer *et al.*, 2012, 2015; O'Sullivan *et al.*, 2015; Augustin-Bauditz *et al.*, 2016]. This can occur even in experiments on “pure” single particle type samples such as Snomax bacterial and illite NX mineral particles [Beydoun *et al.*, 2016, 2017]. Excluding the early freezing droplets would erroneously omit information on these important rare INPs whose greater ice-activity cause freezing at anomalously warm but atmospherically relevant temperatures.

3. Important method details should be documented. These include details related to the production of pure water used for droplet generation (including any additional filtration steps), any characterization of the purity of the water, and presentation of the freezing spectra for control droplets. Details regarding the substrate used and how it was prepared and cleaned are also important. Temperature calibration procedures should also be documented. DFTs are very subject to contamination, requiring new clean surfaces and sample handling vessels to be used. This is especially a concern when working with very ice-active biological particles such as Snomax and other bacteria. Droplet preparation methods such as the pipette, syringe, or microfluidic technique used, how the particle sample was (re-)suspended in the water, and the length of time the particles spent in water prior to analysis are additional method details that may appear trivial but can have important consequences on the observed ice nucleation properties. This is especially critical in DFT comparison studies between different groups using the same samples.

4. We recommend the use of bottled HPLC-grade or similar purchased water for droplet generation, as opposed to MilliQ-produced water. MilliQ systems can certainly produce high quality water with freezing temperatures near the homogeneous limit but are subject to sudden unannounced changes in their water quality, and are also limited by the quality of the source water fed into the MilliQ system. Our own experiences and frustrations caused by the variability of MilliQ water has caused us to exclusively use HPLC-grade bottled water that we further filter with a 0.02 μm Anotop filter and then store in a clean glass bottle in the refrigerator.

5. Based on the findings in this study, we recommend silanized cover slips as the primary substrate for DFT as they are the least expensive option that display the most consistent freezing behavior. Alternatively, if the cost of gold wafers is not prohibitive and measures are taken to avoid scratching the surface, then gold is a suitable substrate. Additionally, we note the incredible potential of microfluidic devices used in this study and others. We also recommend autopipettors over syringes for droplet generation due to their ease of use and reduction of potential contamination from repeated use compared to syringes.

6. Droplet volumes and particle-in-water concentrations should be standardized as much as possible. The commonly used ice active surface site density metric (n_s , n_m) has regrettably been found to not properly normalize and correct for differences in the particle surface area or mass present in droplets during DFT. For example, just by changing particle concentration the n_s values we retrieved for illite NX shifted by several orders of magnitude (Beydoun et al., 2016). Many groups purposefully vary particle concentration to access different observable freezing temperatures, but the ice nucleation properties retrieved using

different concentrations of the same system may not be consistent. The best way to evaluate this (in)consistency is to ensure overlap in the n_s spectrum retrieved versus temperature, so these values can be directly compared at the same temperature. This requires using small steps in particle concentration of about a factor of 5. Reporting the raw freezing spectra also helps to evaluate these issues. Standardizing the total particle surface area present, by standardizing the droplet volume and particle concentration used, may also reduce these discrepancies.

7. Interferences from the substrate and/or immersion oil used, the pure water, and other potentially unrecognized sources should be regularly evaluated using pure water controls that are prepared using identical procedures as the sample droplets are. Controls should be run with a frequency determined by the level of variability in the background freezing spectrum observed using these controls, and by how close the particle sample's freezing spectrum lies compared to the background spectra. Any new batch of purchased substrates must be evaluated to assess batch-to-batch differences, which we have observed for silanized glass cover slips. Studies of low ice-activity systems such as soot particles and biomass burning aerosol require careful and extensive background control experiments. In our measurements of biomass burning aerosol we prepare a droplet array on a silanized cover slip that consists of a 1:1 ratio of pure water control droplets and BBA-containing sample droplets (Figure 3.12). This provides a direct assessment of any interferences from the same substrate used for sample analysis, and equal statistics for control and sample droplets.

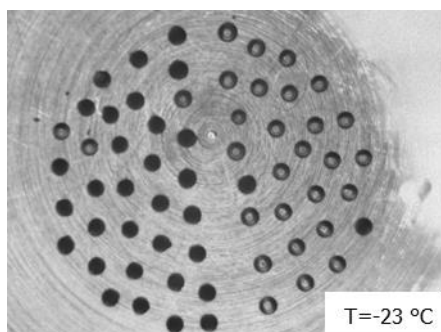


Figure 3.12. Image of droplets containing biomass burning aerosol (left half) and pure water droplets (right half) immersed in squalene oil on a silanized glass cover slip. Droplets containing aerosol sample have mostly frozen (turned dark) and pure water droplets have remained largely unfrozen (grey) at -23 °C.

8. DFTs are often evaluated by comparing measurements to published results for the same particle system. Unfortunately, we lack good reliable INP standards for proper comparison and calibration. Snomax is commonly used [Wex *et al.*, 2015] but we identified serious issues stemming from the instability of the most ice-active ice nucleants in Snomax over time (Polen *et al.*, 2016). This precludes Snomax as a reliable INP standard. Good comparisons have been found using illite NX minerals, but it is critical to ensure that an identical particle sample is used by each method [Hiranuma *et al.*, 2015b]. Methods that collect aerosolized particles must take special care to account for their collection efficiency versus size. Just placing some material from the bulk sample into water can avoid these issues. The ice activity of mineral particles can also change with time spent in water, or by attack from strong acids. The very ice-active K-feldspar minerals are especially subject to degradation in water due to surface ion etching [Holdren and Berner, 1979; Banfield and Eggleton, 1990; Peckhaus *et al.*, 2016]. Harrison *et al.* [2016] found that a particular type of feldspar, BCS 376, was able to maintain its IN activity over many months in water. Engineered nanoparticles from inert metal oxides with reproducible particles sizes, surface

properties, and pore sizes may be the most reliable type of INP standard, though this has not yet been evaluated [Archuleta *et al.*, 2005; Findenegg *et al.*, 2008; Marcolli *et al.*, 2016; Alstadt *et al.*, 2017]. Until then illite NX mineral particles are likely the best INP standard choice, provided all the above caveats are accounted for.

This study and the above series of recommendations are intended to shine light on some potential sources of inconsistencies between droplet freezing methods and create a simple, unified analysis and representation for all ice nucleation community members to follow for future publications. Many researchers already have much of the above information available before publication and use that data for detailed analysis. In the interest of moving the community forward, we seek increased transparency regarding the aforementioned information by documenting important method details and the raw spectra for background water freezing control in all publications using droplet freezing methods.

4 The unstable ice nucleation properties of Snomax® bacterial particles

This is an accepted manuscript of an article published by the American Geophysical Union in *Journal of Geophysical Research – Atmospheres* on 09/10/2016, available online at <https://agupubs.onlinelibrary.wiley.com/doi/abs/10.1002/2016JD025251>

Polen, M., E. Lawlis, and R. C. Sullivan (2016), The unstable ice nucleation properties of Snomax® bacterial particles, *J. Geophys. Res. Atmos.*, *121*(19), 11,666-11,678, doi:10.1002/2016JD025251.

4.1 Abstract

Snomax® is often used as a surrogate for biological ice nucleating particles (INPs) and has recently been proposed as an INP standard for evaluating ice nucleation methods. We have found the immersion freezing properties of Snomax particles to be substantially unstable, observing a loss of ice nucleation ability over months of repeated droplet freezing measurements of the same batch of Snomax stored as dry pellets in a freezer. This reflects the fragility of the most ice active large protein aggregates, and presents issues for the use of Snomax as an INP standard. The ice nucleation properties we determined using a fresh Snomax batch agreed well with the recent method intercomparison from the INUIT project, while an older batch did not. Using an oil-immersion droplet freezing technique, repeated

freezes of Snomax droplets resulted in a decrease in ice nucleation ability after successive refreezes. We attribute this to the disruption or displacement of the most ice active protein aggregates that are thought to contain the ice nucleants. Partitioning of the protein aggregates from the droplet into the immersion oil that is accelerated by droplet freezing events could explain the observed decrease in freezing ability. Droplets in mineral oil or low viscosity silicone oil experienced a smaller reduction in freezing temperature than when squalene oil was used. The effect of the immersion oil may be specific to proteinaceous biological particles and we have not observed it in non-proteinaceous materials. Caution is warranted in the use of oil-immersion droplet freezing methods to determine immersion freezing properties.

4.2 Introduction

Heterogeneous ice nucleation in the atmosphere is catalyzed by rare ice nucleating particles (INPs). INPs are responsible for cloud glaciation at temperatures between 0 and -38 °C and can be composed of inorganic (e.g. mineral dust), or carbonaceous material (e.g. cellulose and other biological particles, or soot particles) [Schnell and Vali, 1976; DeMott *et al.*, 2003; Cziczo *et al.*, 2004; Murray *et al.*, 2012; Hiranuma *et al.*, 2015c]. Ice nucleation is responsible for most precipitation over land [Mülmenstädt *et al.*, 2015], and it has large impacts on cloud optical properties, lifetime, and structure [Yin *et al.*, 2002; Lohmann and Feichter, 2005; DeMott *et al.*, 2010]. Therefore, it is pertinent to understand what particle properties impart INPs with this rare ability and how that ice nucleation ability changes over time. The scarce nature of atmospheric INPs, the wide number of different INP sources, and the corresponding ice nucleation properties of different types of INPs represent significant challenges to acquiring a comprehensive understanding of

heterogeneous ice nucleation. The rarity of INPs that typically compose about ten in a million atmospheric particles also creates important challenges in properly distinguishing and characterizing INPs in complex mixed atmospheric aerosol samples.

Oil-immersion methods have been used to determine the immersion freezing properties of particles since Bigg [1953] first introduced the technique. Several groups have recently published results using oil-immersion experiments to examine the immersion freezing of different particle systems [Zobrist *et al.*, 2006; Koop and Zobrist, 2009; Stan *et al.*, 2009a; Broadley *et al.*, 2012; Wright and Petters, 2013; Pummer *et al.*, 2015; Zolles *et al.*, 2015]. Depositing droplets into oil provides the advantage of inhibiting water diffusion and evaporation. This prevents droplet shrinkage and preserves droplet volume. It also inhibits the Wegener-Bergeron-Findeison process that causes ice crystals to grow at the expense of liquid droplets, preventing the early freezing of droplets from interfering with neighboring droplets. Additionally, it provides an inert environment that can protect droplets from outside contaminants. The oil-immersion method is particularly well-suited for refreeze experiments. These provide important insight into the repeatable deterministic vs. stochastic nature of heterogeneous ice nucleation, and the rigidity or vulnerability of ice active sites [Shaw *et al.*, 2005; Zobrist *et al.*, 2006, 2007; Wright and Petters, 2013; Wright *et al.*, 2013].

Ice nucleating bacteria, along with other biological particles, are among the most efficient ice nucleating substances observed in the atmosphere. Some bioparticles or their fragments can initiate freezing at temperatures as warm as -1 °C [Maki *et al.*, 1974; Schnell and Vali, 1976; Lindow, 1989; Després *et al.*, 2012]. Certain species of bacteria, such as *Pseudomonas syringae*, express outer membrane proteins capable of freezing water at

temperatures close to 0 °C. These proteins are believed to have evolved as a mechanism of invading plant cells by freezing water to fracture the cell walls [Lindow *et al.*, 1982]. Previous studies have discovered the presence of several distinct freezing proteins within *P. syringae*, dubbed Type I, II, and III. These three types of proteins are able to freeze water heterogeneously in the ranges of -2 to -4 °C, -5 to -7 °C, and below -7 °C, respectively [Yankofsky *et al.*, 1981; Turner *et al.*, 1990]. Turner *et al.* [1990] performed a more intricate study of the protein complexes and derived an alternate system with better defined classes (A, B, and C). For this study, we will refer to the more broadly defined Types I, II, and III, as opposed to the A, B, and C classes defined in Turner *et al.* [1990]. Further analysis found that these three types of proteins are different sized aggregates of the same protein monomer with Type I having the most monomers (around 60) [Ruggles *et al.*, 1993; Lindow, 1995]. While large Type I proteins are typically found in whole cells or affixed to the cell membrane, Type III proteins (~2-12 monomers) are water soluble and can exist outside the cell as macromolecules [Phelps *et al.*, 1986; Govindarajan and Lindow, 1988; Southworth *et al.*, 1988; Hartmann *et al.*, 2013].

Many experimental studies of biological INPs have utilized commercial products made of non-viable cells and cell fragments, such as Snomax®, in place of cell cultures [Ward and DeMott, 1989; Chernoff and Bertram, 2010; Wright *et al.*, 2013; Wex *et al.*, 2015]. Snomax is used as a proxy for *P. syringae* as it has been shown to possess similar ice nucleation properties to live bacteria, and it is readily available as a commercial product for artificial snow generation. Snomax was recently used to create test particles for the inter-comparison of seven different ice nucleation measurement techniques, and as such was proposed as a biological ice nucleant test substance [Wex *et al.*, 2015]. However, Wex

et al. did note that some participants found Snomax to be unstable when stored for weeks or months at a time, and emphasized the importance of properly storing the material in a freezer when not in use. In this manuscript we elucidate several important artifacts regarding the stability and reproducibility of Snomax's freezing properties during storage, as well as during experimentation. Specifically, we found that its ice nucleation ability degrades over time, despite proper handling and storage, diminishing the retrieved concentration of active sites. This instability detracts from the usefulness of this material as a standard in ice nucleation studies. We also observed that the most active ice nucleants that induce freezing at $-2\text{ }^{\circ}\text{C}$ are lost as the droplet sits in oil, and this loss is accelerated by droplet refreezes.

4.3 Methods and Materials

Immersion mode droplet freezing experiments were performed using the Carnegie Mellon University Cold Stage (CMU-CS) system, a custom temperature-controlled chamber (Figure 4.1), similar in design to that used by Wright and Petters [2013]. The CMU-CS is composed of an aluminum body that holds a removable aluminum sample dish, and an aluminum lid with an acrylic window through which droplets are viewed. Air ports on the chamber and lid are used to flow in dry air to prevent fogging of the acrylic window or the oil surface. The bottom of the chamber is cooled by a bidirectional Peltier element (thermoelectric cooler, TEC) that is modulated by a PID controller (TE Technology, Inc.). The heat sink under the Peltier element is a liquid chilled aluminum plate (Lytron) cooled by a recirculating chiller (Thermo Fischer Scientific Inc.) held at $-25\text{ }^{\circ}\text{C}$ for all experiments. All aluminum components are insulated to reduce ambient heat transfer.

For each experiment, a hydrophobic glass cover slip (Hampton Research Corp.) is placed inside the dish. Then 5 mL of squalene (96%, VWR) is pipetted into the dish to provide an inert environment for droplets, following the method of Wright and Petters [2013]. Alternate oils used for select experiments were light mineral oil (NF/FCC, Fischer Scientific) and low viscosity (100 cSt) silicone oil (Gelest Inc.). Suspensions of particles are created shortly before use and are typically used within one day of creation, unless otherwise noted. Immediately before droplet generation, suspensions are shaken by hand to re-suspend all particles. Droplets are created via either a microsyringe (Hamilton Company) or micropipette (Huawei Technologies Co., Ltd.). The glass microsyringe creates droplets of closely reproducible size, but there is an increased probability of contamination after multiple uses. The micropipette prevents contamination through the use of disposable pipette tips, but it produces less consistent droplet sizes. For both methods, $\sim 0.1 \mu\text{L}$ of a suspension of particles in water is deposited onto the surface of the oil; it then falls through the immersion oil onto the cover slip. All droplets, regardless of generation method, have diameters between 500 and 700 μm as measured by optical microscopy.

The droplets are illuminated using an LED light ring above the acrylic window, and the droplets are imaged using a stereomicroscope and digital camera (Amscope). Images are taken at a resolution of 1600 x 1200 with magnification of 7.5X at 0.17 °C intervals. Arrays containing between 30 and 40 droplets can be visualized. An image is recorded every 10 seconds. Images are analyzed manually to determine the temperature at which a liquid droplet (appearing grey) had frozen (appearing black).

A Labview program controls the Peltier element that cools the chamber. A 5 k Ω resistance thermistor inserted into the base of the chamber just below the center of the dish measures the system's temperature and this is used in the PID control loop for the Peltier's temperature set point. The PID settings were optimized to achieve < 1 °C difference between the thermistor and the droplets through the temperature range between 0 and -40 °C, when a K type thermocouple attached to a coverslip was placed in the aluminum dish that contained oil. The temperature is decreased at 1 °C/min from 10 to -40 °C, or until all droplets are frozen. The chamber is then quickly heated back to 10 °C to melt the frozen droplets. With the current methodology, the uncertainty in temperature measurements is ± 0.5 °C. The investigable range for our system is 0 to -22 °C. This is based on where we observe pure water control droplets to begin to freeze, with an average of one droplet (or ~3%) freezing at around -20 °C. This freeze-thaw-freeze cycle is repeated to determine the freezing temperature spectrum of successive refreezes. Temperatures are recorded at 1 Hz from the thermistor by the Labview program.

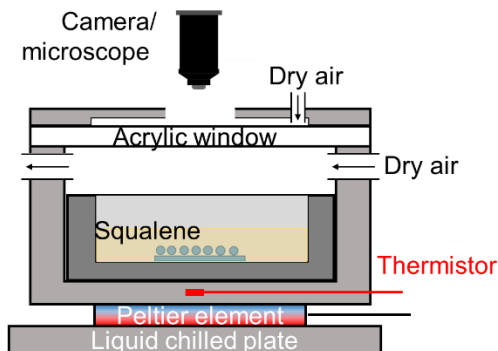


Figure 4.1. Diagram of the CMU-CS immersion freezing cold stage measurement system. The liquid chilled plate is maintained at -25 °C using the recirculating chiller. The Peltier element is ramped between 10 °C and -40 °C, or until all droplets are frozen, typically at 1 °C/min. Dry air above and below the acrylic window keeps the surface of the oil and window dry. Droplets are visualized using the optical microscope and camera, and their temperature determined by the thermistor placed under the aluminum sample dish.

Snomax® (York International) suspensions were created in purified water ($> 18 \text{ M}\Omega\cdot\text{cm}$, $\text{TOC} < 5 \text{ ppb}$) from an in-house MilliQ purification system (EMD Millipore Corporation). The Snomax was kept frozen (-10 °C) as dry pellets at all times and was only removed from the standard lab freezer when Snomax pellets were being weighed to create suspensions. For particle concentrations greater than 0.01 wt%, stock suspensions of that concentration were prepared. For concentrations less than 0.01 wt%, suspensions are diluted with MilliQ water from the stock suspension to produce the appropriate concentration. Water droplets containing suspended Snomax were then placed in the oil in the sample dish, as described above.

4.4 Results and Discussion

4.4.1 Decrease in Ice Nucleation Ability Over Months Timescale

We initially investigated the freezing properties of Snomax to compare our derived freezing properties for an efficient and readily available ice nucleant to recent literature values. The freezing temperature curve we obtained for droplets containing 0.01 wt% Snomax is shown in Figure 4.2. Our original Snomax sample (open diamonds) that was stored in a freezer for 11 months nucleated ice with a median freezing temperature around $-3\text{ }^{\circ}\text{C}$. However, after just one month of frequent experimentation, the entire droplet freezing curve had shifted to below $-6\text{ }^{\circ}\text{C}$. Further experiments the following months yielded the same results. This suggests that the Type I proteins were no longer available to nucleate ice and only the smaller protein aggregates were acting as INPs and inducing the colder freezing temperature. We performed tests on a wide range of Snomax concentrations to probe different freezing temperature regions. The particle mass-normalized ice nucleation active site density parameter, n_m , was calculated from the freezing temperature spectra for all concentrations tested to facilitate the comparison with other methods that use different particle concentrations and different droplet volumes [Vali, 1971; Hoose and Möhler, 2012; Murray *et al.*, 2012]. n_m is a time-independent ice nucleation framework; time-dependent or stochastic freezing has been found to be unimportant in Snomax systems at the cooling rate used here and in other similar studies [Budke and Koop, 2015]. The resulting $n_m(T)$ spectra (Figure 4.3, left) shows a wide variation in n_m values at both -10 and $-5\text{ }^{\circ}\text{C}$ for the initial batch of Snomax. Total ice active site densities of the warmest freezing droplets reach 10^5 mg^{-1} and lower temperature freezing droplets reach 10^9 mg^{-1} . In comparison to the Wex *et al.* [2015] results (grey region in Figure 4.3), our n_m curve

translates to more than one order of magnitude smaller ice active sites per gram of Snomax between -4 and -7 °C, where we retrieve the concentration of Type I active sites. Additionally, the spread in our observed freezing temperature from replicate freezing experiments for the same predicted n_m value approaches 5 °C, for instance at $n_m = 10^4 \text{ mg}^{-1}$ ¹. This spread suggests instability in the very efficient Type I active sites between our different experiments.

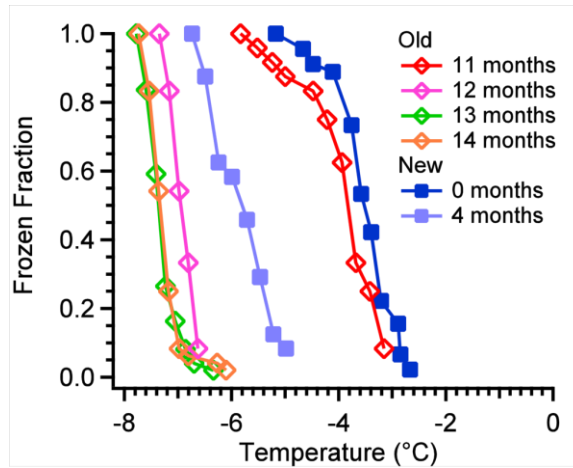


Figure 4.2. Freezing temperature curve of 0.01 wt% Snomax droplets immersed in squalene oil, from the first freezing cycle. Open diamonds represent the old Snomax batch that was stored in a freezer for 11 months before use. The new batch of Snomax (solid squares) was purchased and used immediately. Number of months indicates the time between the date the Snomax batch was received and the respective freezing experiment. After a few months of experiments, the freezing curves shifted to lower temperatures for both the new and old Snomax batches.

A new batch of Snomax was obtained to investigate the possible reasons for the discrepancy between our derived ice active site density and that recently obtained using similar droplet freezing methods by Wex et al. [2015] as part of the INUIT inter-comparison activities. We had purchased our original batch of Snomax eleven months before we first measured its freezing curve using our new system; all experiments of the

original sample were performed between 11 and 14 months of receiving it. During this time the container of Snomax was rarely used and had thus been kept in the freezer and only removed on a few occasions. Infrequently removing the Snomax sample from the freezer, or even just storage in the freezer, may have allowed the material's ice nucleation properties to degrade. Indeed the new Snomax sample exhibited stronger ice nucleation activity, both in the droplet freezing temperature spectrum (Figure 4.2), and the derived n_m values (Figure 4.3). The newer sample of Snomax contained 10^6 and 10^9 mg^{-1} active sites corresponding to the freezing temperatures of the Type I (~ -3.5 °C) and Type III (~ -7 °C) protein aggregates, respectively (Figure 4.3, right). The data for the new Snomax batch shown in Figure 4.3 were all obtained within 3 months of receiving the material. Divergence in n_m values below -20 °C is likely the result of trace contaminants in the water or on the coverslip. The n_m curve obtained from the new Snomax sample agrees well with that published from the INUIT method inter-comparisons. This study performed by Wex et al. [2015] included wet suspension and aerosol generation from a Snomax suspension for measuring the same batch of Snomax; they found that all seven instruments agreed reasonably well with one another. This included measurements from the BINARY system that measures immersion freezing in larger water volumes (wells) than our droplets, and without any immersion oil [Budke and Koop, 2015].

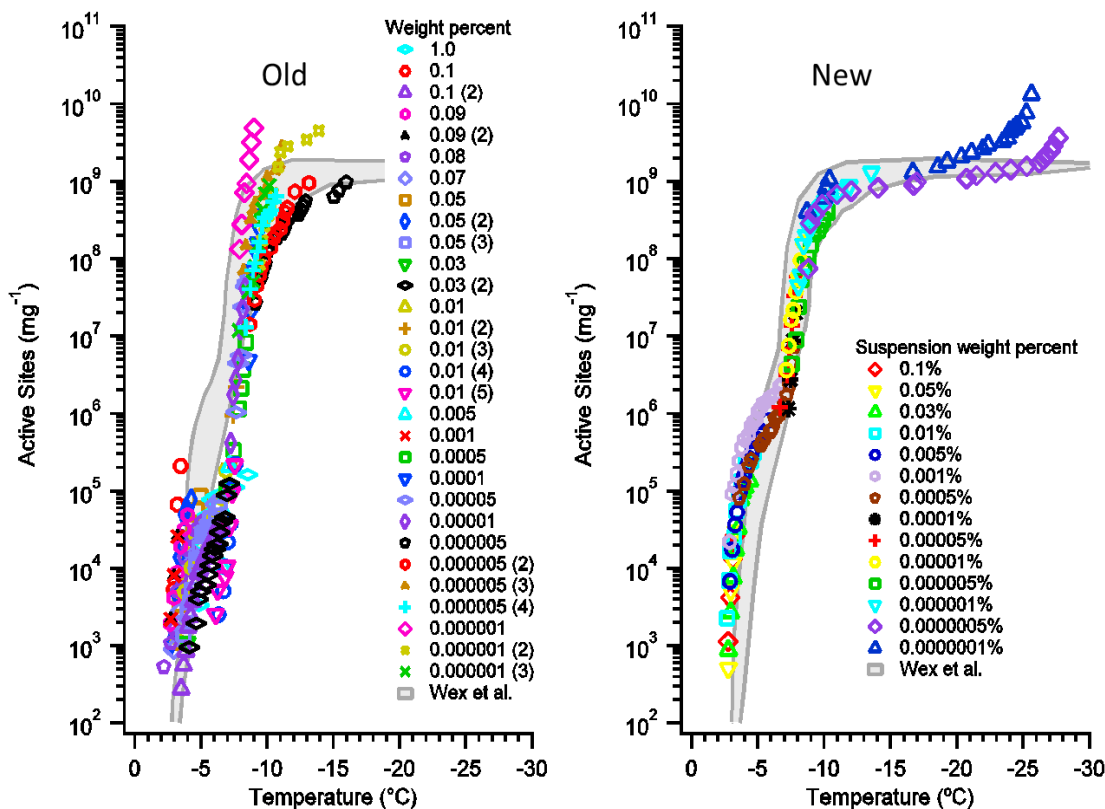


Figure 4.3. Ice nucleation active site density of Snomax normalized to particle mass concentration in the droplets (n_m), as a function of temperature for the old (left) and new (right) batches of Snomax. A wide variety of Snomax in droplet mass concentrations were used, and several concentrations were repeated (indicated by the number in parentheses). Squalene immersion oil was used for all these experiments. Freezing experiments on the new Snomax batch were performed within three months of receiving the material. Experiments of the old Snomax batch were performed between 11 and 14 months after receiving the material. The gray region indicates the bounds of the Wex et al. [2015] results for Snomax. Note the x-axis is reversed to be consistent with the results of Wex et al. [2015].

Figure 4.4 displays a comparison of the median freezing temperature of 0.01 wt% Snomax droplet arrays from Figure 4.2 examined over several months of experiments using either the old or new batch of Snomax. The number of months (bottom axis) for each sample corresponds to the time since we received the Snomax sample from the manufacturer. This is an effective way to quantify the effects of storage time on the freezing

activity of the Snomax samples. Both samples quickly lost all or most of the Type I proteins, which is evident from the median freezing point dropping from -3.5 °C to lower temperatures. Another result we found was the narrowing of the freezing temperature for the old Snomax sample after 11 months. In these findings the 90th and 10th percentile temperatures were all within 1 °C, as opposed to the 11 month data where the spread was almost 2 °C. These results suggest that upon loss of Type I proteins, the remaining INPs are more uniform in freezing activity and freeze at quite similar temperatures. Type III protein complexes are smaller aggregates composed of 2-12 monomers, and they are known to self-aggregate in solution and thus to resist alteration such as by solubilization and denaturation [Turner *et al.*, 1990; Ruggles *et al.*, 1993; Schmid *et al.*, 1997].

Despite the significant decrease in freezing temperature – and thus ice nucleation ability – we observed for Snomax stored over many months, our n_m curve for the new Snomax sample compares well with that of Wex *et al.* [2015] (Figure 4.3). Our observed freezing temperature for the most active Type I region from -2 to -5 °C is slightly warmer than that reported by Wex *et al.* by up to 1 °C. This small difference may indicate Snomax batch-to-batch differences, or that the samples used by the Wex. *et al.* inter-comparison had experienced some loss of the Type I ice nucleating proteins. They took great effort to ensure that their Snomax batch was stored in the freezer except when being used to generate samples. Wex *et al.* distributed samples from the same Snomax batch in insulated cold containers to the different groups involved in the intercomparison. Our experiments used to determine the n_m curve of the new Snomax batch shown in Figure 4.3 were performed within three months of receiving the material. Thus it appears that largely consistent ice nucleation properties and n_m values can be obtained by different groups using different

methods, if a fresh Snomax sample is properly stored in a freezer and used within the first few months. The substantial loss of ice nucleation ability during cold storage over months, and the apparent acceleration of this loss by working with the Snomax sample that we have observed (Figure 4.2 & Figure 4.4) create some significant concerns in the use of Snomax as a reproducible ice nucleant standard. We also do not know how much variability exists between different batches of fresh Snomax. As the Type III ice nucleants that induce freezing at lower temperatures near -7°C appear to resist loss or degradation, Snomax may be an appropriate material for comparison in that temperature range, if the effects from the more active Type I and other nucleants can be reliably separated or accounted for.

The reduction in ice nucleation ability likely represents the loss or alteration of the most efficient large Type I protein aggregates that freeze at very mild temperatures around -3°C . This reflects the fragility of these large protein aggregates. This could have important consequences for the alteration of the ice nucleation properties of biological ice nucleating particles during atmospheric transport and cloud cycles, where the particles will be exposed to large changes in temperature, water vapor, sunlight, and reactive trace gases [Attard *et al.*, 2012; Amato *et al.*, 2015].

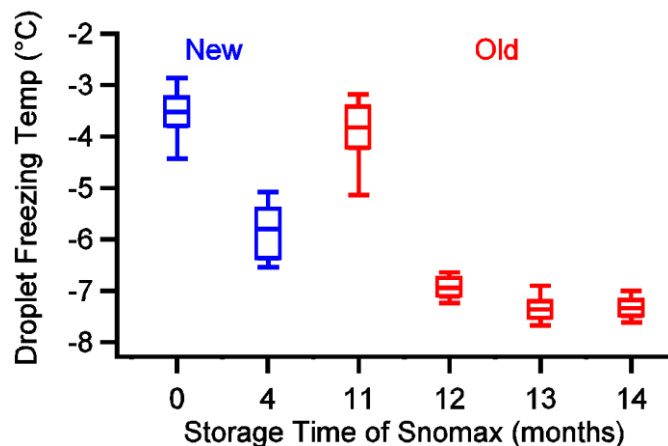


Figure 4.4. Comparison of the freezing temperature of an array of droplets with 0.01 wt% Snomax particles in squalene from the old or new Snomax batch. The bottom axis represents the amount of time the sample was in our possession before the given experiment, and stored in a freezer when not in use. The box and whisker plot displays the median and quartile freezing temperature as the lines in the box, and the 10th and 90th percentiles as the whisker lines.

4.4.2 Effect of Immersion Oil on Snomax Freezing Temperature during

Refreezes

We also performed droplet refreeze experiments, to test our system's capacity to conduct this type of experiment. Refreeze cycling can provide valuable insights into the repeatable deterministic versus stochastic nature of ice nucleation and the rigidity or vulnerability of ice active sites. Figure 4.5 shows three example freeze-thaw-refreeze experiments for four different mass concentrations of Snomax in droplets immersed in squalene. During these refreeze experiments we unexpectedly observed that the freezing temperature curves for Snomax droplets shifted to lower freezing temperatures with each successive freeze/thaw cycle. At moderate to high mass concentrations of Snomax, the median freezing temperature in the temperature spectrum decreased from -3 °C toward -7 °C, and remained at -7 °C for subsequent freezes (Figure 4.5). Since the observed droplet

freezing temperature never fell below -7°C , we conclude that the smaller Type III protein aggregates are more stable to alteration following freeze/thaw cycling. Our initial hypothesis was that the largest Type I protein aggregates were being disrupted to create smaller aggregates through the freeze/thaw process. This would explain the loss of freezing at the warmest temperature, which is attributed to the Type I aggregates, and the shift towards the lower freezing temperature that is attributed to the smaller Type II & III aggregates. It could also explain why no further decrease in freezing temperature was observed after several freeze/thaw cycles, as the smallest Type III aggregates are thought to only contain ~2-12 protein monomers each. At low concentrations, we expect that Type I proteins are no longer present in each and every droplet, due to their lower abundance compared to the Type III proteins, and freezing therefore only occurs close to -7°C . This would explain the lack of a temperature decrease following refreezes (Figure 4.5), consistent with our hypothesis that the smaller protein aggregates are stable. Another explanation for this stability is the ability for smaller complexes to self-aggregate, which could replenish the Type III proteins that freeze at -7°C [Govindarajan and Lindow, 1988; Schmid *et al.*, 1997]. The new Snomax batch displayed the same patterns of decreasing freezing temperature after successive refreezes.

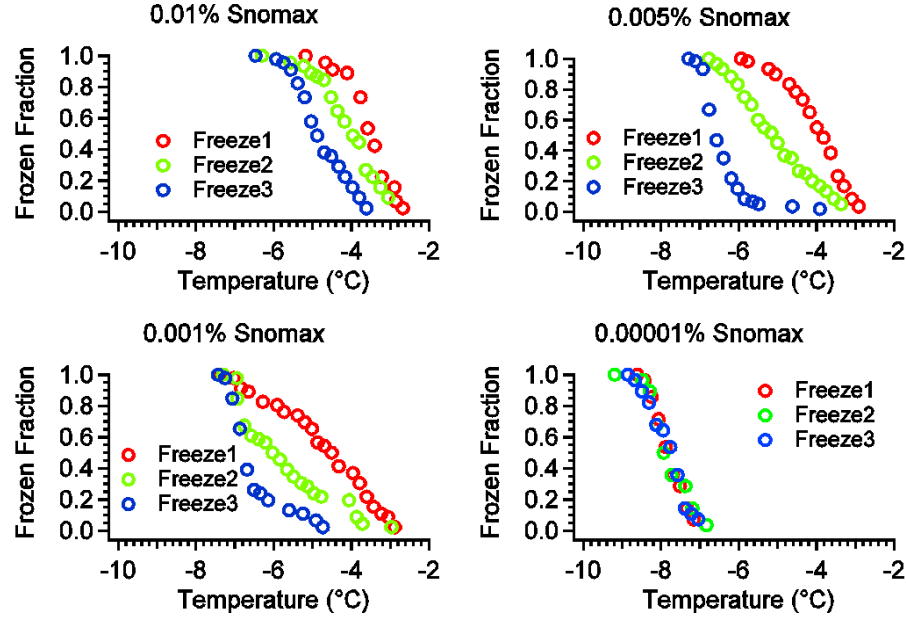


Figure 4.5. Freezing curves for multiple refreezes of the same Snomax containing droplets in squalene oil, at decreasing Snomax in water concentrations going from the top left to bottom right panels. The new Snomax sample was used for all these experiments. Repeated freezing decreased the ice nucleation activity of Snomax, and this effect was observed in the three highest concentrations shown. The lowest concentration (bottom right) does not show this behavior. The droplet array was immediately thawed at 10 °C after each freezing cycle, and then the subsequent cooling cycle was initiated.

In an attempt to rule out particle coagulation and settling effects on the observed freezing temperature spectra, and to determine the timescale over which the ice nucleants remain freely suspended in the droplets, we created suspensions of Snomax that we: 1) froze immediately, 2) put into an array of droplets in squalene oil and froze after 24 hours, and 3) were left for 2 days before the suspension was mixed, and droplets were then made and immediately frozen. In this set of experiments we found that after droplets were left in the array-form in oil for 24 hours the freezing temperature curve had shifted such that all droplets froze below -6 °C. This indicates that after sitting for 24 hours in oil all the Type I proteins have lost their activity, which could be due to coagulation or settling of particles

inside the droplet [Emersic *et al.*, 2015]. Snomax particles left suspended in bulk water, outside of oil, for 48 hours had their freezing spectra shifted by only 1-2 °C compared to normal suspensions frozen immediately. This suggests that some of the most efficient ice nucleants are lost with time spent in water, possibly due to particle coagulation and/or settling, or aqueous chemistry or protein denaturation, but a large proportion still remained after 2 days. Therefore, the larger loss of ice nucleation activity observed in droplets left in an oil-immersed array for a day does not appear to be fully explained by particle coagulation or settling, or aqueous chemistry.

Budke and Koop [2015] recently suggested that hydrophobic biological particles, such as fungal spores and pollen grains, may partition from the aqueous droplet into the surrounding oil phase during oil-immersion droplet freezing experiments. This could remove INP-containing material from the water droplet, which could reduce the observed freezing efficiency and retrieved n_m values. Large protein aggregates tend to remain affixed to the hydrophobic bacterial cell membrane [Govindarajan and Lindow, 1988; Turner *et al.*, 1991; Lindow, 1995]. Partitioning of biological material into the immersion oil seemed to be a plausible alternate explanation for the observed decrease in freezing temperature following refreezes of Snomax droplets. To test if oil partitioning effects could be important in oil immersion droplet freezing measurements of bacterial cells and cell fragments, we performed refreeze experiments using other common oils, including mineral oil and silicone oil, and without using any oil. No-oil experiments were performed using 1 μ L droplets, larger than the 0.1 μ L droplets normally used, to prevent significant droplet evaporation. Due to their larger size, fewer droplets could be imaged in the no-oil refreeze experiments. Regardless of the smaller droplet number in the array, no evident changes

were observed between successive freezes at similar Snomax mass per droplet concentrations. Figure 4.6 shows the freezing curves of twenty-four 1 μ L droplets in air for five consecutive freezes; no differences between the freezing temperature curves from the five refreezes are evident in these no-oil experiments.

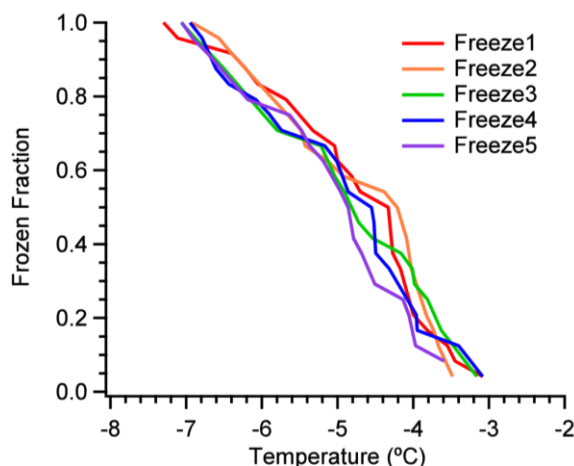


Figure 4.6. Freezing curves from five freeze/thaw cycles of the same 0.0001 wt% Snomax in an array of twenty-four 1 μ L droplets on the cold stage and exposed to air. No immersion oil was used in this experiment, to eliminate possible oil partitioning effects.

4.4.3 Effects of Different Immersion Oils on Droplet Refreezes

We also investigated the effect of using alternate oils as the inert environment in which droplets are immersed, as this could change the rate or degree of hydrophobic partitioning of material into the oil. Mineral oil and silicone oil were used for these tests as they were readily available and have been used in oil immersion experiments previously [Hoffer, 1961; Marcolli *et al.*, 2007; Koop and Zobrist, 2009; Pinti *et al.*, 2012]. Droplet freezing curves were found to decrease only slightly over multiple refreezes for these immersion oils. In Figure 4.7, the median freezing temperatures of successive freeze thaw cycles (denoted as time from first freeze) for a 0.0063 wt% suspension of Snomax in each

of the three oils tested are plotted. The largest decreases in median freezing temperature following refreezes are observed when squalene oil was used. The silicone oil also displays some decrease in freezing temperature, while almost no change is observed when mineral oil was used. Note that for all three immersion oils the median freezing temperatures for the first freezing experiments are the same within our measurement uncertainty of ± 0.5 °C.

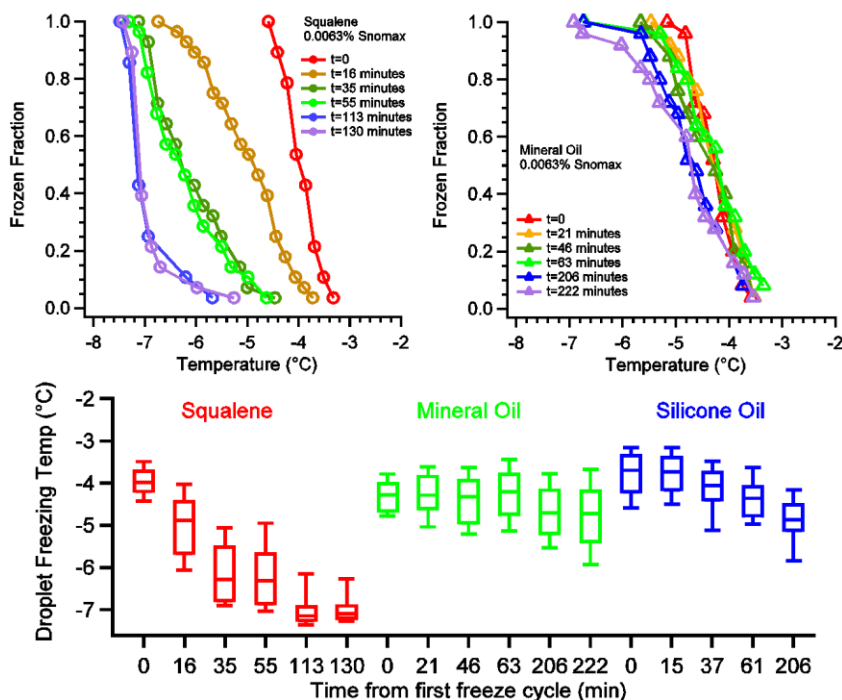


Figure 4.7. Top plots show freezing temperature spectra of 0.0063 wt% Snomax for five consecutive freezes in squalene (top left) and six consecutive freezes in mineral oil (top right). Bottom plot shows the droplet freezing temperatures as a box and whisker plot for the same 0.0063 wt% Snomax droplets after subsequent refreezes in squalene (red circles), mineral oil (green triangles), and silicone oil (blue diamonds). The values on the bottom axis correspond to the amount of time in minutes between the first freeze and the respective freeze for that experiment. All three droplet arrays were created using the same Snomax suspension.

In an effort to explain these differences, Table 4.1 lists several properties that may govern the partitioning and transport of particles and material between the aqueous and hydrophobic oil phases. The octanol-water partitioning parameter, K_{ow} , which is extremely

high for squalene and relatively low for both mineral oil and silicone oil, seems to be related to the observed decrease in freezing temperature following refreezes, which we interpret to be caused by hydrophobic particle/protein aggregate partitioning. The value of K_{ow} for squalene is a predicted value from the U.S. EPA's EPI Suite, mineral oil's K_{ow} is the lowest value as reported by Fischer's material safety data sheet for the product, and the value of K_d is reported for polydimethylsiloxane (PDMS) as a lower limit approaching that of monomeric PDMS. Based on these reported values, the high K_{ow} of squalene, a large 30 carbon molecule with no polar functional groups, may facilitate the partitioning of hydrophobic proteins from the Snomax-containing droplets into the surrounding oil. We also note that squalene is the only oil used that comes from a natural source (96% stated purity) and could potentially contain other compounds that damage large protein aggregates, such as organic acids [Turner *et al.*, 1991]. These or other effects could explain why we observe the greatest reduction in the droplet freezing temperature following refreezes when squalene oil was used. This loss of the most active ice nucleants is attributed to the loss of the large Type I proteins aggregates from the droplets, and we would expect the largest aggregates would undergo the greatest extent of any hydrophobic partitioning, in the absence of any transport barriers.

Additionally, we note the time between the initial freeze and each successive freeze on Figure 4.7 to explore if any change in freezing temperature can be attributed to the time the droplet had spent in the oil. No significant change was observed when the droplets were immersed in mineral oil for a similar amount of time as immersed in squalene oil, where significant changes were observed. This indicates that time effects do not play an important role, at least not for time periods of up to 200 minutes when mineral oil was used. Mineral

oil has a hydrophobic partitioning constant that is 100-1000 times larger than that of silicone oil, yet no change was observed for refreezes performed in the mineral oil. As expected, the solubility of water in each of these oils has an inverse trend versus the K_{ow} parameter. Squalene has the lowest saturated water solubility in that oil, followed by mineral oil, then silicone oil. We note that the mineral oil has a lower viscosity compared to the silicone oil, and a larger oil-water interfacial tension. How these different fluid properties might interact such that ice nucleating particles or material are removed or altered from the droplets during refreezes when immersed in silicone and squalene oil but not in mineral oil is not evident to us. More extensive dehydration of the droplets when immersed in silicone oil versus mineral oil, due to the larger water solubility and smaller interfacial tension, is one possible explanation. The resulting reduction in droplet volume and the increase in the concentration of any solutes present could decrease the freezing temperature. Note that dehydration alone does not change the total number of particles and their ice active sites present in the droplets.

Table 4.1. Reported fluid properties of the three immersion oils used in our droplet freezing experiments

	Squalene	Mineral Oil, light	Silicone Oil
Composition	C ₃₀ H ₅₀	Saturated hydrocarbons	Trimethylsiloxy-terminated polydimethylsiloxane
Specific gravity (kg/m ³)	858 ⁽¹⁾	830 ⁽³⁾	966 ⁽⁶⁾
Hydrophobicity (log K _{ow})	14.12 (EPI predicted) ⁽¹⁾	6 ⁽³⁾	≥ 3.6 (log K _d) ⁽⁷⁾
Dynamic viscosity (cP)	12 ⁽¹⁾	≤ 27.8 (calc)	96.6 (calc)
Kinematic viscosity (cSt)	14 (calc)	≤ 33.5 ⁽³⁾	100 ⁽⁶⁾
Interfacial tension with water (mN/m)	23-27 ⁽²⁾	62 ⁽⁴⁾	40 ⁽⁸⁾
Solubility of water in oil (mg/L)	0.124 ⁽²⁾	40 ⁽⁵⁾	>500 ⁽⁹⁾

1. [National Center for Biotechnology Information, 2016]

6. [Fendinger *et al.*, 1997]2. [Klucker *et al.*, 2012]

7. [Gelest Inc., 1998]

3. [Stan *et al.*, 2009a]8. [Alvarez *et al.*, 2011]4. [Moyle *et al.*, 2012]9. [Ismail *et al.*, 2009]5. [Pahlavanpour *et al.*, 2003]

4.4.4 Effects of Time versus Refreezes on Loss of Most Efficient Ice

Nucleants

We propose that droplet freezing accelerates the migration of hydrophobic particles into the oil phase, by simply displacing the hydrophobic/insoluble material into the surrounding oil. Experiments exploring this effect are illustrated in Figure 4.8, where an array of Snomax droplets were frozen immediately after depositing them into squalene oil (solid lines), and another array of droplets containing the same suspension was deposited into squalene oil but not frozen until several hours after depositing the array in the oil (dashed lines). After freezing and thawing the droplets repeatedly for over an hour, the

fraction frozen curve shifted significantly to lower temperatures, as observed previously (Figure 4.5). However, waiting for 90 minutes before the first freeze only slightly shifted the freezing curve to resemble the second freeze of the immediately frozen array. Assuming that slow mass transport causes the extent of the hydrophobic partitioning of the biological particles to increase as a function of time, we would expect our waiting-before-freezing droplets (dashed lines, Figure 4.8) to freeze at a lower temperature than all of the immediate-freezing droplets (solid lines, Figure 4.8) because a larger fraction of the particles should have partitioned into the oil when we waited before freezing. However, if there is no time-dependent partitioning of these ice nucleating particles, the waiting would have no impact on the measured freezing curves and the red and orange dashed lines would lie directly on the red and orange solid lines, respectively, in Figure 4.8. We find that the droplets from the first freeze of the waiting array have freezing temperature spectra that lie close to the second and third refreezes for the immediately frozen array. This suggests that the process of refreezing has a significant effect on particle partitioning and loss of the most active ice nucleants, whereas the time the droplets spend immersed in the oil is a minor contributor to the hydrophobic partitioning or other loss mechanisms of the biological ice nucleating particles. As no change was observed for the refreeze experiments using the mineral oil (Figure 4.7), this also indicates that the ice nucleating particles are not lost through time-dependent processes when immersed in mineral oil on the timescale of the 200 minutes used for the complete refreeze experiments.

This shift to lower freezing temperatures following droplet refreezes or just time the droplets have spent in oil has not been observed in the other particle systems we have studied using our droplet freezing cold stage. We have completed dozens of freezing

experiments on droplets containing illite NX mineral powder [Hiranuma *et al.*, 2015b], Arizona test dust, microcrystalline and fibrous cellulose [Hiranuma *et al.*, 2015b], and fresh and photochemically aged biomass burning aerosol particles. Squalene immersion oil was used in all these experiments. In none of these systems was any decrease in the freezing temperature following refreezes observed. This behavior appears to be unique to Snomax, and may extend to other more realistic biological particle systems. We plan to test authentic bacterial cultures including native *Pseudomonas syringae* to further explore this behavior. Further experiments should be performed with other hydrophobic and biological samples as well, to test for significant method artifacts caused by the immersion oil in commonly used droplet freezing methods. As no change in the freezing curves following refreezes conducted over 200 minutes was observed when mineral immersion oil was used, this type of higher-viscosity and lower-hydrophobicity oil may be more suitable and induce fewer artifacts than the very hydrophobic squalene oil.

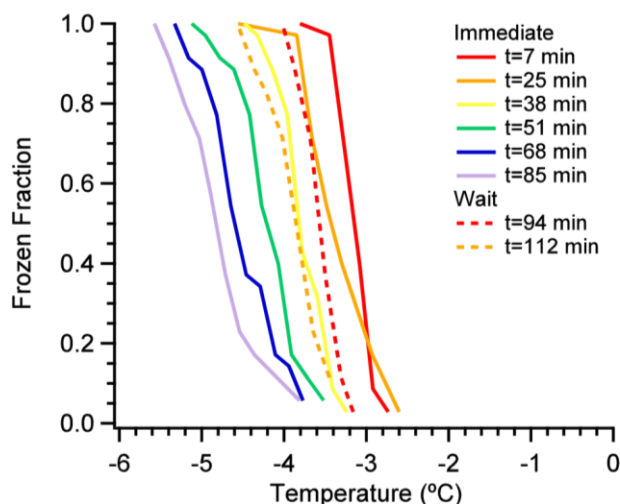


Figure 4.8. Freezing curves of 0.03 wt% Snomax droplets immersed in squalene oil and frozen immediately after droplet array creation (solid lines), or after waiting 90 minutes to begin the freezing (dashed lines). The

time indicated for each line corresponds to when that freezing was started relative to the time the droplet array was deposited into the squalene oil.

4.4.5 Comparison to Other Oil Immersion Droplet Freezing Experiments on Bacterial Particles

Previously published droplet freezing results in which a similar squalene oil-immersion method was used did not report any changes in the freezing properties following refreezes such as we have observed in our experiments. Wright et al. [2013] used Icemax suspended in droplets, which is another commercial product made from *P. syringae* cells and fragments. In their work, squalene was used as the inert immersion oil and 40 freeze/thaw cycles per array were reported for droplets 50-300 μm in diameter. They generated their droplets by briefly shaking the Icemax-water suspension with the squalene oil to create a random distribution of Icemax droplets dispersed throughout the oil. This represents a quite different droplet generation technique than the microsyringe or pipette method we used, and produced much smaller droplets compared to ours. Examining their figures reveals no permanent loss of ice nucleation activity within the first several refreezes. There are several possible explanations for the very different results of the refreeze experiments observed by Wright et al. [2013] and our results. First, smaller droplets have a larger surface area to volume ratio, facilitating the partitioning of large Type I aggregates into the oil. Second, vigorous mixing of the Icemax/water suspension and squalene oil may displace the hydrophobic material from the aqueous phase into the oil before freezing experiments are performed, thus preventing any effects that actual droplet freezing or time-dependent transport may induce on this partitioning. Consistent with this, we note that in the results reported by Wright et al. [2013], no droplets froze at

temperatures above ~ -4 °C. Whereas we observed freezing as warm as -2 °C for the first freezing experiments, indicating the presence of the most active ice nucleants in our Snomax droplets during the first freeze. Lastly, manufacturing differences between Icemax and Snomax may alter the distribution of the different types of ice nucleating protein aggregates, and the hydrophobic partitioning of these ice active complexes. Differences in the specific strain of *P. syringae* used, how it was cultured and manufactured into non-viable freeze-dried pellets, and any wetting agents or surfactants added to the material could create these differences between the Snomax and Icemax commercial materials.

4.5 Conclusions

Several important concerns have been revealed regarding the use of Snomax as a surrogate for biological ice nucleants, and as an ice nucleating particle standard. The significant decrease in the measured droplet freezing temperatures over a period of months of sample pellet freezer storage indicates that the ice nucleants in Snomax particles are unstable. This decay in ice nucleation ability appears to be accelerated when the Snomax sample is removed from freezer storage to prepare samples using the material. Clearly this will prevent the regular use of Snomax as a reproducible ice nucleation standard particle system. The initial freezes of Snomax droplets produced ice nucleation properties comparable to literature values, and this helps to validate the performance of our new droplet freezing cold stage system. However, successive freeze/thaw cycles of the same droplets caused the freezing curves to shift to lower temperatures. This is believed to be caused by partitioning of large Type I protein aggregates – the most efficient ice nucleants – from droplets into the surrounding immersion oil phase. When oils other than squalene were tested, the freezing curves decreased only slightly for silicone oil and were unchanged

within our measurement uncertainties for mineral oil. Experiments without oil where the droplets were just exposed to air displayed no changes following refreezes. The reduction in freezing temperature observed using squalene oil was found to be primarily due to the effect of the freezing process itself, with a smaller contribution from the time the droplet spent immersed in the oil. We have only observed this droplet refreeze method artifact for Snomax containing droplets, and not in our droplet freezing experiments using squalene immersion oil to study the ice nucleation properties of illite NX mineral powder, Arizona test dust, cellulose powder, or authentic biomass burning aerosol. We suspect these oil partitioning effects could also impact oil-immersion droplet freezing measurements of other hydrophobic biological particles, as suggested by Budke and Koop [2015]. The use of less viscous and less hydrophobic immersion oils such as light mineral oil appears to reduce or eliminate these effects, based on these Snomax droplet experiments.

Our results clearly indicate that the most efficient ice nucleants that freeze at the warmest temperatures, up to -2°C , are also the most vulnerable to alteration or loss through both time and temperature change effects, and effects of oil partitioning. The smaller Type III protein aggregates that freeze around -7°C appear to be much more resistant to alteration by the pathways studied here. Based on our findings and those of previous studies [Turner *et al.*, 1990; Ruggles *et al.*, 1993; Schmid *et al.*, 1997], the most efficient ice nucleants would be expected to be the most vulnerable to such alteration and irreversible loss. Therefore, the immersion freezing properties obtained from fresh Snomax or other bacterial particles may not accurately represent the ice nucleation properties of realistic atmospheric biological particles.

5 Entrained ash and soil particles: an unrecognized source of ice nucleating particles from biomass burning

This is a manuscript in preparation to be submitted to *Geophysical Research Letters* published by the American Geophysical Union.

Polen, M., L. Jahn, T. Brubaker, J. Somers, L. Jahl, and R. C. Sullivan (to be submitted),
Entrained ash and soil particles: an unrecognized source of ice nucleating particles
from biomass burning.

5.1 Abstract

Heterogeneous ice nucleation initiated by ice nucleating particles (INP) strongly influences cloud structure and precipitation. Previous studies found inconsistencies in the emissions and freezing properties of INPs from biomass burning. The entrainment of ice-active soil and ash particles into the smoke plume by intense updraft velocities, particularly in wildfires, could explain this inconsistency. We experimentally investigated INPs present in bottom ashes produced by burning tall grasses and wood. The combustion of wood produced no INP activity in the ash, while grass burns produced ash with significant INP activity up to -10 °C. Higher fire power combustion of grasses compared to wood appears

to drive the formation of ice-active minerals in the ash. Soil minerals retain significant freezing ability following combustion. This suggests that the higher combustion efficiency and temperature of grasses make them more likely to produce and emit INPs in the form of entrained ash and soil particles.

5.2 Introduction

Ice nucleation is responsible for most precipitation over land [Mülmenstädt *et al.*, 2015]. In the atmosphere, heterogeneous ice nucleation is caused by ice nucleating particles (INPs) at temperatures above -38 °C. Major atmospheric INP components include mineral dusts [Fornea *et al.*, 2009; Atkinson *et al.*, 2013; Hiranuma *et al.*, 2014a], biological components [Pummer *et al.*, 2012; Augustin *et al.*, 2013; Hiranuma *et al.*, 2015c; Wex *et al.*, 2015; Polen *et al.*, 2016], or to a lesser extent carbonaceous material [DeMott, 1990b; Schill *et al.*, 2014]. Recently, soil has been found to possess ice nucleating particles related to biological components as well as minerals and organic material that are ice-active in various temperature regimes [Conen *et al.*, 2011; O'Sullivan *et al.*, 2014; Tobo *et al.*, 2014; Hill *et al.*, 2016]. Thus it is important to understand mechanisms of mineral particle production and of the entrainment of soil and mineral particles into the atmosphere so we can understand their contributions to atmospheric INPs. Several studies have explored the impacts of biomass burning on atmospheric ice nucleation, finding inconsistencies in INP production that are not explained by fuel type or combustion conditions [Petters *et al.*, 2009b; Prenni *et al.*, 2012; McCluskey *et al.*, 2014]. Petters *et al.* [2009b] correlated INP production positively with potassium fraction and inorganic fraction and negatively with organic carbon fraction. This suggests that soot and inorganic components may be the major contributor to INPs from biomass-burning emissions, or that hotter flaming

combustion – which increases the inorganic fraction relative to the organic fraction [Johansson *et al.*, 2003; Rissler *et al.*, 2005]– enhances the production or entrainment of INPs. However, we also know that soot from simple hydrocarbon combustion is generally a rather weak INP [Mossop, 1963; DeMott, 1990b; Dymarska *et al.*, 2006; Murray *et al.*, 2012]. In addition, Levin *et al.* [2016] found that only ~50% of ice crystals generated from laboratory biomass burns contained black carbon soot. These facts point to some other component besides soot in biomass-burning emissions acting as INPs, particularly at warmer temperatures above -20 °C where soot is not known to be ice-active.

Ash or soil dust particle entrainment could explain discrepancies between burns and the correlations between inorganic aerosol fraction and INP production [Bodí *et al.*, 2014]. Some airborne studies over wildfires have observed ash and soil particles up to 1 mm in diameter at concentrations of >10 particles m^{-3} [Radke *et al.*, 1991]. Ash composition is dependent on combustion temperature [Misra *et al.*, 1993; Balfour and Woods, 2013]. Balfour and Woods [2013] showed that medium-to-high temperature combustion (500-900 °C) of branches and needles results in mostly crystalline products while low temperature combustion (300 °C) produces predominantly amorphous components. Ice nucleation in volcanic ash and mineral dust particles is known to be driven in large part by crystalline phases [Yakobi-Hancock *et al.*, 2013; Kulkarni *et al.*, 2015; Wang *et al.*, 2016b]. Soil can contain biological, organic, and mineral phases; all of these components could enhance the ice nucleating potential of the combustion emissions. Additionally, a few recent studies found soil markers in wildfire emissions [Maudlin *et al.*, 2015; Schlosser *et al.*, 2017]. These ash and soil components would also represent important and unrecognized sources of INPs released by biomass burning, especially

through large intense wildfires, and help to explain the sometimes unexpectedly high freezing activity of biomass-burning emissions. Unlike soil, large ash particles can remain in the atmosphere for hours due to their low density and fractal shape that reduce their depositional velocity [Andreae *et al.*, 2004]. However, recent measurements of wildfire emissions in the US found that fine soil dust is also present in coarse particulate matter at elevated levels in downwind locations [Schlosser *et al.*, 2017].

Several ambient and laboratory studies have investigated the ice nucleation properties of combustion ash. A study of sugar cane burns produced some of the first direct observations of combustion-produced ash acting as INPs [Pueschel and Langer, 1973]. INP counts increased greatly when the cane leaf skeleton disintegrated thus releasing particles composed of inorganic refractory material. Two studies have examined the ice nucleating properties of different types of combustion ash. Umo *et al.* [2015] analyzed the ice nucleating ability of bottom ash from coal and wood combustion, as well as domestic bottom ash and coal fly ash. Both wood and coal ash samples were generated using stoves intended for efficient burning of solid fuels. They found that the fly ash from coal was the most ice-active of those tested with a median freezing temperature as warm as -20 °C, and that all the ash types had moderate, but variable, ice nucleating activity. Grawe *et al.* [2016] similarly analyzed wood and coal bottom ash and coal fly ash for ice nucleating activity. They found the coal fly ash to be most active with freezing occurring as high as -29 °C.

Recent studies have looked exclusively at ash produced by coal and wood burning, which is used predominantly in small-scale or controlled, highly efficient combustion. However, no studies to our knowledge have examined the ice nucleating properties of ash from tall grass fuels, one of the dominant biomass fuels that is known to emit INP, though

inconsistently [Petters *et al.*, 2009b; Levin *et al.*, 2016]. Grass and brush act as the fuel for nearly 80% of wildfires in the United States [Ahrens, 2013]. Due to the heat intensity generated by grass fires, ash particles can be entrained and dispersed into the free troposphere [Andreae *et al.*, 2004; Grawe *et al.*, 2016], and this may also be true of soil particles [Maudlin *et al.*, 2015; Schlosser *et al.*, 2017]. The high fire power from tall grass fires also produces chlorine and chloride emissions that can impact atmospheric chemistry [Levin *et al.*, 2010; Ahern *et al.*, 2018]. In addition, with increasing global temperatures, we expect drought conditions in grasslands to become more extreme, exacerbating the frequency and intensity of wildfires [McKenzie *et al.*, 2004; Scholze *et al.*, 2006; Westerling *et al.*, 2006; Pitman *et al.*, 2007; Stevens-Rumann *et al.*, 2018].

In this study we measured the ice nucleating particles present in the bottom ash following various laboratory grass and wood burns to explore their potential contribution to atmospheric INP produced by biomass burning. XRD analysis was conducted to correlate the ice nucleating activity of particles to their crystallinity and composition. Soil collected along with one of the grasses was added to the fuel prior to combustion to further investigate soil as a source of INP in biomass-burning emissions. A subsequent study will examine the chemical properties of the bottom ash and soil in more detail, as well as the biomass-burning aerosol particle fraction.

5.3 Samples and Methodology

Ash samples were collected from biomass burns performed in the CMU combustion facility in the Air Quality Laboratory. Fuels were weighed in a metal pan that held the sample during combustion. Between burns the pan was emptied and rinsed with MilliQ water. Roughly half of the fuel weight was lit on fire and allowed to burn until the flames

began to die down. Gradually the rest of the weighed fuel was added to maintain flaming-phase combustion until it was all consumed. Then the fire was allowed to extinguish itself and cool. Ash samples were collected into zippered plastic bags until analysis. Fuels included Cutgrass (Georgia, USA), Hay (Pennsylvania, USA), Birch wood (purchased from hardware store), *Panicum virgatum* (Pennsylvania, USA), and an unidentified wetland grass (North Carolina, USA). The soil sample was collected in the same location as the unidentified wetland grass (North Carolina, USA). For one experiment (cutgrass + soil), the fuel was weighed and burned the same way, but 100 g of soil was sprinkled over the fuel in the pan immediately before burning.

Ash samples were ground with a mortar and pestle to a fine powder. Ground samples were sieved to less than 63 μm (U.S.A. Standard Testing Sieve, Fischer Scientific Company) by putting the sieve in an ultrasonic bath for five minutes. Particles larger and smaller than 63 μm were stored in separate 50 mL plastic Falcon tubes. Only the sub-63 μm samples were analyzed for this study. For immersion freezing measurements ~ 0.001 mg of ash sample was suspended in 10 mL of HPLC-grade water (~ 0.01 wt%).

Ice nucleation ability was determined using our cold stage (CMU-CS) method as described by Polen et al. [2016, 2018]. Briefly, droplets containing particles are immersed in squalene oil on a hydrophobic cover slip in an aluminum sample dish. The dish sits atop a thermoelectric element that provides fine temperature control. A three-stage thermoelectric air chiller is used as a heat sink for the system. Droplet temperature measurements have an uncertainty of ± 0.5 $^{\circ}\text{C}$. Approximately 70-90 (40-50) droplets with a volume of 0.1 μL (1.0 μL) are deposited into the oil using a variable electronic micropipette. Droplets images are acquired every 5-6 seconds using a CMOS camera, and

freezing is detected based on the change in grayscale value using a custom Matlab program. The program also determines the droplet diameter. All freezing experiments were run in triplicate. Samples analyzed using this method are referred to below as “Droplet-in-oil”.

Ice nucleation ability was also measured for two samples using the new microfluidic device described by Brubaker et al. [2018] and used for some measurements by Polen et al. [2018]. Briefly, a “store-and-create” PDMS device is created using standard soft lithography methods. Droplets are completely encased in squalene oil, which we have shown reduces our background freezing temperature significantly [Brubaker et al., 2018; Polen et al., 2018]. For this study, two different channel geometries were used: 1) a device capable of holding 720 droplets of 6 nL in volume, and 2) a device capable of holding 40 droplets of 13 nL in volume. The 13 nL array was run in triplicate to obtain a mean. Samples analyzed using this method are referred to below as “Microfluidic”. Background droplet freezing caused by trace impurities in the filtered HPLC-grade water or by droplet-substrate interactions were determined for both methods by regularly running pure water droplet control assays [Polen et al., 2018].

Brunauer-Emmett-Teller (BET) surface area analysis was performed to determine bulk particle surface area (Gemini VII 2390, Micromeritics) and is reported with other sample parameters in Table 5.1. The measured BET surface area to mass ratio was used to compute the ice active surface density (n_s) metric that normalizes for surface area [Vali, 1971; Polen et al., 2018]. X-ray diffraction (XRD) spectra were measured for all samples over the 2θ range 10° - 70° with a step size of 0.013. (X'Pert Pro MPD, PANalytical). XRD retrieves the crystallinity vs. amorphous content and the crystalline/mineral phases present in the ash and soil samples [Engelbrecht et al., 2009]. Relative phase amounts were

determined via Rietveld refinement using the closest matching spectra available in the crystallography open database (COD).

5.4 Results and Discussion

5.4.1 Dependence of ash freezing ability on fuel type and combustion

efficiency

We found that wood ash is much less ice active than grass ash. The droplet freezing temperature spectrum for different ashes, as well as the NC soil, and pure water controls are shown in Figure 5.1. The same particle mass concentration of ~0.01 wt % was used in all cases, but note the droplets-in-oil are much larger than the microfluidic droplets, and thus contain more particle mass and surface area. Overall the grass fuels produce ash that is fairly active and all types show similar trends. Results from cutgrass and NC grass are shown here while additional fuels are reported in the Supporting Information. Using our droplets-in-oil method, we see that each grass ash sample exhibits a very similar freezing temperature spectrum with 50% of droplets freezing in the range of -22 °C to -24 °C. However, the birch fuel (red filled circles) has no activity distinguishable from the pure water control (solid line). This is true in the case of our microfluidic assays as well (open red circles, dashed line), where we see no freezing for birch ash or pure water until below -26 °C, and the median freezing temperature is ~-33 °C. Converting these droplet temperature freezing spectra to ice active site density spectra requires a background correction using the $K(T)$ or $c_{INP}(T)$ metric, which accounts for the INP number per droplet volume [Vali, 1971; Polen *et al.*, 2018]. Background correction is done because droplet-in-oil freezing methods frequently suffer from substrate interaction or pure water contamination [Polen *et al.*, 2018].

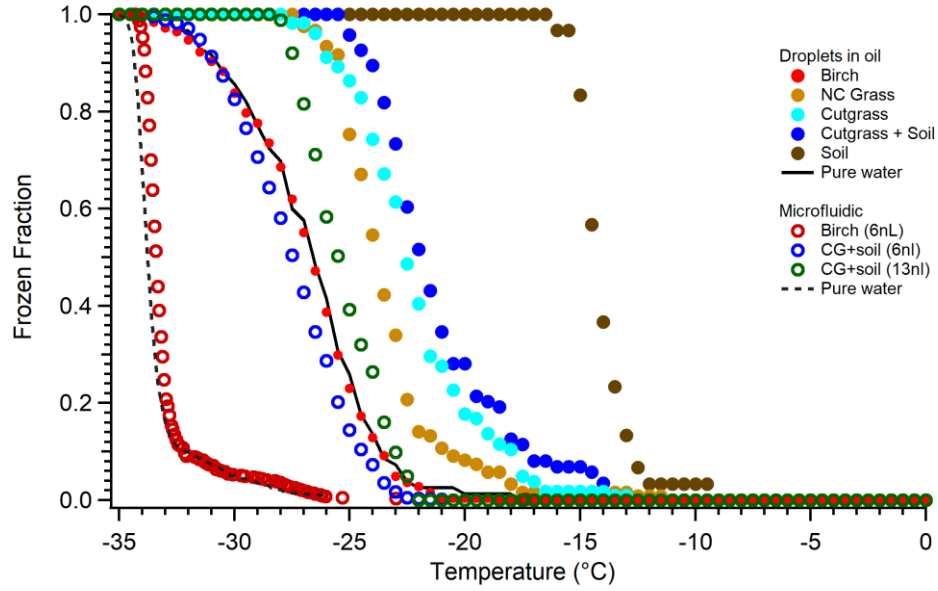


Figure 5.1. Averaged droplet freezing temperature spectra from triplicate arrays of all ash samples using the droplet-in-oil method (filled circles). Two grasses are shown: cutgrass (cyan) and NC grass (orange). In addition, a microfluidic device was used to measure birch ash (red, open) and cutgrass + soil (blue and green, open). The microfluidic birch ash was the only sample run once, not in triplicate. Microfluidic droplets (open circles) were generated in two different sizes for the cutgrass + soil sample, 6 nL (blue, open) and 13 nL (green, open). Average pure water controls are shown for both systems in black (solid, droplets-in-oil; dashed, microfluidic). Particle weight percent concentrations are around 0.01 wt% in all cases; particle surface area concentrations are shown in Table 5.1.

Differences in total particle surface area present are largely accounted for by converting the freezing temperature spectra to n_s , though we have found n_s to not fully correct for differences in particle surface area [Beydoun *et al.*, 2016]. In Figure 5.2 we see an even stronger deviation between the ice activity plotted as n_s of ashes from grasses versus from wood fuels. Birch ash (red) possesses $n_s < 10^2$ until below -30 °C. This is due to the low ice activity and high BET surface area of the birch ash. One important note is

that we did not background correct these samples by subtracting the pure water c_{INP} from the sample c_{INP} . Instead we are attributing all of the background ice activity to the birch ash's surface area, which means its actual ice activity is even lower still. The motivation for this choice is so that it is easier to visualize the comparison of birch with grass fuels. In this case, birch has such a low activity and such a high BET surface area that it is easily distinguishable from other samples. However, not subtracting the background freezing spectrum is not advised for most other cases [Chapter 3].

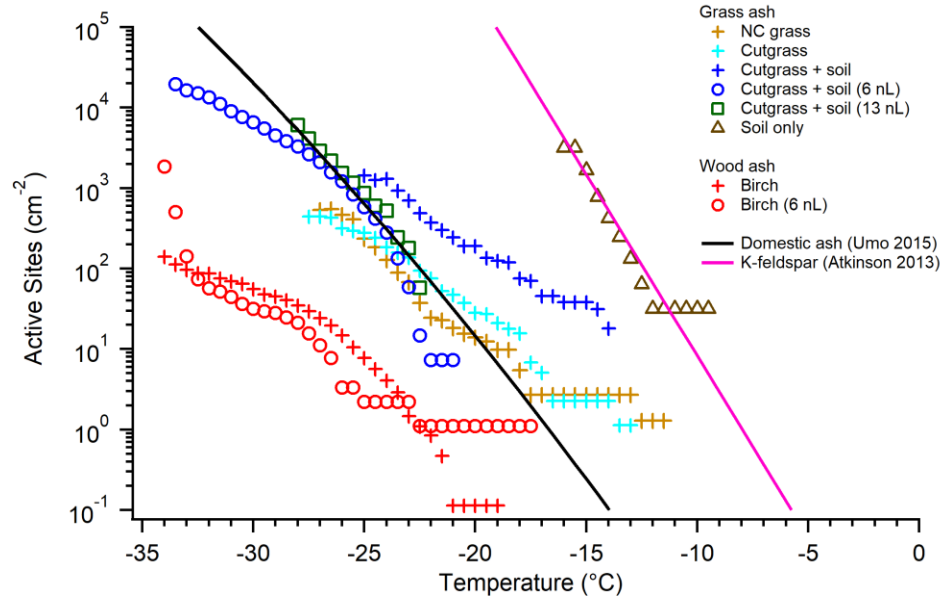


Figure 5.2. Plot of average ice active site density, n_s , of various ash samples. Cross symbols are bottom ash samples measured using the droplet in oil method. Circles are ash samples measured in the microfluidic device using 6 nL droplets, and squares for 13 nL droplets. Triangles are measurements of soil using the droplet-in-oil method. The solid black line shows a fit for a domestic bottom ash sample from Umo et al. [2015]. Solid pink line is the fit of K-feldspar minerals from Atkinson et al. [2013].

For comparison we include the n_s fit for domestic bottom ash from Umo et al. [2015] in Figure 5.2. This is one of the only n_s spectral fits reported in the literature for the ice nucleating activity of combustion ash. Our data for grass ash shows the same general freezing activity as this domestic ash, while our birch wood is significantly less active. Umo et al. burned unspecified wood that may be very different than the birch wood used in our study, and they also used an efficient solid-fuel stove. The BET surface area of our wood ash was substantially higher than any of our grass samples and all of the samples reported by Umo et al. [2015] (Table 5.1). This could suggest that birch burns less efficiently and produces a high amount of amorphous carbonaceous material with poor ice activity that remains in the bottom ash. During our experiments birch took about 10 minutes to completely burn, while the same mass of grass burned in 3 minutes, reflecting the higher fire power and combustion temperature of the dry tall grasses. Qualitative inspection of the burn conditions (e.g. intensity, heat, flame height, time) between the wood and grass burns leads us to believe the wood burns at much lower temperatures than grasses under our open pan combustion conditions.

Table 5.1 Ash sample characteristics for our samples and related literature reports. BET surface area values, total particle surface area per droplet, and mineral phase % composition from XRD analysis.

	Birch	NC grass	Cutgrass	Cutgrass + NC soil	NC soil	Hay	<i>Panicum virgatum</i>	Domestic Wood ^d	K- feldspar ^e
BET (m ² /g)	275.5821	20.7561	16.8278	4.3701	1.632	3.4997	37.8354	3.87	3.2
Surface area per droplet (cm ²)	a: 2.76×10 ⁻² b: 1.65×10 ⁻³	a: 2.08×10 ⁻²	a: 1.68×10 ⁻²	a: 4.37×10 ⁻³ b: 2.62×10 ⁻⁵ c: 5.68×10 ⁻⁵	a: 1.63×10 ⁻³	a: 3.5×10 ⁻³ b: 1.65×10 ⁻³	a: 3.78×10 ⁻²	N/A	N/A
SiO ₂		19.4		60.6	63.8	Y		0.7	3.9
Na-rich plagioclase feldspar				23.8	27.4				16
Na-rich alkali feldspar				9.5	8.9				80.1
KCl		11.3	14.9	1.2			3		
K ₂ SO ₄			36.2	3.9		Y			
Dolomite			46	1.2					
mixed sulfates		12.5	2.9					7.7	
NaCl		34							
graphite		19.3					33.3		
CaCO ₃	100					Y	63.7	4.3	
Fe oxides								7.4	
Mg oxide								7.7	

a: droplets in oil; b: 6 nL microfluidic droplets, c: 13 nL microfluidic droplets; d: data from [Umo et al. 2015]; e: data from [Atkinson et al. 2013], Y: indicates that component is present but hasn't been quantified because of low sample mass

XRD analysis was used to investigate this hypothesis by determining the bulk crystalline composition of the ash and soil samples. The XRD results of the birch ash (Figure 5.3, Table 5.1) show a high proportion of amorphous material and only a small amount of calcium carbonate crystalline content. A high amorphous content of the ash is expected for lower temperature burns [Balfour and Woods, 2013; Bodí *et al.*, 2014]. Calcium carbonate (CaCO_3), or calcite, is a very weak INP, and it is not surprising that this ash sample has so little ice activity [Atkinson *et al.*, 2013; Yakobi-Hancock *et al.*, 2013]. On the other hand, the grass ashes contain a much lower amorphous fraction, and various crystalline materials including potassium salts and quartz, as well as graphitic carbon for the NC grass. Quartz (SiO_2) has been shown to act as a fairly weak INP previously [Atkinson *et al.*, 2013]. However, further contributions to ice nucleating properties from these other minerals present in these ash samples has not been explored. The XRD analysis is also not sensitive to less abundant crystalline phases that may have high ice-activity. Though we suspect that highly soluble alkali salts, such as KCl, will not act as INPs. Overall, our results indicate that the INP potential for ash produced during biomass combustion is highly dependent on combustion efficiency and temperature as this largely controls the crystalline mineral content of the ash, which in turn are likely responsible for the most ice-active ash components. While our wood burning results do not agree with previous studies on wood ash, our findings suggest that the fuel may not be as important as the combustion conditions. High efficiency stoves as used by Umo *et al.* will not necessarily simulate conditions in our open pan or a natural wildfire. In wildfires there is a wide range of combustion efficiency, phases, and fire intensity. Better understanding this range of combustion conditions and how they impact the properties of the ash and aerosol

produced would better inform the expected impact of certain fires on regional atmospheric composition, and the abundance and freezing temperature spectra of the emitted INPs [Akagi *et al.*, 2011; van Leeuwen *et al.*, 2014].

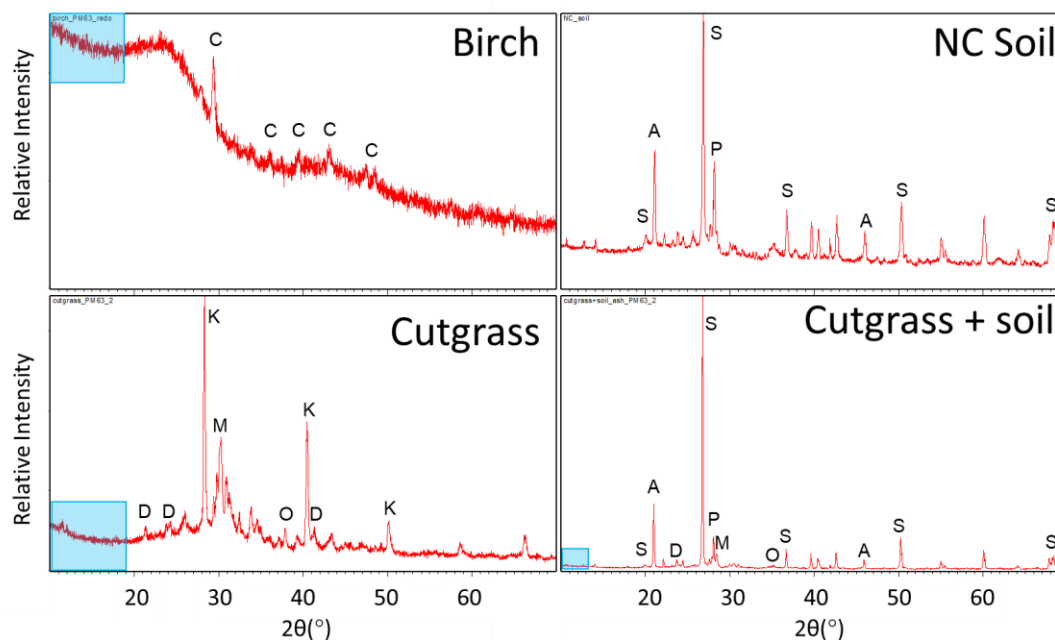


Figure 5.3. XRD results for ash produced from open pan combustion of birch wood, soil, cutgrass, and cutgrass + soil. Amorphous material is indicated by a rise in intensity at lower 2θ values. Amorphous content is visible in both birch ash and cutgrass ash, but not in the other samples. Peaks in each spectrum are assigned by matching to a database of known spectra. C: calcite, K: KCl, O: K_2SO_4 , M: Mixed sulfates, A: alkali feldspars, S: SiO_2 , P: plagioclase feldspars, D: dolomite, blue region: amorphous material. Assignments can be found in Table 5.1.

5.4.2 Influence of combusted soil particles on the resulting ash

A recent study showed that soil components can be entrained into wildfire emissions [Schlosser *et al.*, 2017]. In this study we wanted to determine if the highly active biological or mineral phases of soil are able to maintain their ice nucleating ability through the combustion process. During one of the burn experiments, we added soil to the pile of

cutgrass fuel to determine if the soil would still have active ice-nucleating components after experiencing intense combustion conditions and could thus be a source of INPs. In Figure 5.1 freezing temperature spectra are shown for the original soil (brown), cutgrass (cyan), and cutgrass + soil (blue). All the droplets containing unburned soil froze above -16.5 °C, and the cutgrass + soil sample shows ~8% of droplets possess INPs that freeze above -16.5 °C. Less than 2% of droplets in cutgrass ash alone froze at -15 °C. When comparing cutgrass to the cutgrass + soil sample there is a consistently 1-2 °C higher freezing temperature for the cutgrass + soil throughout the freezing spectrum. When comparing n_s in Figure 5.2, we see that the cutgrass + soil results (blue) lie directly between the soil (brown) and cutgrass (cyan) for the droplets-in-oil method. These results suggest that some INPs remain in the cutgrass + soil ash sample that have maintained the higher ice nucleating activity of the soil compared to the cutgrass, following combustion of the cutgrass + soil fuel.

Due to the smaller sized droplets and lower particle surface area concentration per droplet, the microfluidic measurements show a slightly different trend. Here the cutgrass + soil ash (blue circles and green squares in Figure 5.1) have much lower activity at lower temperatures with the earliest freezing droplets but the trend rapidly approaches the Umo et al. [2015] fit for domestic ash and the droplet-in-oil results around -23 °C. The benefit of using both these droplet freezing techniques is the ability to see both the low population of rare high activity INPs in the droplet-in-oil method and the high population of low activity INPs at lower temperatures using the microfluidic droplets.

The XRD results (Figure 5.3) confirm our hypothesis that the soil mineral components are still present after high temperature grass combustion. We see that all the

major soil components (SiO_2 , Na/Ca-feldspar, K-feldspar) remain after experiencing combustion. The cutgrass + soil contains all the components observed in the XRD spectra of the soil and the cutgrass alone. The soil used in this study contains known ice-active mineral components, the plagioclase (Na/Ca) and alkali (Na/K) feldspars. Additionally, we see very similar freezing behavior between our soil sample and the K-feldspar n_s fit from Atkinson et al. [2013] (Figure 5.2); K-feldspars are more ice-active than Na/Ca-feldspars [Atkinson et al., 2013; Peckhaus et al., 2016].

5.5 Conclusions and Atmospheric Implications

We sought to determine the role of biomass burning bottom ash on ice nucleating particle (INP) production from biomass combustion, as this has not been previously considered as a source of INPs to the atmosphere. Grasses, which burn much hotter than wood, produce ash that is much more ice active because the higher combustion temperature results in more crystalline versus amorphous material in the ash. Therefore, the combustion efficiency is likely a major factor in determining the potential for ash to act as a source of INPs, and this is influenced by the fuel type and moisture content. Minerals naturally present in soil were also found to maintain at least some of their ice activity following grass fuel combustion. These minerals had high ice-activity similar to K-feldspar minerals. Soil minerals should also be considered as a potentially significant source of INP released from intense biomass burning and the resulting strong convection. These soil minerals emitted by biomass burning could also be an important factor in the inconsistency of INP production commonly observed from biomass combustion.

Wildfires and prescribed burns have been shown to emit INPs, while laboratory burns are known to produce INPs albeit inconsistently. Our findings suggest that the

temperature and efficiency of combustion have a strong impact on the production of INPs and their freezing properties. High temperature combustion typical of grass fires is more likely to produce and expose ice-active mineral phases to the atmosphere in the combustion ash produced. These minerals may also be emitted in the smaller biomass-burning aerosol particles. Considering brush and grass fires make up nearly 80% of wildfires in the US, more studies on the emissions of ash, soil, minerals, and aerosol from grass combustion are required to properly understand the role of biomass burning as a source of INPs. Additionally, fires with higher temperatures will induce higher updraft velocities more conducive to entraining ash, soil, and other minerals into mixed-phase cloud levels. An important consequence of these findings is that mineral particles measured in ice crystal residues could be mistakenly attributed to mineral “dust” instead of biomass ash or entrained soil, which would misinform INP sources and their atmospheric distribution in global models.

6 The impact of aging on ice nucleating particles produced from biomass burning

6.1 Abstract

Biomass burning aerosol (BBA) has been shown to act as ice nucleating particles (INPs), but the inconsistency of the amount of INPs and activity of those INPs makes understanding the impact of biomass burning on clouds highly uncertain. Little is known about the impacts of chemical aging on BBA in the atmosphere, but we suspect that aging is likely to enhance the ice nucleating ability of BBA by oxidizing the soot surfaces to be more favorable to ice formation or increasing the amount of active particles by oxidizing volatile compounds to create organic aerosol. This chapter discusses the results we have obtained over several years of biomass burning experiments where we determined the freezing activity and the effects of aging of the BBA. We found that tall grasses tend to produce fairly weak ice nucleating particles that increase in ice-activity slightly upon aging. We found one example of a grass species that produces BBA that is more ice-active before aging, which we attribute to freezing depression caused by soluble secondary organic aerosol created by the aging process. We also found that BBA produced from wood combustion has weak freezing ability compared to grass combustion, similar to the trends presented in the previous chapter on INPs in biomass-burning ash. We began experiments with a very low background method using microfluidics to measure the often weak activity ice nucleating particles produced by BBA. At present these results are inconsistent but this method shows promise for measuring very weak INPs such as in BBA. The results of these

experiments will be further explored in future experiments and will hopefully lead to a more complete understanding of the INPs produced from biomass burning and how these are altered by chemical aging during transport.

6.2 Introduction

Wildfires have tremendous impacts on natural environments, crop land, infrastructure, property, and air quality [Huff *et al.*, 2015; Liu *et al.*, 2015; Stephens *et al.*, 2016; Prendergast-Miller *et al.*, 2017; Stavi *et al.*, 2017; Forzieri *et al.*, 2018]. In a report on economic impacts of wildfires in San Diego County, Rahn found that the cost of wildfires in 2003 alone cost the county over \$2 billion with nearly half of that cost coming from loss and damages to property [Rahn, 2009]. Aside from direct damage to land and property, wildfires create high concentrations of particulate matter (PM), nitrogen oxides (NO_x), and volatile organic compounds (VOCs) [Yokelson *et al.*, 1997, 1999; Goode *et al.*, 2000; Christian *et al.*, 2003; Stavi *et al.*, 2017; Forzieri *et al.*, 2018]. These emissions reduce visibility, decrease air quality through emission of harmful particles and gases as well as ozone precursors, and impact radiative forcing, cloud formation, and precipitation. Prescribed burns are often used to reduce the impact of wildfires on the environment and property, but these burns still release large amounts of PM, NO_x, and VOCs [Stith *et al.*, 1981; Lee *et al.*, 2005; Mazzoleni *et al.*, 2007]. Many predictions suggest that with the exacerbation of climate change in the coming decades wildfires will increase in frequency and severity with worsening drought conditions [McKenzie *et al.*, 2004; Scholze *et al.*, 2006; Westerling *et al.*, 2006; Pitman *et al.*, 2007; Stevens-Rumann *et al.*, 2018]. Therefore it is important that we understand what the complete array of emissions from biomass burning are and how they impact the environment and us.

Biomass burning is known to produce particles that are able to nucleate into cloud droplets, called a cloud condensation nucleus (CCN) [Penner *et al.*, 1992; Petters *et al.*, 2009a; Latham *et al.*, 2013]. This property means that biomass burning can influence the formation of clouds and the radiation budget on a regional scale [Penner *et al.*, 1992; Engelhart *et al.*, 2012]. Over the last decade, biomass burning aerosol (BBA) has been shown to contain ice nucleating particles (INP) [Petters *et al.*, 2009b; Prenni *et al.*, 2012; Levin *et al.*, 2014, 2016; McCluskey *et al.*, 2014]. However, the results from these experiments remain inconsistent depending on the fuel used and burn conditions. Some attempts have been made to correlate the IN activity to variables and aerosol properties in the experiments. Petters *et al.* [2009b] found positive correlations to potassium and inorganic fraction within particles and a negative correlation to organic carbon fraction. Levin *et al.* [2016] found that lower INP concentration correlated with lower modified combustion efficiency (a measure of the combustion completeness), absorbance at 850 nm (corresponding to black carbon aerosol), and the elemental carbon to total carbon ratio. Each of these results suggests that higher efficiency burns and increased mineral and black carbon fractions will enhance ice nucleation activity from burns. The INPs produced by biomass burning are still not understood, despite attempts to correlate the ice-activity to particle properties. Mineral phases, soot, and condensed organics are the likely candidates for INPs produced by biomass burning.

Soot is the highest concentration particle phase component produced by incomplete combustion. It is composed largely of graphitic carbon and has a fractal morphology [Popovicheva *et al.*, 2015]. Levin *et al.* [2014] found that removing soot from BBA using laser incandescence reduced the amount of INPs in the smoke by ~40%. This result

suggests that soot may be responsible for some of the freezing activity, but it cannot be the only component in BBA that is ice-active. Similar results were found by McCluskey et al. [2014] using EDX to determine the composition of ice crystal residuals sampled from wildfires and prescribed burns. In this study they sampled air downstream of various fires and collected ice crystals that were nucleated using a CFDC onto TEM grids. They found that some of the grids collected contained no soot. Thus, soot could not be entirely responsible for the IN activity observed in those BBA samples. Traditional measurements of soot from hydrocarbon combustion also suggest the weakness of soot as an INP that typically does not initiate immersion freezing until below $-30\text{ }^{\circ}\text{C}$ [DeMott, 1990b; Dymarska et al., 2006; Koehler et al., 2009; Friedman et al., 2011]. Despite this weakness, soot is still the dominant particle type in biomass-burning plumes and could influence ice nucleation in clouds at sufficiently cold temperature ($< -30\text{ }^{\circ}\text{C}$), especially if it is the only ice-active particle type remaining; the more ice-active INPs will have already nucleated ice at warmer temperatures lower in the cloud's evolution. Some calculations have suggested that atmospheric aging could greatly enhance the ice activity of soot. Lupi and Molinero [2014] found through molecular dynamics simulations that by modifying a graphitic surface with $-\text{OH}$ functionalities the ice activation temperature could be increased by greater than $5\text{ }^{\circ}\text{C}$. By adding $-\text{OH}$ groups to graphitic carbon, the surface becomes capable of participating in the hydrogen bonding network of ice. This could make chemically oxidized/aged soot a much more likely candidate to act as an INP in the atmosphere. On the other hand, a few studies have found that deposition freezing is only slightly enhanced on oxidized soot, but this has not been determined for immersion-mode ice nucleation [Dymarska et al., 2006; Koehler et al., 2009]. The contradictory results regarding the

importance of soot and soot oxidation on its role as an INP makes modeling the impacts of soot emissions on atmospheric ice nucleation highly unconstrained [Hoose *et al.*, 2010].

Biomass burning produces a large variety and amount of organic compounds that can range from volatile to extremely low volatility, and their volatility changes rapidly upon exposure to oxidants in the atmosphere [Donahue *et al.*, 2006; Gilman *et al.*, 2015; Tkacik *et al.*, 2017]. VOCs continue to undergo gas-phase oxidation until they condense onto pre-existing particles or nucleate new particles, producing secondary organic aerosol (SOA). Highly viscous (or glassy) SOA has been suggested as an INP by several groups, though it tends to have quite low ice-activity with deposition freezing onset typically occurring below -45 °C [Prenni *et al.*, 2009; Wang *et al.*, 2012; Berkemeier *et al.*, 2014; Schill *et al.*, 2014]. Immersion freezing initiated by SOA is highly unlikely as the water will destroy the viscous phase state thought to be required to drive ice-activity of organic systems. Deposition freezing of SOA appears to require a tight range of thermodynamic conditions of temperature and relative humidity that preserves the viscous state while initiating ice nucleation. Möhler *et al.* [2008] found that thick coatings of lab-generated SOA condensed onto mineral dust particle decreases the ice nucleating ability of Arizona Test Dust and illite in the deposition regime. Similar results have been found for the coating of soot particles [Kulkarni *et al.*, 2016]. However, no studies to my knowledge have examined the ice nucleation properties of SOA produced in a biomass burning plume and its effects on primary ice nucleation particles emitted within the plume. Most of the above studies have focused on SOA formation from pure organic compounds (e.g. α -pinene and naphthalene) and these may not accurately represent the ice nucleation properties of SOA produced from the complex emissions of biomass-burning combustion.

Mineral phases are a less obvious component of BBA, though we know they can be present [Reid *et al.*, 1998; Li *et al.*, 2003; McCluskey *et al.*, 2014]. The exact origin of mineral phases in BBA is not known. Loose mineral dust particles from the soil could be mobilized and entrained during intense combustion [Gaudichet *et al.*, 1995]. Dust and soil particles that deposited on the plant can also be resuspended by the strong convection produced during combustion. Additionally, recent findings from myself and others have indicated that ash particles are a possible ice nucleant produced by biomass combustion [see Chapter 5]. Ash is predominantly composed of mineral phases and has moderate ice nucleating activity [Umo *et al.*, 2015; Grawe *et al.*, 2016]. Little else is known about the origin of mineral phases in BBA. However, if crystalline mineral phases are able to be emitted in biomass burning plumes, then these are likely to participate in atmospheric ice nucleation [Connolly *et al.*, 2009; Wex *et al.*, 2014; Hiranuma *et al.*, 2015a; Beydoun *et al.*, 2016].

All of the above components may be partly or wholly responsible for the variable IN activity observed in biomass burning aerosol. This chapter discusses the experiments we have conducted to better understand the impact of biomass burning aerosol on atmospheric ice nucleation, to identify the source of ice nucleants in BBA, and to determine the effects of chemical aging on these ice nucleants. Our initial hypotheses for this work are: 1) atmospheric oxidation will improve soot IN activity by allowing it to facilitate ice crystal formation, 2) oxidation of VOCs in smoke will create new SOA particles that can act as additional particle surfaces that initiate ice formation, and 3) oxidation of VOCs could lead to a decrease in ice nucleating activity if condensation of viscous SOA occurs on the soot surfaces. The following sections will describe the progress we made on this work and what

insights we have gained so far. Most of the results will be about the ice nucleation data because that was my focus in this project, but some data acquired by my colleagues of particle composition analysis using SEM and Aerosol Mass Spectrometer will be used to facilitate assignment of this ice-activity and any changes observed when possible.

6.3 Biomass burning experimental setup

Biomass burning experiments were performed in the CMU chamber reactor. The reactor is composed of a 12 m³ Teflon bag with ports for injecting emissions from the combustion event and for connecting instruments to sample the emissions. Fuels were first weighed and placed in a metal pan to be burned. The fuel was lit using a butane lighter in a few locations to promote full ignition and emissions were drawn up a ventilated chimney. From the chimney, the emissions were pulled into the chamber by a Dekati educator diluter with a 10:1 dilution flow of clean air until a concentration of around 100 µg/m³ is reached. The chamber aerosol was sampled from the reactor for several hours until we started aging the sample. Aging was performed by injecting an oxidant into the chamber after the first half of the experiment has finished. Oxidants used in these experiments include: OH radicals generated by H₂O₂ UV photolysis (for low NO_x), photolysis of HONO (for high NO_x), or ozone (O₃). After aging, we continued to sample for the same amount of time as for the fresh sample to maintain a similar sampling volume. Some of the later experiments performed in 2017/2018 included the use of a thermodenuder, which heated the aerosol to ~300 °C to volatilize organic compounds and removed those compounds with activated carbon before the aerosol entered the chamber. Over the course of these experiments many of the methods changed to some extent and thus an overview of those details will be provided here and will be explored later when those method details changed.

The earliest burns only relied on the sampling filter or an impinger for collection. Impingers are devices that sample air by circulating it through a vial of water to collect particles by impaction. Later in 2015 I started using the Scanning Mobility Particle Sizer (SMPS) to obtain aerosol size, mass, and surface area measurements to calculate total particle surface area over the course of the experiments. In 2016 we started to use the Aerosol Mass Spectrometer (AMS) to get more information regarding changes in the particle composition over the course of the experiments. Additionally, we started to add in other sampling instruments on occasion such as the Micro-Orifice Uniform Deposition Impactor (MOUDI) to collect SEM and TEM grids for subsequent electron microscopy analysis. By 2017 we regularly measured gas-phase CO/CO₂ directly from the burn and gas-phase NO_x and O₃ from the chamber. In 2018 we started to implement the measurement of supermicron particles using the Aerosol Particle Sizer (APS).

6.4 2015 initial BBA experiments

The initial experiments to study INPs in BBA in 2015 included a lot of optimizing and trial-and-error to determine what experiments should be run and what methods we should use to get the best data possible. This section will discuss this process and identify important findings from the 2015 experiments that informed the improved design of future experiments.

The first important factor we had to determine for these experiments was the best way to collect aerosol samples from the chamber. We needed a method for transferring combustion particles from the chamber into water droplets with as little particle loss as possible. The method also had to be easy to replicate at least twice per day and yield enough signal to observe ice nucleation above the background freezing spectrum using the droplet

freezing cold stage (CMU-CS). We started with 25 mm diameter, 400 nm pore size nuclepore membrane filters because they were readily available in the lab, and nuclepore filters have a smooth surface making it fairly easy to extract collected particles with water. One of the concerns with these filters was the large pore size. We expect soot particles to have a mode diameter around 100 nm and a 400 nm pore would have less than 100% collection efficiency for typical soot particles. Our droplet freezing results (Figure 6.1) displayed ice-activity quite close to the background pure water signal and so we abandoned using these filters after just two burns to evaluate some alternative methods.

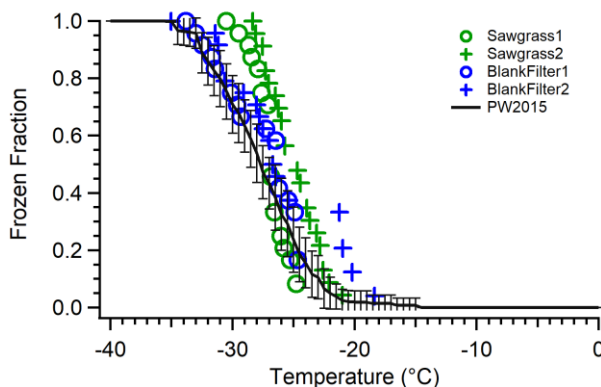


Figure 6.1. Freezing spectra of first sawgrass burn collected on a nuclepore filter, compared to pure water and a blank filter. Droplets used for this experiment were 0.1 μ L, particle concentration in the chamber was unknown because no SMPS was used. Error bars on the pure water indicate the standard deviation of pure MilliQ water droplets taken throughout 2015.

After the first attempt using nuclepore filters we tested two alternate methods of collecting particles by impaction. We ran a single burn where we compared collection using the MOUDI to collect particles onto a glass coverslip that we use as a substrate for the CMU-CS, and collection of aerosol into water using an impinger. The MOUDI pulls air at a high flow rate through ten orifice stages that get progressively smaller to allow size-

segregated collection of particles. One of the major concerns with this collection method is we have no way to quantitate or reduce bouncing of particles off the substrate without coating it in an adhesive or grease, which would interfere with subsequent freezing of the particle samples. Additionally, we needed to have a consistent 30 Lpm of flow which could not be sustained for multiple hour experiments in a 12 m³ bag. Impingers are typically used to collect biological aerosol directly into water by using a circulating air flow. This seemed like a promising method because we could skip the step of extracting the particles into water. However, we had to be concerned with dilution ratios as well as repeatedly filling the impinger to maintain the same water volume during experiments because of accelerated water evaporation. Despite this, we continued the use of the impinger collection method for several weeks.

The impinger was successfully used to collect aerosol from a number of burns including six sawgrass burns and one eucalyptus burn. The findings from these experiments show there is a slight ice nucleation signal above the pure water background for about half of the sawgrass burns. Activity above background only becomes evident around -27 °C to -30 °C when about 50% of the droplets had normally frozen in pure water. The eucalyptus burn showed similar trends to these sawgrass burns. An example temperature freezing spectrum for these experiments is shown in the following subsection (Figure 6.2). With regards to aging, most of the experiments that involved aging showed a higher freezing temperature for the aged sample than the fresh sample. However, not much can be said beyond this because most of the signal is within or close to our background freezing spectrum. These results showed that we may not have enough INP signal to continue to use the 10 mL of water we needed to run the impinger properly. In addition, as experiments

progressed the amount of time being dedicated to cleaning and drying the impinger between burns and between fresh and aged samples became rather significant. Thus, we decided to use larger diameter filters with smaller pore sizes because we had less constraints when using in-line filters and nuclepore filters are the easiest filters to extract particles off of. All future BBA experiments were run using nuclepore filter collection (47 mm diameter, 50 nm pore size). We only were able to run three experiments using these filters in 2015 and the results were similar to those found in the impinger with little-to-no signal above our background.

6.4.1 Aging of sawgrass burning aerosol slightly enhances INP

One interesting result from all of the burns in 2015 was the trend of chemical aging enhancing the ice-activity of INPs produced by sawgrass burns (Figure 6.2). We see that in the freezing spectrum as well as the n_s plot, aged sawgrass emissions have higher IN activity compared to fresh BBA. The freezing spectrum shows error bars that depict the standard error between different burn experiments. The experiments used in this plot are a combination of impinger aerosol collection and filter collection. For most experiments the fresh emissions were within or near the background signal of the pure water controls. The averaged n_s spectra depict the particle surface area normalized ice-active site density. Total particle surface area is determined by averaging the SMPS measured surface area through the sampling period. Aged BBA again consistently displays higher activity compared to fresh by a factor of 2-3 at temperatures below -23 °C. Above this temperature the aged BBA is much more active. These ice-active site densities are quite similar in magnitude to the ash samples discussed in the preceding Chapter 5. For these experiments aging by OH radicals under low NO_x was performed. This mechanism of aging is non-selective and will

oxidize soot and organic particle surfaces, as well as oxidize organic vapors, producing SOA or potential causing fragmentation that increases volatility and leads to evaporation of organic aerosol. Therefore, we do not get a clear indication what the ice active surface is and what is altered by the hydroxyl radical exposure. Additionally, many of these experiments were performed without use of the AMS, which will provide particle composition information. Thus, we cannot directly or even indirectly identify what is causing the increase in IN activity, though we suspect the change is likely caused by the aging of soot particle surfaces or the creation of new particle material such as SOA that is able to act as INP.

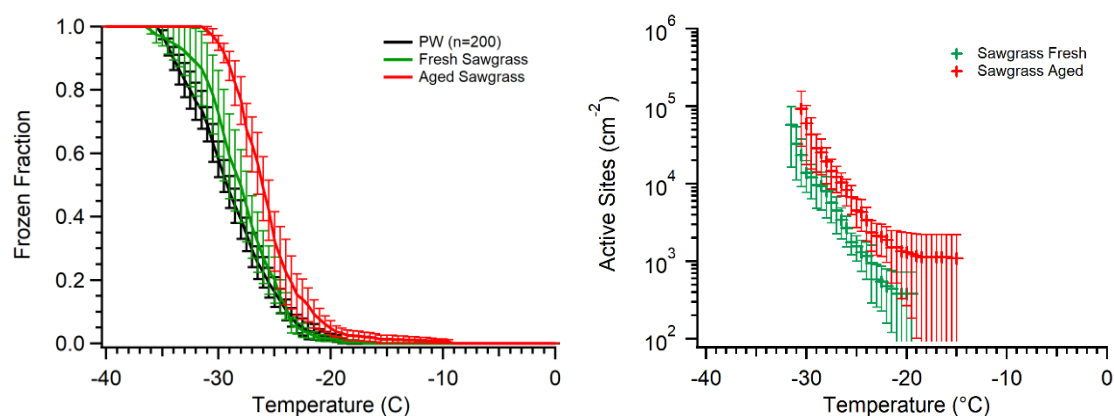


Figure 6.2. Temperature freezing spectrum (left) and ice-active site density (n_s) spectrum (right) for fresh and aged sawgrass samples obtained in 2015. Droplets used for this experiment were 0.1 μL . Particle concentration in the chamber was 20-30 $\mu\text{g}/\text{m}^3$ for each of these 5 sawgrass burns. Error bars represent the standard error of the frozen fraction and n_s for respective sample types. The pure water tests indicate the number of pure water control droplets (n) included in this analysis.

6.5 Probing INP production from a variety of fuels

By 2016, we decided to use the nuclepore filter collection method, so aerosol collection remained constant but other variables in these experiments were altered for various reasons as will be discussed. This year we focused on studying different types of fuels to determine what would give us a good signal for ice nucleation experiments, and also because we were running low on the sawgrass and cutgrass fuels we expected to produce INP.

For many months we were out of tall grass fuel samples to run and had to obtain fuels from different sources. Hence our experiments conducted of many different fuel types. We started a collaboration with the Phipps Conservatory in Pittsburgh and used some of the grasses they were disposing of as our fuels for several experiments. We also burned several types of wood. These ended up providing some interesting results, specifically, that woods in general seem to contain much weaker IN activity than grasses. We also were given organic hay from a local farm by a colleague, Victoria Hofbauer.

One other issue that was prevalent during the 2016 experiments was issues with the freezing temperature of our background water controls continuing to increase and display much higher variability than normal. This important method artifact was a major motivation behind the extensive pure water filtration methods and different substrates tested in Chapter 3, as we could not distinguish between high background freezing and low INP signal in most cases for these 2016 experiments. Despite this, I believe the results presented in this section are distinguishable from the background because many of the experimental findings from this year were very close to our 2015 background water signal. As an example, Figure 6.3 contains two different experiments that both possess nearly

identical freezing spectra despite having very different particle concentrations, which would not be likely if the background water signal was actually as variable as was found for the 2016 pure water tests. Therefore, the background data presented for comparison to in this section will be the pure water tests from 2015.

The following are some of the more interesting findings we obtained during the 2016 BBA experiments. These include the lack of INP production from wood burning, the potential emission of ice-active soil particles from biomass burning, and more evidence that aging may increase the ice-activity of INPs emitted from another species of tall grass.

6.5.1 Comparison of ice-activity of BBA produced from wood vs. tall grasses

Two BBA experiments were performed during 2016 on woods: one of birch wood and the other on fatwood. Birch is a type of tree that is widespread and found over much of the Northern Hemisphere in temperate and boreal climates. Fatwood is the heartwood of pine trees; it contains a high amount of resin and is typically used for starting fires. Resinous pine trees exist in all climates around the globe. Both of these woods produced a high concentration of particles in the chamber but had no INP activity above the pure water background (Figure 6.3). Compared to the grasses run in 2015/2016 these woods generated much more particulate mass (birch: $65 \mu\text{g}/\text{m}^3$; fatwood $500 \mu\text{g}/\text{m}^3$; typical grass in 2015: $20\text{-}30 \mu\text{g}/\text{m}^3$) and had no observable ice-activity compared to the pure water controls. This finding is consistent with previous findings that some grasses seem to create ice-active particles when they are burned but woods in general generate either far less or no INPs, and their ice-activity is much weaker, corresponding to low immersion freezing

temperatures < -30 °C. Additionally, we saw no difference in the IN activity between fresh and aged BBA from these woods.

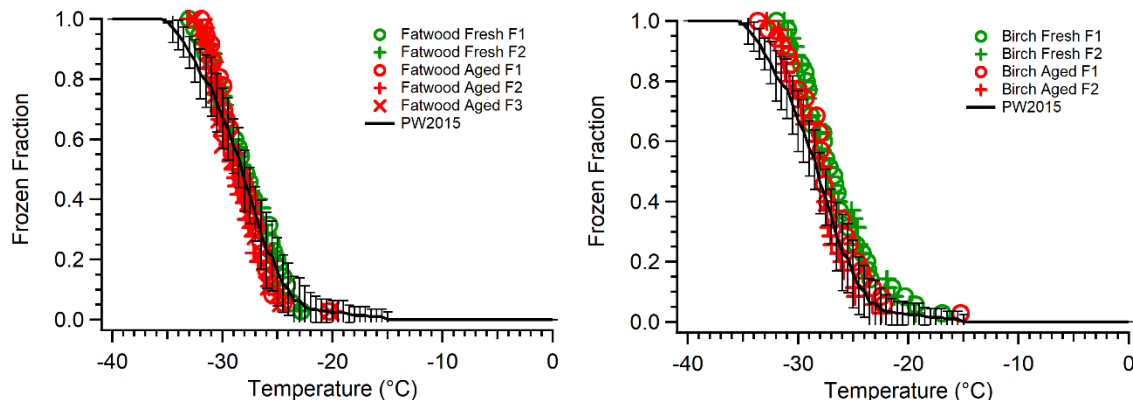


Figure 6.3. Droplet freezing temperature spectra for BBA produced by combustion of fatwood (left) and birch wood (right). Both show ice-activity similar to the pure water background signal. Droplets used for these experiments were 0.1 μ L. Particle concentration in the chamber was 65 μ g/ m^3 for the birch burn and 500 μ g/ m^3 for the fatwood burn. Error bars represent standard deviation of the frozen fraction of replicate arrays for respective sample types.

The fatwood used here is a particularly interesting case because it is very high in resin, which makes the produced smoke aerosol rich in very fractal soot particles (Figure 6.4 left). We discovered this during the experiment when the combustion room quickly became filled with smoke after only burning 4 or 5 sticks of fatwood. The results of this experiment suggest that soot is not a major factor in ice nucleation for immersion mode nucleation studies, at least from this type of wood. Combustion of fatwood resulted in nearly 500 μ g/ m^3 of almost completely soot particles in the chamber (Figure 6.4 right), yet we found that the ice-activity of this aerosol was no better than pure water controls. Comparing to the previous sawgrass experiments where we find an enhancement of INPs between -25 °C and -30 °C with a much lower aerosol mass concentration of 20-30 μ g/ m^3

suggests that there are ice-active components other than soot that can act as an INP. An alternative explanation is that the soot particle properties are in some way different for grasses and wood, causing soot produced from tall grass combustion to be more ice-active. This could be possible if soot structure is related to fire intensity, but to my knowledge this is not known. We do not have enough evidence to conclude which of these explanations is correct, but it seems unlikely that the soot from grass and wood burns is different enough to explain the difference in freezing ability. A more likely explanation is that the minerals produced through combustion that we see in the ash are responsible for the IN activity, and the more intense combustion of grasses compared to woods would drive the production of these ice-active minerals. Unfortunately, determining the mineral phases present in BBA is much more challenging experimentally than the ash analysis discussed in Chapter 5. There is not typically enough aerosol mass that can be collected to perform bulk XRD analysis. Obtaining an electron diffraction pattern from individual particles using TEM analysis is also feasible [Wang *et al.*, 2016a]. We are attempting this challenging analysis

using the facilities available to us through User Proposal awarded by the DOE Environmental Molecular Science Laboratory (EMSL).

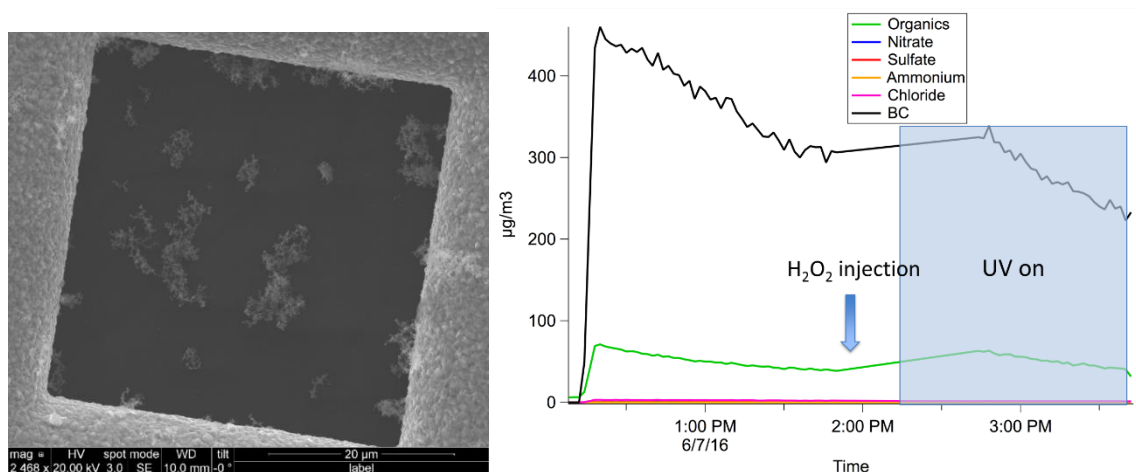


Figure 6.4. Left: SEM image of fresh chamber particles collected during the fatwood burn. Large soot aggregates display highly fractal structure, suggesting high elemental carbon composition. Right: Results from the Soot-Particle Aerosol Mass Spectrometer (SP-AMS) showing the much higher black carbon (BC) content compared to other aerosol chemical components.

The trend of wood producing ash particles with lower ice-activity than grasses was discussed in the previous Chapter 5. We know from direct observation that woods tend to burn slower and with lower temperature than grasses. While 500 g of grass will burn in 3 minutes, the same amount of wood takes 10 minutes or more to extinguish itself under the same conditions. As mentioned previously, combustion power and temperature are correlated to the amount of amorphous material present in the ash [Balfour and Woods, 2013], and while it is not currently known, the same may be true of the aerosol produced,

or that ash may be lofted along with the aerosol formed. Our results in this section seem to hint that that may be the case.

6.5.2 Contribution of root combustion and soil to ice-activity of biomass-burning aerosol

Some recent results have suggested lofted soil particles could act as INPs in the atmosphere [Tobo *et al.*, 2014; Hill *et al.*, 2016]. No studies have directly tested whether soil is lofted by wildfires to my knowledge, but some have suggested it as a possible mechanism and recent studies have found soil markers in biomass-burning plumes [Maudlin *et al.*, 2015; Schlosser *et al.*, 2017]. We obtained a grass sample of *Arundo perennis* from Phipps Conservatory that included the root system with soil still attached to the plant. *Arundo perennis* is a reed plant that has origins in the wetlands near the Mediterranean Sea and Northern Africa, but it also exists in wetlands in the Southern United States. We decided to run a pair of burns on the sample: one with the root system and soil removed from the plant and one with the roots and soil intact. This resulted in one of the most interesting and surprising results reported in this dissertation: the aerosol produced from the combustion of the *Arundo*+roots sample contained measurable INPs while the *Arundo* sample with roots and soil did not. The droplet freezing spectra are shown in Figure 6.5. Interestingly only the fresh sample of *Arundo*+roots had any measurable INPs. This is likely because the larger soil/roots particles will have settled to the chamber walls within the first few hours of sampling, and thus they would not have been collected on the second H₂O₂/UV aged filter. It is also possible that the chemical aging impaired the freezing ability of the INPs present in this BBA. The *Arundo*+roots sample possessed particles that are highly ice-active at ~-25 °C, while the *Arundo* sample and both aged

samples all were only as ice-active as the pure water controls. The AMS analysis found no noticeable difference between chemical compositions of these two types of aerosol. The IR laser that enables BC particle measurement in the SP-AMS was not working for these experiments and thus no measurement of soot is available, just the organic carbon and inorganic salts.

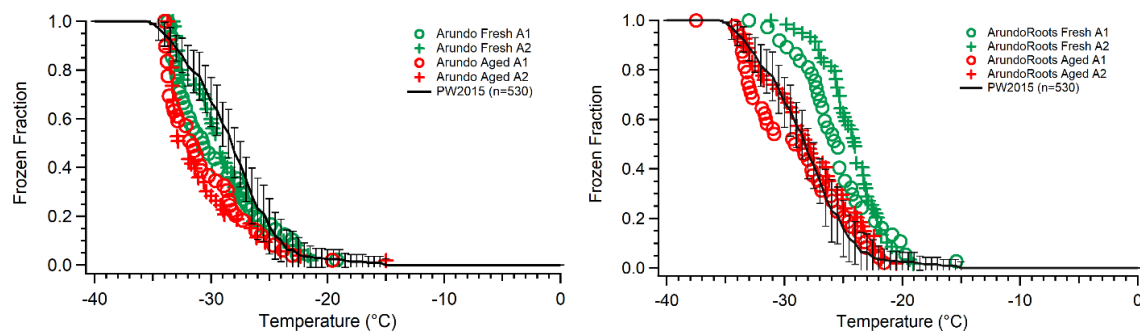


Figure 6.5. Temperature freezing spectra for *Arundo perennis* (left) and *Arundo* with roots and soil attached (right) including aged samples (red). Two arrays for each sample are shown for reproducibility. Droplets used for these experiments were 0.1 μL . Particle concentration in the chamber was 54 $\mu\text{g}/\text{m}^3$ for the *Arundo* burn and 29 $\mu\text{g}/\text{m}^3$ for the *Arundo*+roots burn. Error bars represent standard deviation of the frozen fraction for respective sample types. The pure water controls indicate the number of droplets of pure water included in this analysis.

6.5.3 Enhancement of ice-activity following aging of BBA from cutgrass

combustion

For two of the cutgrass burns in 2016 we found moderate ice nucleating ability, similar to previous sawgrass burns. Freezing spectra are shown in Figure 6.6. For these experiments OH radical oxidative aging was performed similar to previous Sawgrass experiments (Figure 6.2). Unfortunately, only one array of droplets for each of these experiments was run the reproducibility cannot be assessed. However, we see enhancement

in ice-activity from the increased freezing temperature compared to pure water, with a slightly higher activity for the aged sample. Additionally, the aged samples consistently have early freezing droplets at temperatures well above the median freezing temperature. Although this is possibly caused by pure water itself, the fresh cutgrass BBA samples never displayed this behavior. One other burn of cutgrass was performed where the ice-activity was equivalent to pure water.

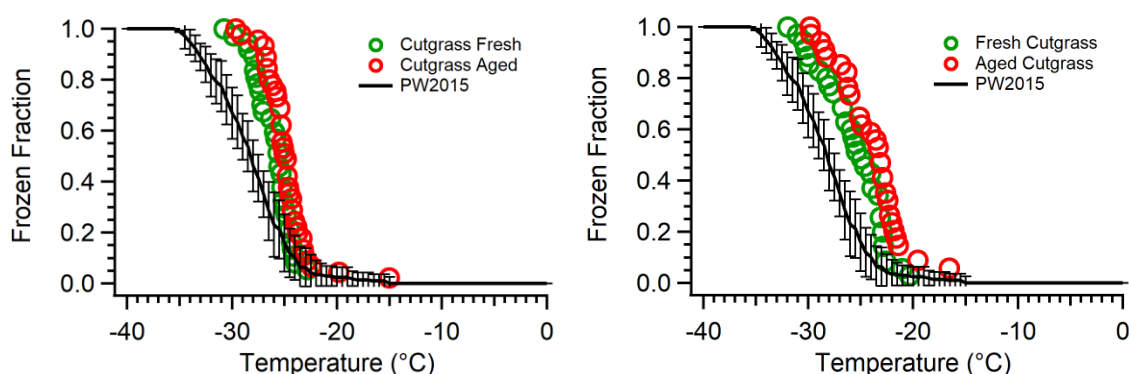


Figure 6.6. Freezing spectra for fresh and aged cutgrass BBA for two different chamber experiments. Droplets used for these experiments were 0.1 μL . Particle concentration in the chamber was 60 $\mu\text{g}/\text{m}^3$ (left) and 20 $\mu\text{g}/\text{m}^3$ (right). Error bars represent standard deviation of the frozen fraction for respective sample types. The left graph shows the same cutgrass burn as the data presented in Figure 6.7.

Aerosol compositional measurements from the SP-AMS are shown for one of the cutgrass burns in Figure 6.7. For cutgrass we see very different properties compared to the birch wood. Cutgrass produces very little soot and has a OA:BC ratio greater than 1. Overall there is much lower particle mass but the IN activity of these particles is greater than that of birch. The AMS results do not provide a great deal of insight into what type of chemical alterations of the aerosol particles are occurring throughout the experiment. We can see that depositional aerosol losses to the chamber walls are the biggest change for organics and black carbon for the majority of the experiment. One interesting observation

is the limited formation of SOA particles once OH radical aging begins; no obvious formation of new particles or new aerosol mass was evident in the SMPS aerosol size distribution either. This finding suggests that little new particle mass was formed once OH radicals were introduced, which could suggest that aging was impacting the INP not by producing SOA but perhaps by oxidation of the soot particle surfaces or other mineral particles not visible in the AMS. We cannot say definitively with the data we have what particle chemical aging mechanism led to the observed slight enhancement of ice-activity in the cutgrass BBA, but these results suggest that aging that results in little SOA production but potentially the oxidation of soot or mineral particles surfaces is an important mechanism that can enhance the ice-activity of BBA.

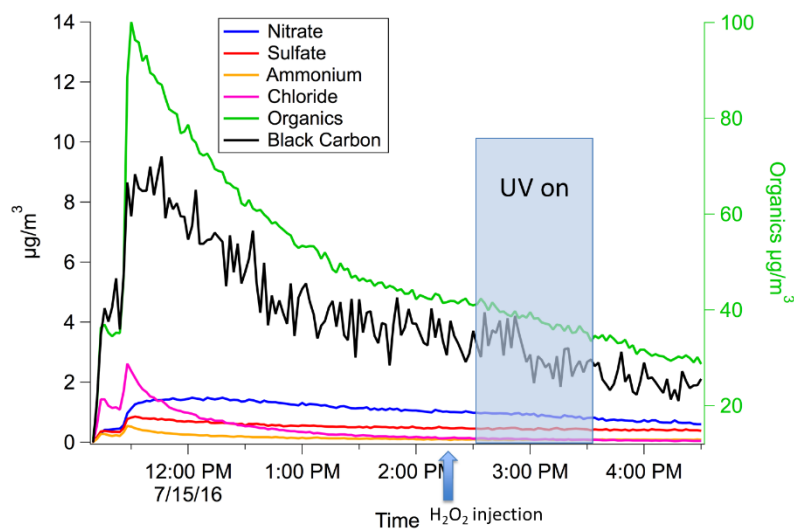


Figure 6.7. SP-AMS measurements of aerosol composition from one cutgrass burn. All measured species concentrations are depicted on the left axis except organics shown on the right axis. Aging occurs by OH radicals when the UV lights are turned on, shown by the blue shaded region. The data is taken from the same burn as the left graph in Figure 6.6.

6.6 Isolating important fuels for INP measurements

In 2017 a significant amount of effort was spent in refining our experimental methods and optimizing all steps in the experiments, particularly the filter collection and the ice nucleation measurements using droplet freezing assays. We largely resolved the high pure water background freezing issues that were a significant interference in the 2016 experiments, and revised our methods to include to background freezing controls more frequently. We also started freezing pure water and BBA samples side-by-side in the CMU-CS to obtain a direct assessment of the ice-activity of a BBA sample relative to the pure water background, when both types of droplets are on the same substrate. We transitioned to using only bottled HPLC-grade water that we also filter before performing any or control freezing experiments to further reduce background contamination, as discussed in Chapter 3. For many of these experiments we decided it was best to freeze larger droplets to increase the particle surface area present in each per droplet. This increases the observed droplet freezing temperature spectrum, allowing us to more readily determine weakly active INPs present in BBA that often have critical freezing temperatures near the pure water background freezing regime.

We decided to perform BBA experiments by filling a small 2 m³ Teflon chamber bag to do initial test experiments on different fuels to identify fuels that produce INPs with a clearly distinguishable ice-activity that can be resolved from the background freezing, before we continue to conduct experiments that examine the effects of aging. The benefit of filling and sampling from the small Teflon bag is we get much higher particle concentrations due to the smaller volume and it is much easier to clean the small bag in a short amount of time by air flushing between testing different fuels. Two BBA experiments

can typically be run per day with 2 hours of aerosol filter collection for each, as opposed to one type of fuel being tested using the large 12 m³ chamber due to the longer flushing times required. The downside to these experiments is we can only study and sample fresh BBA because the particle wall loss rate is much faster and we start off with only 2 m³ instead of 12 m³ of chamber volume to sample from. This also means sampling cannot be done using any high flow samplers, such as the MOUDI, and thus we cannot collect any particle samples for offline electron microscopy analysis from these BBA samples. Therefore, to make the most efficient use of our efforts, we screened fuel samples using the small bag and if we found reasonable ice-activity from the BBA produced, we identified that fuel for subsequent large chamber experiments where we can perform aging and aerosol collection with all of our typical instrumentation and samplers.

The following sections explore the experiments completed in 2017 including more tests on the impact of soil on INPs emitted by biomass burning, an interesting result where aging decreased the ice-activity of the BBA, and our first foray into using a low-background freezing microfluidic device for improved measurements of INPs in BBA.

6.6.1 Investigating the impact of soil and roots on INPs emitted by combustion of cutgrass and *Arundo*

We performed several more tests of the soil and roots incorporation into fuels and how that can impact the INPs produced by biomass burning. The findings from these experiments are inconclusive and require further investigation, including more individual particle analysis to relate the observed ice nucleation properties to the chemical composition of the BBA. The first burn re-examined the same *Arundo perennis* sample with roots and soil attached. The overall ice-activity was similar to the first experiment

shown above in Figure 6.5, with consistent freezing for four different droplet arrays with median freezing temperature, $T_{50} = -23\text{ }^{\circ}\text{C}$ (Figure 6.8). While this result is similar to the previous finding, we would have expected higher IN activity with 10X higher particle mass concentration and using 10X larger droplet sizes. In addition we have a somewhat higher pure water background signal due to larger droplet volumes. Median freezing temperature for 0.1 μL pure water droplets is $28.5\text{ }^{\circ}\text{C}$, while median freezing temperature for 1.0 μL droplets is $26.1\text{ }^{\circ}\text{C}$. In comparing the n_s plots of each of these burns (Figure 6.8 right) we see that the 2016 burn of *Arundo*+roots had a higher ice activity. This is likely a result of the particle having similar activity but being diluted by both the larger droplets and higher particle concentration in the chamber. So in fact we see the opposite to what we would have expected. These findings suggest the activity may not be consistent with soil or roots acting as INPs. For future tests, we implemented the APS to measure larger supermicron aerosol particles that cannot be measured by the SP-AMS and SMPS. These larger particles could help to explain why the *Arundo*+roots sample produced more ice-active INP. However, to date we have not observed more than 40 particles/ m^3 using the APS for any of the recent burns.

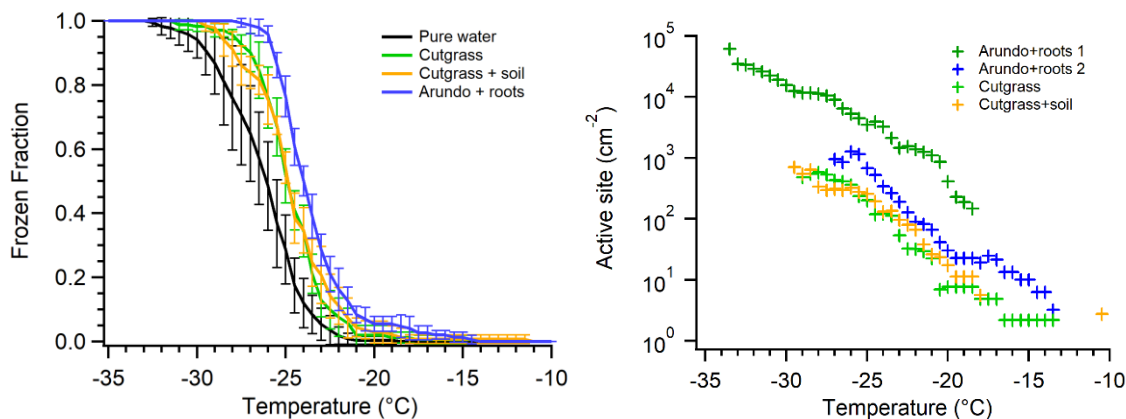


Figure 6.8. Left: Temperature freezing spectra comparing *Arundo*+roots, cutgrass, and cutgrass+soil. Droplets used for these experiments were 1.0 μL . Particle concentration in the chamber was 1700 $\mu\text{g}/\text{m}^3$ for the cutgrass burn, 1000 $\mu\text{g}/\text{m}^3$ for the cutgrass+soil burn and 500 $\mu\text{g}/\text{m}^3$ for the *Arundo*+roots burn. Pure water data is a statistical average of the pure water droplets frozen side-by-side with each of these BBA samples. Error bars show standard deviation of multiple runs of the same sample. Right: n_s plot showing data from both *Arundo*+roots burns (2016 (Figure 6.5) in dark green, 2017 in blue), cutgrass (light green), cutgrass+soil (orange).

Unfortunately, we did not have enough remaining *Arundo* sample to run another burn with no roots, so we decided to test a different soil and grass. We did two burns: one using cutgrass as fuel and another using cutgrass topped with soil that we collected from North Carolina where the cutgrass was also collected. Sprinkling soil onto the fuel was intended to elevate the opportunity for loose soil mineral particles to be entrained into the intense updrafts during combustion. The result for this experiment was slightly lower ice activity than the *Arundo* experiment with a median freezing temperature at -24°C and a similarly high water background due to larger droplet volumes, as shown in Figure 6.8. However, we observed no discernible difference between the freezing spectrum of cutgrass with soil added and cutgrass without. This means that added soil had no observable impact on the INPs in the BBA produced by this burn. The ice nucleation properties of the soil was also

tested by itself at the time and has quite strong IN activity (Figure 5.1). We know from our ash analysis from this same burn (Chapter 5) that at least some soil particles were able to survive the combustion process and maintain their IN activity; the ice-activity of the produced ash was increased when the soil was added to the fuel (Figure 5.2), while the activity of the aerosol from the same burn was not changed. We cannot say with confidence whether this experiment is representative of how lofting of soil will occur in wildfires, and still need to perform more experiments to determine how much, if any, of the soil can enhance the INPs produced by biomass burning in the real atmosphere.

6.6.2 Investigation of the impact of aging on wiregrass BBA

We ran several burns of another tall grass, wiregrass, to determine its impact ice-activity and potential contribution to atmospheric INP. We found in our first experiment that the fresh sample of wiregrass BBA was more active than the aged sample (Figure 6.9 left). The aged wiregrass BBA sample was also much more variable between different droplet freezing arrays, as denoted by the standard deviation in Figure 6.9 (left). Aged wiregrass overlaps with the standard deviation of pure water controls measured on the same substrate along with the BBA samples, which implies that the aging reduced the activity of whatever particles were active in the first sample. However, reduction of activity is expected between fresh and aged samples because of overall particle loss during the experiment. Therefore, to compare the aged and fresh samples we must normalize to the particle surface area concentration in the chamber during the respective sampling times. In converting to the n_s metric we find that the aged sample is still weaker than the fresh sample (Figure 6.9 right).

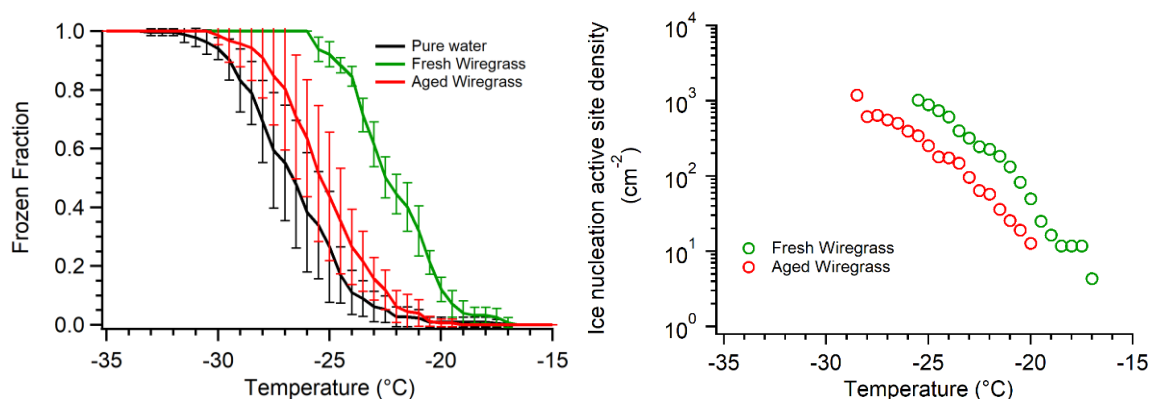


Figure 6.9. Freezing temperature spectra of wiregrass BBA before and after H₂O₂ aging compared against pure water controls (left) and corresponding ice active site density (n_s) plots for the fresh and aged samples (right). Droplets used for these experiments were 1.0 μ L. Particle concentration in the chamber was 146 μ g/m³. Error bars represent standard deviation between different droplet arrays of the sample. 1.0 μ L droplets were used for all these measurements.

From the AMS data we find that the organic aerosol concentration is high, which then upon H₂O₂/UV aging increases greatly. Significant SOA formation is observed to occur in the wiregrass BBA; this is the biggest difference in comparison to the other BBA aging experiments discussed so far, including for other tall grasses such as cutgrass, sawgrass, and *Arundo* where little to no additional organic aerosol was observed to be produced by aging. This large increase in SOA may be the cause of the decreased IN activity of the aged wiregrass sample observed in Figure 6.9. If soluble SOA particles are present in the droplets the increased soluble fraction of aged wiregrass BBA could depress the freezing temperature caused by any soot or other particles able to nucleate the droplet [Murphy and Koop, 2005]. An alternative explanation could be soot or other particle surfaces being coated in an insoluble SOA layer. If this were the case then the ice-active site may be inhibited and particles would be unable to act as INPs. This could suggest that given enough

SOA in the immersion mode will actually decrease the IN activity of other non-soluble INPs.

6.6.3 Testing a new microfluidic device for assessment of INPs in BBA with reduced background freezing interference

For one experiment in late 2017 we were able to use the new microfluidic chip developed in our lab by Thomas Brubaker in collaboration with Prof. Shelley Anna to determine the ice nucleation properties of BBA. The benefits of this method are discussed in Chapter 3, but the biggest improvement is the very low background freezing temperature of pure water droplets. In this first device, up to 40 droplets having a volume of 80 nL could be trapped. In Figure 6.10, we see the comparison of pure water and sawgrass BBA analyzed with the microfluidic device with the traditional cold plate method. Both methods show enhanced activity for both fresh and aged wiregrass BBA over the respective pure water controls. When comparing the n_s spectra, we see that for the traditional method the ice active site density is the same for fresh and aged wiregrass BBA, but with the microfluidic device the n_s values are not equivalent. It is not clear why there would be a difference between fresh and aged samples for one type of measurement but not another. This result is not expected and indicates an issue with one of the methods at this time. However, we find that the measurements using the traditional cold plate and microfluidic fall along a similar trend in n_s , which is an indication that these methods in combination may be able to probe INPs over the full supercooled mixed-phase cloud temperature regime between 0 and -40 °C. The larger 0.1 or 1.0 μ L droplet volume of the cold stage droplet-on-substrate approach is better able to measure rare highly-active INPs that freeze at warm temperatures, while the lower background freezing temperature of the 6 nL microfluidic

droplets in the enables measurements of weaker INPs down to $-33\text{ }^{\circ}\text{C}$. This was the first attempt to use the microfluidic device, and following the success demonstrated here this approach was further improved upon and used in subsequent BBA experiments that took place in 2018.

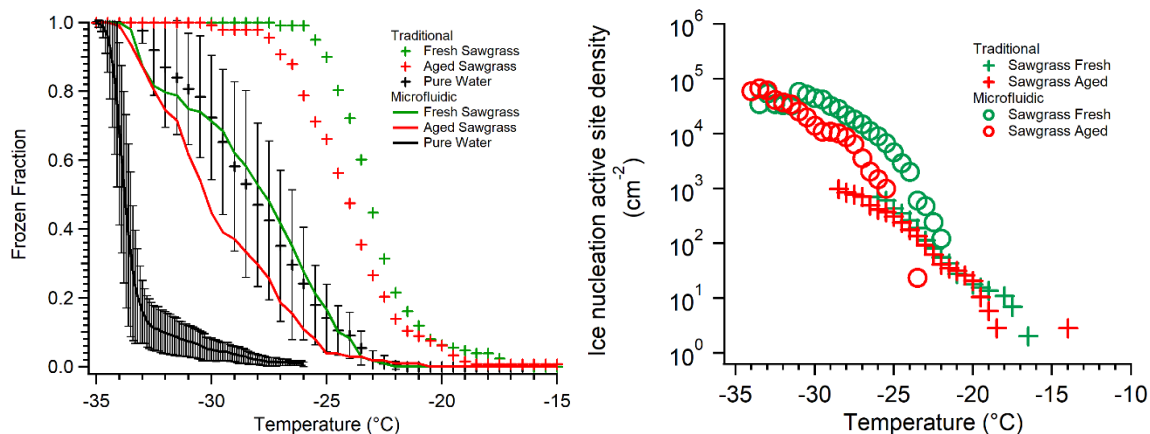


Figure 6.10. Comparison of droplet freezing spectra for fresh and aged BBA from a sawgrass burn between the traditional cold plate method ($1.0\text{ }\mu\text{L}$ droplets, crosses) and the microfluidic device (80 nL droplets, lines). Particle concentration in the chamber was $434\text{ }\mu\text{g}/\text{m}^3$. All datasets are averaged over 3 or 4 arrays of droplets. Error bars are standard deviation of pure water samples.

6.7 Initial BBA experiments using high-volume droplet arrays

Measurements of INPs from BBA in experiments conducted in 2018 were all performed using a new iteration of the microfluidic device that can examine up to 720 droplets simultaneously. A series of biomass-burning experiments was designed to directly explore the effects of different types of aging to develop more mechanistic insight into how aging alters particle properties and their ice nucleation ability: non-selective OH radical aging, soot-specific OH radical aging, and dark ozonolysis that targets oxidation of organic

aerosol and its condensable organic vapors. Two fuels, sawgrass and cutgrass, have been used so far in these experiments to explore the differences between fuels. These fuels were selected based on their availability to us, and on the significant and reproducible INP signal typically measured in the initial experiments described above. Only some of these collected BBA samples have been subjected to droplet freezing assays to measure their INP to this point. The results of the assays performed to date are not consistent, but some of the interesting results are discussed below, along with plans for further experiments to further investigate our hypotheses regarding how chemical aging alters the ice nucleation properties of BBA.

6.7.1 Effect of dark ozonolysis on the ice-activity of sawgrass BBA

Dark ozonolysis was used to selectively oxidize nascent organic vapors added to the chamber from biomass-burning. Ozone reacts readily with double bonds that are commonly present in organics emitted by biomass burning, such as the suite of terpenes (e.g. α -pinene), resulting in increased oxidation state that reduces volatility, driving the formation of SOA. Ozonolysis in the dark also avoid photolysis that can lead to fragmentation instead of functionalization of organics; this would increase volatility [Tkacik *et al.*, 2017]. Ozone does not readily oxidize soot surfaces without photolysis and will react more quickly with unsaturated organic vapors than with soot particle surfaces. The sawgrass ozonolysis results show a moderate increase in ice-activity over the fresh BBA sample (Figure 6.11). Interestingly, the microfluidic system seems to measure droplets containing a single INP. We know this because there is a dramatic shift in the freezing temperature between droplets that have INP and those that freeze homogeneously. In this example, only about 50% of fresh BBA-containing droplets possess an INP, while

60-85% of aged BBA-containing droplets possess an INP. With the microfluidic measurements, we can see that aged and fresh aerosol have similar freezing temperatures for most droplets but that more droplets contain these ice-active particles. This could suggest that aging increases the number of particles that are ice active but not the temperature at which they are active, or that the ice-activity of existing INPs has been increased. Therefore, it may be coincidence that aged sawgrass BBA has a higher activity, but further analysis must be done to determine if this is consistently the case.

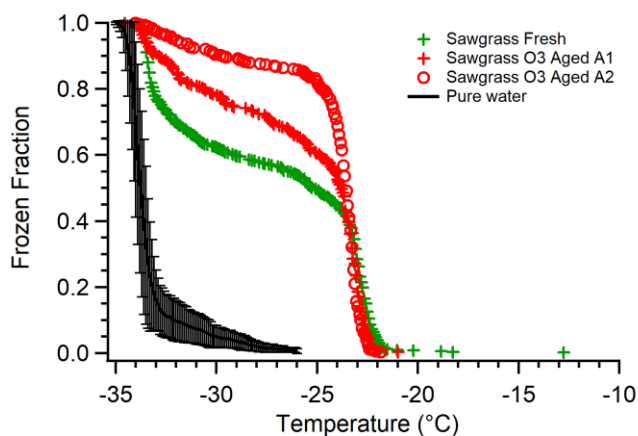


Figure 6.11. Freezing spectra of fresh sawgrass BBA and O₃-aged BBA obtained using 6 nL droplets in the microfluidic device. All BBA samples are based on one array from a single device. The error bars for the pure water data are the standard deviation of several replicate runs.

The AMS data is shown in Figure 6.12. We see that only a small increase in OA occurs at the time of ozone introduction. This suggests that little there was little SOA formation. This do not confirm nor deny the possibility that the fresh and aged particles have similar activity, but that the particle concentration per droplet is different. For each of the runs on the microfluidic chip.

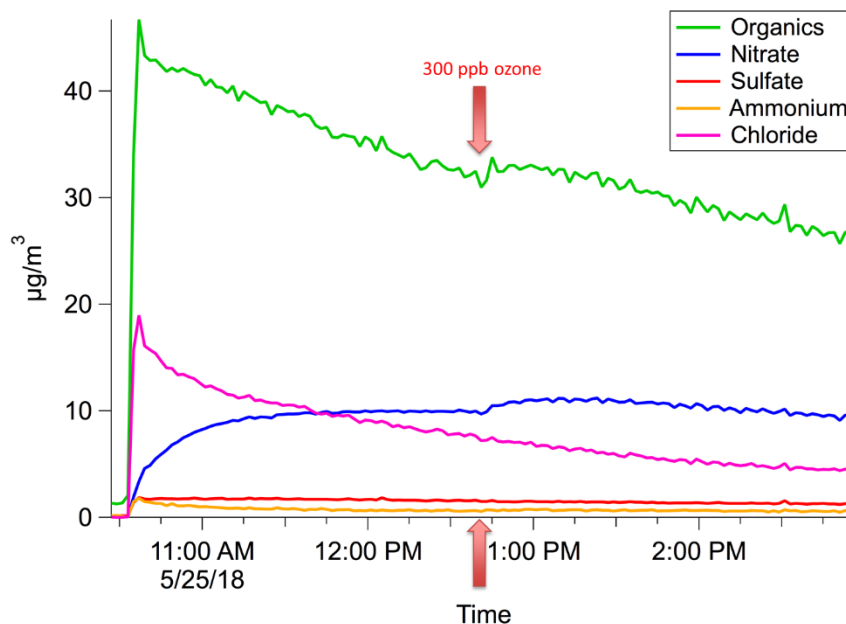


Figure 6.12. SP-AMS measurements of aerosol composition from sawgrass ozonolysis. Aging occurs by dark ozonolysis; ozone was injected at the red arrow. During this experiment the SP laser that measures BC was not functioning.

6.7.2 Effect of dark ozonolysis on the ice-activity of cutgrass BBA

Cutgrass BBA aging via dark ozonolysis resulted in inconsistent IN activity. The fresh cutgrass aerosol did not give the same result between two replicate arrays. Similar to the sawgrass ozonolysis results presented above, the same freezing median temperature was found for both fresh BBA droplet arrays, but very different fractions of droplets possessed those INP. This finding highlights the single particle nature of the microfluidic device. The median freezing temperature of the strongest INPs from both fresh arrays was consistently around -23 to -25 °C. However, the fraction of droplets inferred to contain those INPs based on their observed freezing temperature were very different between the two different arrays: A1 had ~20% of droplets containing INP, and A1 with nearly 100% of droplets containing INPs. This inconsistency could depict a weakness to this form of

analysis for the microfluidic technique. The inconsistency shown in the cutgrass fresh sample (Figure 6.13) as well as the sawgrass-O₃ aged sample (Figure 6.11) imply that the 6 nL droplets are not having consistent concentrations of particles within them. This is likely a result of the filter extract having such a low concentration of particle to begin with. Further tests will need to be run to see if this is the case for all BBA experiments. If so, several solutions can be attempted: 1) concentration of particle extract by reducing the washing volume or evaporating some of the water off, 2) injecting more particles into the chamber, which is not easily controlled aside from burning more fuel, 3) collecting for longer times, which makes an all-day experiment even longer, and 4) using larger droplet volume to ensure that all droplets contain at least one particle. Alternatively, a new method of analyzing these results could be used, for instance by only analyzing the droplets that are known to possess a single particle we can assign that activity to individual particles in the BBA. One more interesting finding is the lack of strong INPs in the aged BBA sample. The ice-activity is fairly weak and non-uniform for the aged sample. This could mean the cutgrass IN activity is negatively impacted by ozonolysis, but further replicates are needed to confirm this finding.

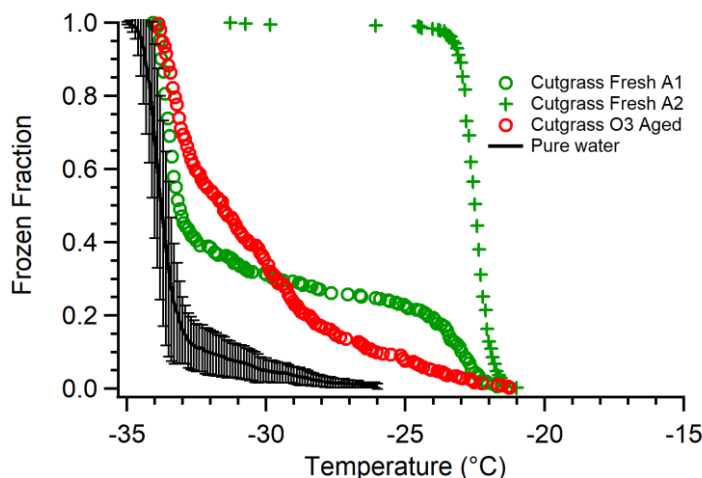


Figure 6.13 Freezing spectra of cutgrass BBA fresh and O₃-aged using 6 nL droplets in the microfluidic device. All BBA samples are based on one array from a single device. The error bars on the pure water data are standard deviation of several runs.

6.8 Conclusions

Understanding the impact of biomass burning aerosol on ice nucleation in the atmosphere is important for being able to model cloud properties, precipitation, and climate change in an increasingly warmer and drier climate. The experiments presented above are an attempt to elucidate some of the uncertainties in this understanding, by investigating the sources of INPs emitted by biomass burning, and exploring how atmospheric chemical aging might alter the physicochemical and ice nucleation properties of these INPs. More experiments must be done to further explore and confirm our initial findings, but we have achieved big steps in method development and variable identification. This will increase the success of future experiments on BBA. Some of the major results from this work are:

- BBA from tall grasses, such as sawgrass and cutgrass, tend to increase in ice nucleation ability upon aging with OH radicals. We suspect this is due to oxidation of soot particle surfaces that increases their hydrophilicity and ice nucleation properties.
- Wood combustion aerosol, similar to ash, appears to have much lower ice nucleating ability than that produced by tall grass combustion. The higher fire intensity of grass vs. wood combustion that can drive the formation of ice-active minerals is a likely factor that explains this important difference.
- Soil and/or roots may contribute to the INPs and IN activity of particles produced by biomass burning.
- Wiregrass BBA is the only sample we studied to be negatively impacted by aging of the aerosol, possibly resulting from the significant amount of SOA produced, whereas the other grasses produced much less or no SOA under similar aging. Soluble SOA mass condensed on the particles that depresses the freezing point of INP-containing droplets is one possible explanation. The large amount of condensed SOA may have also prevented the oxidation of soot particle surfaces that appears to enhance freezing ability.
- Our new microfluidic droplet freezing device provides very low background temperature freezing that is critical for measuring INPs in BBA experiments, but may suffer from inconsistent particle number per droplet due to the small nanoliter droplet volumes used.

7 Conclusions

In this dissertation I used the cold stage (CMU-CS) that I designed to measure the ice nucleating ability of various particle types relevant to the atmosphere and investigate what makes these particles ice-active. I used the cold stage to measure the ice nucleation of pure water and found that different substrates and water sources are more or less suitable for these ice nucleation measurements. I also tested the ice nucleating ability of Snomax as a standard for biological ice nucleation, but found that it is not time stable and its activity can be altered by freeze-thaw cycling. I examined the ice nucleating ability of ash particles from biomass combustion and found that mineral phases from higher efficiency combustion, particularly from grass burns, are the most likely candidates for ice nucleation in ash. Additionally, I found that ice active soil minerals are able to survive the combustion process and still possess ice nucleating ability. In measuring the effects of aging on ice nucleating particles from biomass burning aerosol I found several cases in which aerosols were stronger INPs upon aging and another case where the opposite was true.

In Chapter 3, I discuss the topic of elevated freezing of pure water and how throughout the use of the CMU-CS we have suffered with bouts of water contamination from various unexpected sources that cause droplets to freeze at artificially high temperatures and thus interfere with droplet freezing assays of particle systems of interest. I explore many of the tests I performed to navigate these contamination issues and find solutions to improve these droplet freezing methods. I found that oil-immersed droplet-on-substrate methods provide the best results using the CMU-CS. However, a new microfluidic approach provides even superior results with background freezing temperatures of pure water droplets near the homogeneous freezing limit for most droplets,

far better than any droplet-on-substrate method that I explored. In particular, I found that gold substrates upon first use provide the least ice-active surface, while Vaseline-coated surfaces are especially prone to contamination due to non-uniform coating. I have provided a list of considerations for all ice nucleation researchers to follow during droplet freezing experiments and in representing their data. These considerations are intended to promote an open discussion and transparency around the limitations of various substrate-based ice nucleation techniques and encourage the ice nucleating community to share their methods for dealing with these limitations and experimental artifacts, and method improvements that are developed along the way.

As discussed in Chapter 4, I started testing the CMU-CS with a proposed standard for biological ice nucleating particles, Snomax. However, I found that Snomax was not as consistent as was previously suggested. In these experiments Snomax did not maintain its strongest ice nucleating proteins with extended storage or repeated removal from the freezer. It also did not maintain the strongest IN proteins when it was frozen multiple times in squalene oil. This finding was the first time that the ice-activity of Snomax was found to degrade over time during storage and use. Interestingly, I found that the weaker ice nucleating proteins do not seem to be degraded or removed, which suggests that these weaker protein monomers are much more stable or less hydrophilic compared to the larger more ice-active protein aggregates. In performing this work, I established that Snomax may be a surrogate for biological ice nucleation, but it should be used with caution.

I then used the CMU-CS to measure the ice nucleating properties of ash generated by the combustion of various biomass fuels in Chapter 5. Ash has only recently been examined as a potential ice nucleating particle and in these studies the wood fuel used is

burned using a high-efficiency stove [Umo *et al.*, 2015]. However, these ashes will not necessarily have the same characteristics to ashes produced in wildfires, especially when the fuel in the wildfire is a grass. In this dissertation I found that ashes from grass burns are more ice-active than ashes from wood burns. Using XRD I discovered that the amount of crystalline material was much higher for grasses than for the wood ashes analyzed. I found that the ice activity and the more crystalline nature of the grass ash was similar to the results found in Umo *et al.* [2016] for domestic wood combustion. This suggests that the higher efficiency of the grass burn is similar to the high-efficiency stoves used in the Umo *et al.* study. Thus, the crystalline phases produced by the combustion are the probable explanation for the higher ice-activity of ash from tall grass and higher efficiency wood burning. However, under less efficient conditions, wood are likely to produce ash that is more similar in nature to my wood combustion ash, which was found to be essentially inactive, due to the lack of crystalline material present. One type of grass was burned with soil added to it to investigate the survivability of soil particles and their ice nuclei through the combustion event. I found that ashes generated from the grass plus soil burn still possessed some high temperature ice-active particles similar to the soil alone in an unburned state. These findings suggest that high temperature combustion can create crystalline particles that can act as INPs and that soil particles are able to maintain their strong ice nucleating abilities despite experiencing combustion conditions.

In Chapter 6 I discuss my measurements of the freezing temperature and ice active site density spectra of INPs emitted in biomass burning smoke and investigated the impact that simulated atmospheric oxidative aging has on these emissions. This is a field that has not been explored directly aside from several studies that have explored the effects of long

range transport on ice nucleating particles emitted by biomass burning and probed oxidation effects on soot surfaces [Dymarska *et al.*, 2006; Prenni *et al.*, 2012]. No one has previously examined the impact of aging on real biomass burning smoke in a controlled manner. I found that in most cases the ice-activity of BBA from tall grass combustion was enhanced by oxidative aging. This is most likely caused by the oxidation of soot particles surfaces in the BBA, which enhances ice-activity by increasing the hydrophilicity of the soot surface. I found, similar to the ash, that wood BBA is a weaker ice nucleant than grass BBA. This finding could suggest that the larger ash and smaller aerosol particles produced in biomass burning are more similar than previously realized. Whether these are related or not will be discussed as a potential future direction. The wood burns tended to produce more fractal, soot-rich aerosol, while the grasses produced a fair amount of organic compounds as well as soot. Aging did not affect the initially low ice-activity of the wood BBA. Additionally, I explore some initial measurements using the microfluidic device. The lower background freezing temperature (also discussed in Chapter 3) provides a useful measurement technique because of the weak ice nucleating ability of BBA. These results showed some inconsistencies in freezing behavior. Specifically, multiple freezes of the same sample of BBA produced variable droplet populations containing the particles. This finding suggests that the method is able to measure very low particle concentrations, but more work needs to be done to understand how this can be extrapolated to the overall ice activity of the sample. The differences appear to be related to inconsistencies in the particle concentration contained within each nanoliter microfluidic droplet more than the particles' actual ice-activity.

7.1 Future Directions

There are still many unanswered questions surrounding this research into the nature of ice nucleating particles emitted by biomass burning. One of the biggest open questions stems from the impacts of chemical aging on the ice nucleants present in biomass burning aerosol. Some of the experiments I performed showed moderate increases in ice-activity caused by oxidation, but not all results were consistent. Specifically, in the case of wiregrass which showed a decrease in INPs, while other burns produced no INPs at all. To explore this more thoroughly, experiments should be conducted more meticulously. For instance, burning a single type of grass and measuring the ice-activity for each of the different aging mechanisms (i.e. dark ozonolysis, OH+UV, and thermodenuder and OH+UV). Also making sure to, as much as possible, keep burning conditions (e.g. particle number, fuel burned) consistent is important to improving reproducibility.

Another major question that comes out of this dissertation is the potential impact of mineral phases produced by biomass burning. I found that mineral phases in ash are the most probable source of INP in ash, and I also found that aerosols have similar activity to what was found in the ashes. This finding could suggest that the aerosol is in some way connected to the mineral phases in the ash. It is important but difficult for us to understand whether the aerosol emitted from biomass burning contains these ash particles. One way to do so could be by using a laser ablation single-particle mass spectrometer, such as the LAAPTOF, to observe in real time the inorganic particle composition present in the aerosol. Additionally, SEM-EDX could be used to examine the structure and physicochemical properties of individual aerosol particles and to compare their composition to ash particles. These measurements could identify if suspended ash mineral

particles is responsible at all for the ice nucleation ability of BBA. The similar trends I see between the ice-activity of the ash and aerosol and the weak ice-activity of ash and BBA from wood versus ash suggest that there may be some ash mineral components acting as INP in the aerosol as well. If that is the case, then this would be the first time anyone has described the IN activity of BBA in relation to the ash produced by the burn.

More work should be done towards understanding the role of soil particles in biomass burning emissions. I have shown that the ice nuclei in soil particles can survive the combustion process, but I have not been able to show that soil aerosol particles are definitely generated by burns. This work could require larger fuel beds with more soil than I used in my experiments. To test for the existence of soil in the aerosol a tracer approach could be applied. For instance, spiking a soil sample with a mineral that will survive the combustion conditions and is not found in the fuel could be one way to check for the presence of soil particles in the emissions. A few studies have found soil markers in BBA, and if these soil components can be shown to cause elevated ice nucleating particles and ice-activity in BBA that will be an important novel finding [Maudlin *et al.*, 2015; Schlosser *et al.*, 2017].

8 Appendix A

This section contains the Igor Pro code I have designed over the course of this thesis to analyze droplet freezing spectra and perform statistics for all figures included above.

8.1 Temperature Calibrations

This section of code is used to perform temperature calibrations using the most current iteration of the CMU-CS.

```
#pragma rtGlobals=3          // Use modern global access method and strict wave access.

Function TempCalsNew()
    Coldplate()
    TEC()
    T1()
    //    T2()
end
Function Coldplate()
    wave ColdplateTime
    wave ColdplateTemp

    variable i = 0
    variable sizeCP = dimSize(ColdplateTime,0)
    variable newSize = trunc(dimSize(ColdplateTime,0)/30)

    Make/O/N=(sizeCP) modColdplate

    Make/O/N=(newSize) finalTime
    Make/O/N=(newSize) finalCP

    variable j = 0 //counts the FinalTime wave
    variable counter = 0 //this holds the place of i as it goes through the loops

    for (j = 0; j < newSize; j += 1) //Works through FinalTime/finalCP
        for (i = counter; i < sizeCP; i += 1) //works through the Coldplate times
            and temps
                //This divides all times into 30 second intervals; if 0 then time is
                XX:XX:00 or XX:XX:30
                modColdplate [i] = round(mod(ColdplateTime[i], 30))

                if (modColdplate [i] == 0)
                    finalTime[j] = ColdplateTime[i]
                    finalCP [j] = ColdplateTemp[i]
                    counter = i+1
```

```

                                break
                            endif
                        endfor
                    endfor
end
////////////////////////////////////
Function TEC()
    wave TECTime
    wave TECTemp
    wave finalTime

    variable i = 0
    variable sizeTEC = dimSize(TECTime,0)
    variable newSize = dimSize(finalTime,0)

    Make/O/N=(sizeTEC) modTEC
    Make/O/N=(sizeTEC) quotTEC

    Make/O/N=(newSize) finalTEC

    variable j = 0 //counts the FinalTime wave
    variable counter = 0 //this holds the place of i as it goes through the loops
    variable quotFinal

    for (j = 0; j < newSize; j += 1) //Works through FinalTime/finalTEC
        quotFinal = trunc(finalTime[j]/30)
        for (i = counter; i < sizeTEC; i += 1) //works through the TEC times and
temps
            //This divides all times into 30 second intervals; if 0 then time is
            XX:XX:00 or XX:XX:30
            modTEC [i] = round(mod(round(TECTime[i]), 30))
            //This will be used to compare to the FinalTime
            quotTEC [i] = trunc(TECTime[i]/30)

            if (modTEC [i] == 0 && quotTEC[i] == quotFinal)
                finalTEC [j] = TECTemp[i]
                counter = i+1
                break
            elseif(quotTEC[i] == quotFinal && modTEC[i] == 1) //TEC temp
is passed the FinalTemp
                finalTEC [j] = (TECTemp[i] + TECTemp[i-1])/2
                counter = i + 1
                break
            elseif(quotTEC[i] == quotFinal-1 && modTEC[i] == 29 &&
modTEC[i+1] != 0)

```

```

        finalTEC[j] = TECTemp[i]
        counter = i + 1
        break
    elseif(quotTEC[i] == quotFinal && modTEC[i] > 1)
        print "error missing TEC data at ", finalTime[j]
        break
    endif
endfor
endfor
end

////////////////////////////////////

Function T1()
    wave T1Time
    wave T1Temp
    wave finalTime

    variable i = 0
    variable sizeT1 = dimSize(T1Time,0)
    variable newSize = dimSize(finalTime,0)

    Make/O/N=(sizeT1) modT1
    Make/O/N=(sizeT1) quotT1

    Make/O/N=(newSize) finalT1

    variable j = 0 //counts the FinalTime wave
    variable counter = 0 //this holds the place of i as it goes through the loops
    variable quotFinal

    for (j = 0; j < newSize; j += 1) //Works through FinalTime/finalT1
        quotFinal = trunc(finalTime[j]/30)
        for (i = counter; i < sizeT1; i += 1) //works through the T1 times and
            temps
                //This divides all times into 30 second intervals; if 0 then time is
                XX:XX:00 or XX:XX:30
                modT1 [i] = round(mod(round(T1Time[i]), 30))
                //This will be used to compare to the FinalTime
                quotT1 [i] = trunc(T1Time[i]/30)

                if (modT1 [i] == 0 && quotT1[i] == quotFinal)
                    finalT1 [j] = T1Temp[i]
                    counter = i+1
                    break
                endif
            endfor
        endfor
    endfor
end

```

```

elseif(quotT1[i] == quotFinal && modT1[i] == 1) //T1 temp is
passed the FinalTemp
    finalT1 [j] = (T1Temp[i] + T1Temp[i-1])/2
    counter = i + 1
    break
elseif(quotT1[i] == quotFinal-1 && modT1[i] == 29 &&
modT1[i+1] != 0)
    finalT1[j] = T1Temp[i]
    counter = i + 1
    break
elseif(quotT1[i] == quotFinal && modT1[i] > 1)
    print "error missing T1 data at ", finalTime[j]
    break
endif
endfor
endfor
end

```

```

////////////////////////////////////

```

```

Function T2()

```

```

    wave T2Time
    wave T2Temp
    wave finalTime

```

```

    variable i = 0
    variable sizeT2 = dimSize(T2Time,0)
    variable newSize = dimSize(finalTime,0)

```

```

    Make/O/N=(sizeT2) modT2
    Make/O/N=(sizeT2) quotT2

```

```

    Make/O/N=(newSize) finalT2

```

```

    variable j = 0 //counts the FinalTime wave
    variable counter = 0 //this holds the place of i as it goes through the loops
    variable quotFinal

```

```

    for (j = 0; j < newSize; j += 1) //Works through FinalTime/finalT2
        quotFinal = trunc(finalTime[j]/30)
        for (i = counter; i < sizeT2; i += 1) //works through the T2 times and

```

```

temps

```

```

        //This divides all times into 30 second intervals; if 0 then time is
        XX:XX:00 or XX:XX:30
        modT2 [i] = round(mod(round(T2Time[i], 30))

```



```

//This will be used to compare to the FinalTime
quotT2 [i] = trunc(T2Time[i]/30)

if (modT2 [i] == 0 && quotT2[i] == quotFinal)
    finalT2 [j] = T2Temp[i]
    counter = i+1
    break
elseif(quotT2[i] == quotFinal && modT2[i] == 1) //T2 temp is
passed the FinalTemp
    finalT2 [j] = (T2Temp[i] + T2Temp[i-1])/2
    counter = i + 1
    break
elseif(quotT2[i] == quotFinal-1 && modT2[i] == 29 &&
modT2[i+1] != 0)
    finalT2[j] = T2Temp[i]
    counter = i + 1
    break
elseif(quotT2[i] == quotFinal && modT2[i] > 1)
    print "error missing T2 data at ", finalTime[j]
    break
endif
endfor
endfor
end
////////////////////////////////////

```

8.2 Post analysis

This section of code is used to get the raw data into a useful formation as well as calculate FF, calibrated temperatures, and *CINP*.

```

#pragma rtGlobals=3          // Use modern global access method and strict wave access.

function RunThis()
    Make/D Additional_Radius_Information
    wave Radii
    Additional_Radius_Information[2] = mean(Radii)
    wave Temperature, Frozen_Fraction, Droplets_Frozen
    TempCal(Temperature, Frozen_Fraction, Droplets_Frozen)
    wave Tactual, Cum_Frozen
    TempInterpolate (Tactual, Frozen_Fraction)//, Cum_Frozen)
    FFInterpolate (Tactual, Frozen_Fraction)
    wave FFAllTemp, FFAllFF
    BWPlotData(FFAllTemp,FFAllFF)
    wave AllTemp, AllFF, Additional_Radius_Information
    CIN(AllTemp, AllFF, Additional_Radius_Information)
    wave StepTemp, StepFF
    CINSTEP(StepTemp, StepFF, Additional_Radius_Information)

```

```
//Corrects the temperature of a curve based on a given calibration
Function TempCal(Temperature, Frozen_Fraction, Droplets_Frozen)
    wave Temperature
    wave Frozen_Fraction
    wave Droplets_Frozen

    Duplicate/O Temperature, Tactual
    Duplicate/O Frozen_Fraction, Cum_Frozen
    variable frozen = Droplets_Frozen[0]

    variable i
    variable size = dimSize(Temperature,0)

    for (i = 0; i < size; i += 1)
//      Old calibrations
//      if (Temperature[i] >= 0)
//          Tactual[i] = Temperature[i] + 1.2
//      elseif (Temperature[i] >= -10)
//          Tactual[i] = Temperature[i] + 1.7
//      elseif (Temperature[i] >= -20)
//          Tactual[i] = Temperature[i] + 1.95
//      elseif (Temperature[i] >= -30)
//          Tactual[i] = Temperature[i] + 2.15
//      else
//          Tactual[i] = Temperature[i] + 2.25
//      endif
//      //Old coldplate simple calibration
//      Tactual[i] = 0.945*Temperature[i] - 0.35 //Calibration in squalene using
//      MilliQ water from 12/2016 averaged between
//      //T1 and T2
//      intercepts weighting T1 greater as it was near center of dish

//      Tactual[i] = 0.965*Temperature[i] - 0.1 //Calibration in squalene from
//      4/11/17-4/12/17 Same slope for both, intercept taken as the middle of both
//      Tactual[i] = 0.95027*Temperature[i] + 0.65916 //Calibration after a
//      weekend of TEC being hot. Slight change in TEC efficacy.7/10/17
//      Tactual[i] = 0.897825*Temperature[i] -1.2 //Calibration with soaking 600
//      s, at the start of the acrylic chamber 9/14/17 done in EXCEL
//      Tactual[i] = 0.92257*Temperature[i] + -1.2839 //Cal done after another
//      warm weekend 3/12/18 Slope has changed with the addition of soaking for last few
//      months
//      Tactual[i] = 0.9265*Temperature[i] + -1.0553 //3/14/18
```

```

        //      Tactual[i] = 1.0712*Temperature[i] - 1.5137 //Calibration for PDMS
(Tom's)
    endfor

    Cum_Frozen = Frozen_Fraction * frozen
end

//Creates waves of 0.5 degree interval temperature data, and interpolates the frozen
fraction.
function TempInterpolate (Tactual, Frozen_Fraction)//, Cum_Frozen)
    wave Tactual
    wave Frozen_Fraction
    //wave Cum_Frozen

    Make/O/N=81 AllTemp //will include all 0.5 temperature intervals between 0 and
-40
    Make/O/N=81 AllFF //corresponding frozen fraction values
    AllTemp = p*-0.5

    variable Alli //index of the AllTemp
    variable dataIndex //counter for tactual/cumfrozen/frozenfraction
    variable dataSize = dimSize(Tactual,0)
    variable dataSlope //slope between current and next point
    variable frac0 //theoretical y intercept of the slope between current point and next
point

    //Interpolating FF for all intervalled temps
    for(dataIndex = 0; dataIndex < dataSize; dataIndex += 1)
        dataSlope = (Frozen_Fraction[dataIndex+1] -
Frozen_Fraction[dataIndex])/(Tactual[dataIndex+1]-Tactual[dataIndex])
        frac0 = Frozen_Fraction[dataIndex] - dataSlope * Tactual[dataIndex]

        for(Alli = 0; Alli < 81; Alli += 1)
            if (AllTemp[Alli] < Tactual[dataIndex] && AllTemp[Alli] >=
Tactual[dataIndex+1])
                AllFF[Alli] = dataSlope * AllTemp[Alli] + frac0
            elseif (AllTemp[Alli] < Tactual[dataIndex])
                AllFF[Alli] = 1
            endif
        endfor

    endfor

    Make/O/N=81 StepTemp //will include all 0.5 temperature intervals between 0
and -40
    Make/O/N=81 StepFF //corresponding frozen fraction values

```

```

StepTemp = p*-0.5
variable stepIndex, Allstepi

//Stepping the FF with each temp
for(stepIndex = 0; stepIndex < dataSize; stepIndex += 1)

    for(Allstepi = 0; Allstepi < 81; Allstepi += 1)
        if (StepTemp[Allstepi] < Tactual[stepIndex] &&
StepTemp[Allstepi] >= Tactual[stepIndex+1])
            StepFF[Allstepi] = Frozen_Fraction[stepIndex]
        elseif (StepTemp[Allstepi] < Tactual[stepIndex])
            StepFF[Allstepi] = 1
        endif
    endfor

endfor

end

//Creates a wave of 0.05 fraction intervals for the frozen fraction and interpolates
temperature
function FFInterpolate (Tactual, Frozen_Fraction)
    wave Tactual
    wave Frozen_Fraction

    Make/O/N=20 FFAllTemp = 0 //corresponding temp values
    Make/O/N=20 FFAllFF = 0 //will include all 0.05 FF intervals between 0 and 1
    FFAllFF = (p+1)*0.05

    variable FFi //index of the FFAllFF
    variable dataIndex //counter for tactual/cumfrozen/frozenfraction
    variable dataSize = dimSize(Tactual,0)
    variable dataSlope
    variable frac0

    for(dataIndex = 0; dataIndex < dataSize; dataIndex += 1)
        dataSlope = (Frozen_Fraction[dataIndex+1] -
Frozen_Fraction[dataIndex])/(Tactual[dataIndex+1]-Tactual[dataIndex])
        frac0 = Frozen_Fraction[dataIndex] - dataSlope * Tactual[dataIndex]

        for(FFi = 0; FFi < 20; FFi += 1)
            if (FFAllFF[FFi] >= Frozen_Fraction[dataIndex] &&
FFAllFF[FFi] <= Frozen_Fraction[dataIndex+1])
                FFAllTemp[FFi] = (FFAllFF[FFi] - frac0) / dataSlope
            endif
        endfor
    endfor
endfunction

```

```

1)                                     if (FFAllFF[FFi] == 1 && Frozen_Fraction[dataIndex] ==
                                     FFAllTemp[FFi] = Tactual[dataIndex]
                                     endif
                                     endif
                                     endfor
                                     endfor
end

```

//Outputs box and whisker plot values for any FFAllTemp and FFAllFF curves

Function BWPlotData(FFAllTemp, FFAllFF, [numPlots, plotNum])

```

    wave FFAllTemp, FFAllFF
    variable numPlots, plotNum
    variable plotHeight

```

```

    if (!ParamIsDefault(numPlots))
        plotHeight = plotNum/numPlots
    else
        plotHeight = 0
    endif

```

```

    Make/O/N=5 BWPlotFF = {0.10,0.25,0.50,0.75,0.90}
    Make/O/N=5 BWPlotTemp
    Make/O/N=5 BWPlotter

```

```

    BWPlotter[p] = plotHeight

```

```

    variable i
    BWPlotTemp[0]= FFAllTemp[1]
    BWPlotTemp[1]= FFAllTemp[4]
    BWPlotTemp[2]= FFAllTemp[9]
    BWPlotTemp[3]= FFAllTemp[14]
    BWPlotTemp[4]= FFAllTemp[17]

```

```

end

```

//Mimics Markus Petters (Hader 2014) analysis of concentration if IN per volume, will work with PW and samples

//Outputs Cinp, the amount of ice nucleating stuff per mL of the sample

Function CIN(AllTemp, AllFF, Additional_Radius_Information)

```

    wave AllTemp, AllFF, Additional_Radius_Information
    Make/N = 1 DropVolume
    //0.8x zoom is 96 px/mm

```

```

//0.9x zoom is 106 px/mm
//1x zoom is 123 px/mm
variable PixPermm = 96
DropVolume[0] = (4/3*PI*(Additional_Radius_Information[2] / PixPermm
*1000)^3)*10^-12 //mL
//((4/3*PI*averageRadius^3)*10^-12)

variable size = dimSize(AllFF,0)
Make/N = (size) IN_conc_permL
Duplicate/O AllTemp, Temp_CIN

IN_conc_permL = -ln(1 - AllFF)/(DropVolume[0]) //per mL

//Make/N = 81 CINCorrect = IN_conc_permL Sample - IN_conc_permL PW

end

//Mimics Markus Petters (Hader 2014) analysis of concentration if IN per volume, will
work with PW and samples
//Outputs CinpStep, the Cinp using stepped FF and Temperature data. Same function,
different inputs and outputs (for RunThis())
Function CINSTep(StepTemp, StepFF, Additional_Radius_Information)
    wave StepTemp, StepFF, Additional_Radius_Information
    Make/N = 1 DropVolumeStep
    //0.8x zoom is 96 px/mm
    //0.9x zoom is 106 px/mm
    //1x zoom is 123 px/mm
    variable PixPermm = 96 //pixels per mm
    DropVolumeStep[0] = (4/3*PI*(Additional_Radius_Information[2] / PixPermm
*1000)^3)*10^-12 //mL
    //((4/3*PI*averageRadius^3)*10^-12)

    variable size = dimSize(StepFF,0)
    Make/N = (size) IN_conc_permLStep
    Duplicate/O StepTemp, Temp_CINStep

    IN_conc_permLStep = -ln(1 - StepFF)/(DropVolumeStep[0]) //per mL

    //Make/N = 81 CINCorrect = IN_conc_permL Sample - IN_conc_permL PW
    This will do the difference between sample and water per array

end

Function CINCorrect(CIN, CINPW)
    wave CIN, CINPW
    variable correctionIndex

```

Make/N = 81 CINCorrected = CIN - CINPW

end

//Sample code: Saves a picture, copy into the console and change the name of the png file
SavePICT/S/EF=1/E=-5/I/RES=300/W=(0,0,0,0) as "TempCal_041217.png"

//Sample code for graphing

//Plot all FF data on same plot, need to edit the inputs here
//Mode 3 changes to markers, marker 8 changes to circles, msize 5 changes circle radius,
mrkThick 2 changes the circle thickness
ModifyGraph mode=3,marker=8,msize=5,mrkThick=2;DelayUpdate
//ModifyGraph rgb(frac3)=(16384,65280,16384) //Changes color
Legend //Creates a legend
ModifyGraph fSize=14,axThick=1.5;DelayUpdate //Sets font size and axis thickness
Label left "\\Z14Frozen Fraction";DelayUpdate //Sets the y-axis label
Label bottom "\\Z14Temperature (°C)";DelayUpdate //Sets the x-axis label
SetAxis left 0,1;DelayUpdate //Sets the y-axis range
ModifyGraph minor=1;DelayUpdate //Adds minor ticks
SetAxis bottom -40,0;DelayUpdate //Sets x-axis range
ModifyGraph margin(right)=20 //Sets margin size
Legend/C/N=text0/J/X=6.00/Y=2.00
Legend/C/N=text0/J/B=1
Legend/C/N=text0/J/F=0

//Plots INAS data on single graph, need to edit the inputs here
Legend
ModifyGraph mode=3,marker=8,msize=5,mrkThick=2;DelayUpdate
//ModifyGraph rgb(frac3)=(16384,65280,16384)
ModifyGraph fSize=14,axThick=1.5;DelayUpdate
Label left "\\Z14Active Sites (mg\\S-1\\M\\Z14)";DelayUpdate //Label left "\\Z14INP
(L\\S-1\\M\\Z14)"
Label bottom "\\Z14Temperature (°C)";DelayUpdate
SetAxis left 1,1000000000;DelayUpdate
ModifyGraph minor=1;DelayUpdate
SetAxis bottom -40,0;DelayUpdate
ModifyGraph margin(right)=20
Legend/C/N=text0/J/X=6.00/Y=2.00
Legend/C/N=text0/J/B=1

8.3 Active site density calculations

This section of code is used to calculate n_s and n_m for different types of samples measured over the course of this dissertation.

```
#pragma rtGlobals=3          // Use modern global access method and strict wave access.

//ns for suspensions of sample
function ns_suspensions(INPcorr, Temp, massPercent, DropVolume, BET)
wave INPcorr, Temp, DropVolume //INPcorr is IN_conc_permL
variable massPercent, BET //BET in cm2/g

Make/O/N = (1) SA_sus = massPercent * DropVolume[0] * BET
Make/O/N = (1) Mass_sus = massPercent * DropVolume[0]
variable size = dimSize(INPcorr,0)
Make/O/N = (size) ns_susp = INPcorr*DropVolume[0] / SA_sus[0] //unit based on BET
value //Volume is removed from INP to not double it.
Make/O/N = (size) nm_susp = INPcorr*DropVolume[0] / Mass_sus[0]

end

//This will retrieve SA from SMPS data for BBA burns or other chamber experiments.
//To run make sure the data is just the data you need for specific runs (e.g. aged/fresh)
function GetSA_nsRefined(Total_Conc__nm__cm__, Start_Time, INPcorr,
FlowRate_cm,averageVol, volWashWater)
    wave Total_Conc__nm__cm__ //nm^2/cm^3
    wave Start_Time
    wave INPcorr                //This is the already corrected INP
concentration after background subtraction of water, already volume corrected
    variable FlowRate_cm        //cm^3/min (around 1800-2000)
    variable averageVol //calculated elsewhere in CIN it's in mL
    variable volWashWater //Volume of wash water used to extract filters/impinger
final volume (mL) usually 3 mLs
    variable scanTime = 2 //Time per scan for the SMPS in minutes

//    variable volumemL = ((4/3*PI*averageRadius^3)*10^-12) ///converts from radius
to volume in mL, mL per drop

    Make/O/N = (1) SA                //nm^2
    Make/O/N = (1) SAperDrop //nm^2

    SA = sum(Total_Conc__nm__cm__) * scanTime * FlowRate_cm
    SAperDrop = SA * averageVol / volWashWater //gives the total amount of SA of
particle per droplet in the array

    variable index
    variable size = dimSize(INPcorr,0)
    Make/O/N = (size) ns = INPcorr / SAperDrop[0] * averageVol
```



```

        Make/O/N = (size) nscm = ns * 10^14 // 1cm^2 = 10^14 nm^2
//      Make/O/N = (size) ns_A

```

```

//      ns_A = ns*S_AperDrop

```

```

end

```

8.4 Statistical Analysis

This section of code is used to perform different types of statistical analysis used in this dissertation.

```

#pragma rtGlobals=3          // Use modern global access method and strict wave access.

```

```

//The FF must be a stepFF in order to work correctly

```

```

Function CombiningData(AllTemp, FF1, DropNum1, FF2, DropNum2//, FF3,
DropNum3, FF4, DropNum4//, FF5, DropNum5, FF6, DropNum6, FF7, DropNum7,
FF8, DropNum8, FF9, DropNum9, FF10, DropNum10, FF11, DropNum11, FF12,
DropNum12, FF13, DropNum13)

```

```

    wave AllTemp, FF1, DropNum1, FF2, DropNum2//, FF3, DropNum3, FF4,
DropNum4//, FF5, DropNum5, FF6, DropNum6, FF7, DropNum7, FF8, DropNum8,
FF9, DropNum9, FF10, DropNum10, FF11, DropNum11, FF12, DropNum12, FF13,
DropNum13

```

```

    variable size = dimSize(AllTemp,0)

```

```

    Make/O/N=(size) CombineTemp = AllTemp

```

```

    Make/O/N=(size) AllCum1 = FF1*DropNum1[0]

```

```

    Make/O/N=(size) AllCum2 = FF2*DropNum2[0]

```

```

//    Make/O/N=(size) AllCum3 = FF3*DropNum3[0]

```

```

//    Make/O/N=(size) AllCum4 = FF4*DropNum4[0]

```

```

//    Make/O/N=(size) AllCum5 = FF5*DropNum5[0]

```

```

//    Make/O/N=(size) AllCum6 = FF6*DropNum6[0]

```

```

//    Make/O/N=(size) AllCum7 = FF7*DropNum7[0]

```

```

//    Make/O/N=(size) AllCum8 = FF8*DropNum8[0]

```

```

//    Make/O/N=(size) AllCum9 = FF9*DropNum9[0]

```

```

//    Make/O/N=(size) AllCum10 = FF10*DropNum10[0]

```

```

//    Make/O/N=(size) AllCum11 = FF11*DropNum11[0]

```

```

//    Make/O/N=(size) AllCum12 = FF12*DropNum12[0]

```

```

//    Make/O/N=(size) AllCum13 = FF13*DropNum13[0]

```

```

//

```

```

    Make/O/N=(size) AllCount1 = AllCum1[p] - AllCum1[p-1]

```

```

    Make/O/N=(size) AllCount2 = AllCum2[p] - AllCum2[p-1]

```

```

//    Make/O/N=(size) AllCount3 = AllCum3[p] - AllCum3[p-1]

```

```

//    Make/O/N=(size) AllCount4 = AllCum4[p] - AllCum4[p-1]

```

```

//    Make/O/N=(size) AllCount5 = AllCum5[p] - AllCum5[p-1]

```

```

//      Make/O/N=(size) AllCount6 = AllCum6[p] - AllCum6[p-1]
//      Make/O/N=(size) AllCount7 = AllCum7[p] - AllCum7[p-1]
//      Make/O/N=(size) AllCount8 = AllCum8[p] - AllCum8[p-1]
//      Make/O/N=(size) AllCount9 = AllCum9[p] - AllCum9[p-1]
//      Make/O/N=(size) AllCount10 = AllCum10[p] - AllCum10[p-1]
//      Make/O/N=(size) AllCount11 = AllCum11[p] - AllCum11[p-1]
//      Make/O/N=(size) AllCount12 = AllCum12[p] - AllCum12[p-1]
//      Make/O/N=(size) AllCount13 = AllCum13[p] - AllCum13[p-1]

      Make/O/N=(size) CombineCount =
AllCount1+AllCount2//+AllCount3+AllCount4//+AllCount5+AllCount6+AllCount7+All
Count8+AllCount9+AllCount10+AllCount11+AllCount12+AllCount13
      Make/O/N=1 CombineDrop =
DropNum1+DropNum2//+DropNum3+DropNum4//+DropNum5+DropNum6+DropNum
7+DropNum8+DropNum9+DropNum10+DropNum11+DropNum12+DropNum13
      Make/O/N=(size) CombineCum = CombineCount[p]+CombineCum[p-1]
      Make/O/N=(size) CombineFF = CombineCum/CombineDrop
end

```

```

//FFAllFF, FFAllTemp
Function BWStats(temp1, INP1, temp2, INP2)//, temp3,INP3, temp4, INP4)//, temp5,
INP5, temp6, INP6, temp7, INP7)//, temp8, INP8, temp9, INP9, temp10, INP10, temp11,
INP11, temp12, INP12, temp13, INP13)//, temp14, INP14, temp15, INP15, temp16,
INP16, temp17, INP17, temp18, INP18, temp19, INP19, temp20, INP20, temp21,
INP21)//, temp22, INP22, temp23, INP23)//, temp24, INP24//, temp25, INP25, temp26,
INP26)

      wave temp1, INP1, temp2, INP2//, temp3,INP3, temp4, INP4//, temp5, INP5,
temp6, INP6, temp7, INP7//, temp8, INP8, temp9, INP9, temp10, INP10, temp11, INP11,
temp12, INP12, temp13, INP13//, temp14, INP14, temp15, INP15, temp16, INP16,
temp17, INP17, temp18, INP18, temp19, INP19, temp20, INP20, temp21, INP21//,
temp22, INP22, temp23, INP23//, temp24, INP24//, temp25, INP25, temp26, INP26

      variable i
      variable size = dimSize(temp1,0)
      variable entries = 2

      make/o/n=(size) FF = INP1
      make/o/n=(size) Tempavg
      make/o/n=(size) Tempsdev
      make/o/n=(size) TempstdError
      make/o/n=(size) TempmarginError
      ///make/o/n=(size) INPconfidenceUpper
      ///make/o/n=(size) INPconfidenceLower
      make/o/n=(entries) currentINP
      make/o/n=(entries) currentTemp

```

```

    for(i= 0; i < size; i +=1)
        currentTemp[0] = temp1[i]
        currentTemp[1] = temp2[i]
//      currentTemp[2] = temp3[i]
//      currentTemp[3] = temp4[i]
//      currentTemp[4] = temp5[i]
//      currentTemp[5] = temp6[i]
//      currentTemp[6] = temp7[i]
//      currentTemp[7] = temp8[i]
//      currentTemp[8] = temp9[i]
//      currentTemp[9] = temp10[i]
//      currentTemp[10] = temp11[i]
//      currentTemp[11] = temp12[i]
//      currentTemp[12] = temp13[i]
//      currentTemp[13] = temp14[i]
//      currentTemp[14] = temp15[i]
//      currentTemp[15] = temp16[i]
//      currentTemp[16] = temp17[i]
//      currentTemp[17] = temp18[i]
//      currentTemp[18] = temp19[i]
//      currentTemp[19] = temp20[i]
//      currentTemp[20] = temp21[i]
//      currentTemp[21] = temp22[i]
//      currentTemp[22] = temp23[i]
//      currentTemp[23] = temp24[i]
//      currentTemp[24] = temp25[i]
//      currentTemp[25] = temp26[i]

        currentINP[0] = INP1[i]
        currentINP[1] = INP2[i]
//      currentINP[2] = INP3[i]
//      currentINP[3] = INP4[i]
//      currentINP[4] = INP5[i]
//      currentINP[5] = INP6[i]
//      currentINP[6] = INP7[i]
//      currentINP[7] = INP8[i]
//      currentINP[8] = INP9[i]
//      currentINP[9] = INP10[i]
//      currentINP[10] = INP11[i]
//      currentINP[11] = INP12[i]
//      currentINP[12] = INP13[i]
//      currentINP[13] = INP14[i]
//      currentINP[14] = INP15[i]
//      currentINP[15] = INP16[i]
//      currentINP[16] = INP17[i]

```

```

//      currentINP[17] = INP18[i]
//      currentINP[18] = INP19[i]
//      currentINP[19] = INP20[i]
//      currentINP[20] = INP21[i]
//      currentINP[21] = INP22[i]
//      currentINP[22] = INP23[i]
//      currentINP[23] = INP24[i]
//      currentINP[24] = INP25[i]
//      currentINP[25] = INP26[i]

      wavestats/q currentTemp
      Tempavg[i] = V_avg
      Tempsdev[i] = V_sdev
      TempstdError[i] = Tempsdev[i]/sqrt(entries)
      TempmarginError[i] = TempstdError[i] *1.96 //use this for error bars
//      INPconfidenceUpper[i] = INPavg[i] + INPmarginError[i]
//      INPconfidenceLower[i] = INPavg[i] - INPmarginError[i]

    endfor

end

//Stats for Paul FIN data 3/23/17
//These must have equal intervals for all data I think. 10/17/17
//AllIFF, AllTemp, other
Function Stats(temp1, INP1, temp2, INP2, temp3,INP3)//, temp4, INP4, temp5, INP5,
temp6, INP6, temp7, INP7, temp8, INP8, temp9, INP9, temp10, INP10, temp11, INP11,
temp12, INP12, temp13, INP13)//, temp14, INP14, temp15, INP15, temp16, INP16,
temp17, INP17, temp18, INP18, temp19, INP19, temp20, INP20, temp21, INP21)//,
temp22, INP22, temp23, INP23)//, temp24, INP24//, temp25, INP25, temp26, INP26)
    wave temp1, INP1, temp2, INP2, temp3,INP3//, temp4, INP4, temp5, INP5,
temp6, INP6, temp7, INP7, temp8, INP8, temp9, INP9, temp10, INP10, temp11, INP11,
temp12, INP12, temp13, INP13//, temp14, INP14, temp15, INP15, temp16, INP16,
temp17, INP17, temp18, INP18, temp19, INP19, temp20, INP20, temp21, INP21//,
temp22, INP22, temp23, INP23//, temp24, INP24//, temp25, INP25, temp26, INP26

    variable i
    variable size = dimSize(temp1,0)
    variable entries = 3

    make/o/n=(size) Temp = p*-0.5
    make/o/n=(size) INPavg
    make/o/n=(size) INPsdev
    make/o/n=(size) INPstdError

```

```

make/o/n=(size) INPmarginError
////make/o/n=(size) INPconfidenceUpper
////make/o/n=(size) INPconfidenceLower
make/o/n=(entries) currentINP
make/o/n=(entries) currentTemp

for(i= 0; i < size; i +=1)
    currentTemp[0] = temp1[i]
    currentTemp[1] = temp2[i]
    currentTemp[2] = temp3[i]
//    currentTemp[3] = temp4[i]
//    currentTemp[4] = temp5[i]
//    currentTemp[5] = temp6[i]
//    currentTemp[6] = temp7[i]
//    currentTemp[7] = temp8[i]
//    currentTemp[8] = temp9[i]
//    currentTemp[9] = temp10[i]
//    currentTemp[10] = temp11[i]
//    currentTemp[11] = temp12[i]
//    currentTemp[12] = temp13[i]
//    currentTemp[13] = temp14[i]
//    currentTemp[14] = temp15[i]
//    currentTemp[15] = temp16[i]
//    currentTemp[16] = temp17[i]
//    currentTemp[17] = temp18[i]
//    currentTemp[18] = temp19[i]
//    currentTemp[19] = temp20[i]
//    currentTemp[20] = temp21[i]
//    currentTemp[21] = temp22[i]
//    currentTemp[22] = temp23[i]
//    currentTemp[23] = temp24[i]
//    currentTemp[24] = temp25[i]
//    currentTemp[25] = temp26[i]

    currentINP[0] = INP1[i]
    currentINP[1] = INP2[i]
    currentINP[2] = INP3[i]
//    currentINP[3] = INP4[i]
//    currentINP[4] = INP5[i]
//    currentINP[5] = INP6[i]
//    currentINP[6] = INP7[i]
//    currentINP[7] = INP8[i]
//    currentINP[8] = INP9[i]
//    currentINP[9] = INP10[i]
//    currentINP[10] = INP11[i]
//    currentINP[11] = INP12[i]

```

```

//      currentINP[12] = INP13[i]
//      currentINP[13] = INP14[i]
//      currentINP[14] = INP15[i]
//      currentINP[15] = INP16[i]
//      currentINP[16] = INP17[i]
//      currentINP[17] = INP18[i]
//      currentINP[18] = INP19[i]
//      currentINP[19] = INP20[i]
//      currentINP[20] = INP21[i]
//      currentINP[21] = INP22[i]
//      currentINP[22] = INP23[i]
//      currentINP[23] = INP24[i]
//      currentINP[24] = INP25[i]
//      currentINP[25] = INP26[i]

      wavestats/q currentINP
      INPavg[i] = V_avg
      INPsdev[i] = V_sdev
      INPstdError[i] = INPsdev[i]/sqrt(entries)
      INPmarginError[i] = INPstdError[i] *1.96 //use this for error bars
//      INPconfidenceUpper[i] = INPavg[i] + INPmarginError[i]
//      INPconfidenceLower[i] = INPavg[i] - INPmarginError[i]

    endfor

end

```

```

//Function GetListofShit() //Courtesy of E-Dog
//      setdatafolder root:
//
//      //print StringList("*", ";")
//
//      string test = DataFolderDir(1)
//      //print test
//      test = stringfromlist(1,test,":")
//      test = stringfromlist(0,test,";")
//      //print test
//      //string test2 = stringfromlist()
//      variable test2 = itemsinlist(test, ",")
//      variable i
//      string test3
//
//      make/o/n=0 compiled_FF
//      make/o/n=0 compiled_Temps

```

```

//
//      display
//      for(i = 0 ; i < test2 ; i+=1)
//          test3 = stringfromlist(i,test,"")
//          string test4 = "root:"+test3+":"
//          setdatafolder $test4
//          wave alltemp = alltemp
//          wave allFF = allFF
//
//          wave compiled_FF = root:compiled_FF
//          concatenate/np {allFF},compiled_FF
//
//          wave compiled_Temps = root:compiled_Temps
//          concatenate/np {allTemp},compiled_Temps
//
//          //appendtograph allFF vs allTemp
//      endfor
//      setdatafolder root:
//
//      display compiled_FF vs compiled_Temps
//
//
//
//end
//
////Makes full waves of all intervalled data and runs stats on them.
//
//function Tester()
//setdatafolder root:
//wave compiled_Temps = root:compiled_Temps
//wave compiled_FF = root:compiled_FF
//
//duplicate/o compiled_Temps storeTemps
//duplicate/o compiled_FF storeFF
//
//variable i,j
//make/o/n=0 compiledFF_sdev
//make/o/n=0 compiledFF_avg
//
//for(i = 0 ; i < (40.5/0.5) ; i +=1)
//    storeTemps[] = compiled_Temps[p] == (-i/2) ? compiled_Temps[p] : Nan
//    storeFF[] = compiled_Temps[p] == (-i/2) ? compiled_FF[p] : Nan
//    wavestats/q storeFF
//    make/o/n=1 Sdev_store
//    Sdev_store = V_sdev
//    make/o/n=1 Avg_store

```

```
//      Avg_store = V_avg
//      concatenate/np {Sdev_store},compiledFF_sdev
//      concatenate/np {Avg_store},compiledFF_avg
//
//
//endfor
//
//
//
//end
```


References

- Ahern, A. T., L. Goldberger, L. Jahl, J. Thornton, and R. C. Sullivan (2018), Production of N_2O_5 and ClNO_2 through Nocturnal Processing of Biomass-Burning Aerosol, *Environ. Sci. Technol.*, *52*(2), 550–559, doi:10.1021/acs.est.7b04386.
- Ahrens, M. (2013), *Brush, Grass, and Forest Fires*, Quincy, MA.
- Akagi, S. K., R. J. Yokelson, C. Wiedinmyer, M. J. Alvarado, J. S. Reid, T. Karl, J. D. Crounse, and P. O. Wennberg (2011), Emission factors for open and domestic biomass burning for use in atmospheric models, *Atmos. Chem. Phys.*, *11*(9), 4039–4072, doi:10.5194/acp-11-4039-2011.
- Alstadt, V. J., J. N. Dawson, D. J. Losey, S. K. Sihvonen, and M. A. Freedman (2017), Heterogeneous Freezing of Carbon Nanotubes: A Model System for Pore Condensation and Freezing in the Atmosphere, *J. Phys. Chem. A*, *121*(42), 8166–8175, doi:10.1021/acs.jpca.7b06359.
- Alvarez, N. J., W. Lee, L. M. Walker, and S. L. Anna (2011), The effect of alkane tail length of CiE8 surfactants on transport to the silicone oil-water interface, *J. Colloid Interface Sci.*, *355*(1), 231–236, doi:10.1016/j.jcis.2010.11.077.
- Amato, P., M. Joly, C. Schaupp, E. Attard, O. Möhler, C. E. Morris, Y. Brunet, and A.-M. Delort (2015), Survival and ice nucleation activity of bacteria as aerosols in a cloud simulation chamber, *Atmos. Chem. Phys.*, *15*(11), 6455–6465, doi:10.5194/acp-15-6455-2015.
- Andreae, M. O., D. Rosenfeld, P. Artaxo, A. Costa, G. Frank, K. Longo, and M. Silva-Dias (2004), Smoking Rain Clouds over the Amazon, *Science* (80-.), *303*(5662), 1337–1342, doi:10.1126/science.1092779.
- Archuleta, C. M., P. J. DeMott, and S. M. Kreidenweis (2005), Ice nucleation by surrogates for atmospheric mineral dust and mineral dust/sulfate particles at cirrus temperatures, *Atmos. Chem. Phys.*, *5*(10), 2617–2634, doi:10.5194/acp-5-2617-2005.
- Atkinson, J. D., B. J. Murray, M. T. Woodhouse, T. F. Whale, K. J. Baustian, K. S. Carslaw, S. Dobbie, D. O’Sullivan, T. L. Malkin, and D. O’Sullivan (2013), The importance of feldspar for ice nucleation by mineral dust in mixed-phase clouds, *Nature*, *498*, 355–358, doi:10.1038/nature12278.
- Attard, E., H. Yang, A.-M. Delort, P. Amato, U. Pöschl, C. Glaux, T. Koop, and C. E. Morris (2012), Effects of atmospheric conditions on ice nucleation activity of *Pseudomonas*, *Atmos. Chem. Phys.*, *12*(22), 10667–10677, doi:10.5194/acp-12-10667-2012.
- Augustin-Bauditz, S., H. Wex, S. Kanter, M. Ebert, D. Niedermeier, F. Stolz, A. Prager, and F. Stratmann (2014), The immersion mode ice nucleation behavior of mineral

- dusts : A comparison of different pure and surface modified dusts, *Geophys. Res. Lett.*, *41*, 7375–7382, doi:10.1002/2014GL061317.
- Augustin-Bauditz, S., H. Wex, C. Denjean, S. Hartmann, J. Schneider, S. Schmidt, M. Ebert, and F. Stratmann (2016), Laboratory-generated mixtures of mineral dust particles with biological substances: characterization of the particle mixing state and immersion freezing behavior, *Atmos. Chem. Phys.*, *16*(9), 5531–5543, doi:10.5194/acp-16-5531-2016.
- Augustin, S. et al. (2013), Immersion freezing of birch pollen washing water, *Atmos. Chem. Phys.*, *13*(21), 10989–11003, doi:10.5194/acp-13-10989-2013.
- Balfour, V. N., and S. W. Woods (2013), The hydrological properties and the effects of hydration on vegetative ash from the Northern Rockies, USA, *CATENA*, *111*, 9–24, doi:10.1016/j.catena.2013.06.014.
- Banfield, J. F., and R. A. Eggleton (1990), Analytical transmission electron microscope studies of plagioclase, muscovite, and K-feldspar weathering, *Clays Clay Miner.*, *38*(1), 77–89.
- Baustian, K. J., M. E. Wise, and M. A. Tolbert (2010), Depositional ice nucleation on solid ammonium sulfate and glutaric acid particles, *Atmos. Chem. Phys.*, *10*(2004), 2307–2317.
- Berkemeier, T., M. Shiraiwa, U. Pöschl, and T. Koop (2014), Competition between water uptake and ice nucleation by glassy organic aerosol particles, *Atmos. Chem. Phys.*, *14*(22), 12513–12531, doi:10.5194/acp-14-12513-2014.
- Beydoun, H., M. Polen, and R. C. Sullivan (2016), Effect of particle surface area on ice active site densities retrieved from droplet freezing spectra, *Atmos. Chem. Phys.*, *16*(20), 13359–13378, doi:10.5194/acp-16-13359-2016.
- Beydoun, H., M. Polen, and R. C. Sullivan (2017), A new multicomponent heterogeneous ice nucleation model and its application to Snomax bacterial particles and a Snomax-illite mineral particle mixture, *Atmos. Chem. Phys.*, *17*(22), 13545–13557, doi:10.5194/acp-17-13545-2017.
- Bi, Y., R. Cabriolu, and T. Li (2016), Heterogeneous ice nucleation controlled by the coupling of surface crystallinity and surface hydrophilicity, *J. Phys. Chem. C*, *120*(3), 1507–1514, doi:10.1021/acs.jpcc.5b09740.
- Bigg, E. K. (1953), The formation of atmospheric ice crystals by the freezing of droplets, *Q. J. R. Meteorol. Soc.*, *79*(342), 510–519, doi:10.1002/qj.49707934207.
- Bithi, S. S., and S. A. Vanapalli (2010), Behavior of a train of droplets in a fluidic network with hydrodynamic traps, *Biomicrofluidics*, *4*(4), 044110, doi:10.1063/1.3523053.
- Bodí, M. B., D. A. Martin, V. N. Balfour, C. Santín, S. H. Doerr, P. Pereira, A. Cerdà, and J. Mataix-Solera (2014), Wildland fire ash: Production, composition and eco-hydrogeomorphic effects, *Earth-Science Rev.*, *130*, 103–127, doi:10.1016/j.earscirev.2013.12.007.

- Boukellal, H., Š. Selimović, Y. Jia, G. Cristobal, and S. Fraden (2009), Simple, robust storage of drops and fluids in a microfluidic device, *Lab Chip*, 9(2), 331–338, doi:10.1039/B808579J.
- Broadley, S. L., B. J. Murray, R. J. Herbert, J. D. Atkinson, S. Dobbie, T. L. Malkin, E. Condliffe, and L. Neve (2012), Immersion mode heterogeneous ice nucleation by an illite rich powder representative of atmospheric mineral dust, *Atmos. Chem. Phys.*, 12, 287–307, doi:10.5194/acp-12-287-2012.
- Brubaker, T., P. Cheng, M. Polen, V. Ekambaram, S. Anna, and R. Sullivan (2018), The Development and Characterization of a “Store and Create” Microfluidic Device to Determine Heterogeneous Freezing Properties of Ice Nucleating Particlestle, *To be Submitt.*
- Budke, C., and T. Koop (2015), BINARY: an optical freezing array for assessing temperature and time dependence of heterogeneous ice nucleation, *Atmos. Meas. Tech.*, 8, 689–703, doi:10.5194/amt-8-689-2015.
- Bundke, U., B. Nillius, R. Jaenicke, T. Wetter, H. Klein, and H. Bingemer (2008), The fast Ice Nucleus chamber FINCH, *Atmos. Res.*, 90(2–4), 180–186, doi:10.1016/j.atmosres.2008.02.008.
- Bunker, K. W., S. China, C. Mazzoleni, a. Kostinski, and W. Cantrell (2012), Measurements of ice nucleation by mineral dusts in the contact mode, *Atmos. Chem. Phys. Discuss.*, 12(8), 20291–20309, doi:10.5194/acpd-12-20291-2012.
- Burkhardt, U., and B. Kärcher (2011), Global radiative forcing from contrail cirrus, *Nat. Clim. Chang.*, 1(1), 54–58, doi:10.1038/nclimate1068.
- Campbell, J. M., F. C. Meldrum, and H. K. Christenson (2015), Is ice nucleation from supercooled water insensitive to surface roughness?, *J. Phys. Chem. C*, 119(2), 1164–1169, doi:10.1021/jp5113729.
- Chen, T., W. B. Rossow, and Y. Zhang (2000), Radiative Effects of Cloud-Type Variations, *J. Clim.*, 13(1), 264–286, doi:10.1175/1520-0442(2000)013<0264:REOCTV>2.0.CO;2.
- Chernoff, D. I., and A. K. Bertram (2010), Effects of sulfate coatings on the ice nucleation properties of a biological ice nucleus and several types of minerals, *J. Geophys. Res.*, 115(March), D20205, doi:10.1029/2010jd014254.
- Choi, S.-J., T.-H. Kwon, H. Im, D.-I. Moon, D. J. Baek, M.-L. Seol, J. P. Duarte, and Y.-K. Choi (2011), A Polydimethylsiloxane (PDMS) Sponge for the Selective Absorption of Oil from Water, *ACS Appl. Mater. Interfaces*, 3(12), 4552–4556, doi:10.1021/am201352w.
- Christian, T. J., B. Kleiss, R. J. Yokelson, R. Holzinger, P. J. Crutzen, W. M. Hao, B. H. Saharjo, and D. E. Ward (2003), Comprehensive laboratory measurements of biomass-burning emissions: 1. Emissions from Indonesian, African, and other fuels, *J. Geophys. Res.*, 108(D23), 4719, doi:10.1029/2003JD003704.
- Christner, B. C., C. E. Morris, C. M. Foreman, R. Cai, and D. C. Sands (2008), Ubiquity

- of biological ice nucleators in snowfall., *Science*, 319(5867), 1214, doi:10.1126/science.1149757.
- Collier, K. N., and S. D. Brooks (2016), Role of Organic Hydrocarbons in Atmospheric Ice Formation via Contact Freezing, *J. Phys. Chem. A*, acs.jpca.6b11890, doi:10.1021/acs.jpca.6b11890.
- Conen, F., C. E. Morris, J. Leifeld, M. V. Yakutin, and C. Alewell (2011), Biological residues define the ice nucleation properties of soil dust, *Atmos. Chem. Phys.*, 11(18), 9643–9648, doi:10.5194/acp-11-9643-2011.
- Connolly, P. J., O. Möhler, P. R. Field, H. Saathoff, R. Burgess, T. Choularton, and M. Gallagher (2009), Studies of heterogeneous freezing by three different desert dust samples, *Atmos. Chem. Phys.*, 9(8), 2805–2824, doi:10.5194/acp-9-2805-2009.
- Cox, S. J., Z. Raza, S. M. Kathmann, B. Slater, and A. Michaelides (2013), The microscopic features of heterogeneous ice nucleation may affect the macroscopic morphology of atmospheric ice crystals, *Faraday Discuss.*, 167, 389, doi:10.1039/c3fd00059a.
- Creamean, J. M. et al. (2013), Dust and Biological Aerosols from the Sahara and Asia Influence Precipitation in the Western U.S., *Science* (80-.), 339(6127), 1572–1578, doi:10.1126/science.1227279.
- Cziczo, D. J., D. M. Murphy, P. K. Hudson, and D. S. Thomson (2004), Single particle measurements of the chemical composition of cirrus ice residue during CRYSTAL-FACE, *J. Geophys. Res. Atmos.*, 109, D04201, doi:10.1029/2003JD004032.
- Cziczo, D. J., L. Ladino, Y. Boose, Z. A. Kanji, P. Kupiszewski, S. Lance, S. Mertes, and H. Wex (2017), Measurements of Ice Nucleating Particles and Ice Residuals, *Meteorol. Monogr.*, 58(April), 8.1-8.13, doi:10.1175/AMSMONOGRAPHS-D-16-0008.1.
- Davis, R. D., S. Lance, J. a. Gordon, and M. a. Tolbert (2015), Long Working-Distance Optical Trap for in Situ Analysis of Contact-Induced Phase Transformations, *Anal. Chem.*, 150522112254007, doi:10.1021/acs.analchem.5b00809.
- DeMott, P. J. (1990a), An Exploratory Study of Ice Nucleation by Soot Aerosols, *J. Appl. Meteorol.*
- DeMott, P. J. (1990b), An Exploratory Study of Ice Nucleation by Soot Aerosols, *J. Appl. Meteorol.*, 29, 1072–1079, doi:10.1175/1520-0450(1990)029<1072:AESOIN>2.0.CO;2.
- DeMott, P. J., K. Sassen, M. R. Poellot, D. Baumgardner, D. C. Rogers, S. D. Brooks, A. J. Prenni, and S. M. Kreidenweis (2003), African dust aerosols as atmospheric ice nuclei, *Geophys. Res. Lett.*, 30(14), 1732, doi:10.1029/2003GL017410.
- DeMott, P. J., M. D. Petters, A. J. Prenni, C. M. Carrico, S. M. Kreidenweis, J. L. Collett, and H. Moosmüller (2009), Ice nucleation behavior of biomass combustion particles at cirrus temperatures, *J. Geophys. Res.*, 114(D16), D16205, doi:10.1029/2009JD012036.

- DeMott, P. J., A. J. Prenni, X. Liu, S. M. Kreidenweis, M. D. Petters, C. H. Twohy, M. S. Richardson, T. Eidhammer, and D. C. Rogers (2010), Predicting global atmospheric ice nuclei distributions and their impacts on climate., *Proc. Natl. Acad. Sci. U. S. A.*, *107*(25), 11217–22, doi:10.1073/pnas.0910818107.
- DeMott, P. J. et al. (2017), Comparative measurements of ambient atmospheric concentrations of ice nucleating particles using multiple immersion freezing methods and a continuous flow diffusion chamber, *Atmos. Chem. Phys.*, *17*(18), 11227–11245, doi:10.5194/acp-17-11227-2017.
- Després, V. R. et al. (2012), Primary biological aerosol particles in the atmosphere: a review, *Tellus B*, *64*(1), doi:10.3402/tellusb.v64i0.15598.
- Diao, Y., A. S. Myerson, T. A. Hatton, and B. L. Trout (2011), Surface Design for Controlled Crystallization: The Role of Surface Chemistry and Nanoscale Pores in Heterogeneous Nucleation, *Langmuir*, *27*(9), 5324–5334, doi:10.1021/la104351k.
- Diehl, K., M. Debertshäuser, O. Eppers, H. Schmithüsen, S. K. Mitra, and S. Borrmann (2014), Particle surface area dependence of mineral dust in immersion freezing mode: investigations with freely suspended drops in an acoustic levitator and a vertical wind tunnel, *Atmos. Chem. Phys.*, *14*(22), 12343–12355, doi:10.5194/acp-14-12343-2014.
- Donahue, N. M., A. L. Robinson, C. O. Stanier, and S. N. Pandis (2006), Coupled Partitioning, Dilution, and Chemical Aging of Semivolatile Organics, *Environ. Sci. Technol.*, *40*(8), 2635–2643, doi:10.1021/es052297c.
- Dupont, J.-C., and M. Haeffelin (2008), Observed instantaneous cirrus radiative effect on surface-level shortwave and longwave irradiances, *J. Geophys. Res.*, *113*(D21), D21202, doi:10.1029/2008JD009838.
- Durant, A. J., and R. a. Shaw (2005), Evaporation freezing by contact nucleation inside-out, *Geophys. Res. Lett.*, *32*(October), 1–4, doi:10.1029/2005GL024175.
- Durant, A. J., R. A. Shaw, W. I. Rose, Y. Mi, and G. G. J. Ernst (2008), Ice nucleation and overseeding of ice in volcanic clouds, *J. Geophys. Res. Atmos.*, *113*(9), 1–13, doi:10.1029/2007JD009064.
- Dymarska, M., B. J. Murray, L. Sun, M. L. Eastwood, D. a. Knopf, and A. K. Bertram (2006), Deposition ice nucleation on soot at temperatures relevant for the lower troposphere, *J. Geophys. Res.*, *111*(D4), D04204, doi:10.1029/2005JD006627.
- Emersic, C., P. J. Connolly, S. Boulton, M. Campana, and Z. Li (2015), Investigating the discrepancy between wet-suspension-and dry-dispersion-derived ice nucleation efficiency of mineral particles, *Atmos. Chem. Phys.*, *15*(19), 11311–11326, doi:10.5194/acp-15-11311-2015.
- Engelbrecht, J. P., E. V. McDonald, J. A. Gillies, R. K. M. “Jay” Jayanty, G. Casuccio, and A. W. Gertler (2009), Characterizing Mineral Dusts and Other Aerosols from the Middle East—Part 2: Grab Samples and Re-Suspensions, *Inhal. Toxicol.*, *21*(4), 327–336, doi:10.1080/08958370802464299.
- Engelhart, G. J., C. J. Hennigan, M. a. Miracolo, a. L. Robinson, and S. N. Pandis (2012),

- Cloud condensation nuclei activity of fresh primary and aged biomass burning aerosol, *Atmos. Chem. Phys.*, *12*(15), 7285–7293, doi:10.5194/acp-12-7285-2012.
- Feingold, G., A. McComiskey, T. Yamaguchi, J. S. Johnson, K. S. Carslaw, and K. S. Schmidt (2016), New approaches to quantifying aerosol influence on the cloud radiative effect, *Proc. Natl. Acad. Sci.*, *113*(21), 5812–5819, doi:10.1073/pnas.1514035112.
- Fendinger, N., R. Lehmann, and E. Mihaich (1997), Polydimethylsiloxane, in *Organosilicon Materials*, edited by G. Chandra, pp. 181–223, Springer.
- Findenegg, G. H., S. Jähnert, D. Akcakayiran, and A. Schreiber (2008), Freezing and Melting of Water Confined in Silica Nanopores, *ChemPhysChem*, *9*(18), 2651–2659, doi:10.1002/cphc.200800616.
- Fitzner, M., G. C. Sossó, S. J. Cox, and A. Michaelides (2015), The Many Faces of Heterogeneous Ice Nucleation: Interplay Between Surface Morphology and Hydrophobicity, *J. Am. Chem. Soc.*, *137*(42), 13658–13669, doi:10.1021/jacs.5b08748.
- Fornea, A. P., S. D. Brooks, J. B. Dooley, and A. Saha (2009), Heterogeneous freezing of ice on atmospheric aerosols containing ash, soot, and soil, *J. Geophys. Res. Atmos.*, *114*(13), 1–12, doi:10.1029/2009JD011958.
- Forzieri, G., A. Bianchi, F. B. e Silva, M. A. Marin Herrera, A. Leblois, C. Laval, J. C. J. H. Aerts, and L. Feyen (2018), Escalating impacts of climate extremes on critical infrastructures in Europe, *Glob. Environ. Chang.*, *48*, 97–107, doi:10.1016/j.gloenvcha.2017.11.007.
- Fraux, G., and J. P. K. Doye (2014), Note: Heterogeneous ice nucleation on silver-iodide-like surfaces, *J. Chem. Phys.*, *141*(21), 216101, doi:10.1063/1.4902382.
- Friedman, B., G. Kulkarni, J. Beránek, A. Zelenyuk, J. A. Thornton, and D. J. Cziczo (2011), Ice nucleation and droplet formation by bare and coated soot particles, *J. Geophys. Res.*, *116*(D17), D17203, doi:10.1029/2011JD015999.
- Fröhlich-Nowoisky, J., T. C. J. Hill, B. G. Pummer, P. Yordanova, G. D. Franc, and U. Pöschl (2015), Ice nucleation activity in the widespread soil fungus <i>Mortierella alpina</i>, *Biogeosciences*, *12*(4), 1057–1071, doi:10.5194/bg-12-1057-2015.
- Fukuta, N. (1975), A Study of the Mechanism of Contact Ice Nucleation, *J. Atmos. Sci.*, *32*(8), 1597–1603, doi:10.1175/1520-0469(1975)032<1597:ASOTMO>2.0.CO;2.
- Garcia, E., T. C. J. Hill, A. J. Prenni, P. J. DeMott, G. D. Franc, and S. M. Kreidenweis (2012), Biogenic ice nuclei in boundary layer air over two U.S. high plains agricultural regions, *J. Geophys. Res. Atmos.*, *117*(17), 1–12, doi:10.1029/2012JD018343.
- Gaudichet, A., F. Echalar, B. Chatenet, J. P. Quisefit, G. Malingre, H. Cachier, P. Buat-Menard, P. Artaxo, and W. Maenhaut (1995), Trace elements in tropical African savanna biomass burning aerosols, *J. Atmos. Chem.*, *22*(1–2), 19–39,

doi:10.1007/BF00708179.

- Gelest Inc. (1998), Silicone fluids: stable inert media, *Prod. Broch.*, 27. Available from: <http://www.gelest.com/goods/pdf/siliconefluids.pdf> (Accessed 10 April 2016)
- Gettelman, A., X. Liu, S. J. Ghan, H. Morrison, S. Park, A. J. Conley, S. A. Klein, J. Boyle, D. L. Mitchell, and J.-L. F. Li (2010), Global simulations of ice nucleation and ice supersaturation with an improved cloud scheme in the Community Atmosphere Model, *J. Geophys. Res.*, 115(D18), D18216, doi:10.1029/2009JD013797.
- Gibbs, A., M. Charman, W. Schwarzacher, and A. C. Rust (2015), Immersion freezing of supercooled water drops containing glassy volcanic ash particles, *GeoResJ*, 7, 66–69, doi:10.1016/j.grj.2015.06.002.
- Gilman, J. B., B. M. Lerner, W. C. Kuster, P. D. Goldan, C. Warneke, P. R. Veres, J. M. Roberts, J. A. de Gouw, I. R. Burling, and R. J. Yokelson (2015), Biomass burning emissions and potential air quality impacts of volatile organic compounds and other trace gases from fuels common in the US, *Atmos. Chem. Phys.*, 15(24), 13915–13938, doi:10.5194/acp-15-13915-2015.
- Goode, J. G., R. J. Yokelson, D. E. Ward, R. A. Susott, R. E. Babbitt, M. A. Davies, and W. M. Hao (2000), Measurements of excess O₃, CO₂, CO, CH₄, C₂H₄, C₂H₂, HCN, NO, NH₃, HCOOH, CH₃COOH, HCHO, and CH₃OH in 1997 Alaskan biomass burning plumes by airborne Fourier transform infrared spectroscopy (AFTIR), *J. Geophys. Res. Atmos.*, 105(D17), 22147–22166, doi:10.1029/2000JD900287.
- Gorbunov, B., A. Baklanov, N. Kakutkina, H. . Windsor, and R. Toumi (2001), Ice nucleation on soot particles, *J. Aerosol Sci.*, 32(2), 199–215, doi:10.1016/S0021-8502(00)00077-X.
- Govindarajan, a G., and S. E. Lindow (1988), Size of bacterial ice-nucleation sites measured in situ by radiation inactivation analysis., *Proc. Natl. Acad. Sci. U. S. A.*, 85(5), 1334–1338, doi:10.1073/pnas.85.5.1334.
- Grawe, S., S. Augustin-Bauditz, S. Hartmann, L. Hellner, J. B. C. Pettersson, A. Prager, F. Stratmann, and H. Wex (2016), The immersion freezing behavior of ash particles from wood and brown coal burning, *Atmos. Chem. Phys.*, 16(21), 13911–13928, doi:10.5194/acp-16-13911-2016.
- Gurganus, C., A. B. Kostinski, and R. A. Shaw (2011), Fast Imaging of Freezing Drops: No Preference for Nucleation at the Contact Line, *J. Phys. Chem. Lett.*, 2(12), 1449–1454, doi:10.1021/jz2004528.
- Gurganus, C. W., J. C. Charnawskas, a B. Kostinski, and R. a. Shaw (2014), Nucleation at the Contact Line Observed on Nanotextured Surfaces, *Phys. Rev. Lett.*, 113(23), 235701, doi:10.1103/PhysRevLett.113.235701.
- Hader, J. D., T. P. Wright, and M. D. Petters (2014), Contribution of pollen to atmospheric ice nuclei concentrations, *Atmos. Chem. Phys.*, 14(11), 5433–5449, doi:10.5194/acp-14-5433-2014.

- Harrison, A. D., T. F. Whale, M. A. Carpenter, M. A. Holden, L. Neve, D. O’Sullivan, J. Vergara Temprado, and B. J. Murray (2016), Not all feldspars are equal: a survey of ice nucleating properties across the feldspar group of minerals, *Atmos. Chem. Phys.*, *16*(17), 10927–10940, doi:10.5194/acp-16-10927-2016.
- Hartmann, S., D. Niedermeier, J. Voigtländer, T. Clauss, R. A. Shaw, H. Wex, A. Kiselev, and F. Stratmann (2011), Homogeneous and heterogeneous ice nucleation at LACIS: operating principle and theoretical studies, *Atmos. Chem. Phys.*, *11*(4), 1753–1767, doi:10.5194/acp-11-1753-2011.
- Hartmann, S., S. Augustin, T. Clauss, H. Wex, T. Šantl-Temkiv, J. Voigtländer, D. Niedermeier, and F. Stratmann (2013), Immersion freezing of ice nucleation active protein complexes, *Atmos. Chem. Phys.*, *13*(11), 5751–5766, doi:10.5194/acp-13-5751-2013.
- Häusler, T., L. Witek, L. Felgitsch, R. Hitzenberger, and H. Grothe (2018), Freezing on a Chip—A New Approach to Determine Heterogeneous Ice Nucleation of Micrometer-Sized Water Droplets, *Atmosphere (Basel)*, *9*(4), 140, doi:10.3390/atmos9040140.
- Haywood, J., and O. Boucher (2000), Estimates of the direct and indirect radiative forcing due to tropospheric aerosols: A review, *Rev. Geophys.*, *38*(4), 513–543, doi:10.1029/1999RG000078.
- Heymsfield, A. J., L. M. Miloshevich, C. Twohy, G. Sachse, and S. Oltmans (1998), Upper-tropospheric relative humidity observations and implications for cirrus ice nucleation, *Geophys. Res. Lett.*, *25*(9), 1343–1346, doi:10.1029/98GL01089.
- Hill, T. C. J., B. F. Moffett, P. J. DeMott, D. G. Georgakopoulos, W. L. Stump, and G. D. Franc (2014), Measurement of ice nucleation-active bacteria on plants and in precipitation by quantitative PCR, *Appl. Environ. Microbiol.*, *80*(4), 1256–1267, doi:10.1128/AEM.02967-13.
- Hill, T. C. J., P. J. Demott, Y. Tobo, J. Frohlich-Nowoisky, B. F. Moffett, G. D. Franc, and S. M. Kreidenweis (2016), Sources of organic ice nucleating particles in soils, *Atmos. Chem. Phys.*, *16*(11), 7195–7211, doi:10.5194/acp-16-7195-2016.
- Hiranuma, N., M. Paukert, I. Steinke, K. Zhang, G. Kulkarni, C. Hoose, M. Schnaiter, H. Saathoff, and O. Möhler (2014a), A comprehensive parameterization of heterogeneous ice nucleation of dust surrogate: laboratory study with hematite particles and its application to atmospheric models, *Atmos. Chem. Phys.*, *14*(23), 13145–13158, doi:10.5194/acp-14-13145-2014.
- Hiranuma, N., N. Hoffmann, a. Kiselev, a. Dreyer, K. Zhang, G. Kulkarni, T. Koop, and O. Möhler (2014b), Influence of surface morphology on the immersion mode ice nucleation efficiency of hematite particles, *Atmos. Chem. Phys.*, *14*(5), 2315–2324, doi:10.5194/acp-14-2315-2014.
- Hiranuma, N. et al. (2015a), A comprehensive laboratory study on the immersion freezing behavior of illite NX particles: a comparison of 17 ice nucleation measurement techniques, *Atmos. Chem. Phys.*, *15*(5), 2489–2518, doi:10.5194/acp-15-2489-2015.

- Hiranuma, N. et al. (2015b), A comprehensive laboratory study on the immersion freezing behavior of illite NX particles: a comparison of 17 ice nucleation measurement techniques, *Atmos. Chem. Phys.*, *15*(5), 2489–2518, doi:10.5194/acp-15-2489-2015.
- Hiranuma, N. et al. (2015c), Ice nucleation by cellulose and its potential contribution to ice formation in clouds, *Nat. Geosci.*, *8*, 273–277, doi:10.1038/ngeo2374.
- Hoffer, T. E. (1961), A Laboratory Investigation of Droplet Freezing, *J. Meteorol.*, *18*(6), 766–778, doi:10.1175/1520-0469(1961)018<0766:ALIODF>2.0.CO;2.
- Hoffmann, N., A. Kiselev, D. Rzesanke, D. Duft, and T. Leisner (2013), Experimental quantification of contact freezing in an electrodynamic balance, *Atmos. Meas. Tech.*, *6*(9), 2373–2382, doi:10.5194/amt-6-2373-2013.
- Holdren, G. R., and R. A. Berner (1979), Mechanism of feldspar weathering—I. Experimental studies, *Geochim. Cosmochim. Acta*, *43*(8), 1161–1171, doi:10.1016/0016-7037(79)90109-1.
- Hoose, C., and O. Möhler (2012), Heterogeneous ice nucleation on atmospheric aerosols: a review of results from laboratory experiments, *Atmos. Chem. Phys.*, *12*(20), 9817–9854, doi:10.5194/acp-12-9817-2012.
- Hoose, C., J. E. Kristjánsson, J.-P. Chen, and A. Hazra (2010), A Classical-Theory-Based Parameterization of Heterogeneous Ice Nucleation by Mineral Dust, Soot, and Biological Particles in a Global Climate Model, *J. Atmos. Sci.*, *67*(8), 2483–2503, doi:10.1175/2010JAS3425.1.
- Hoyle, C. R. et al. (2011), Ice nucleation properties of volcanic ash from Eyjafjallajökull, *Atmos. Chem. Phys.*, *11*(18), 9911–9926, doi:10.5194/acp-11-9911-2011.
- Huff, A. K., S. Kondragunta, H. Zhang, and R. M. Hoff (2015), Monitoring the Impacts of Wildfires on Forest Ecosystems and Public Health in the Exo-Urban Environment Using High-Resolution Satellite Aerosol Products from the Visible Infrared Imaging Radiometer Suite (VIIRS), *Environ. Health Insights*, *9s2*, EHL.S19590, doi:10.4137/EHL.S19590.
- Iannone, R., D. I. Chernoff, a. Pringle, S. T. Martin, and a. K. Bertram (2011), The ice nucleation ability of one of the most abundant types of fungal spores found in the atmosphere, *Atmos. Chem. Phys.*, *11*(3), 1191–1201, doi:10.5194/acp-11-1191-2011.
- Inada, T., H. Tomita, and T. Koyama (2014), Ice nucleation in water droplets on glass surfaces: From micro- to macro-scale, *Int. J. Refrig.*, *40*, 294–301, doi:10.1016/j.ijrefrig.2013.11.024.
- Ismail, A. E., G. S. Grest, D. R. Heine, M. J. Stevens, and M. Tsige (2009), Interfacial structure and dynamics of siloxane systems: pdms-vapor and pdms-water, *Macromolecules*, *42*(8), 3186–3194, doi:10.1021/ma802805y.
- Johansson, L. S., C. Tullin, B. Leckner, and P. Sjövall (2003), Particle emissions from biomass combustion in small combustors, *Biomass and Bioenergy*, *25*(4), 435–446, doi:10.1016/S0961-9534(03)00036-9.

- Joly, M., E. Attard, M. Sancelme, L. Deguillaume, C. Guilbaud, C. E. Morris, P. Amato, and A. M. Delort (2013), Ice nucleation activity of bacteria isolated from cloud water, *Atmos. Environ.*, *70*, 392–400, doi:10.1016/j.atmosenv.2013.01.027.
- Jung, S., M. K. Tiwari, and D. Poulikakos (2012), Frost halos from supercooled water droplets, *Proc. Natl. Acad. Sci.*, *109*(40), 16073–16078, doi:10.1073/pnas.1206121109.
- Kiselev, A., F. Bachmann, P. Pedevilla, S. J. Cox, A. Michaelides, D. Gerthsen, and T. Leisner (2017), Active sites in heterogeneous ice nucleation—the example of K-rich feldspars, *Science* (80-.), *355*(6323), 367–371, doi:10.1126/science.aai8034.
- Klucker, M., F. Dalençon, P. Probeck, and J. Haensler (2012), AF03, An Alternative Squalene Emulsion-Based Vaccine Adjuvant Prepared by a Phase Inversion Temperature Method, *J. Pharm. Sci.*, *101*(12), 4490–4500, doi:10.1002/jps.23311.
- Koehler, K. a, P. J. DeMott, S. M. Kreidenweis, O. B. Popovicheva, M. D. Petters, C. M. Carrico, E. D. Kireeva, T. D. Khokhlova, and N. K. Shonija (2009), Cloud condensation nuclei and ice nucleation activity of hydrophobic and hydrophilic soot particles., *Phys. Chem. Chem. Phys.*, *11*(36), 7906–20, doi:10.1039/b905334b.
- Koop, T., and B. J. Murray (2016), A physically constrained classical description of the homogeneous nucleation of ice in water, *J. Chem. Phys.*, *145*(21), 211915, doi:10.1063/1.4962355.
- Koop, T., and B. Zobrist (2009), Parameterizations for ice nucleation in biological and atmospheric systems., *Phys. Chem. Chem. Phys.*, *11*(46), 10839–10850, doi:10.1039/b914289d.
- Koop, T., H. P. Ng, L. T. Molina, and M. J. Molina (1998), A New Optical Technique to Study Aerosol Phase Transitions: The Nucleation of Ice from H₂SO₄ Aerosols, *J. Phys. Chem. A*, *102*(45), 8924–8931, doi:10.1021/jp9828078.
- Koop, T., B. Luo, a Tsias, and T. Peter (2000), Water activity as the determinant for homogeneous ice nucleation in aqueous solutions, *Nature*, *406*(6796), 611–4, doi:10.1038/35020537.
- Korolev, A. (2007), Limitations of the Wegener–Bergeron–Findeisen Mechanism in the Evolution of Mixed-Phase Clouds, *J. Atmos. Sci.*, *64*(9), 3372–3375, doi:10.1175/JAS4035.1.
- Korolev, A. et al. (2017), Mixed-Phase Clouds: Progress and Challenges, *Meteorol. Monogr.*, *58*, 5.1-5.50, doi:10.1175/AMSMONOGRAPHIS-D-17-0001.1.
- Kulkarni, G., M. Nandasiri, A. Zelenyuk, J. Beranek, N. Madaan, A. Devaraj, V. Shutthanandan, S. Thevuthasan, and T. Varga (2015), Effects of crystallographic properties on the ice nucleation properties of volcanic ash particles, *Geophys. Res. Lett.*, *42*(8), 3048–3055, doi:10.1002/2015GL063270.
- Kulkarni, G. et al. (2016), Ice nucleation activity of diesel soot particles at cirrus relevant temperature conditions: Effects of hydration, secondary organics coating, soot morphology, and coagulation, *Geophys. Res. Lett.*, *43*(7), 3580–3588,

doi:10.1002/2016GL068707.

- Latham, T. L., A. J. Beyersdorf, K. L. Thornhill, E. L. Winstead, M. J. Cubison, A. Hecobian, J. L. Jimenez, R. J. Weber, B. E. Anderson, and A. Nenes (2013), Analysis of CCN activity of Arctic aerosol and Canadian biomass burning during summer 2008, *Atmos. Chem. Phys.*, *13*(5), 2735–2756, doi:10.5194/acp-13-2735-2013.
- Lawson, R. P., and A. Gettelman (2014), Impact of Antarctic mixed-phase clouds on climate, *Proc. Natl. Acad. Sci.*, *111*(51), 18156–18161, doi:10.1073/pnas.1418197111.
- Lee, S., K. Baumann, J. J. Schauer, R. J. Sheesley, L. P. Naeher, S. Meinardi, D. R. Blake, E. S. Edgerton, A. G. Russell, and M. Clements (2005), Gaseous and Particulate Emissions from Prescribed Burning in Georgia, *Environ. Sci. Technol.*, *39*(23), 9049–9056, doi:10.1021/es051583l.
- van Leeuwen, T. T. et al. (2014), Biomass burning fuel consumption rates: a field measurement database, *Biogeosciences*, *11*(24), 7305–7329, doi:10.5194/bg-11-7305-2014.
- Levin, E. J. T. et al. (2010), Biomass burning smoke aerosol properties measured during Fire Laboratory at Missoula Experiments (FLAME), *J. Geophys. Res.*, *115*(D18), D18210, doi:10.1029/2009JD013601.
- Levin, E. J. T., G. R. McMeeking, P. J. DeMott, C. S. McCluskey, C. E. Stockwell, R. J. Yokelson, and S. M. Kreidenweis (2014), A New Method to Determine the Number Concentrations of Refractory Black Carbon Ice Nucleating Particles, *Aerosol Sci. Technol.*, *48*(12), 1264–1275, doi:10.1080/02786826.2014.977843.
- Levin, E. J. T. et al. (2016), Ice Nucleating Particle Emissions from Biomass Combustion and the Potential Importance of Soot Aerosol, *J. Geophys. Res. Atmos.*, *120*(9), 4282–4303, doi:10.1002/2016JD024879.
- Li, J., M. Posfai, P. V. Hobbs, and P. R. Buseck (2003), Individual Aerosol Particles from Biomass Burning in Southern Africa: 2. Compositions and Aging of Inorganic Particles, *J. Geophys. Res.*, *108*, 1–12, doi:10.1029/2002JD002310.
- Li, K., S. Xu, W. Shi, M. He, H. Li, S. Li, X. Zhou, J. Wang, and Y. Song (2012), Investigating the effects of solid surfaces on Ice nucleation, *Langmuir*, *28*(29), 10749–10754, doi:10.1021/la3014915.
- Lindow, S. E. (1989), Localization of Ice Nucleation Activity and the iceC Gene Product in *Pseudomonas syringae* and *Escherichia coli*, *Mol. Plant-Microbe Interact.*, *2*(5), 262, doi:10.1094/MPMI-2-262.
- Lindow, S. E. (1995), Membrane fluidity as a factor in production and stability of bacterial ice nuclei active at high subfreezing temperatures., *Cryobiology*, *32*(3), 247–258.
- Lindow, S. E., D. C. Arny, and C. D. Upper (1982), Bacterial ice nucleation: a factor in frost injury to plants., *Plant Physiol.*, *70*(4), 1084–1089, doi:10.1104/pp.70.4.1084.
- Liu, J. C., G. Pereira, S. A. Uhl, M. A. Bravo, and M. L. Bell (2015), A systematic review

- of the physical health impacts from non-occupational exposure to wildfire smoke, *Environ. Res.*, *136*, 120–132, doi:10.1016/j.envres.2014.10.015.
- Lo, C.-W., V. Sahoo, and M.-C. Lu (2017), Control of Ice Formation, *ACS Nano*, *11*(3), 2665–2674, doi:10.1021/acsnano.6b07348.
- Lohmann, U., and K. Diehl (2006), Sensitivity Studies of the Importance of Dust Ice Nuclei for the Indirect Aerosol Effect on Stratiform Mixed-Phase Clouds, *J. Atmos. Sci.*, *63*(3), 968–982, doi:10.1175/JAS3662.1.
- Lohmann, U., and J. Feichter (2005), Global indirect aerosol effects: a review, *Atmos. Chem. Phys.*, *5*(3), 715–737, doi:10.5194/acp-5-715-2005.
- Lüönd, F., O. Stetzer, A. Welti, and U. Lohmann (2010), Experimental study on the ice nucleation ability of size-selected kaolinite particles in the immersion mode, *J. Geophys. Res.*, *115*(D14), D14201, doi:10.1029/2009JD012959.
- Lupi, L., and V. Molinero (2014), Does hydrophilicity of carbon particles improve their ice nucleation ability?, *J. Phys. Chem. A*, *118*(35), 7330–7, doi:10.1021/jp4118375.
- Maki, L. R., E. L. Galyan, M. M. Chang-Chien, and D. R. Caldwell (1974), Ice nucleation induced by pseudomonas syringae., *Appl. Microbiol.*, *28*(3), 456–459.
- Mangan, T. P., J. D. Atkinson, J. W. Neuberg, D. O’Sullivan, T. W. Wilson, T. F. Whale, L. Neve, N. S. Umo, T. L. Malkin, and B. J. Murray (2017), Heterogeneous Ice Nucleation by Soufriere Hills Volcanic Ash Immersed in Water Droplets, edited by V. C. Smith, *PLoS One*, *12*(1), e0169720, doi:10.1371/journal.pone.0169720.
- Marcolli, C. (2014), Deposition nucleation viewed as homogeneous or immersion freezing in pores and cavities, *Atmos. Chem. Phys.*, *14*(4), 2071–2104, doi:10.5194/acp-14-2071-2014.
- Marcolli, C., S. Gedamke, T. Peter, and B. Zobrist (2007), Efficiency of immersion mode ice nucleation on surrogates of mineral dust, *Atmos. Chem. Phys.*, *7*(2003), 5081–5091.
- Marcolli, C., B. Nagare, A. Welti, and U. Lohmann (2016), Ice nucleation efficiency of AgI: review and new insights, *Atmos. Chem. Phys.*, *16*(14), 8915–8937, doi:10.5194/acp-16-8915-2016.
- Mason, R. H., C. Chou, C. S. McCluskey, E. J. T. Levin, C. L. Schiller, T. C. J. Hill, J. A. Huffman, P. J. Demott, and A. K. Bertram (2015), The micro-orifice uniform deposit impactor-droplet freezing technique (MOUDI-DFT) for measuring concentrations of ice nucleating particles as a function of size: Improvements and initial validation, *Atmos. Meas. Tech.*, *8*(6), 2449–2462, doi:10.5194/amt-8-2449-2015.
- Maudlin, L. C., Z. Wang, H. H. Jonsson, and A. Sorooshian (2015), Impact of wildfires on size-resolved aerosol composition at a coastal California site, *Atmos. Environ.*, *119*, 59–68, doi:10.1016/j.atmosenv.2015.08.039.
- Mazzoleni, L. R., B. Zielinska, and H. Moosmüller (2007), Emissions of Levoglucosan, Methoxy Phenols, and Organic Acids from Prescribed Burns, Laboratory Combustion

- of Wildland Fuels, and Residential Wood Combustion, *Environ. Sci. Technol.*, *41*(7), 2115–2122, doi:10.1021/es061702c.
- McCluskey, C. S., P. J. DeMott, A. J. Prenni, E. J. T. Levin, G. R. McMeeking, A. P. Sullivan, T. C. J. Hill, S. Nakao, C. M. Carrico, and S. M. Kreidenweis (2014), Characteristics of atmospheric ice nucleating particles associated with biomass burning in the US: Prescribed burns and wildfires, *J. Geophys. Res. Atmos.*, *119*(17), 10458–10470, doi:10.1002/2014JD021980.
- McKenzie, D., Z. Gedalof, D. L. Peterson, and P. Mote (2004), Climatic Change, Wildfire, and Conservation, *Conserv. Biol.*, *18*(4), 890–902, doi:10.1111/j.1523-1739.2004.00492.x.
- Misra, M. K., K. W. Ragland, and A. J. Baker (1993), Wood ash composition as a function of furnace temperature, *Biomass and Bioenergy*, *4*(2), 103–116, doi:10.1016/0961-9534(93)90032-Y.
- Möhler, O., A. Nink, H. Saathoff, S. Schaefer, M. Schnaiter, W. Schöck, and U. Schurath (2001), *The Karlsruhe aerosol chamber facility AIDA : technical description and first results of homogeneous and heterogeneous ice nucleation experiments*, Geneva.
- Möhler, O. et al. (2003), Experimental investigation of homogeneous freezing of sulphuric acid particles in the aerosol chamber AIDA, *Atmos. Chem. Phys.*, *3*(1), 211–223, doi:10.5194/acp-3-211-2003.
- Möhler, O., P. J. DeMott, G. Vali, and Z. Levin (2007), Microbiology and atmospheric processes: the role of biological particles in cloud physics, *Biogeosciences Discuss.*, *4*(4), 2559–2591, doi:10.5194/bgd-4-2559-2007.
- Möhler, O., S. Benz, H. Saathoff, M. Schnaiter, R. Wagner, J. Schneider, S. Walter, V. Ebert, and S. Wagner (2008), The effect of organic coating on the heterogeneous ice nucleation efficiency of mineral dust aerosols, *Environ. Res. Lett.*, *3*(2), 025007, doi:10.1088/1748-9326/3/2/025007.
- Morris, C. E., D. G. Georgakopoulos, and D. C. Sands (2004), Ice nucleation active bacteria and their potential role in precipitation, *J. Phys. IV*, *121*, 87–103, doi:10.1051/jp4:2004121004.
- Morris, C. E., D. C. Sands, B. a Vinatzer, C. Glaux, C. Guilbaud, A. Buffière, S. Yan, H. Dominguez, and B. M. Thompson (2008), The life history of the plant pathogen *Pseudomonas syringae* is linked to the water cycle., *ISME J.*, *2*(3), 321–334, doi:10.1038/ismej.2007.113.
- Morris, C. E., D. C. Sands, C. Glaux, J. Samsatly, S. Asaad, A. R. Moukahel, F. L. T. Gonçalves, and E. K. Bigg (2013), Urediospores of rust fungi are ice nucleation active at > −10 °C and harbor ice nucleation active bacteria, *Atmos. Chem. Phys.*, *13*(8), 4223–4233, doi:10.5194/acp-13-4223-2013.
- Mossop, S. C. (1963), Atmospheric ice nuclei, *Zeitschrift für Angew. Math. und Phys. ZAMP*, *14*(5), 456–486, doi:10.1007/BF01601253.
- Moyle, T. M., L. M. Walker, and S. L. Anna (2012), Predicting conditions for microscale

- surfactant mediated tipstreaming, *Phys. Fluids*, 24(8), doi:10.1063/1.4746253.
- Mülmenstädt, J., O. Sourdeval, J. Delanoë, and J. Quaas (2015), Frequency of occurrence of rain from liquid-, mixed-, and ice-phase clouds derived from A-Train satellite retrievals, *Geophys. Res. Lett.*, 42(15), 6502–6509, doi:10.1002/2015GL064604.
- Murphy, D. M., and T. Koop (2005), Review of the vapour pressures of ice and supercooled water for atmospheric applications, *Q. J. R. Meteorol. Soc.*, 131(608), 1539–1565, doi:10.1256/qj.04.94.
- Murray, B. J., S. L. Broadley, T. W. Wilson, S. J. Bull, R. H. Wills, H. K. Christenson, and E. J. Murray (2010), Kinetics of the homogeneous freezing of water., *Phys. Chem. Chem. Phys.*, 12(35), 10380–7, doi:10.1039/c003297b.
- Murray, B. J., S. L. Broadley, T. W. Wilson, J. D. Atkinson, and R. H. Wills (2011), Heterogeneous freezing of water droplets containing kaolinite particles, *Atmos. Chem. Phys.*, 11(9), 4191–4207, doi:10.5194/acp-11-4191-2011.
- Murray, B. J., D. O’Sullivan, J. D. Atkinson, and M. E. Webb (2012), Ice nucleation by particles immersed in supercooled cloud droplets., *Chem. Soc. Rev.*, 41(19), 6519–54, doi:10.1039/c2cs35200a.
- National Center for Biotechnology Information (2016), Squalene, CID=638072, *PubChem Compd. Database*, Chemical and Physical Properties. Available from: <https://pubchem.ncbi.nlm.nih.gov/compound/squalene#section=Top> (Accessed 24 March 2016)
- O’Sullivan, D., B. J. Murray, T. L. Malkin, T. F. Whale, N. S. Umo, J. D. Atkinson, H. C. Price, K. J. Baustian, J. Browse, and M. E. Webb (2014), Ice nucleation by fertile soil dusts: relative importance of mineral and biogenic components, *Atmos. Chem. Phys.*, 14(4), 1853–1867, doi:10.5194/acp-14-1853-2014.
- O’Sullivan, D., B. J. Murray, J. F. Ross, T. F. Whale, H. C. Price, J. D. Atkinson, N. S. Umo, and M. E. Webb (2015), The relevance of nanoscale biological fragments for ice nucleation in clouds., *Sci. Rep.*, 5, 8082, doi:10.1038/srep08082.
- O’Sullivan, D., B. J. Murray, J. F. Ross, and M. E. Webb (2016), The adsorption of fungal ice-nucleating proteins on mineral dusts: A terrestrial reservoir of atmospheric ice-nucleating particles, *Atmos. Chem. Phys.*, 16(12), 7879–7887, doi:10.5194/acp-16-7879-2016.
- O, K.-T., and R. Wood (2016), Exploring an approximation for the homogeneous freezing temperature of water droplets, *Atmos. Chem. Phys.*, 16(11), 7239–7249, doi:10.5194/acp-16-7239-2016.
- Pahlavanpour, B., M. Martins, and M. Eklund (2003), Study of Moisture Equilibrium in Oil-Paper System with Temperature Variation, in *Proceedings of the 7th International Conference on Properties and Applications of Dielectric Materials*, pp. 1124–1129.
- Pandey, R. et al. (2016), Ice-nucleating bacteria control the order and dynamics of interfacial water, *Sci. Adv.*, 2(4), e1501630–e1501630, doi:10.1126/sciadv.1501630.

- Peckhaus, A., A. Kiselev, T. Hiron, M. Ebert, and T. Leisner (2016), A comparative study of K-rich and Na/Ca-rich feldspar ice-nucleating particles in a nanoliter droplet freezing assay, *Atmos. Chem. Phys.*, *16*(18), 11477–11496, doi:10.5194/acp-16-11477-2016.
- Penner, J. E., R. E. Dickinson, and C. A. O'Neill (1992), Effects of Aerosol from Biomass Burning on the Global Radiation Budget, *Science* (80-.), *256*(5062), 1432–1434, doi:10.1126/science.256.5062.1432.
- Petters, M. D., C. M. Carrico, S. M. Kreidenweis, A. J. Prenni, P. J. DeMott, J. L. Collett, and H. Moosmüller (2009a), Cloud condensation nucleation activity of biomass burning aerosol, *J. Geophys. Res.*, *114*(D22), D22205, doi:10.1029/2009JD012353.
- Petters, M. D. et al. (2009b), Ice nuclei emissions from biomass burning, *J. Geophys. Res.*, *114*(D7), D07209, doi:10.1029/2008JD011532.
- Phelps, P., T. H. Giddings, M. Prochoda, and R. Fall (1986), Release of cell-free ice nuclei by *Erwinia herbicola*., *J. Bacteriol.*, *167*(2), 496–502.
- Pietsch, R. B., R. F. David, L. C. Marr, B. Vinatzer, and D. G. Schmale (2015), Aerosolization of Two Strains (Ice+ and Ice-) of *Pseudomonas syringae* in a Collison Nebulizer at Different Temperatures, *Aerosol Sci. Technol.*, (June), 00–00, doi:10.1080/02786826.2015.1010636.
- Pinti, V., C. Marcolli, B. Zobrist, C. R. Hoyle, and T. Peter (2012), Ice nucleation efficiency of clay minerals in the immersion mode, *Atmos. Chem. Phys.*, *12*, 5859–5878, doi:10.5194/acp-12-5859-2012.
- Pitman, A. J., G. T. Narisma, and J. McAneney (2007), The impact of climate change on the risk of forest and grassland fires in Australia, *Clim. Change*, *84*(3–4), 383–401, doi:10.1007/s10584-007-9243-6.
- Polen, M., E. Lawlis, and R. C. Sullivan (2016), The unstable ice nucleation properties of Snomax® bacterial particles, *J. Geophys. Res. Atmos.*, *121*(19), 11,666–11,678, doi:10.1002/2016JD025251.
- Polen, M., T. Brubaker, J. Somers, and R. C. Sullivan (2018), Cleaning up our water: reducing interferences from non-homogeneous freezing of “pure” water in droplet freezing assays of ice nucleating particles, *Atmos. Meas. Tech. Discuss.*, 1–31, doi:10.5194/amt-2018-134.
- Popovicheva, O. B., V. Kozlov, G. Engling, E. Diapouli, N. Persiantseva, M. Timofeev, T. Fan, D. Saraga, and K. Eleftheriadis (2015), Small-Scale Study of Siberian Biomass Burning: I. Smoke Microstructure, *Aerosol Air Qual. Res.*, *15*(7), 1558–1568, doi:10.4209/aaqr.2014.09.0206.
- Prendergast-Miller, M. T., A. B. de Menezes, L. M. Macdonald, P. Toscas, A. Bissett, G. Baker, M. Farrell, A. E. Richardson, T. Wark, and P. H. Thrall (2017), Wildfire impact: Natural experiment reveals differential short-term changes in soil microbial communities, *Soil Biol. Biochem.*, *109*, 1–13, doi:10.1016/j.soilbio.2017.01.027.
- Prenni, A. J., M. D. Petters, S. M. Kreidenweis, C. L. Heald, S. T. Martin, P. Artaxo, R.

- M. Garland, A. G. Wollny, and U. Pöschl (2009), Relative roles of biogenic emissions and Saharan dust as ice nuclei in the Amazon basin, *Nat. Geosci.*, 2(6), 402–405, doi:10.1038/ngeo517.
- Prenni, A. J., P. J. DeMott, A. P. Sullivan, R. C. Sullivan, S. M. Kreidenweis, and D. C. Rogers (2012), Biomass burning as a potential source for atmospheric ice nuclei: Western wildfires and prescribed burns, *Geophys. Res. Lett.*, 39(11), n/a-n/a, doi:10.1029/2012GL051915.
- Pruppacher, H. R. (1995), A New Look at Homogeneous Ice Nucleation in Supercooled Water Drops, *J. Atmos. Sci.*, 52, 1924–1933, doi:10.1175/1520-0469(1995)052<1924:ANLAHI>2.0.CO;2.
- Pueschel, R. F., and G. Langer (1973), Sugar cane fires as a source of ice nuclei in Hawaii, *J. Appl. Meteorol.*, 12(3), 549–551.
- Pummer, B. G., H. Bauer, J. Bernardi, S. Bleicher, and H. Grothe (2012), Suspendable macromolecules are responsible for ice nucleation activity of birch and conifer pollen, *Atmos. Chem. Phys.*, 12(5), 2541–2550, doi:10.5194/acp-12-2541-2012.
- Pummer, B. G. et al. (2015), Ice nucleation by water-soluble macromolecules, *Atmos. Chem. Phys.*, 15(8), 4077–4091, doi:10.5194/acp-15-4077-2015.
- Radke, L. F., D. a Hegg, P. V Hobbs, J. D. Nance, J. H. Lyons, K. K. Laursen, R. E. Weiss, P. J. Riggan, and D. E. Ward (1991), Particulate and Trace Gas Emissions from Large Biomass Fires in North America, in *Global Biomass Burning: Atmospheric, Climatic, and Biospheric Implications*, pp. 209–224.
- Rahn, M. (2009), *Wildfire Impact Analysis*.
- Reicher, N., L. Segev, and Y. Rudich (2018), The Weizmann Supercooled Droplets Observation on a Microarray (WISDOM) and application for ambient dust, *Atmos. Meas. Tech.*, 11(1), 233–248, doi:10.5194/amt-11-233-2018.
- Reid, J. S., P. V. Hobbs, R. J. Ferek, D. R. Blake, J. V. Martins, M. R. Dunlap, and C. Liousse (1998), Physical, chemical, and optical properties of regional hazes dominated by smoke in Brazil, *J. Geophys. Res. Atmos.*, 103(D24), 32059–32080, doi:10.1029/98JD00458.
- Riechers, B., F. Wittbracht, A. Hütten, and T. Koop (2013), The homogeneous ice nucleation rate of water droplets produced in a microfluidic device and the role of temperature uncertainty, *Phys. Chem. Chem. Phys.*, 15(16), 5873, doi:10.1039/c3cp42437e.
- Rigg, Y. J., P. a. Alpert, and D. a. Knopf (2013), Immersion freezing of water and aqueous ammonium sulfate droplets initiated by humic-like substances as a function of water activity, *Atmos. Chem. Phys.*, 13(13), 6603–6622, doi:10.5194/acp-13-6603-2013.
- Rissler, J., J. Pagels, E. Swietlicki, A. Wierzbicka, M. Strand, L. Lillieblad, M. Sanati, and M. Bohgard (2005), Hygroscopic Behavior of Aerosol Particles Emitted from Biomass Fired Grate Boilers, *Aerosol Sci. Technol.*, 39(10), 919–930, doi:10.1080/02786820500331068.

- Rogers, D. C. (1988), Development of a continuous flow thermal gradient diffusion chamber for ice nucleation studies, *Atmos. Res.*, 22(2), 149–181, doi:10.1016/0169-8095(88)90005-1.
- Rogers, D. C., P. J. DeMott, S. M. Kreidenweis, and Y. Chen (1998), Measurements of ice nucleating aerosols during SUCCESS, *Geophys. Res. Lett.*, 25(9), 1383, doi:10.1029/97GL03478.
- Ruggles, J. a, M. Nemecek-Marshall, and R. Fall (1993), Kinetics of appearance and disappearance of classes of bacterial ice nuclei support an aggregation model for ice nucleus assembly., *J. Bacteriol.*, 175(22), 7216–21.
- Šantl-Temkiv, T. et al. (2015), Characterization of airborne ice-nucleation-active bacteria and bacterial fragments, *Atmos. Environ.*, 109, 105–117, doi:10.1016/j.atmosenv.2015.02.060.
- Schill, G. P., K. Genareau, and M. A. Tolbert (2013), Deposition and immersion mode nucleation of ice by three distinct samples of volcanic ash, *AIP Conf. Proc.*, 1527, 867–870, doi:10.1063/1.4803408.
- Schill, G. P., D. O. De Haan, and M. a Tolbert (2014), Heterogeneous Ice Nucleation on Simulated Secondary Organic Aerosol., *Environ. Sci. Technol.*, doi:10.1021/es4046428.
- Schlosser, J. S., R. A. Braun, T. Bradley, H. Dadashazar, A. B. Macdonald, A. A. Aldhaif, M. A. Aghdam, A. H. Mardi, P. Xian, and A. Sorooshian (2017), Analysis of aerosol composition data for western United States wildfires between 2005 and 2015: Dust emissions, chloride depletion, and most enhanced aerosol constituents, *J. Geophys. Res. Atmos.*, 8951–8966, doi:10.1002/2017JD026547.
- Schmid, D., D. Pridmore, G. Capitani, R. Battistutta, J. R. Neeser, and A. Jann (1997), Molecular organisation of the ice nucleation protein InaV from *Pseudomonas syringae*, *FEBS Lett.*, 414(3), 590–594, doi:10.1016/S0014-5793(97)01079-X.
- Schnell, R. C., and G. Vali (1972), Atmospheric ice nuclei from decomposing vegetation, *Nature*, 236, 163–165, doi:10.1038/236163a0.
- Schnell, R. C., and G. Vali (1976), Biogenic Ice Nuclei: Part I. Terrestrial and Marine Sources, *J. Atmos. Sci.*, 33(8), 1554–1564, doi:10.1175/1520-0469(1976)033<1554:BINPIT>2.0.CO;2.
- Scholze, M., W. Knorr, N. W. Arnell, and I. C. Prentice (2006), A climate-change risk analysis for world ecosystems, *Proc. Natl. Acad. Sci.*, 103(35), 13116–13120, doi:10.1073/pnas.0601816103.
- Sgro, A. E., and D. T. Chiu (2010), Droplet freezing, docking, and the exchange of immiscible phase and surfactant around frozen droplets, *Lab Chip*, 10(14), 1873, doi:10.1039/c001108h.
- Shaw, R. A., A. J. Durant, and Y. Mi (2005), Heterogeneous Surface Crystallization Observed in Undercooled Water, *J. Phys. Chem. B*, 109(20), 9865–9868, doi:10.1021/jp0506336.

- Shilling, J. E., T. J. Fortin, and M. a. Tolbert (2006), Depositional ice nucleation on crystalline organic and inorganic solids, *J. Geophys. Res.*, *111*(D12), D12204, doi:10.1029/2005JD006664.
- Southworth, M. W., P. K. Wolber, and G. J. Warren (1988), Nonlinear relationship between concentration and activity of a bacterial ice nucleation protein, *J. Biol. Chem.*, *263*(29), 15211–15216.
- Stan, C. A., S. K. Y. Tang, and G. M. Whitesides (2009a), Independent Control of Drop Size and Velocity in Microfluidic Flow-Focusing Generators Using Variable Temperature and Flow Rate, *Anal. Chem.*, *81*(6), 2399–2402, doi:10.1021/ac8026542.
- Stan, C. a, G. F. Schneider, S. S. Shevkoplyas, M. Hashimoto, M. Ibanescu, B. J. Wiley, and G. M. Whitesides (2009b), A microfluidic apparatus for the study of ice nucleation in supercooled water drops., *Lab Chip*, *9*(16), 2293–305, doi:10.1039/b906198c.
- Stavi, I., D. Barkai, Y. M. Knoll, H. A. Glion, I. Kutra, A. Brook, and E. Zaady (2017), Fire impact on soil-water repellency and functioning of semi-arid croplands and rangelands: Implications for prescribed burnings and wildfires, *Geomorphology*, *280*, 67–75, doi:10.1016/j.geomorph.2016.12.015.
- Steinke, I. et al. (2016), Ice nucleation activity of agricultural soil dust aerosols from Mongolia, Argentina, and Germany, *J. Geophys. Res. Atmos.*, *121*(22), 559–576, doi:10.1002/2016JD025160.
- Stephens, S. L., J. D. Miller, B. M. Collins, M. P. North, J. J. Keane, and S. L. Roberts (2016), Wildfire impacts on California spotted owl nesting habitat in the Sierra Nevada, *Ecosphere*, *7*(11), e01478, doi:10.1002/ecs2.1478.
- Stevens-Rumann, C. S., K. B. Kemp, P. E. Higuera, B. J. Harvey, M. T. Rother, D. C. Donato, P. Morgan, and T. T. Veblen (2018), Evidence for declining forest resilience to wildfires under climate change, edited by F. Lloret, *Ecol. Lett.*, *21*(2), 243–252, doi:10.1111/ele.12889.
- Stevens, B., and G. Feingold (2009), Untangling aerosol effects on clouds and precipitation in a buffered system, *Nature*, *461*(7264), 607–613, doi:10.1038/nature08281.
- Stith, J. L., L. F. Radke, and P. V Hobbs (1981), Particle emissions and the production of ozone and nitrogen oxides from the burning of forest slash, *Atmos. Environ.*, *15*(1), 73–82, doi:10.1016/0004-6981(81)90127-X.
- Stocker, T., D. Qin, G.-K. Plattner, M. Tignor, S. Allen, J. Boschung, A. Nauels, Y. Xia, V. Bex, and P. Midgley (2013), *IPCC, 2013: Climate Change 2013: The Physical Science Basis. Contribution of Working Group I to the Fifth Assessment Report of the Intergovernmental Panel on Climate Change*, Cambridge University Press, Cambridge, UK and New York, NY, USA.
- Storelvmo, T., J. E. Kristjánsson, U. Lohmann, T. Iversen, A. Kirkevåg, and Ø. Seland (2008), Modeling of the Wegener–Bergeron–Findeisen process—implications for

- aerosol indirect effects, *Environ. Res. Lett.*, 3(4), 045001, doi:10.1088/1748-9326/3/4/045001.
- Storelvmo, T., C. Hoose, and P. Eriksson (2011), Global modeling of mixed-phase clouds: The albedo and lifetime effects of aerosols, *J. Geophys. Res.*, 116(D5), D05207, doi:10.1029/2010JD014724.
- Stratmann, F., A. Kiselev, S. Wurzler, M. Wendisch, J. Heintzenberg, R. J. Charlson, K. Diehl, H. Wex, and S. Schmidt (2004), Laboratory Studies and Numerical Simulations of Cloud Droplet Formation under Realistic Supersaturation Conditions, *J. Atmos. Ocean. Technol.*, 21(6), 876–887, doi:10.1175/1520-0426(2004)021<0876:LSANSO>2.0.CO;2.
- Sullivan, R. C., L. Miñambres, P. J. DeMott, A. J. Prenni, C. M. Carrico, E. J. T. Levin, and S. M. Kreidenweis (2010), Chemical processing does not always impair heterogeneous ice nucleation of mineral dust particles, *Geophys. Res. Lett.*, 37(24), L24805, doi:10.1029/2010GL045540.
- Sun, M., S. S. Bithi, and S. A. Vanapalli (2011), Microfluidic static droplet arrays with tuneable gradients in material composition, *Lab Chip*, 11(23), 3949, doi:10.1039/c1lc20709a.
- Szakáll, M., K. Diehl, S. K. Mitra, and S. Borrmann (2009), A Wind Tunnel Study on the Shape, Oscillation, and Internal Circulation of Large Raindrops with Sizes between 2.5 and 7.5 mm, *J. Atmos. Sci.*, 66(3), 755–765, doi:10.1175/2008JAS2777.1.
- Tabazadeh, A., Y. S. Djikaev, and H. Reiss (2002), Surface crystallization of supercooled water in clouds, *Proc. Natl. Acad. Sci.*, 99(25), 15873–15878, doi:10.1073/pnas.252640699.
- Tajiri, T., K. Yamashita, M. Murakami, A. Saito, K. Kusunoki, N. Orikasa, and L. Lilie (2013), A Novel Adiabatic-Expansion-Type Cloud Simulation Chamber, *J. Meteorol. Soc. Japan. Ser. II*, 91(5), 687–704, doi:10.2151/jmsj.2013-509.
- Tarn, M. D. et al. (2018), The study of atmospheric ice-nucleating particles via microfluidically generated droplets, *Microfluid. Nanofluidics*, 22(5), 52, doi:10.1007/s10404-018-2069-x.
- Thomas, C., D. Lampert, and D. Reible (2014), Remedy performance monitoring at contaminated sediment sites using profiling solid phase microextraction (SPME) polydimethylsiloxane (PDMS) fibers, *Environ. Sci. Process. Impacts*, 16(3), 445–452, doi:10.1039/C3EM00695F.
- Tkacik, D. S. et al. (2017), A dual-chamber method for quantifying the effects of atmospheric perturbations on secondary organic aerosol formation from biomass burning emissions, *J. Geophys. Res. Atmos.*, 122(11), 6043–6058, doi:10.1002/2016JD025784.
- Tobo, Y. (2016), An improved approach for measuring immersion freezing in large droplets over a wide temperature range, *Sci. Rep.*, 6(1), 32930, doi:10.1038/srep32930.

- Tobo, Y., P. J. DeMott, T. C. J. Hill, a. J. Prenni, N. G. Swoboda-Colberg, G. D. Franc, and S. M. Kreidenweis (2014), Organic matter matters for ice nuclei of agricultural soil origin, *Atmos. Chem. Phys.*, *14*(16), 8521–8531, doi:10.5194/acp-14-8521-2014.
- Turner, M. a., F. Arellano, and L. M. Kozloff (1990), Three separate classes of bacterial ice nucleation structures, *J. Bacteriol.*, *172*(5), 2521–2526.
- Turner, M. a., F. Arellano, and L. M. Kozloff (1991), Components of ice nucleation structures of bacteria, *J. Bacteriol.*, *173*(20), 6515–6527.
- Twohy, C. H., M. D. Petters, J. R. Snider, B. Stevens, W. Tahnk, M. Wetzel, L. Russell, and F. Burnet (2005), Evaluation of the aerosol indirect effect in marine stratocumulus clouds: Droplet number, size, liquid water path, and radiative impact, *J. Geophys. Res.*, *110*(D8), D08203, doi:10.1029/2004JD005116.
- Twohy, C. H. et al. (2010), Relationships of Biomass-Burning Aerosols to Ice in Orographic Wave Clouds, *J. Atmos. Sci.*, *67*(8), 2437–2450, doi:10.1175/2010JAS3310.1.
- Umo, N. S., B. J. Murray, M. T. Baeza-Romero, J. M. Jones, a. R. Lea-Langton, T. L. Malkin, D. O’Sullivan, L. Neve, J. M. C. Plane, and A. Williams (2015), Ice nucleation by combustion ash particles at conditions relevant to mixed-phase clouds, *Atmos. Chem. Phys.*, *15*(9), 5195–5210, doi:10.5194/acp-15-5195-2015.
- Vali, G. (1971), Quantitative Evaluation of Experimental Results an the Heterogeneous Freezing Nucleation of Supercooled Liquids, *J. Atmos. Sci.*, *28*, 402–409, doi:10.1175/1520-0469(1971)028<0402:QEOERA>2.0.CO;2.
- Vali, G. (1999), Ice Nucleation - Theory: A Tutorial, *NCAR/ASP 1999 Summer Colloq.*, 1–22.
- Vali, G. (2008), Repeatability and randomness in heterogeneous freezing nucleation, *Atmos. Chem. Phys.*, *8*(16), 5017–5031, doi:10.5194/acp-8-5017-2008.
- Vali, G. (2014), Interpretation of freezing nucleation experiments: singular and stochastic; sites and surfaces, *Atmos. Chem. Phys.*, *14*(11), 5271–5294, doi:10.5194/acp-14-5271-2014.
- Vali, G., and E. J. Stansbury (1966), Time-Dependent Characteristics of the Heterogeneous Nucleation of Ice, *Can. J. Phys.*, *44*(3), 477–502, doi:10.1139/p66-044.
- Vali, G., P. J. DeMott, O. Möhler, and T. F. Whale (2015), Technical Note: A proposal for ice nucleation terminology, *Atmos. Chem. Phys.*, *15*(18), 10263–10270, doi:10.5194/acp-15-10263-2015.
- Varanasi, K. K., T. Deng, J. D. Smith, M. Hsu, and N. Bhate (2010), Frost formation and ice adhesion on superhydrophobic surfaces, *Appl. Phys. Lett.*, *97*(23), 234102, doi:10.1063/1.3524513.
- Vergara-Temprado, J., A. K. Miltenberger, K. Furtado, D. P. Grosvenor, B. J. Shipway, A. A. Hill, J. M. Wilkinson, P. R. Field, B. J. Murray, and K. S. Carslaw (2018), Strong control of Southern Ocean cloud reflectivity by ice-nucleating particles, *Proc. Natl.*

- Acad. Sci.*, 115(11), 2687–2692, doi:10.1073/pnas.1721627115.
- Wagner, R., A. Kiselev, O. Möhler, H. Saathoff, and I. Steinke (2016), Pre-activation of ice-nucleating particles by the pore condensation and freezing mechanism, *Atmos. Chem. Phys.*, 16(4), 2025–2042, doi:10.5194/acp-16-2025-2016.
- Wang, B., A. T. Lambe, P. Massoli, T. B. Onasch, P. Davidovits, D. R. Worsnop, and D. a. Knopf (2012), The deposition ice nucleation and immersion freezing potential of amorphous secondary organic aerosol: Pathways for ice and mixed-phase cloud formation, *J. Geophys. Res.*, 117(D16), D16209, doi:10.1029/2012JD018063.
- Wang, B., T. H. Harder, S. T. Kelly, D. S. Piens, S. China, L. Kovarik, M. Keiluweit, B. W. Arey, M. K. Gilles, and A. Laskin (2016a), Airborne soil organic particles generated by precipitation, *Nat. Geosci.*, 9(6), 433–437, doi:10.1038/ngeo2705.
- Wang, B., D. A. Knopf, S. China, B. W. Arey, T. H. Harder, M. K. Gilles, and A. Laskin (2016b), Direct observation of ice nucleation events on individual atmospheric particles, *Phys. Chem. Chem. Phys.*, 18(43), 29721–29731, doi:10.1039/C6CP05253C.
- Ward, P. J., and P. J. DeMott (1989), Preliminary experimental evaluation of Snomax (TM) snow inducer, nucleus *Pseudomonas syringae*, as an artificial ice for weather modification, *J. Weather Modif.*, 21(1), 9–13.
- Welti, A., F. Lüönd, O. Stetzer, and U. Lohmann (2009), Influence of particle size on the ice nucleating ability of mineral dusts, *Atmos. Chem. Phys.*, 9(18), 6705–6715, doi:10.5194/acp-9-6705-2009.
- Westerling, A. L., H. G. Hidalgo, D. R. Cayan, and T. W. Swetnam (2006), Warming and earlier spring increase Western U.S. forest wildfire activity, *Science* (80-.), 313(5789), 940–943, doi:10.1126/science.1128834.
- Wex, H., P. J. DeMott, Y. Tobo, S. Hartmann, M. Rösch, T. Clauss, L. Tomsche, D. Niedermeier, and F. Stratmann (2014), Kaolinite particles as ice nuclei: learning from the use of different kaolinite samples and different coatings, *Atmos. Chem. Phys.*, 14(11), 5529–5546, doi:10.5194/acp-14-5529-2014.
- Wex, H. et al. (2015), Intercomparing different devices for the investigation of ice nucleating particles using Snomax[®] as test substance, *Atmos. Chem. Phys.*, 15(3), 1463–1485, doi:10.5194/acp-15-1463-2015.
- Whale, T. F., B. J. Murray, D. O’Sullivan, T. W. Wilson, N. S. Umo, K. J. Baustian, J. D. Atkinson, D. A. Workneh, and G. J. Morris (2015), A technique for quantifying heterogeneous ice nucleation in microlitre supercooled water droplets, *Atmos. Meas. Tech.*, 8(6), 2437–2447, doi:10.5194/amt-8-2437-2015.
- Wheeler, M. J., R. H. Mason, K. Steunenberg, M. Wagstaff, C. Chou, and A. K. Bertram (2015), Immersion Freezing of Supramicron Mineral Dust Particles: Freezing Results, Testing Different Schemes for Describing Ice Nucleation, and Ice Nucleation Active Site Densities, *J. Phys. Chem. A*, 119(19), 4358–4372, doi:10.1021/jp507875q.
- Wilson, T. W. et al. (2015), A marine biogenic source of atmospheric ice-nucleating

- particles, *Nature*, 525(7568), 234–238, doi:10.1038/nature14986.
- Wright, T. P., and M. D. Petters (2013), The role of time in heterogeneous freezing nucleation, *J. Geophys. Res. Atmos.*, 118(9), 3731–3743, doi:10.1002/jgrd.50365.
- Wright, T. P., M. D. Petters, J. D. Hader, T. Morton, and A. L. Holder (2013), Minimal cooling rate dependence of ice nuclei activity in the immersion mode, *J. Geophys. Res. Atmos.*, 118(18), 10,535–10,543, doi:10.1002/jgrd.50810.
- Yakobi-Hancock, J. D., L. a. Ladino, and J. P. D. Abbatt (2013), Feldspar minerals as efficient deposition ice nuclei, *Atmos. Chem. Phys.*, 13(22), 11175–11185, doi:10.5194/acp-13-11175-2013.
- Yankofsky, S. a., Z. Levin, T. Bertold, and N. Sandlerman (1981), Some Basic Characteristics of Bacterial Freezing Nuclei, *J. Appl. Meteorol.*, 20, 1013–1019, doi:10.1175/1520-0450(1981)020<1013:SBCOBF>2.0.CO;2.
- Yin, Y., S. Wurzler, Z. Levin, and T. G. Reisin (2002), Interactions of mineral dust particles and clouds: Effects on precipitation and cloud optical properties, *J. Geophys. Res. Atmos.*, 107(23), 1–14, doi:10.1029/2001JD001544.
- Yokelson, R. J., R. Susott, D. E. Ward, J. Reardon, and D. W. T. Griffith (1997), Emissions from smoldering combustion of biomass measured by open-path Fourier transform infrared spectroscopy, *J. Geophys. Res. Atmos.*, 102(D15), 18865–18877, doi:10.1029/97JD00852.
- Yokelson, R. J., J. G. Goode, D. E. Ward, R. A. Susott, R. E. Babbitt, D. D. Wade, I. Bertschi, D. W. T. Griffith, and W. M. Hao (1999), Emissions of formaldehyde, acetic acid, methanol, and other trace gases from biomass fires in North Carolina measured by airborne Fourier transform infrared spectroscopy, *J. Geophys. Res. Atmos.*, 104(D23), 30109–30125, doi:10.1029/1999JD900817.
- Zhang, Y., A. Macke, and F. Albers (1999), Effect of crystal size spectrum and crystal shape on stratiform cirrus radiative forcing, *Atmos. Res.*, 52(1–2), 59–75, doi:10.1016/S0169-8095(99)00026-5.
- Zobrist, B. et al. (2006), Oxalic acid as a heterogeneous ice nucleus in the upper troposphere and its indirect aerosol effect, *Atmos. Chem. Phys.*, 6, 3115–3129.
- Zobrist, B., T. Koop, B. P. Luo, C. Marcolli, and T. Peter (2007), Heterogeneous ice nucleation rate coefficient of water droplets coated by a nonadecanol monolayer, *J. Phys. Chem. C*, 111(5), 2149–2155, doi:10.1021/jp066080w.
- Zobrist, B., C. Marcolli, T. Peter, and T. Koop (2008), Heterogeneous Ice Nucleation in Aqueous Solutions: the Role of Water Activity, *J. Phys. Chem. A*, 112(17), 3965–3975, doi:10.1021/jp7112208.
- Zolles, T., J. Burkart, T. Häusler, B. Pummer, R. Hitznerberger, and H. Grothe (2015), Identification of Ice Nucleation Active Sites on Feldspar Dust Particles, *J. Phys. Chem. A*, 119(11), 2692–2700, doi:10.1021/jp509839x.